UNCLASSIFIED

AD NUMBER

AD910446

LIMITATION CHANGES

TO:

Approved for public release; distribution is unlimited. Document partially illegible.

FROM:

Distribution authorized to U.S. Gov't. agencies only; Test and Evaluation; MAR 1973. Other requests shall be referred to Army Materials and Mechanics Research Center, Attn: AMXMR-PL, Watertown, MA 02172. Document partially illegible.

AUTHORITY

darpa, ltr, 19 dec 1974

THIS PAGE IS UNCLASSIFIED

Best
Available
Copy

THIS REPORT HAS BEEN DELIMITED
AND CLEARED FOR PUBLIC RELEASE
UNDER DOD DIRECTIVE 5200.20 AND
NO RESTRICTIONS ARE IMPOSED UPON
ITS USE AND DISCLOSURE.

DISTRIBUTION STATEMENT A

APPROVED FOR PUBLIC RELEASE;
DISTRIBUTION UNLIMITED.

AD910446



AD

AMMRC CTR 73-9

BRITTLE MATERIALS DESIGN, HIGH TEMPERATURE GAS TURBINE

Technical Report By:

Arthur F. McLean, Ford Motor Company, Dearborn, Michigan 48121
Eugene A. Fisher, Ford Motor Company, Dearborn, Michigan 48121
Raymond J. Bratton, Westinghouse Electric Corporation, Pittsburgh, Pennsylvania 15235

March 1973

Interim Report, July 1, 1972 to December 31, 1972

Contract Number DAAG 46-71-C-0162

Sponsored by the Advanced Research Projects Agency

ARPA Order Number 1849

Project Code Number 1D10

Agency Accession Number DA OD 4733

DDC
RECEIVED
JUN 8 1973
C

Distribution limited to U.S. Government agencies only; Test and Evaluation data; March 1973. Other requests for this document must be referred to the Director, Army Materials and Mechanics Research Center, ATTN: AMXMR-PL, Watertown, Massachusetts 02172

Prepared for

ARMY MATERIALS AND MECHANICS RESEARCH CENTER
Watertown, Massachusetts 02172

The findings in this report are not to be construed as an official Advanced Research Projects Agency, Department of the Army, or U.S. Government position, either expressed or implied, unless so designated by other authorized documents.

Mention of any trade names or manufacturers in this report shall not be construed as advertising nor as an official indorsement or approval of such products or companies by the United States Government

DISPOSITION INSTRUCTIONS

Destroy this report when it is no longer needed. Do not return it to the originator.

AMMRC CTR 73-9

BRITTLE MATERIALS DESIGN, HIGH TEMPERATURE GAS TURBINE

Technical Report By:

Arthur F. McLean, Ford Motor Company, Dearborn, Michigan 48121
Eugene A. Fisher, Ford Motor Company, Dearborn, Michigan 48121
Raymond J. Bratton, Westinghouse Electric Corporation, Pittsburgh, Pennsylvania 15235

March, 1973

Interim Report, July 1, 1972 to December 31, 1972

Contract Number DAAG 46-71-C-0162

Sponsored by the Advanced Research Projects Agency

ARPA Order Number 1849

Project Code Number 1D10

Agency Accession Number DA OD 4733

Distribution limited to U.S. Government agencies only: Test and Evaluation data: March 1973. Other requests for this document must be referred to the Director, Army Materials and Mechanics Research Center, ATTN: AMXMR-PL, Watertown, Massachusetts 02172

Prepared for:

ARMY MATERIALS AND MECHANICS RESEARCH CENTER
Watertown, Massachusetts 02172

ABSTRACT

The "Brittle Materials Design, High Temperature Gas Turbine" program is to demonstrate successful use of brittle materials in demanding high temperature structural applications. A small vehicular gas turbine and a large stationary gas turbine, each utilizing uncooled ceramic components, will be used in this iterative design and materials development program. Both the contractor, Ford Motor Company, and the subcontractor, Westinghouse Electric Corporation, have had in-house research programs in this area prior to this contract.

In the vehicular turbine project, steady state and transient stresses were determined for a monolithic turbine rotor of hot-pressed silicon nitride. A new rotor concept, using both hot-pressed and reaction-sintered silicon nitride, has been analyzed for steady-state stresses; work on bonding the two materials appears promising. Improvements in chemically vapor deposited silicon carbide rotors include the forming of hoops of sufficient thickness and the production of material of considerably improved purity. Blade cracking of the first stage ceramic stator was duplicated on a thermal shock test rig, leading to improved durability through a change in the blade design. Some fabrication variables of reaction-sintered silicon nitride were studied, which indicate methods for material improvements.

In the stationary turbine project, a model of the 3-piece stator vane assembly demonstrated that design integrity was maintained when differential motion exceeded design limits fivefold. The 3-dimensional finite element stress and heat transfer analytical program has been applied to rotor blades, and preliminary results are presented. Statistical data treatment has been applied to hot-pressed silicon nitride, and additional property data plus corrosion testing results are presented for hot-pressed silicon carbide. It was found necessary to design and construct a new static rig, delaying testing under turbine conditions until August.

FOREWORD

This report is the third semi-annual technical report of the "Brittle Materials Design, High Temperature Gas Turbine" program initiated by the Advanced Research Projects Agency, ARPA Order Number 1849, and monitored by the Army Materials and Mechanics Research Center, under Contract Number DAAG-46-71-C-0162. This is an incrementally-funded five year program.

Since this is an iterative design and materials development program, design concepts and materials selection and/or properties presented in this report will probably not be those finally utilized. Thus all design and property data contained in the semi-annual reports must be considered tentative, and the reports should be considered to be illustrative of the design, materials, processing, and NDT techniques being developed for brittle materials.

The principal investigator of this program is Mr. A. F. McLean, Ford Motor Company, and the technical monitor is Dr. A. E. Gorum, AMMRC. The authors would like to acknowledge the valuable contributions in the performance of this work by the following people:

Ford Motor Company

D. Alexander, R. R. Baker, P. Beardmore, D. J. Cassidy, J. C. Caverly, J. J. Charneski, D. A. Davis, G. C. DeBell, A. Ezis, W. A. Fate, M. U. Goodyear, D. L. Hartsock, P. H. Havstad, E. R. Herrmann, R. A. Jeryan, C. F. Johnson, K. H. Kinsman, J. A. Mangels, S. V. McGrath, W. E. Meyer, T. G. Mohr, P. F. Nicholls, A. Paluszny, J. J. Schuldies, J. M. Scofield, K. H. Styhr, W. Trela, T. J. Whalen.

Westinghouse Electric Corporation

C. R. Booher, Jr., S. M. DeCorso, J. DeKlerk, E. S. Diaz, D. M. Fantozzi, W. C. Frazier, A. N. Holden, D. D. Lawthers, L. Kish, R. Kossowsky, F. F. Lange, S. Y. Lee, S. D. Leshnoff, D. G. Miller, S. Mumford, T. J. Rahaim, J. D. Roughgarden, R. J. Schaller, S. C. Singhal, S. Twiss, C. Visser, E. H. Wiley, D. D. Wood, W. E. Young.

Army Material and Mechanics Research Center

E. M. Lenoe, R. N. Katz, D. R. Messier, H. Priest

TABLE OF CONTENTS

	Page No.
Title Page	i
Abstract	ii
Forward	iii
Table of Contents	iv
List of Illustrations	v
List of Tables	xv
1. Introduction	1
2. Summary of Progress	9
2.1 Vehicular Turbine Project	9
2.2 Stationary Turbine Project	11
2.3 Materials Technology - Vehicular & Stationary Turbine Projects	13
3. Progress on the Vehicular Turbine Project	15
3.1 Ceramic Rotor Development	15
3.1.1 Design and Analysis	17
3.1.2 Materials and Fabrication	39
3.1.3 Testing	60
3.2 Metal Rotor Development	63
3.2.1 Metal Rotor Development	63
3.3 Ceramic Stators, Shrouds, and Nose Cones	73
3.3.1 Material and Fabrication	74
3.3.2 Testing	80
4. Progress on the Stationary Turbine Project	89
4.1 Stator Vane Development	89
4.1.1 Design	92
4.1.2 Stress Analysis	94
4.1.3 Vane Fabrication	110
4.1.4 Static Rig Testing	116
4.2 Rotor Blade Development	119
4.2.1 Three-Dimensional Finite Element Stress Analysis	120
4.2.2 Stress Analysis of Blades	121
5. Progress on Materials Technology - Vehicular and Stationary Turbine Projects	133
5.1 Materials Engineering Data	133
5.1.1 Physical Properties of Ceramic Materials	135
5.2 Material Sciences	171
5.2.1 Characterization of Reaction Sintered Silicon Nitride	173
5.2.2 Microstructural Characterization of Fully Dense Silicon Nitride and Silicon Carbide	189
5.2.3 Gas-Solid Reactions	204
5.3 Non Destructive Evaluation of Materials	211
5.3.1 Ultrasonic NDE	212
5.3.2 Acoustic Emission	219
5.3.3 X-Ray Radiography	220
6. References	223

LIST OF ILLUSTRATIONS

		Page No.
Figure 1.1	Flow Path Schematic of Vehicular Gas Turbine	2
Figure 1.2	30 Mw Test Turbine Flow Path	3
Figure 1.3	Brittle Material Design/High Temperature Gas Turbine - Breakdown of Major Elements Reported	4
Figure 1.4	Brittle Material Design/High Temperature Gas Turbine - Block Diagram Flow Chart of Iterative Development	6
Figure 3.1	Finite Element Model of First Stage Design C Rotor	19
Figure 3.2	Finite Element Model of Second Stage Design C Rotor	20
Figure 3.3	Radial Stresses in Neck Area of First Stage Rotor at Full Speed	21
Figure 3.4	Radial Stresses in Neck Area of Second Stage Rotor at Full Speed	22
Figure 3.5	Isotherms For Rotors and Attachment Assembly at Full Speed	23
Figure 3.6	Circumferential Stresses in Hub Area of First Stage Rotor at Full Speed	25
Figure 3.7	Circumferential Stresses in Hub Area of First Stage Rotor at Full Speed	26
Figure 3.8	Isotherms for Rotors and Attachment Assembly at Idle Speed	27
Figure 3.9	Transient Stresses in Neck Area of Rotors	29
Figure 3.10	Transient Stresses in Hub Area of Rotors	30
Figure 3.11	Isotherms for Rotors and Attachment Assembly, First Transient	31
Figure 3.12	Isotherms for Rotors and Attachment Assembly, Second Transient	31
Figure 3.13	Five Joint Configurations Studied for the Duo-Density Rotor Concept	33
Figure 3.14	Isotherms Determined for Idle Speed, First Stage Duo-Density Rotor	33

		Page No.
Figure 3.15	Isotherms Determined for Idle Speed, Second Stage Duo-Density Rotor	34
Figure 3.16	Isotherms Determined For Full Speed, First Stage Duo-Density Rotor	34
Figure 3.17	Isotherms Determined for Full Speed, Second Stage Duo-Density Rotor	35
Figure 3.18	Hoop Stresses for First Stage Rotor Joint	36
Figure 3.19	Radial Stresses for Second Stage Rotor Joint	36
Figure 3.20	Hoop Stresses for Second Stage Rotor Joint	37
Figure 3.21	Radial Stresses for Second Stage Rotor Joint	37
Figure 3.22	Duo-Density Turbine Rotor Concept	40
Figure 3.23	Injection Molded Biade Ring for the Duo-Density Rotor	41
Figure 3.24	Simplified Silicon Nitride Components Used for Bonding Studies	43
Figure 3.25	Bonded Duo-Density Shape	43
Figure 3.26	Sectioned Duo-Density Shape	44
Figure 3.27	Magnified View of Joints in Duo-Density Shapes	44
Figure 3.28	Effect of Reaction with Graphite on Silicon Nitride	45
Figure 3.29	Surface of Silicon Nitride After Hot-Pressing with a Molybdemium Foil Barrier to Prevent Reaction	45
Figure 3.30	Microstructure of Duo-Density Bond, Sample HP-162. 500X	47
Figure 3.31	Microstructure of Duo-Density Bond, Sample HP-165. 500X	47
Figure 3.32	Lucas Concept of Hot-Pressing in Silicon Nitride Turbine Rotors	48
Figure 3.33	CVD Silicon Carbide Rotor	50
Figure 3.34	CVD Silicon Carbide Rotor Showing Fully Filled Blades	50

		Page No.
Figure 3.35	Thin Cross Section of CVD Silicon Carbide	51
Figure 3.36	Microstructure of CVD Silicon Carbide at Joint of Two Adjacent Regions. 7100X	51
Figure 3.37	Microstructure of CVD Silicon Carbide at Opaque Region. 7100X	52
Figure 3.38	Microstructure of CVD Silicon Carbide at Translucent Region. 7100X	53
Figure 3.39	Shaped Graphite Punches	54
Figure 3.40	Hot-Pressed Silicon Nitride Blank	54
Figure 3.41	Ultrasonic Machining of Neck Area	55
Figure 3.42	Ultrasonic Tool for Machining Constant Thickness Blades	55
Figure 3.43	Bendix Cavitron Unit Used for Ultrasonic Machining Development	57
Figure 3.44	Disk of Hot-Pressed Silicon Nitride Showing Several Constant Airfoil Blades	58
Figure 3.45	Hot-Pressed Disk with Extra Stock Removed	59
Figure 3.46	Turbine Rotor Test Rig	61
Figure 3.47	Radiographic Reversal Print Showing X-Ray Indications	65
Figure 3.48	Angular Carbide Formation in Long Life Rotor	67
Figure 3.49	Script Type Carbide Formation in Failed Rotor	67
Figure 3.50	Interior Grain Size Comparison Between Long Life and Failed Rotors	68
Figure 3.50a	Grain Size of Failed Rotor. Grain Size Approximately 1/4 inch	68
Figure 3.50b	Grain Size of Long Life Rotor. Grain Size Approximately 1/16 inch	68
Figure 3.51	Two Diameter Mode Shape. 3383 Cycles Per Second	69
Figure 3.52	Two Diameter Plus One Radial Mode Shape 4925 Cycles Per Second	70
Figure 3.53	Design B Ceramic Nose Cone, Stators, and Shrouds	74

		Page No.
Figure 3.54	Particle Size Distribution of Silicon Metal Powder	75
Figure 3.55	First Stage Stator Segments Showing Locating Tabs on Revised Design. A - Revised Design, B - Old Design	76
Figure 3.56	Second Stage Stator Illustrating Experimental Assembly Method	77
Figure 3.57	Microstructure of Joint Between Injection Molded Stator Segments. 150X	78
Figure 3.58	Thermal Shock Test Rig	81
Figure 3.59	First Stage Stator Segments, Normal Design	82
Figure 3.60	Second Stage Stator Segments, Normal Design	83
Figure 3.61	First Stage Stator Segments with Thicker Trailing Edges	83
Figure 3.62	First Stage Stator Segments of Reduced Chord	84
Figure 3.63	Design B Nose Cone Modification	88
Figure 4.1	Schematic of 30 Mw Test Turbine Flow Path	91
Figure 4.2	Kinematic Model of 3 Piece Ceramic Vane Design with Support Structure	93
Figure 4.3	Stress History for Silicon Nitride Airfoils From 1950°F & 2500°F	94
Figure 4.4	Results of Analysis Showing Maximum Transient Thermal Stress at the Leading Edge of a Silicon Nitride Vane	95
Figure 4.5	Temperature Decay Curve for Ceramic Vane Under Emergency Shut Down From 2500°F	96
Figure 4.6	Temperature Contours in Solid Half Size Silicon Nitride Airfoils	96
Figure 4.7	Stress Contours in Solid Half Size Silicon Nitride Airfoils	97
Figure 4.8	Airfoil End Effects Model	98
Figure 4.9	Airfoil End Finite Element Model	99
Figure 4.10	Loads and Interfaces	99

		Page No.
Figure 4.11	One-Dimensional Force Equilibrium Diagram	101
Figure 4.12	Maximum Tensile Contact Stress vs Start-Up Friction With Radial Load and Tolerance as Parameters: Vane-Endcap Silicon Nitride	102
Figure 4.13	Finite Element Geometry - Endcap With Toroidal Groove	103
Figure 4.14	Maximum Plate Stress in Outer Endcap Under Thermal Steady State Showing Groove Depth Effect and Adjustment for Assymetry	104
Figure 4.15	Boundary Conditions Gas Temperature and Film Coefficient	106
Figure 4.16	Cylinder Model Finite Element and Finite Difference	107
Figure 4.17	Temperature vs Time (Cylinder)	108
Figure 4.18	Stress vs Time (Cylinder)	109
Figure 4.19	Major Steps in the Machining of the Airfoil	112
Figure 4.20	Steps in the Grinding of an End Cap	112
Figure 4.21	Plan View Static Test Rig for 2500°F Test of Ceramic Vanes	117
Figure 4.22	Root Model	121
Figure 4.23	Finite Element Root Models - 45° & 60°	122
Figure 4.24	Computer Plot of Ceramic Rotating Blade	123
Figure 4.25	Airfoil, Slice Between Vertical Sections 1000 and 5000	124
Figure 4.26	Airfoil, Slice Between Horizontal Sections 5000 and 8000	125
Figure 4.27	Platform, Slice Between Sections 8000 and 9000	125
Figure 4.28	Platform, Slice Between Horizontal Sections 9000 and 11000	125
Figure 4.29	Platform, Slice Between Horizontal Sections 11000 and 12000	126
Figure 4.30	Radial Stress Contours Airfoil Convex Surface	126
Figure 4.31	Radial Stress Contours Airfoil Middle Surface	127

		Page No.
Figure 4.32	Radial Stress Airfoil Concave Surface	127
Figure 4.33	Vertical Cross Section 300	128
Figure 4.34	Vertical Cross Section 400	129
Figure 4.35	Vertical Cross Section 500	130
Figure 4.36	Vertical Cross Section 700	131
Figure 5.1	Predicted and Measured Failure Stress of Hot Pressed Silicon Nitride for Various Test Modes	138
Figure 5.2	Average Failure Stress for Hot Pressed Silicon Nitride for Various Test Modes as Predicted by Two Parameter Weibuil Theory Based on Volume	139
Figure 5.3	Tensile Specimens	139
Figure 5.4	Tensile Strength as a Function of Temperature and Strain Rate for Hot Pressed Silicon Nitride	141
Figure 5.5	Young's Modulus as a Function of Temperature for Silicon Nitride by Various Methods	141
Figure 5.6	Stress-Rupture Properties of Silicon Nitride He Atmosphere	142
Figure 5.7	Steady State Creep Rate vs 1/T at 10,000 psi in He Atmosphere	143
Figure 5.8	Activation Energy for Viscous Flow for SiO_2 and CaO Doped SiO_2	144
Figure 5.9	Four Point Flexural Strength of Hot Pressed Silicon Nitride vs Temperature for Various Average Loading Rates	145
Figure 5.10	Four Point Flexural Strength of Hot Pressed Silicon Nitride Temperature for Various Average Loading Rates	146
Figure 5.11	Flexural Strength of Hot Pressed Silicon Carbide	146
Figure 5.12	Test Specimen Dimensions	147
Figure 5.13	Flexural Strength of Hot-Pressed Silicon Nitride	148
Figure 5.14	Flexural Strength of Silicon Carbide	148

		Page No.
Figure 5.15	Compression of Creep Silicon Nitride	150
Figure 5.16	Comparison of Thermal Diffusivity Values for Heat Conducted Parallel to the Hot Pressing Direction of Silicon Nitride	150
Figure 5.17	Comparison of Thermal Diffusivity Values for Heat Conducted Perpendicular to the Hot Pressing Direction of Silicon Nitride	151
Figure 5.18	Comparison of Thermal Conductivity Values for Heat Conducted Parallel to the Hot Pressing Direction of Silicon Nitride	151
Figure 5.19	Comparison of Thermal Conductivity Values for Heat Conducted Perpendicular to the Hot Pressing Direction of Silicon Nitride	152
Figure 5.20	Thermal Expansion of Hot Pressed Silicon Nitride as a Function of Temperature	152
Figure 5.21	Average Coefficient of Thermal Expansion vs Temperature Dependence of Direction of Expansion Relative to Hot Press Direction Insignificant Compared to Measurement and Billet to Billet Scatter	153
Figure 5.22	Hot Pressed Silicon Carbide-Thermal Diffusivity and Thermal Expansion	153
Figure 5.23	Notched Cylinder of Silicon Nitride for Thermal Fracture Showing Orientation of Finite Element Mesh	154
Figure 5.24	Schematic Diagram of Ultrasonic Equipment	155
Figure 5.25	Shear Modulus of Hot-Pressed Silicon Nitride	156
Figure 5.26	Shear Modulus of Hot-Pressed Silicon Carbide	156
Figure 5.27	Shear Modulus of Lithium-Aluminum-Silicate	157
Figure 5.28	Surface Appearance of a Silicon Nitride Test Specimen after 250 Hours of Exposure at 2000°F to Combustor Gases Containing 0.5 wt % S, 5 ppm Na, 2 ppm V and 0.6 ppm Mg	160
Figure 5.29	Effect of Fuel Contaminants on the Corrosion of Hot Pressed Silicon Nitride in Turbine Test Passage at 2000°F and 3 atm Pressure	161
Figure 5.30	Surface Appearance of a SiC Test Specimen After 250 Hours of Exposure at 2000°F to Combustor Gases Containing 0.5 wt % S, 5 ppm Na, 2 ppm V and 0.6 ppm Mg	162

		Page No.
Figure 5.31	Effect of Fuel Contaminants on the Corrosion of Hot Pressed SiC in Turbine Test Passage at 2000°F and 3 atm pressure	162
Figure 5.32	Corrosion of Various Materials in Turbine Test Passage, Exposed to Combustor Gases Contaminated with 0.5% Sulfur, 5 ppm Sodium, 2 ppm Vanadium and 0.6 ppm Magnesium	164
Figure 5.33	Low Cycle Fatigue Testing Schedule at 1800°F and 2300°F	165
Figure 5.34	Static Coefficient of Friction for Hot Pressed Silicon Nitride vs Various Materials	165
Figure 5.35	Wear and Fret Test Apparatus	167
Figure 5.36	Surface of Wear and Fret Specimens of Hot Pressed Silicon Nitride	168
Figure 5.37	Cut Away View of Torsion Test Facility Showing Furnace Grips and Strain readout	169
Figure 5.38	The Effect of Alpha-Beta Ratio on the Density of Silicon Nitride	174
Figure 5.39	The Effect of Alpha-Beta Ratio on the Transverse Strength of Silicon Nitride	175
Figure 5.40	The Effect of Density on the Transverse Strength of Silicon Nitride	175
Figure 5.41	The Effect of Alpha-Beta Ratio on the Modulus of Elasticity of Silicon Nitride	176
Figure 5.42	Thermal Expansion of Two Samples of Silicon Nitride of Differing Phase Compositions	176
Figure 5.43	Microstructure of Silicon Nitride of Phase Composition 75% alpha, 25% beta 24,800X	178
Figure 5.44	Microstructure of Silicon Nitride of Phase Composition 10% alpha, 90% beta 24,800X	178
Figure 5.45	Oxidation of Silicon Nitride	180
Figure 5.46	Effect of Glassy Coating on Further Oxidation	181
Figure 5.47	Profile of Cristobalite Formation	182
Figure 5.48	Analyses of Glassy Coating	183

		Page No.
Figure 5.49	Transverse Strength of Silicon Nitride Compositions vs Temperature	185
Figure 5.50	Plot of Transverse Strength of Silicon Nitride vs Various Time-Temperature Relationships	186
Figure 5.51	Microstructure of Silicon Nitride Reaction Sintered for 36 Hours at 2300°F Followed by 4 Hours at 2660°F	187
Figure 5.52	Microstructure of Silicon Nitride Reaction Sintered for 24 Hours at 2300°F Followed by 24 Hours at 2660°F	187
Figure 5.53	Effect of Impurities on Flexural Strength (4 pt. bend) of Silicon Nitride	190
Figure 5.54	Typical Auger Analysis Trace of a Fresh Fracture Surface	191
Figure 5.55	Elements Distribution Profiles, Hot Pressed Silicon Nitride, Auger Analysis	192
Figure 5.56	Light Micrographs Showing Orientation of Lenticular, Non-Densified Silicon Nitride Inclusion in Flexural Test Specimens with Respect to Hot Pressing Direction	194
Figure 5.57	Scanning Electron Micrographs	194
Figure 5.58	Pole-Figure Analysis	195
Figure 5.59	Microprobe Line Traces	198
Figure 5.60	SEM Micrograph of Polished and Etched Surface Hot Pressed SiC	199
Figure 5.61	Replica Transmission Micrographs of Room Temperature Fracture Surfaces	200
Figure 5.62	Replica Transmission Micrograph of 752°F Fracture Surfaces	200
Figure 5.63	Replica Transmission Micrograph of 1115°F Fracture Surfaces	200
Figure 5.64	Replica Transmission Micrograph of 1472°F Fracture Surfaces	201
Figure 5.65	Replica Transmission Micrograph of 1832°F Fracture Surfaces	201
Figure 5.66	SEM Micrograph of Fracture Surfaces, Hot Pressed SiC	201

		Page No.
Figure 5.67	Non-Dispersive X-Ray Analysis, Fracture Surface	202
Figure 5.68	Columnar Structure in CVD-SiC Long Grains	202
Figure 5.69	Replica Transmission Micrograph of Room Temperature Fracture Surfaces	203
Figure 5.70	Oxidation Behavior of Norton's Hot-Pressed SiC in Oxygen at 1 atm Pressure	206
Figure 5.71	Parabolic Plot of Oxidation of SiC in Oxygen at 1 atm Pressure	207
Figure 5.72	Arrhenius Type Plot Showing Parabolic Rate Constant for Oxidation of SiC in 1 atm Oxygen as a Function of Temperature	208
Figure 5.73	Scanning Electron Micrographs of Surfaces of Silicon Carbide Specimens Oxidized for 30 Hours in 1 atm Oxygen at Different Temperatures	209
Figure 5.74	Scanning Electron Micrographs of Surfaces of Silicon Carbide Specimens Oxidized for 20 Hours in 1 atm Oxygen at Different Temperatures	210
Figure 5.75	Block Diagram of Sonic Velocity Measurement System	213
Figure 5.76	Ultrasonic C-Scan of Duo-Density Rotor Segment, Lowest Sensitivity Setting	214
Figure 5.77	Ultrasonic C-Scan of Duo-Density Rotor Segment, Intermediate Sensitivity Setting	214
Figure 5.78	Ultrasonic C-Scan of Duo-Density Rotor Segment, Highest Sensitivity Setting	215
Figure 5.79	Method for Ultrasonically Scanning Interfaces of Duo-Density Rotors	215
Figure 5.80	Schematic of Billet Used for Ultrasonic Flaw Evaluation	217
Figure 5.81	Ultrasonic "A Scan" Pulse Echoes From Silicon Nitride Billet	218
Figure 5.82	10 Megahertz Shear Waves in Hot Pressed Silicon Nitride	219
Figure 5.83	Hot Pressed Silicon Nitride Radiographic Step Block Standard	220

LIST OF TABLES

		Page No.
Table 3.1	Maximum Bore and Neck Stresses	38
Table 3.2	Duty Durability Cycle For Ceramic Turbine Rotors	66
Table 3.3	Property Comparison of Rotor Materials	70
Table 3.4	Second Stage Turbine Rotor Natural Frequencies	71
Table 3.5	Second Stage Rotor Excitation Orders	86
Table 4.1	Comparison of Silicon Nitride Property Data	95
Table 4.2	Summary of Westinghouse Contract Billets HS-130 Silicon Nitride - Phase II	111
Table 4.3	Properties of Norton Hot Pressed Silicon Carbide	113 & 114
Table 5.1	Flexural Failure Tests (Minimums for Statistical Significance)	136
Table 5.2	Minimum Number of Samples for Preliminary Data	137
Table 5.3	Shear Moduli of Silicon Nitride, Silicon Carbide, And Lithium Aluminum Silicate for Various Temperatures	157
Table 5.4	Coefficients or Friction for Silicon Nitride vs Various Materials	166
Table 5.5	Summary of Physical Properties of Reaction-Sintered Silicon Nitride	177
Table 5.6	Weight Gain of Silicon Nitride	182
Table 5.7	Impurity Level of Reaction-Sintered Silicon Nitride (wt %)	184
Table 5.8	Spectrographic Analysis, Hot Pressed Silicon Nitride (wt %)	189
Table 5.9	Range of Impurity Concentrations (wt %) In 10 Billets of HS-130 Grade Silicon Nitride	190
Table 5.10	Concentration of Elements Within the Silicon Nitride Grain (w/o)	193
Table 5.11	Spectrographic Analysis, Hot Pressed SiC, Norton Billet 472-2	196

		Page No.
Table 5.12	Powder X-Ray Diffraction Data, Hot-Pressed SiC, Norton Billet 472-3	197
Table 5.13	Thermochemical Data for the Si-C-O System	205
Table 5.14	Theoretical Values of Maximum Oxygen Pressures to Remove all the Oxide on SiC Surface	205
Table 5.15	Parabolic Rate Constants for Oxidation of SiC in 1 atm Oxygen	208

1. INTRODUCTION

As stipulated by the Advanced Research Projects Agency of the Department of Defense, the major purpose of this program is to demonstrate that brittle materials can be successfully utilized in demanding high temperature structural applications. The gas turbine engine, utilizing uncooled ceramic components in the hot flow path, was chosen as the vehicle for this demonstration. Two hundred hours of operation over a representative duty cycle at ceramic temperatures up to 2500°F is required for the demonstration.

It is the further purpose of this program to develop design technology for ceramic materials on a systems basis requiring close integration of design, engineering, materials selection, materials processing and fabrication, testing and evaluation.

The progress of the gas turbine engine has been closely related to the development of materials capable of withstanding the engine's environment at high operating temperature. Since the early days of the jet engine, new metals have been developed which have allowed a gradual increase in operating temperatures. Today's nickel-chrome superalloys are in use without cooling at turbine inlet gas temperatures of 1800° to 1900°F. However, there is considerable incentive to further increase turbine inlet temperature to improve specific air and fuel consumptions. The use of ceramics in the gas turbine engine as a demonstration vehicle for this program promises to make a major step in increasing turbine inlet temperature. Success will offer significant advances in engine efficiency, power per unit weight, cost, pollution abatement, and fuel utilization.

This program will demonstrate the use of ceramics in two demanding gas turbine applications:

(1) A small-vehicular type of engine (Ford). Such an engine would have a major impact on the technology of mobile field power units, military vehicles and craft. As a consequence of its significantly increased operating temperature it would not only provide more horsepower/unit weight than current engines, but would also provide improved fuel economy. In addition, the benefits of low emissions and multi-fuel capability are attained. A simplified schematic of the flow path of this regenerative type of engine is shown in Figure 1.1. A brief explanation of this flow path will be given to familiarize the reader with the various components considered for ceramics. Air is induced through an intake silencer and filter into a radial compressor, and then is compressed and ducted through one side of each of two rotary regenerators. The hot compressed air is then supplied to a combustion chamber where fuel is added and combustion takes place.

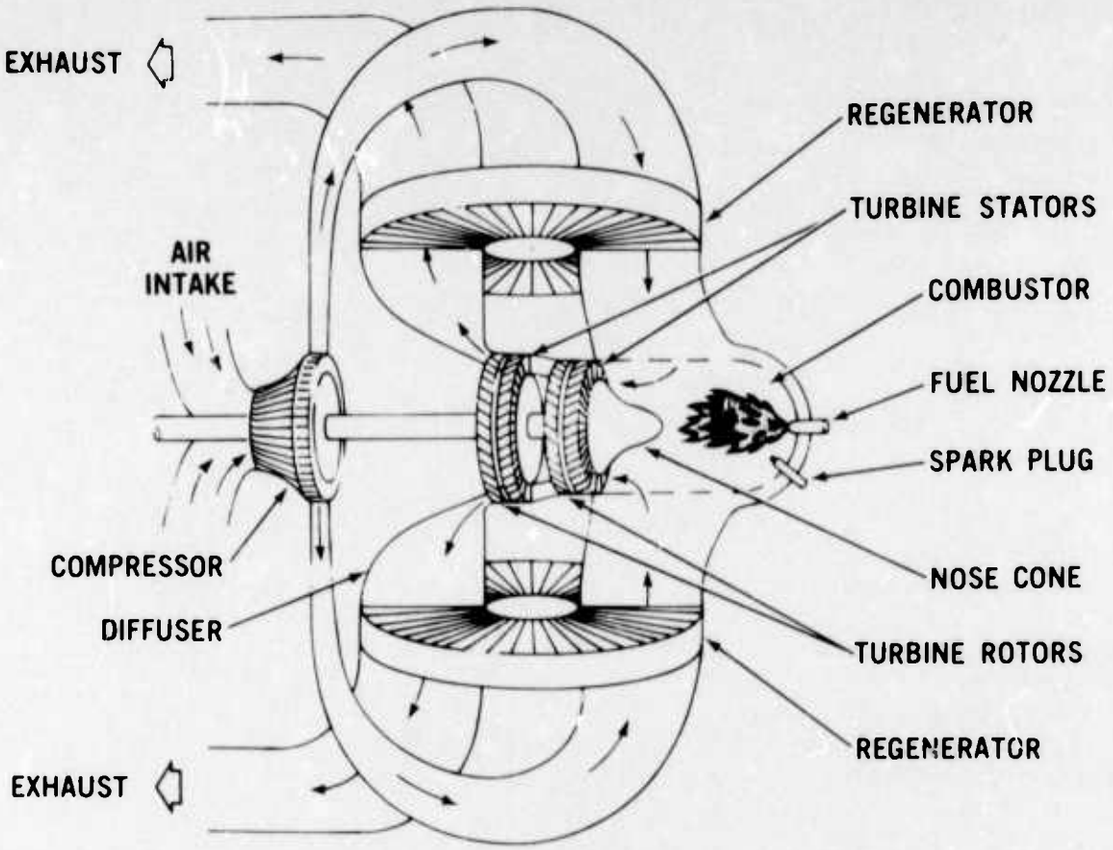


Figure 1.1 — Flow Path Schematic of Vehicular Gas Turbine

The hot gas discharging from the combustor is then directed into the turbine stages by a turbine inlet structure, in this case shown as a nose cone. The gas then passes through the turbine stages which comprise two turbine stators, each having stationary airfoil blades which direct the gas onto each corresponding turbine rotor. In passing through the turbine, the gas expands and generates work to drive the compressor and supply useful power. The expanded turbine exhaust gas is then ducted through the hot side of each of the two regenerators which, to conserve fuel consumption, transfer much of the exhaust heat back into the compressed air.

The parts which are subject to the peak cycle temperature and are made out of superalloys in today's gas turbine are the combustor, the turbine inlet nose cone, the turbine stators and the turbine rotors. These are areas where ceramics could be exploited to the fullest and have been selected for application in the vehicular turbine project.

(2) A large-stationary gas turbine for electric power production (Westinghouse). Such an engine would be most desirable for DOD installations requiring on site power generation. Not only will ceramics facilitate significantly increased operating temperatures with attendant improvement in power and fuel economy, but, because of their improved corrosion-erosion resistance they will also facilitate use of low cost residual fuel. In addition, the environmental benefits of low emissions and lack of cooling water (with its attendant thermal pollution problems) are attained. A simplified sketch of the hot flow path of the engine is shown in Figure 1.2. As with the vehicular turbine project, a brief explanation of the flow path of the stationary turbine will be given to help the reader understand the function of the components to be made from ceramic materials.

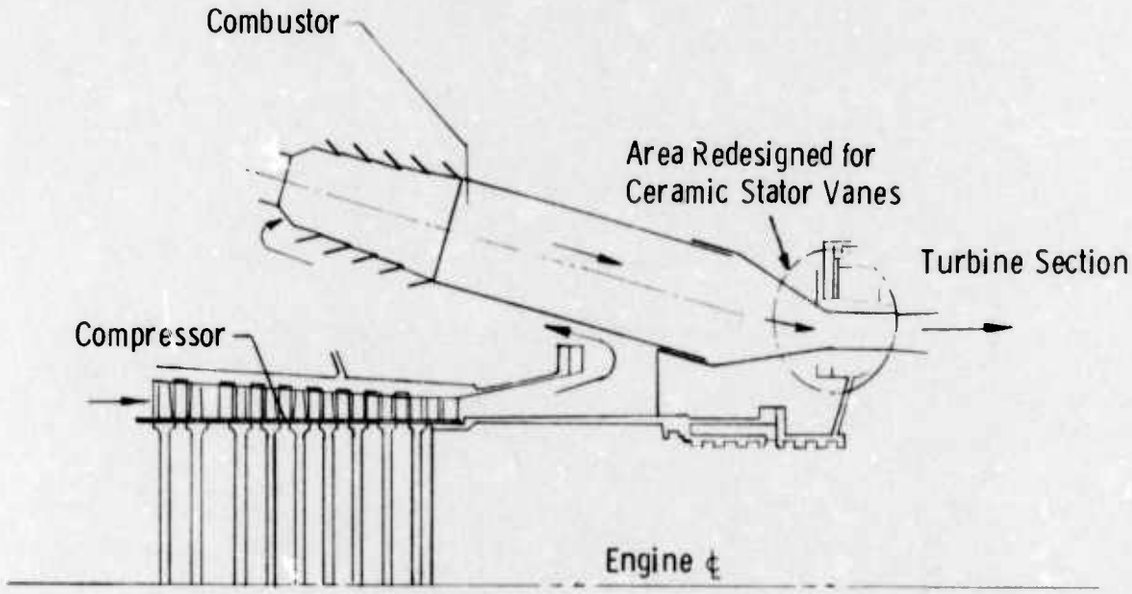


Figure 1.2 — 30 Mw Test Turbine Flow Path

Air is induced through a large intake silencer and filter into an 18 stage axial compressor where it is compressed before entering the combustor housing. The combustor housing supplies air at 650°F to combustion cans assembled in a circumferential array. Air is mixed with distillate fuel or natural gas and ignited in the primary combustion zone. The gas passes down stream through the combustors mixing with secondary air. Flow continues from the combustion section, through the transition zone, and enters the power turbine at a gas temperature of 2500°F. The hot gases expand through the three stage turbine section and are either exhausted through a stack or ducted into a reheat boiler as part of a combined cycle power generating unit.

The parts, where ceramics could be exploited to the fullest, selected for application in the stationary turbine project are the first stage turbine stator vanes and the first stage turbine rotor.

To maintain coherence, progress on the vehicular and stationary turbine projects are reported separately. Also reported separately is the common link between these two programs, materials technology. Information presented under materials technology is general, and does not specifically apply to one or the other of the gas turbine engines. On the other hand, items reported under the vehicular and stationary turbine projects are categorized by components and therefore relate directly to those projects (even these items, however, are indirectly related when it comes to such considerations as design techniques, etc.). Figure 1.3 has been prepared to help the reader understand the interrelationship between the major elements of the report.

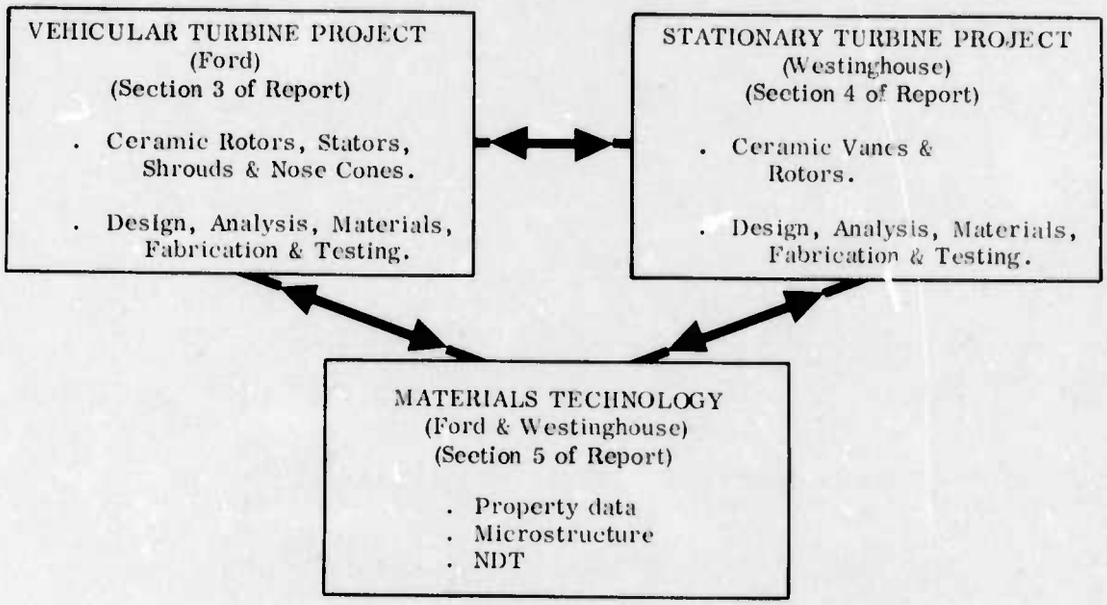


Figure 1.3 — Brittle Material Design/High Temperature Gas Turbine - Breakdown of Major Elements Reported

Successful demonstration of a high temperature gas turbine engine will involve a complex iterative development. One cannot divorce the development of ceramic materials from processes for making parts; no more so can one isolate the design of those parts from how they are made or from what they are made. Likewise, the design of mountings and attachments between metal and ceramic parts within the engine are equally important. Innovation in the control of the environment of critical engine components is another link in the chain. Each of these factors has a relationship with the others, and to obtain success in any one may involve compromises in the others. Testing plays an important role during the iterative development since it provides a positive, objective way of evaluating the various combinations of factors involved. If successful, the test forms the credibility to move on to the next link in the development chain. If unsuccessful, the test flags a warning and prompts feedback to earlier developments to seek out and solve the problem which has resulted in failure. Finally, all of the links in the chain are evaluated by a complete engine test, by which means the ultimate objective of the program will be demonstrated.

Figure 1.4 shows a block diagram flow chart of the major factors involved including the feedback loops, which serves to illustrate this complex and comprehensive iterative development program. The starting point is the concept of a design to use brittle materials. From this, a design layout is prepared and analyzed leading to the detailed design and analysis of the gas turbine engine components made of or involving ceramics. In parallel with the design phase, ceramic materials are developed and screened for application to the gas turbine engine. Process development of candidate ceramics then takes place and material science and property evaluation are used to improve materials and processes, and to feed information back into the design phase. Next with the first detail designs completed and with the process for the selected ceramics reasonably developed, tooling can be designed and fabrication development started to make actual ceramic turbine engine components. Non-destructive testing of these parts will be developed to form a feedback for improving material and fabrication methods. In conjunction with non-destructive evaluation, techniques will be developed for proof testing ceramic components prior to use in engines. In parallel with ceramic part fabrication, proof testing, and non-destructive evaluation, metal parts for the ceramic turbine engine and test rigs are made per the detail design requirements. The ceramic and metal parts are then dimensionally inspected and instrumented for engine testing. Assembly techniques for brittle materials are developed, and testing and durability developments in both test rigs and engines are performed. Failure analysis from test rig and engine testing forms the feedback loops for corrective action; almost all of the factors involved in the development could be affected by experience learned in the test phase of the program. Finally, when engine durability has reached a given level of development, the 200 hour demonstration test will be conducted to meet the program objective.

It should be noted that both the contractor and subcontractor had in-house research programs in this area prior to the initiation of this program. Many ceramic materials were extensively tested and screened leading to the selection of silicon nitride and silicon carbide. In the stationary turbine program, preliminary design concepts were in existence before the award of the contract. In the vehicular turbine program, development was fairly well along and at least one pass had been completed through all of the factors shown in Figure 1.4 prior to the initiation of this program. This one pass, involving many minor iterations led to a vehicular turbine hot flow path having all ceramic stationary components and designated Design 'A'. Based on further experience gained during engine testing, a modified flow path was generated and designated Design 'B'.

Since initiation of this program with AMMRC and ARPA, work on both the vehicular and stationary gas turbine projects was accelerated. Work accomplished during the first reporting period included, for the vehicular turbine project, initial fabrication development and successful preliminary testing of Design 'B' turbine stators and nose cones made of reaction sintered silicon nitride. Design studies of ceramic turbine rotors showed that computed operating stresses can be withstood by dense silicon carbide and dense silicon nitride. Development programs were started to explore several approaches to fabricate rotors in these materials.

Accomplishments on the stationary turbine project during the first reporting period included obtaining physical property data of hot pressed silicon nitride ceramic and identifying microstructural details of this material. The initial design of ceramic stator vanes was completed and calculated vane stresses were reduced 40% by decreasing the stator vane chord.

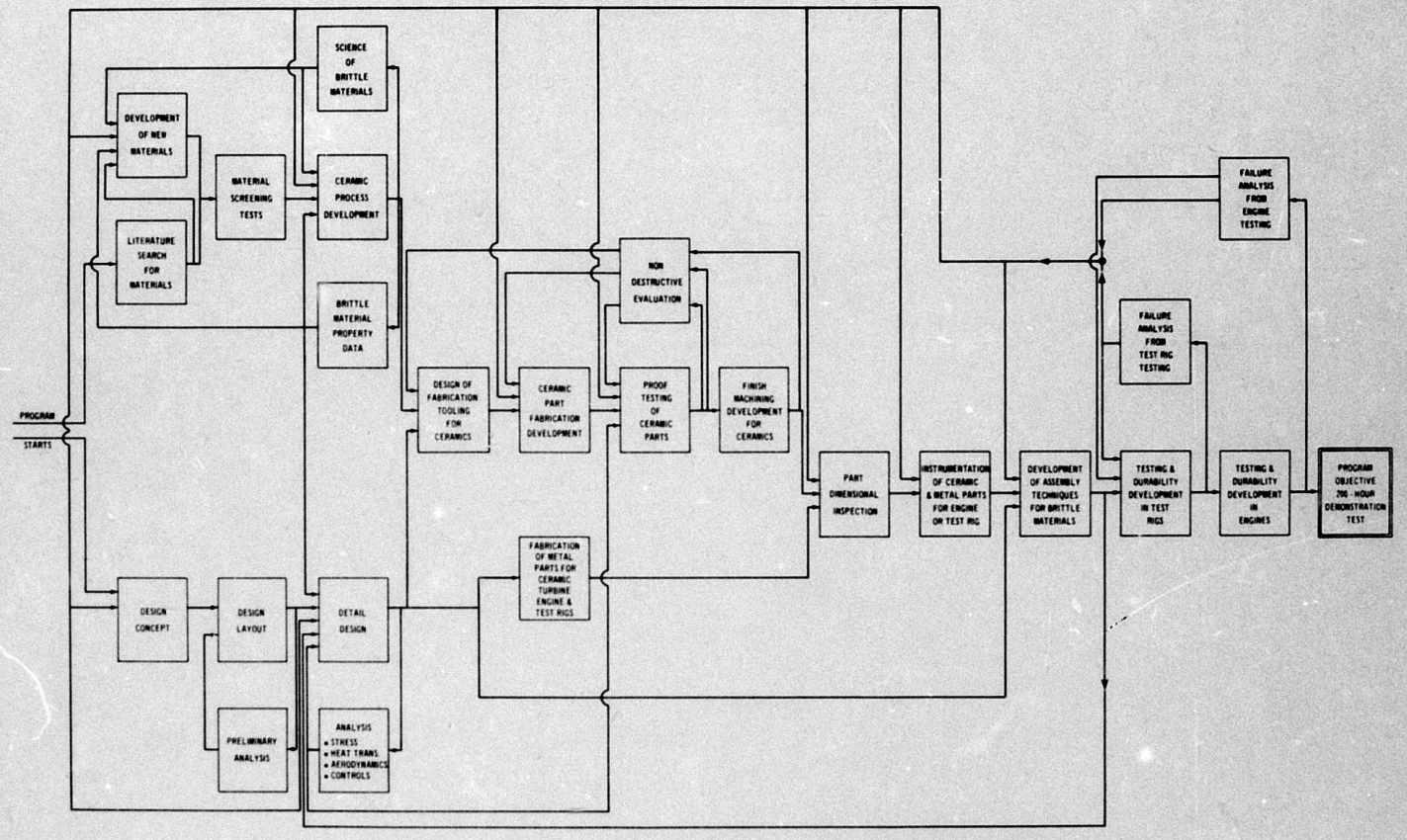


Figure 1.4 — Brittle Material Design/High Temperature Gas Turbine - Block Diagram Flow Chart of Iterative Development

The results of work accomplished during the second reporting period included, for the vehicular turbine project, continued fabrication development as well as rig and engine testing of the second generation design (Design 'B') turbine stators and inlet nose cones. Ceramic turbine rotor design studies were performed on an expanded two-dimensional heat transfer computer program to include rotor attachment designs. Progress was reported on the multi-approaches being explored to fabricate a one-piece, intricately-shaped turbine rotor from candidate high strength ceramic materials.

The results of work accomplished on the stationary turbine project included the stress analysis and design of first stage vanes as well as a preliminary report on the rig for statically testing the stator vanes. Progress on the development of a new three-dimensional, finite-element, stress analysis computer program for subsequent use in ceramic rotor blade design are also reported.

Development in materials technology for both the vehicular and stationary gas turbines was reported and includes continued compliation of material property data, continued characterization of material structure, and development of non-destructive evaluation techniques such as ultrasonics, radiography and acoustic emission.

The results of work accomplished during this third reporting period include, for the vehicular turbine project, considerable emphasis on the development of the ceramic turbine rotor. A new concept for a silicon nitride rotor, termed "duo-density", appears promising based upon the results of stress analyses and fabrication studies. Progress was made on the stress analysis and the development of machining techniques for fabricating monolithic rotors from high-strength hot-pressed materials. A cracking problem in the first stage stator blade appears solved with the aid of a thermal shock test rig; engine testing thus far has corroborated the results of rig testing.

On the stationary turbine project, a full scale model of the first generation stator vane assembly has shown that the design will function when subjected to differential motions well in excess of design limits. Using improved physical property data, the transient thermal stresses in the first stage stator vane have been recalculated. The three-dimensional stress analysis program has been applied for the preliminary determination of a dense silicon nitride rotor blade.

Work on materials technology is continuing in both the vehicular and stationary turbine projects. Additional property data on candidate ceramic materials has been determined, and further relationships of microstructure to properties have been uncovered. A number of processing parameters have been examined for reaction-sintered silicon nitride.

This report covers the progress in the period July 1, 1972 to December 31, 1972.

PRECEDING PAGE BLANK-NOT FILMED

2. SUMMARY OF PROGRESS

2.1 VEHICULAR TURBINE PROJECT

The vehicular turbine project is composed of three primary sections -- design, materials, and testing. Within these primary areas there exist many tasks which must be accomplished in order to achieve the program goal of 200 hours of turbine engine operation over a representative duty cycle at ceramic temperatures up to 2500°F. Each semi-annual report is really a progress report detailing the results of work over a six month time increment, and reporting on the individual accomplishments on the tasks which will culminate in the final program objective.

Work is in progress concurrently in areas of turbine engine component design and analysis, ceramic material and process development, material and engine testing, materials technology, and nondestructive evaluation of ceramic engine components. Progress, made in several of these areas in this reporting period, is summarized in this section of the report.

(1) Design and analytical work for the determination of ceramic rotor stresses is continuing. Considerable emphasis has been placed on the study of the duo-density concept; the rotor blades are made of molded reaction-sintered Si_3N_4 and the hub is made of hot-pressed Si_3N_4. Detailed steady state heat transfer and stress analyses of this concept have been completed, and several possible joint configurations were analyzed. The design of a hot-pressed Si_3N_4 monolithic turbine rotor has also been analyzed, and stresses occurring during steady state and transient operations were calculated. Refer to Section 3.1.1 for a more detailed account of this work.

(2) Development of fabrication techniques for the duo-density turbine rotor has been concentrated on the method of bonding hot-pressed and reaction-sintered silicon nitride. Using a thin layer of alpha Si_3N_4 powder to promote bonding, good joints were obtained between these two materials. Tooling was procured and used successfully for the injection molding of a ring of airfoil blades as an integral unit. Refer to Section 3.1.2 for more detailed information.

(3) Improvements have been made in forming of an integral ring of rotor blades by the chemical vapor deposition of silicon carbide. Hoops of sufficient thickness were formed. Refer to Section 3.1.2 for more information.

(4) A test rig has been designed and construction started for the testing of ceramic turbine rotors. This rig will fully simulate the mechanical and thermal loadings experienced in a gas turbine engine, but uses fewer parts and hence can be quickly rebuilt following a rotor failure. A testing program has also been developed. Refer to Section 3.1.3 for more details of this work.

(5) Improvements have been made in methods for the assembly of stator segments into integral rings. A slip-cast grade of reaction-sintered Si_3N_4 has been developed having a transverse strength of 40-50,000 psi, and is being utilized for rotor shroud rings and for stator assemblies. Refer to Section 3.3.1 for more detailed information.

(6) Previous cracking of first stage stator blades which occurred during engine operation have been duplicated on a thermal shock test rig. Using this rig, testing of variations in blade shape resulted in changes in the blade shape which eliminated the cracks. Engine testing of this modified design stator has produced no blade failures after 14 hours. Refer to Section 3.3.2 for more information, and for additional engine test results.

2.2 STATIONARY TURBINE PROJECT

The stationary turbine project is a design study of brittle materials in a high temperature gas turbine application, culminating with the demonstration of uncooled ceramic stator vanes in a 30 Mw power turbine operating for 200 hours. This operation will consist of 100 sequences of peaking cycle service. A performance simulation of ceramic rotor blades will also be performed by computer. Work is currently in progress in areas of stator vane design and analysis, rotor blade design and analysis based on 3 dimensional finite element stress analysis codes, component fabrication, and material technology. This progress is summarized in this section of the report.

(1) Emphasis was placed upon the mechanical aspects of brittle material design for the first generation stator vane configuration. The 3 piece ceramic stator vane design was reviewed with respect to a full scale kinematic model built to demonstrate the functional behavior of the ceramic vane assembly, insulators and appropriate support structure. Design integrity was preserved when differential motion within the model was 5 times that expected in the 30 Mw turbine. Refer to Section 4.1.1 of this report for more detailed information.

(2) Engineering property data for Norton HS-130 silicon nitride has been used to recalculate transient thermal stresses in the airfoil. A maximum out-of-plane tensile stress of 41,000 psi is expected to occur at the leading edge under emergency shutdown conditions from 2500°F. Steady state stresses generated in the airfoil, as a result of end effects, are also considered. Contact stresses approaching 9600 psi tensile are expected at the airfoil end cap interface, as a combined result of spring and gas pressure loading. Transient thermal stresses in the end cap are expected to reach a maximum tensile stress of 21,200 psi in the steady state condition. Work to date indicates that the strength of silicon nitride exceeds the stress requirement in all cases studied. Refer to Section 4.1.2 for more detailed information.

(3) The Norton Company has experienced difficulty in the initial machining of first generation end caps from HS-130 silicon nitride. Fifteen airfoil sections are complete. Delivery of 40 end caps has been delayed until January 30, 1973. Norton has produced hot pressed silicon carbide with properties roughly equivalent to their high strength silicon nitride. Refer to Section 4.1.3 for more detailed information.

(4) A new static rig has been designed for the testing of ceramic stator vane assemblies in a turbine environment at 2200 and 2500°F. The time required for construction, installation, instrumentation and check out of the test facility will delay static rig testing until August 1973. Refer to Section 4.1.3 for more detailed information.

(5) Elastic stress and heat transfer programs for the 3 dimensional finite element code have been expanded to include anisotropic and temperature dependent materials properties. Completion of a data transfer system makes it possible to use the new system for rotor blade design and analysis at this time. Preliminary results indicate that a maximum tensile stress of 22,700 psi will occur in the dovetail attachment area of a Si_3N_4 blade rotating at 3600 rpm. Refer to Section 4.2.1 and 4.2.2, respectively, for more detailed information on 3 dimensional finite element stress analysis and rotor blade design.

2.3 MATERIALS TECHNOLOGY - VEHICULAR AND STATIONARY TURBINE PROJECTS

Complete property characterization of the ceramic materials for turbine engine use in an enormous task, which will proceed throughout the life span of the contract. This task is also complicated by the fact that many of the materials being investigated are in the developmental stage and improvements in properties are anticipated, which will require that some, if not all of the physical properties must eventually be re-determined. Progress in materials technology is summarized in this section of the report.

(1) Physical property data was obtained for various ceramic materials during this reporting period. Transverse strength measurements were performed on Norton HS-130 hot-pressed silicon nitride and "Refel" reaction-sintered silicon carbide. Shear modulus data was obtained on hot-pressed silicon nitride, hot-pressed silicon carbide, and lithium-aluminum-silicate. Refer to Section 5.1.1 for more information on these results.

(2) Sufficient physical property data are now available to initiate a statistical interpretation of the thermal and mechanical behavior of Norton HS-130 silicon nitride, the material from which first generation vane assemblies for the stationary gas turbine have been fabricated. Using Weibull statistics as a basis, it was found that volume affects strength more than area at elevated temperatures when flexural and tensile data are correlated. Silicon nitride continues to exhibit anisotropy, strain rate sensitivity at elevated temperatures, and temperature dependent material properties. Refer to Section 5.1.1 for additional information.

(3) The flexural strength of Norton hot-pressed silicon carbide compares favorably with HS-130 silicon nitride. Values decrease from 76,000 psi at room temperature to 50,000 psi at 2500°F. Scatter in the data, however, makes it impossible to determine anisotropy or strain rate sensitivity at this stage of the investigation. A tensile strength of 26,200 psi is reported at 2300°F. Preliminary results indicate that the stress rupture properties of silicon carbide are significantly better than silicon nitride. Refer to Section 5.1.1 for the results of this work.

(4) The corrosion-erosion tests in the turbine test passage shows oxidation resistance of silicon nitride continues to appear excellent, and similar preliminary results were obtained for silicon carbide. Weight losses of 10 mg/cm^2 were observed for Norton hot-pressed silicon carbide after 250 hours at 2000°F. Additions of Na, Mg, S and V did not alter the results of either silicon nitride or silicon carbide significantly. Section 5.1.2 details the results of these tests.

(5) The effect of varying the α/β ratio upon properties of reaction-sintered Si_3N_4 was investigated. It was found that density, strength, and elastic modulus were constant up to 65% α. Refer to Section 5.2.1 for a detailed account of this investigation.

(6) In the continuing study of processing parameters, the effect of variations in the nitriding cycle upon the strength of reaction-sintered silicon nitride was investigated. Evidence points to improvements in strength, and a finer grain structure, as nitriding time at high temperatures is reduced. Refer to Section 5.2.1 for more information.

(7) Alkali metal oxide impurities present in the grain boundary phase of hot-pressed silicon nitride have a significant effect on the high temperature properties. Strength is inversely proportional to combined Na, K, and Ca concentration within the range 0.04-0.08 w/o as shown by a reduction in flexural strength at 2300°F from 55,000 to 30,000 psi, respectively. Auger analysis confirms a high concentration of Ca in the grain boundary. Refer to Section 5.2.2 for more details of this study.

(8) The salient features of microstructure have been defined for hot-pressed silicon carbide. Grain morphology and impurity levels were established by electron microscopy and spectrographic analyses. A transition from cleavage to intergranular fracture with temperature was found. Refer to Section 5.2.2 for more information.

3. PROGRESS ON VEHICULAR TURBINE PROJECT

3.1 CERAMIC ROTOR DEVELOPMENT

SUMMARY

The vehicular turbine ceramic rotor development program is continuing with the investigation of several basic concepts simultaneously, using as candidate materials hot-pressed silicon nitride, reaction-bonded silicon nitride and fully dense silicon carbide.

Considerable emphasis is being placed on a "duo-density" silicon nitride rotor program. In this concept, the relatively low-stressed rotor blades are formed from reaction-sintered silicon nitride, thus enabling existing technology to be used to form the complex blade geometry. The disk is fabricated from hot-pressed silicon nitride, which is able to withstand the higher operating stresses which occur in this area. Detailed steady state heat transfer and stress analyses of this concept have been completed. Several configurations of the joint between the two materials were evaluated theoretically. Development work is in progress to fabricate and evaluate these joints. Preliminary results indicate that the bond strength exceeds the strength of the reaction-sintered silicon nitride. Tooling has been obtained and used successfully to fabricate the injection molded blade rings.

Development is continuing on a fully integral blade and disk turbine rotor concept. This design has been analyzed for thermal and mechanical stresses, and basic design modifications have been incorporated as a result of these analyses. This concept is very attractive from a materials strength standpoint. However, it presents fabrication difficulties. Several programs are being conducted, both by Ford and by other companies, to overcome these problems.

The Ford pseudo-isostatic fabrication method has been de-emphasized because of fabrication problems. The primary problem was lack of truly isostatic pressures applied to the blade and disk regions. This non-uniformity in pressure resulted in twisted and fractured blade sections.

The program with Energy Research Corporation to fabricate turbine rotors by chemical vapor deposition (CVD) of silicon carbide has been successful in filling the blade cavity. However, more effort will be required to achieve a completely filled hoop under each blade cavity. Improvements have been made in producing CVD silicon carbide of improved chemical purity.

Ultrasonic machining of a rotor from a hot-pressed silicon nitride blank has continued. Preformed silicon nitride rotor blanks have been successfully hot-pressed and disk contouring tools have been developed to finish these preformed disks to final shape. Developments so far indicate that ultrasonic machining will be a very slow method of making a complete turbine rotor.

Electric discharge machining of dense silicon carbide has been improved during this reporting period. A study was initiated to optimize machine power setting, resulting in material removal rates of 0.206 cubic inch per hour.

A turbine rotor test rig has been designed to use in ceramic rotor development. The rig has been designed to use many engine components, but is considerably simpler than the engine.

3.1.1 DESIGN AND ANALYSIS

Introduction

Heat transfer and stress analyses studies, discussed in earlier reports,[1,2] for two rotor design concepts have been conducted during this reporting period. The monolithic design has continued to be investigated and some minor modifications were made. In addition, a new ceramic rotor design called the "duo-density" concept has been investigated. Engine start-up and full-power-acceleration analyses of the rotor assembly are presented for the monolithic design; steady-state analyses are presented for the "duo-density" concept.

Parametric studies of duo-density bond joint configurations were completed in this reporting period.

The rotor/shaft attachment program is currently entering into the test phase and will not be reported until significant testing has been completed.

Analysis of Design 'C' Monolithic Silicon Nitride Ceramic Rotors

In the previous report,[1] the basic design process for analyzing ceramic components was discussed, and the finite element computer models were illustrated. Results of analyses conducted with some of these models are discussed in this section for cases using fully dense hot-pressed silicon nitride as the rotor material.

It should be noted that the rotor models presented in the last report[1] were Design 'B' rotors while those discussed in this report are Design 'C'. The major difference between the two designs is in the platform area. Design 'B' rotors were connected through a long platform which served as the inner wall of the hot gas flow path. Design 'C' rotors are connected through the hub region. The inner wall of the hot gas flow path is now completed by an shroud on the second stage stator.

The change from Design 'B' to Design 'C' resulted from both mechanical and aerodynamic design considerations. From the mechanical design standpoint, Design 'C' rotors offer a lower inertia resulting from the reduced radius of gyration. The Design 'C' coupling between rotor stages is in an area of lower stresses and increases the symmetry of the rotor design. From the aerodynamic aspect, there is less hot gas leakage between the two rotor stages.

The finite element models of Design 'C' first and second stage rotors are shown in Figures 3.1 and 3.2 respectively. The difference between the Design 'B' and Design 'C' rotors is readily seen with reference to the last report[1]. The rotor assembly model has remained the same, with the exception of separating the long platform from each rotor by use of psuedo material properties where required. The results presented will be based on analyses conducted with the finite element model of the rotor complete with the attachment assembly.

The design of ceramic components is an iterative procedure. The analysis of a complex assembly is used to accurately define the boundary conditions for individual components or problem areas within the assembly. The model of the rotors, complete with the attachment assembly, is used to define the boundary conditions for a more refined and detailed analysis of each rotor.

There are two critical areas where the tensile stresses peak, excluding areas of stress concentration adjacent to the rotor coupling face splines. These critical areas are the rotor neck and the center of the hub at the bore. The stress distributions across the neck of the first and second stage rotors are shown in Figures 3.3 and 3.4 respectively. The stress distributions shown are at full engine speed with steady state thermal boundary conditions. For analytical purposes, full speed conditions assume operation at the maximum turbine inlet gas temperature of 2500°F and 110% of design rotational speed, in order to allow a margin of safety for engine control uncertainties. These are the most severe steady state operating conditions expected. Thermal and mechanical stress distributions are shown separately in order to better indicate the geometrical effects of the design.

It can be seen that the thermal stresses are relatively low and uniform, indicating an even temperature distribution. The front face of the first stage rotor and the rear face of the second stage rotor are slightly cooler than the opposite faces, as shown in Figure 3.5, which accounts for the slightly higher stresses on these surfaces.

The mechanical stresses are higher at the rear face of each rotor, indicating bending in the rotor neck. Even though the blade loads are symmetrical with the rotor disks, the longer trailing-edge-side of each platform causes bending. It can be seen from Figures 3.3 and 3.5 that the first stage rotor disk must withstand a combined stress of 34,000 psi at a material temperature of 2000°F in the neck. The second stage rotor disk must be capable of withstanding a stress of 43,000 psi at 1600°F in the neck.

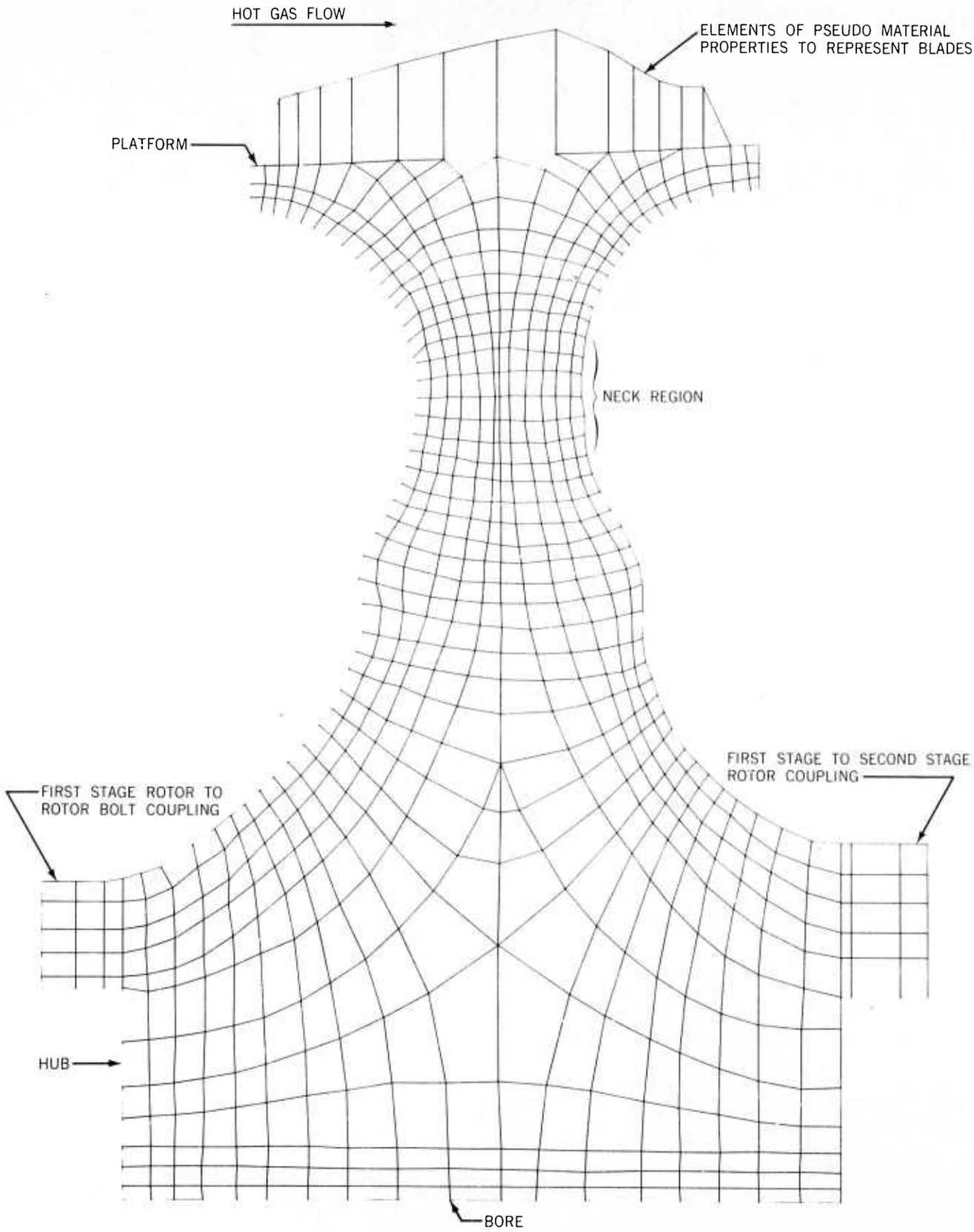


Figure 3.1 Finite Element Model of First Stage Design C Rotor

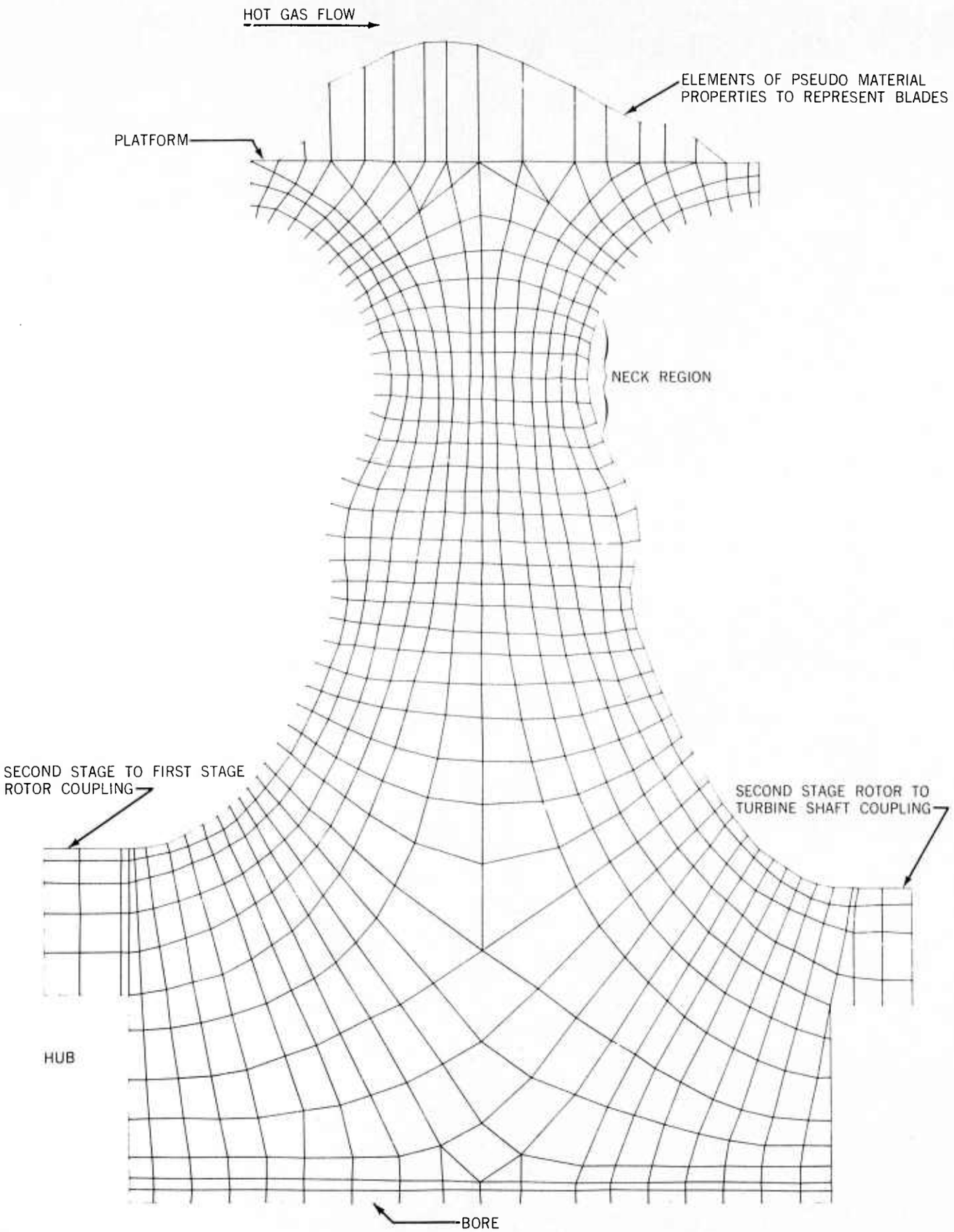


Figure 3.2 Finite Element Model of Second Stage Design C Rotor

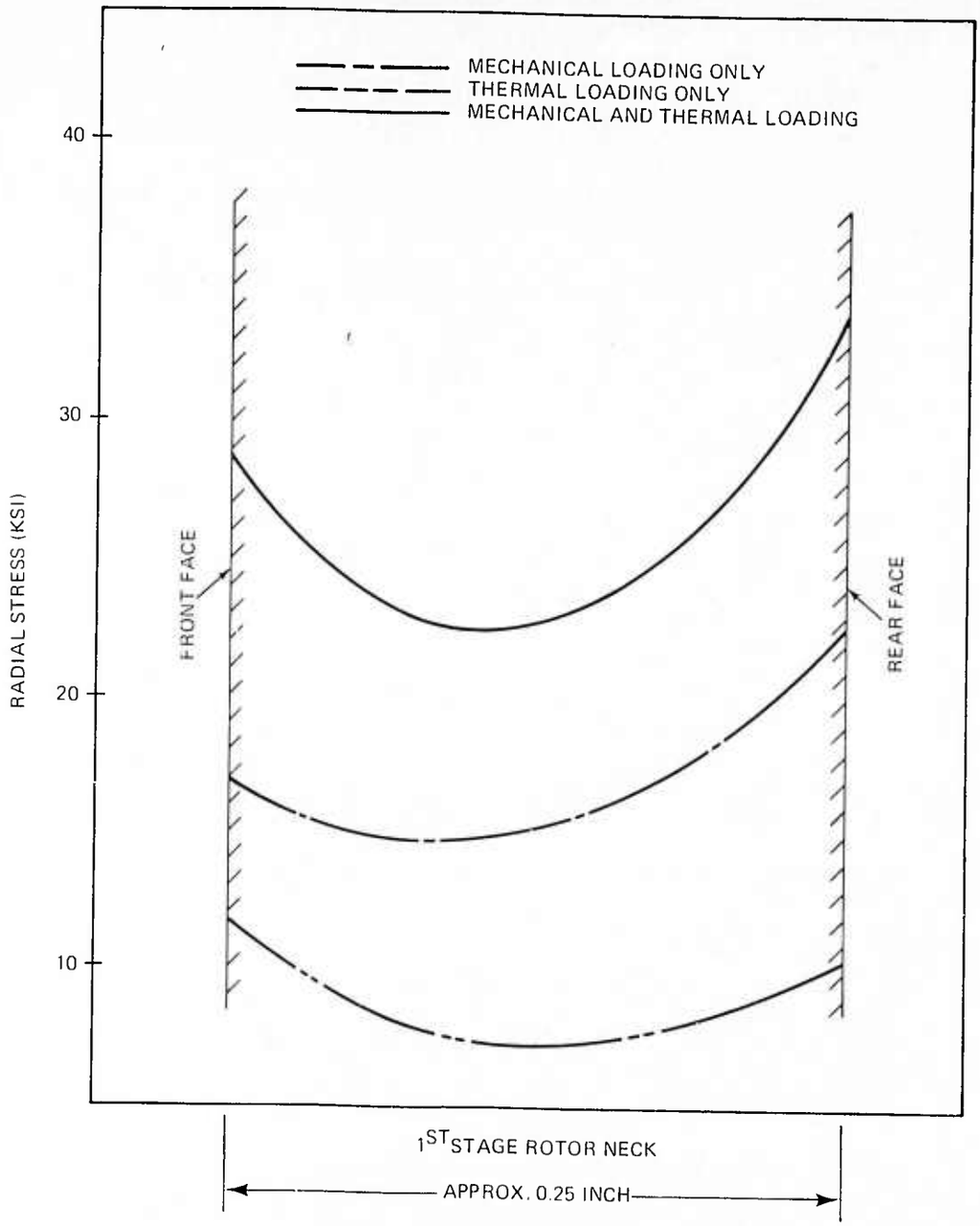


Figure 3.3 Radial Stresses in Neck Area of First Stage Rotor at Full Speed

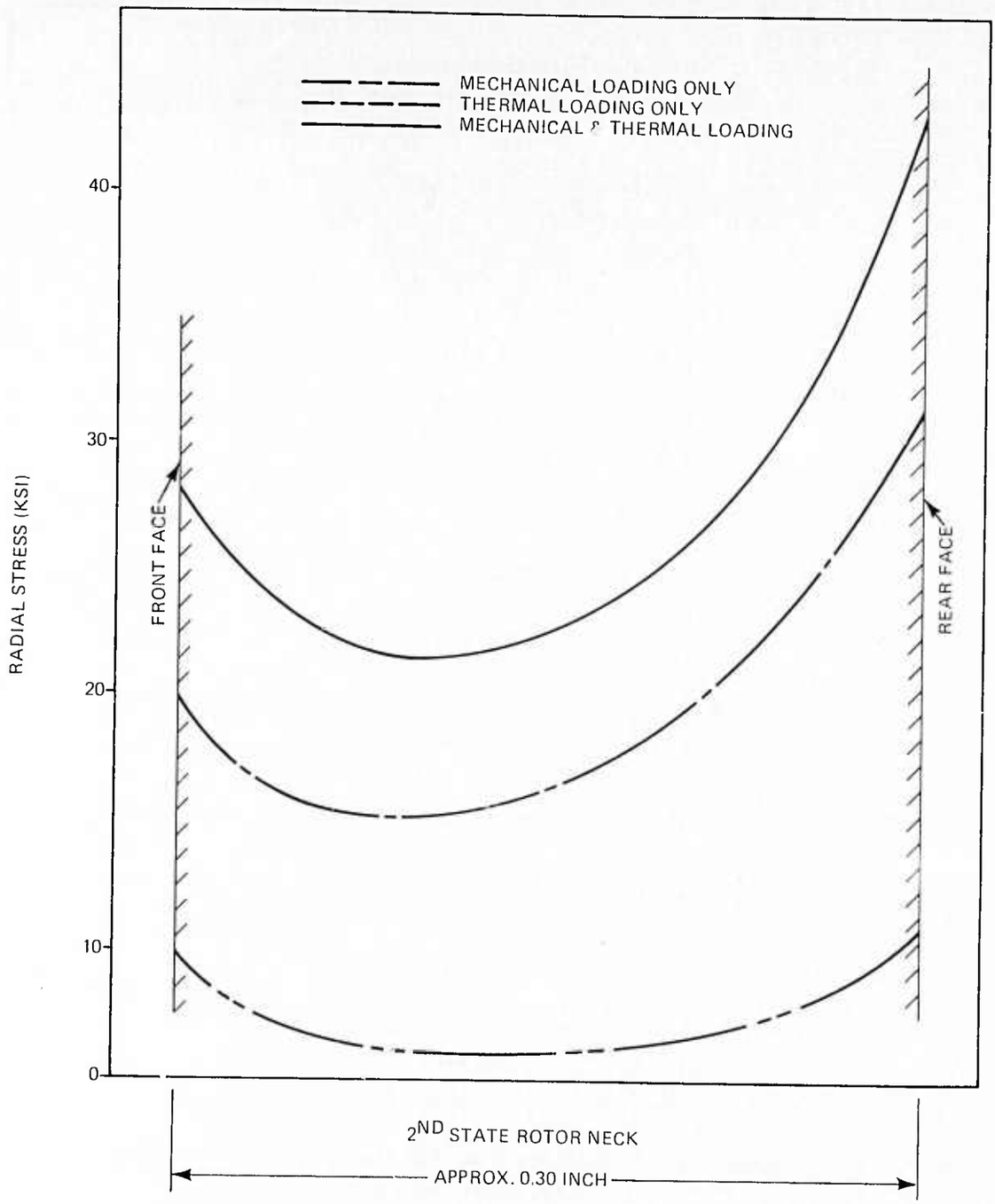


Figure 3.4 Radial Stresses in Neck Area of Second Stage Rotor at Full Speed

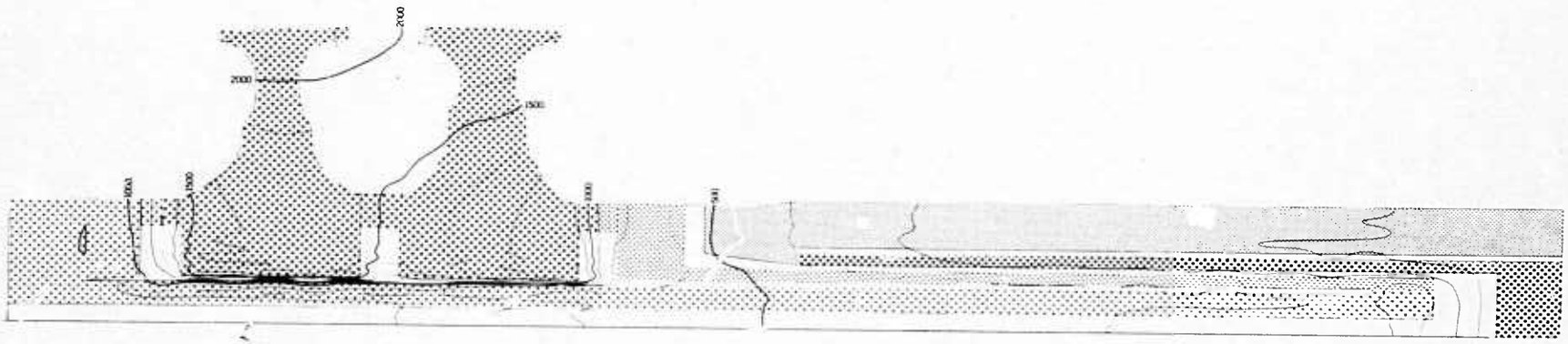


Figure 3.5 Isotherms in °F For Rotors and Attachment Assembly at Full Speed

Figures 3.6 and 3.7 show the distribution of circumferential or hoop stresses at the center of the hub near the bore for the first and second stage rotors respectively. The maximum combined hoop stress occurs at this point. This stress, when extrapolated out to the bore surface, is also 34,000 psi and 43,000 psi for the first and second stage rotors respectively under full speed steady state conditions as explained previously. The respective temperatures at these points on the bore surfaces are 1500°F and 1300°F. Thermal stresses increase towards the ends of each hub as indicated by the thermal gradients shown in Figure 3.5. However, the mechanical stresses decrease over the same region. The net result produces a slightly decreasing stress gradient moving away from the center of the hub.

The stress distribution for idle engine conditions have not been shown since they are not as severe as the full speed stresses. The thermal stresses in the hub region at engine idle conditions are expected to be equivalent to full speed thermal stresses as indicated by isotherms shown in Figure 3.8. The mechanical loading, however, is reduced to only one quarter of that which occurs at full speed, thus producing a much lower total stress distribution for engine idle conditions.

Thus far, only conditions for steady state operation have been discussed. Although these are the maximum sustained stresses the rotors will be subjected to, they are not the peak instantaneous stresses. The peak stresses occur during thermal transients. The first set of transient conditions studied are referred to as the first and second transients. These transients appear to be the most severe of any which might occur under actual engine operating conditions.

The first transient, which models engine start-up, assumes the engine to be at room temperature, then rapidly subjected to idle speed and turbine inlet temperature conditions. A thermal stress analysis of the rotors and attachment assembly was conducted as a function of time. The results of this analysis indicates that the rotor stresses in both the neck and bore regions of the first and second stage rotors reach a maximum value 40 seconds from the initiation of the transient.

The second transient, which models an engine full-power acceleration, assumes that at the time of maximum stress during the first transient the turbine inlet conditions are rapidly increased to full speed. A thermal stress analysis was conducted as a function of time to determine the peak transient stress for this operation.

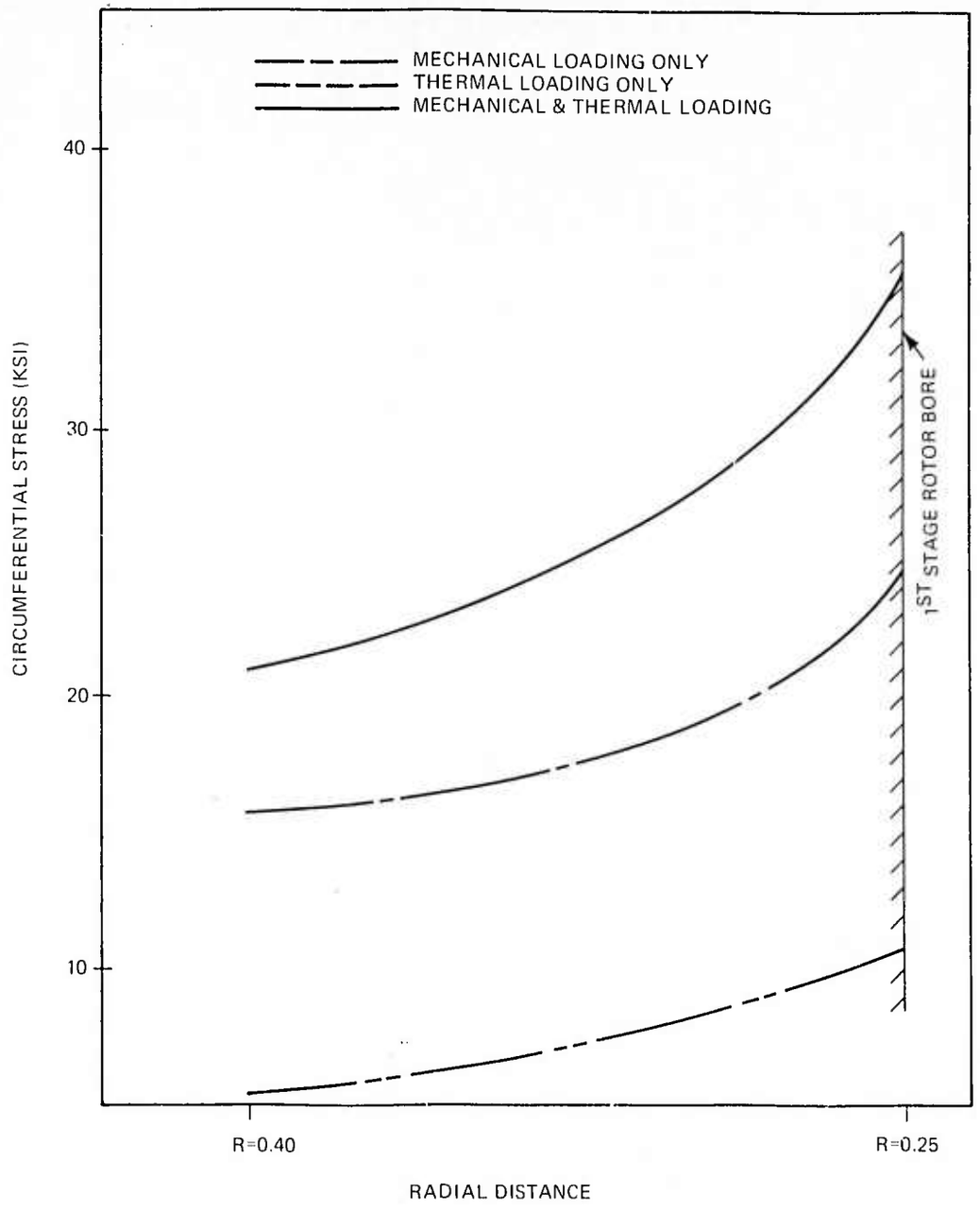


Figure 3.6 Circumferential Stresses in Hub Area of First Stage Rotor at Full Speed

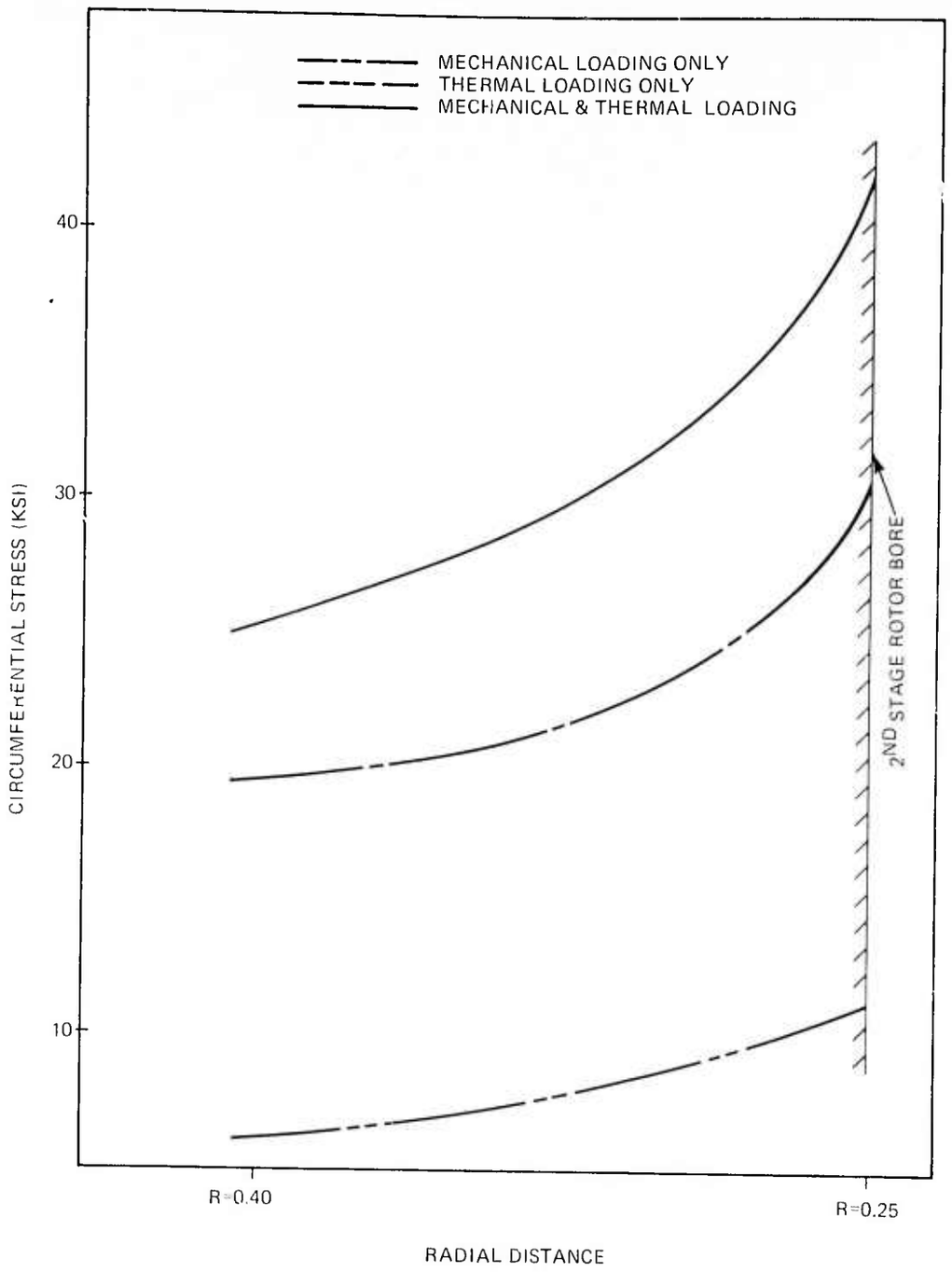


Figure 3.7 Circumferential Stresses in Hub Area of Second Stage Rotor at Full Speed

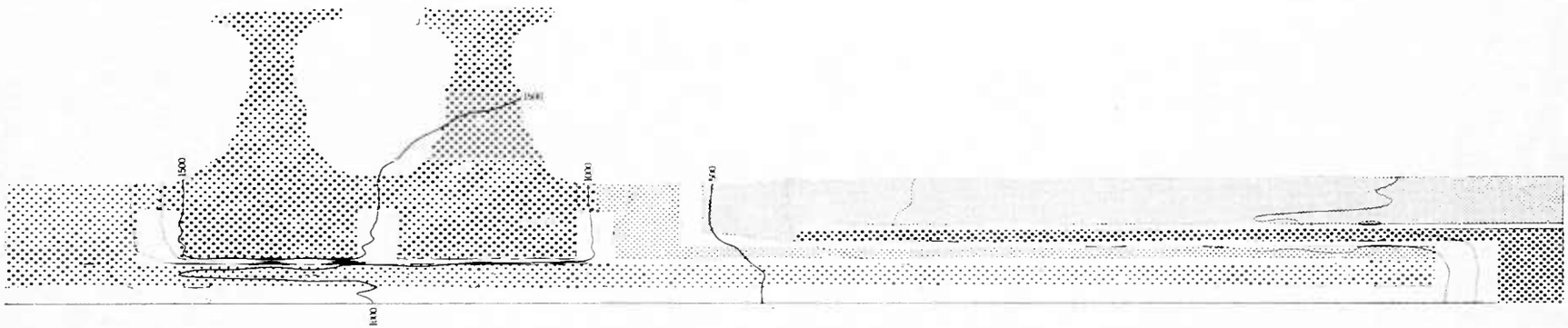


Figure 3.8 Isotherms in °F for Rotors and Attachment Assembly at Idle Speed

Figures 3.9 and 3.10 show the combined mechanical and thermal stresses in the circumferential and radial directions during the first and second transient for both rotor stages. These plots were constructed from the analysis of the rotor-attachment assembly model. Figures 3.11 and 3.12 show the isotherms throughout the assembly during the first and second transients at 40 seconds and 55 seconds respectively from start of the transients. These are the times of maximum stress in each transient. The absolute maximum occurs in the second stage disk at 55 seconds during the second transient. The stresses in both the hub and neck areas are 48,000 psi at 600°F and 1200°F respectively. It should be pointed out that these stresses were not extrapolated out to the surface. Based on the extrapolated steady state stresses (Figures 3.4 and 3.7) the transient stresses may be as much as 25 percent higher at the surface. This will be verified in the refined analysis of the individual rotors, which is currently in progress.

The previous discussion has assumed no load was exerted by the rotor attachment bolt. The rotor bolt was allowed to float as required under varying temperature conditions. However, when the bolt is fixed the load will tend to increase stresses in the hub areas. Stresses will increase in the vicinity of the couplings between the rotor bolt, the first and second stage rotors, and the turbine shaft. This increase is due to shear at the interfaces resulting from friction on the sliding surfaces. At present this friction force has not been evaluated.

The current analysis[1] indicates the required bolt load is approximately 7300 pounds when the engine is at room temperature. This load increases to 8500 pounds during the second transient and then relaxes back to approximately 1400 pounds for steady state operation. This steady state load is required to maintain contact between the coupling surfaces with due consideration of the expected dynamic loads of the assembly. Additional more refined analyses will focus on each individual rotor and will include the previously discussed conditions of idle and full-power steady state, first and second transients, and the corresponding rotor bolt loads. Future studies are planned to analyse the stress distribution following a normal shutdown of the engine (soak-back), a flame-out shutdown from steady state operation and a flame-out shutdown from a start-up transient.

Analysis of Design 'C' Duo-Density Rotors

The duo-density rotor is composed of a ring of blades of molded reaction-sintered silicon nitride bonded to a disk of hot pressed silicon nitride. Please refer to Fig. 3.22 for a sketch of this concept. This section presents the results of the mechanical and thermal stress analyses of the duo-density rotors. Centrifugal and steady state thermal load conditions were determined at both idle and 110% speed as defined in the previous section.

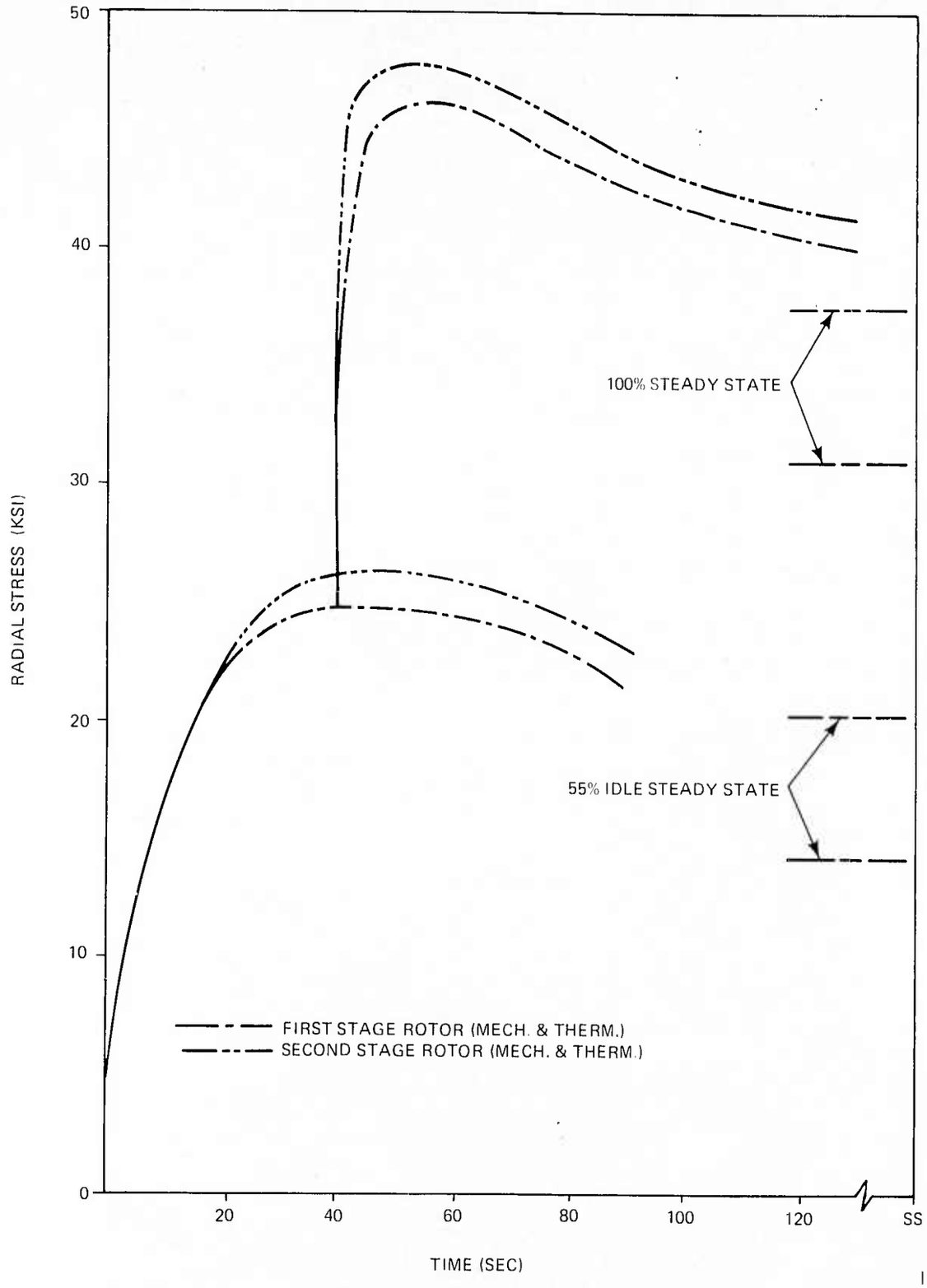


Figure 3.9 Transient Stresses in Neck Area of Rotors

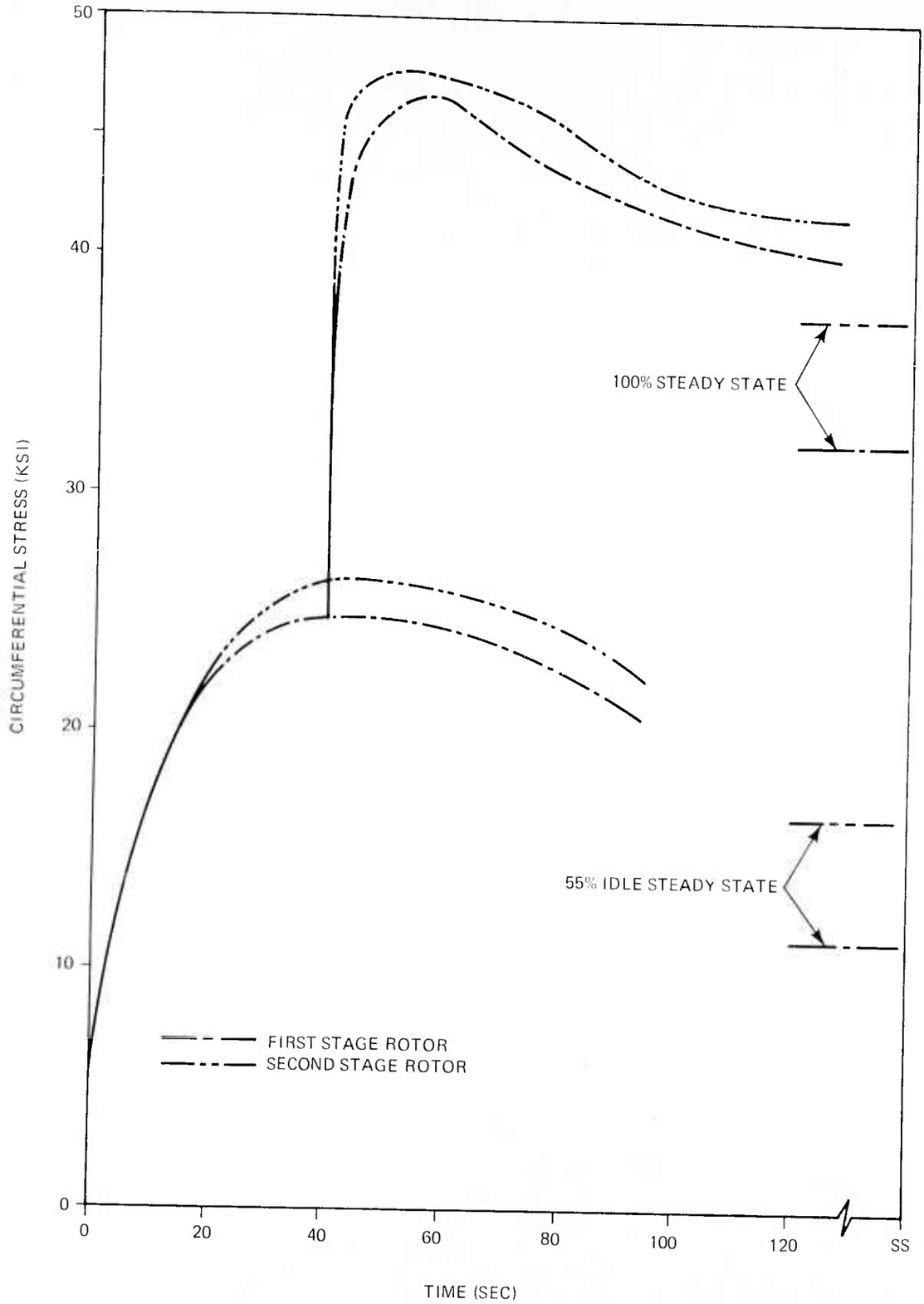


Figure 3.10 Transient Stresses in Hub Area of Rotors

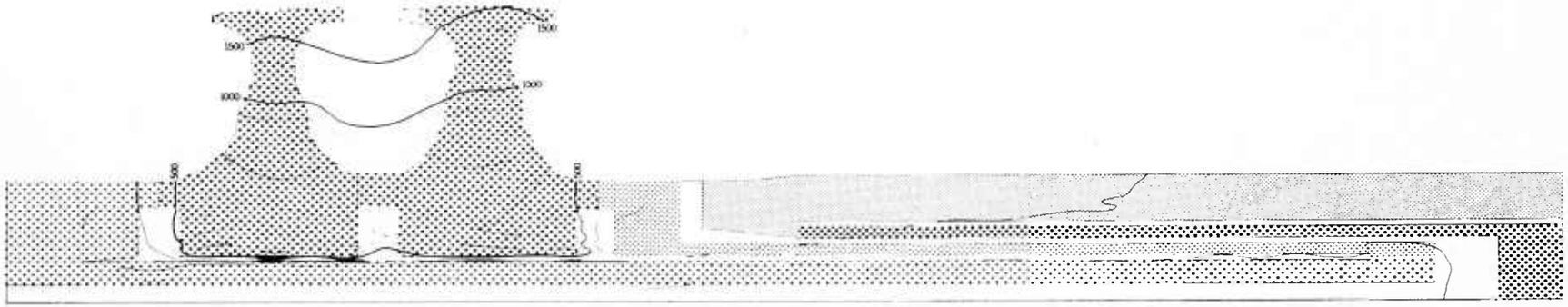


Figure 3.11 Isotherms in °F for Rotors and Attachment Assembly, First Transient

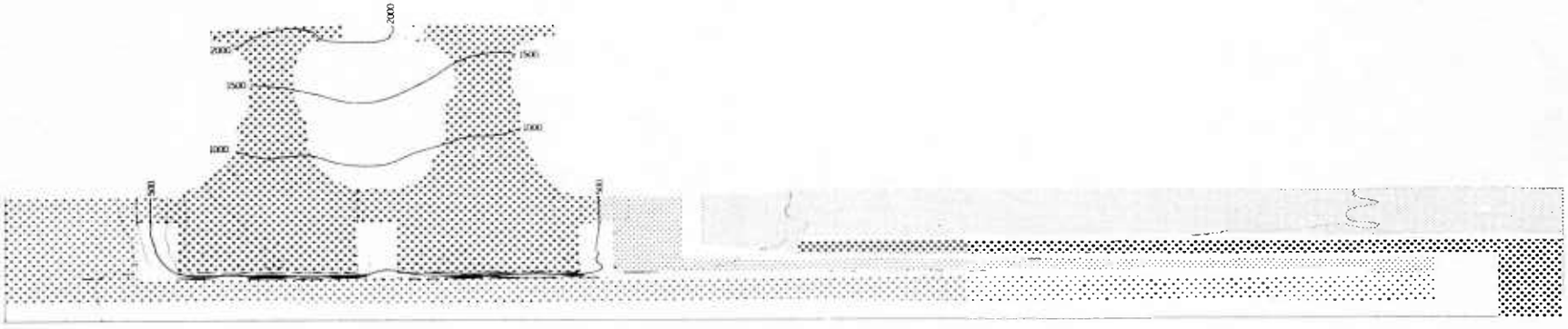


Figure 3.12 Isotherms in °F for Rotors and Attachment Assembly, Second Transient

The location of the joint between the hot pressed and reaction sintered materials is influenced by the stress distribution in the rotor disk. Because high stresses exist at the bore and between the neck and rim of the disk, it is apparent that as much of the disk as possible should be made of the higher-strength, hot-pressed silicon nitride. As a consequence, the location of the joint will be primarily dictated by practical considerations of the bonding process. A study was made to determine stresses for various joint configurations between the two materials.

This study considered five different joint configurations as shown in Fig. 3.13. The straight line configuration (No. 1) resulted in the lowest stresses, not only along the joint surface but also in the neck area.

The analytical methods used in this study were axisymmetric finite element heat transfer and stress programs. Step changes in material properties were assumed to occur across the joint surface. Blade loading was assumed to be uniformly distributed over the rotor platform. Average thermal conductivity values of the reaction-sintered material were used as input into the heat transfer program. An accurate assessment of the temperature and stress distributions in the immediate vicinity of the blades requires a three-dimensional analysis.

The procedure for the thermal stress analyses requires two major steps. The temperature distribution of the rotor assembly is determined from a model of both rotors plus the attachment. Refined models of each rotor, using the temperature distribution from the assembly model, are used to determine the stress distributions. The procedures used in this analysis are similar to those used in the monolithic rotor analysis described in the previous section and in the last report[1].

Steady-state heat transfer analyses were conducted for idle and full speed conditions. Isotherms for the idle condition, first and second stage rotors, are shown in Figures 3.14 and 3.15. Isotherms for the full speed condition, first and second stage rotors, are shown in Figures 3.16 and 3.17.

Stress analyses were performed for the following three conditions:

(1) 110% speed centrifugal loading.

(2) 110% speed centrifugal loading plus steady-state thermal stresses.

(3) Idle speed centrifugal loading plus idle steady-state thermal stresses.

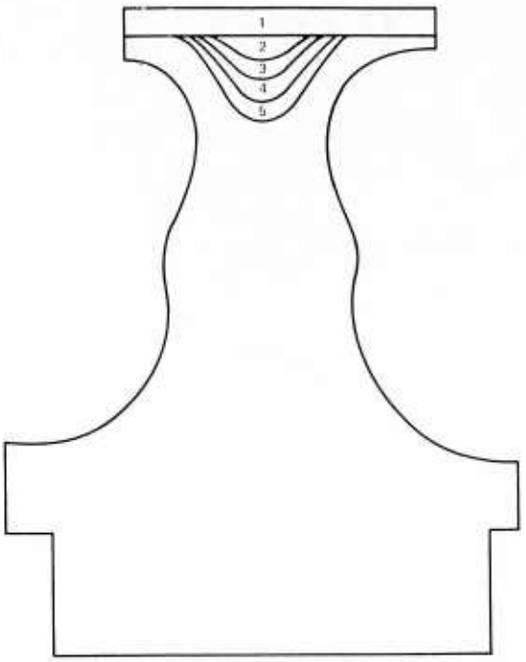


Figure 3.13 Five Joint Configuration Studied for the Duo-Density Rotor Concept

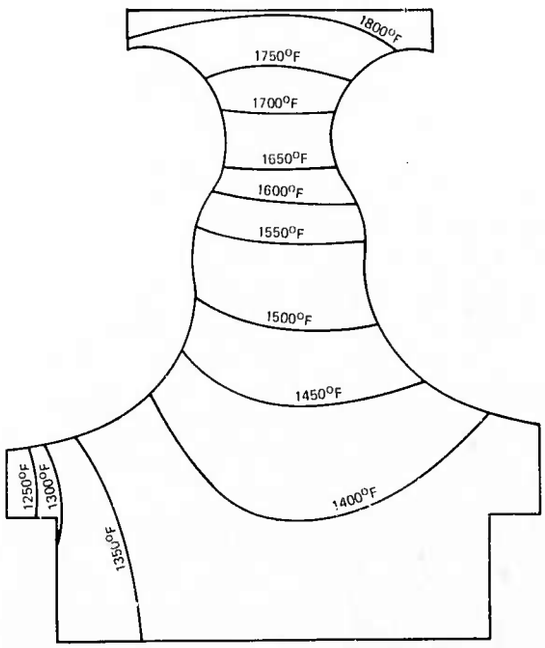


Figure 3.14 Isotherms in °F Determined for Idle Speed, First Stage Duo-Density Rotor

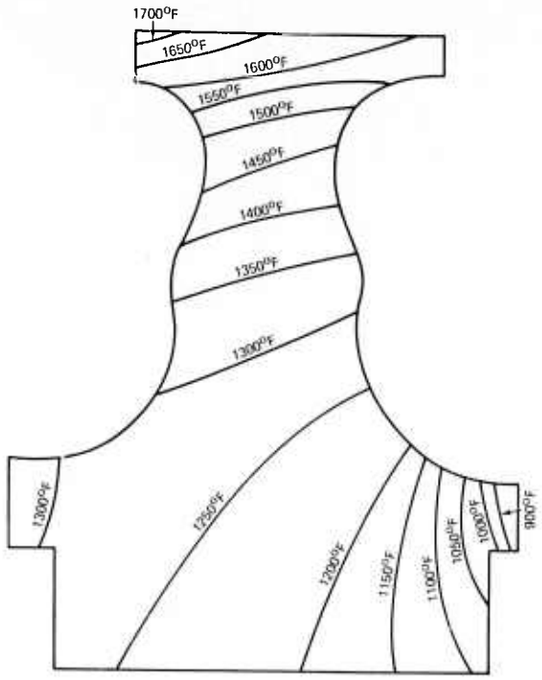


Figure 3.15 Isotherms in °F Determined for Idle Speed, Second Stage Duo-Density Rotor

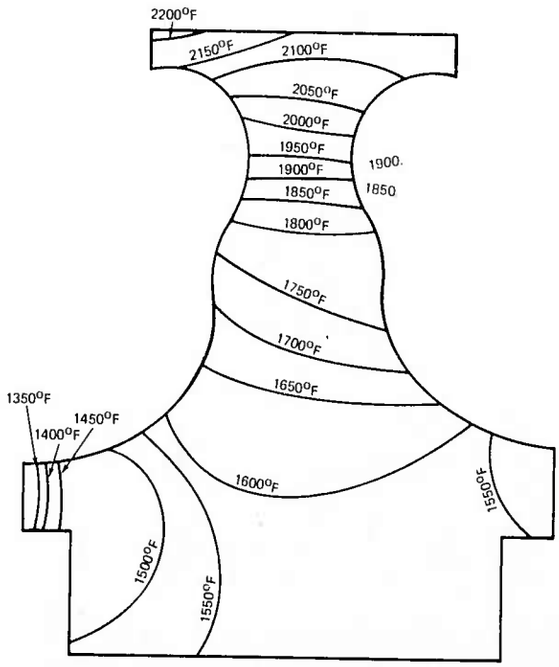


Figure 3.16 Isotherms in °F Determined For Full Speed, First Stage Duo-Density Rotor

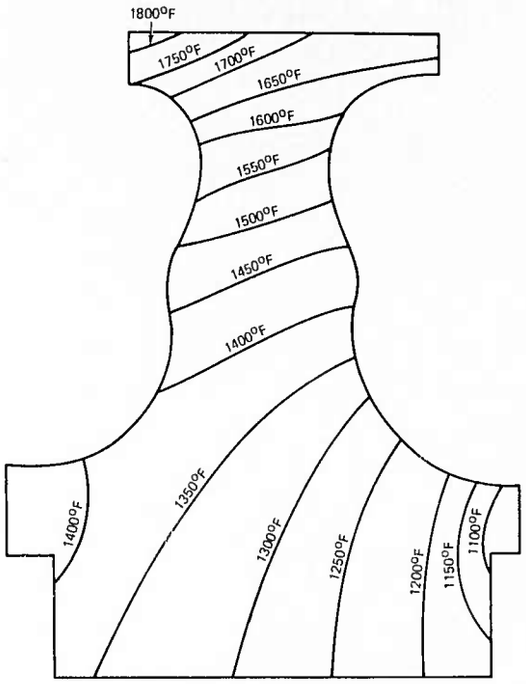


Figure 3.17 Isotherms in °F Determined For Full Speed, Stage Duo-Density Rotor

Figures 3.18 and 3.19 show the distributions of hoop and radial stresses respectively along the joint surface for the first stage rotor. The hoop and radial stresses along the joint surface for the second stage rotor are given in Figures 3.20 and 3.21. These stresses occur in the reaction-sintered silicon nitride portion of the duo-density rotors. The maximum bore and neck stresses occuring in the hot-pressed silicon nitride disk for the three loading conditions are presented in Table 3.1.

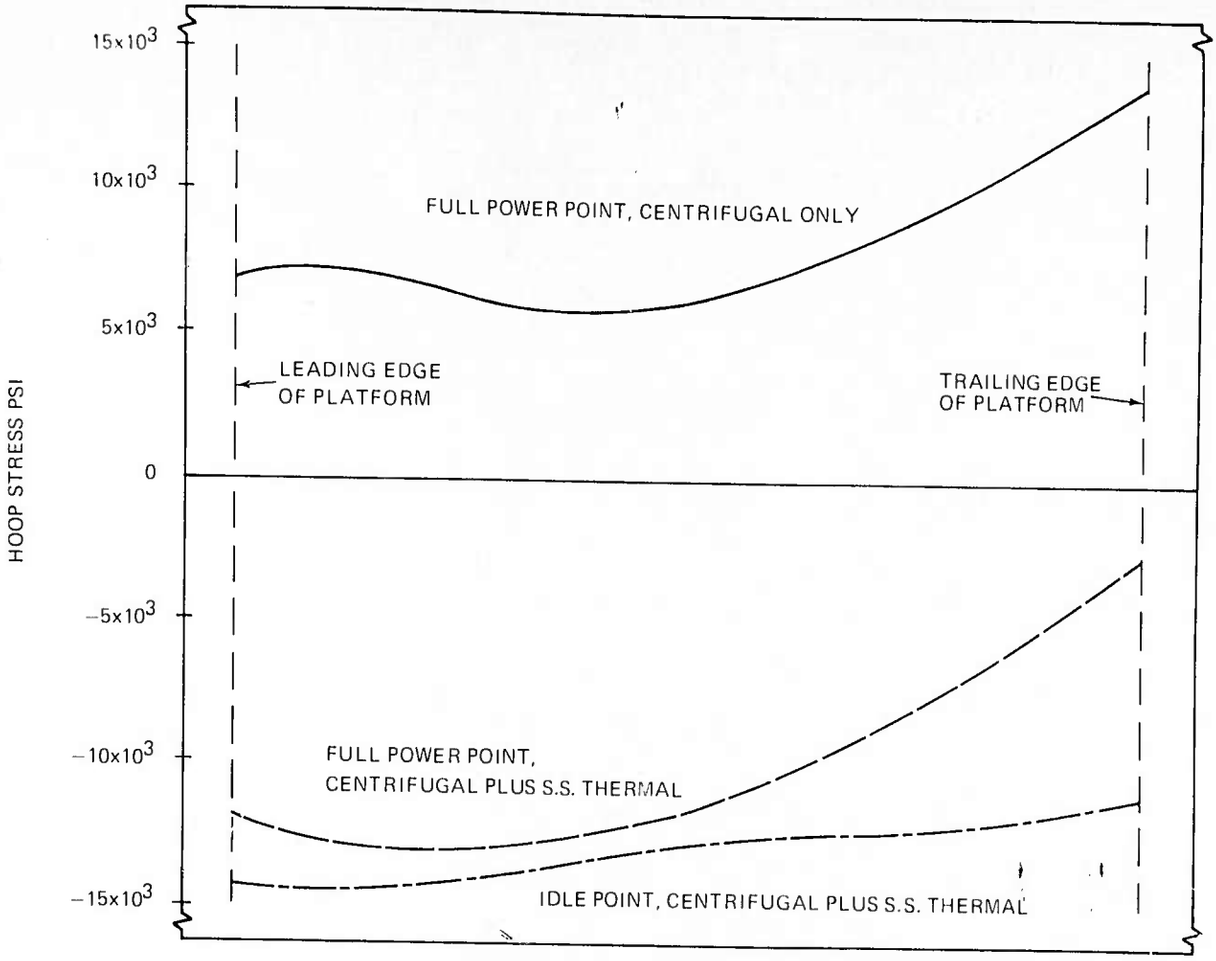


Figure 3.18 Hoop Stresses For First Stage Rotor Joint

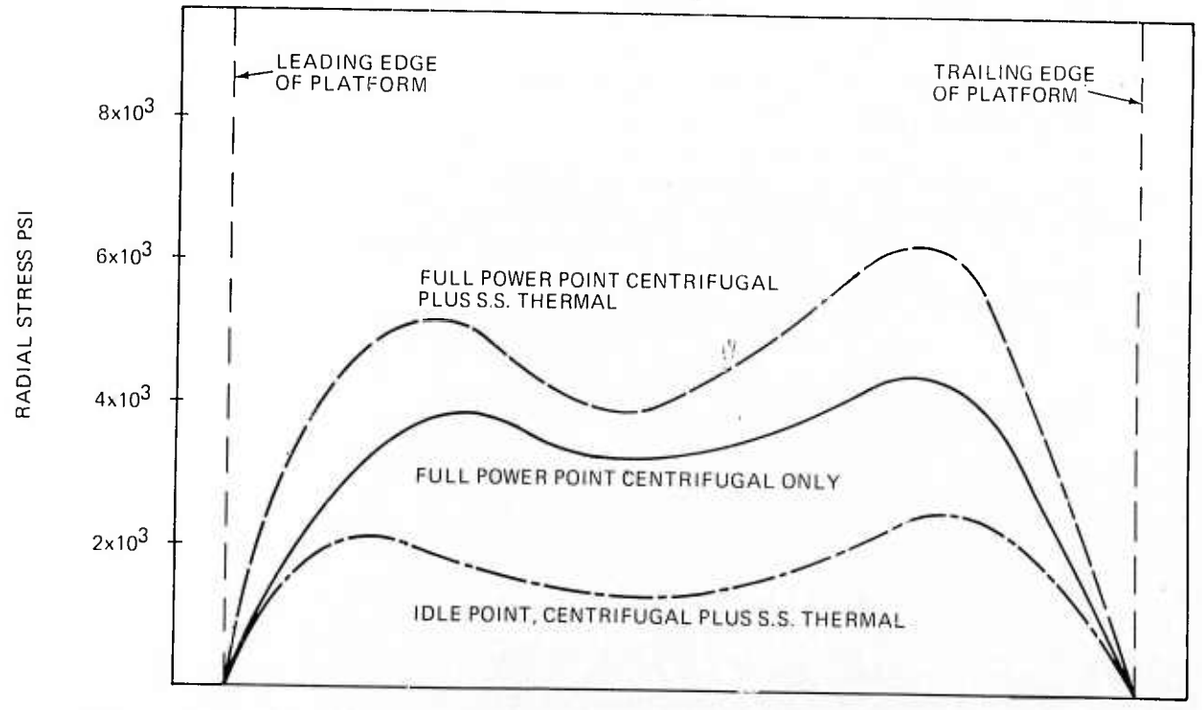


Figure 3.19 Radial Stresses for First Stage Rotor Joint

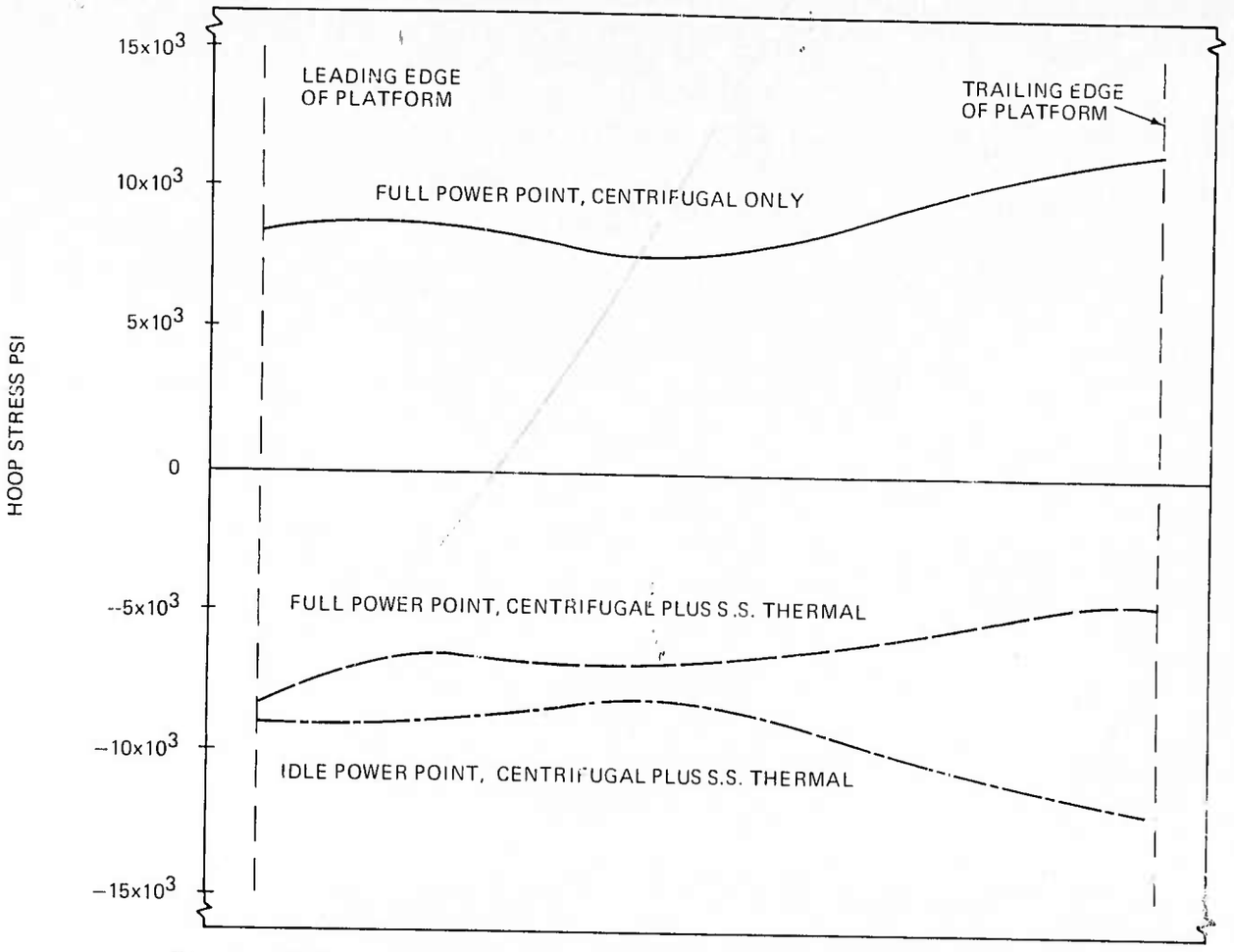


Figure 3.20 Hoop Stresses for Second Stage Rotor Joint

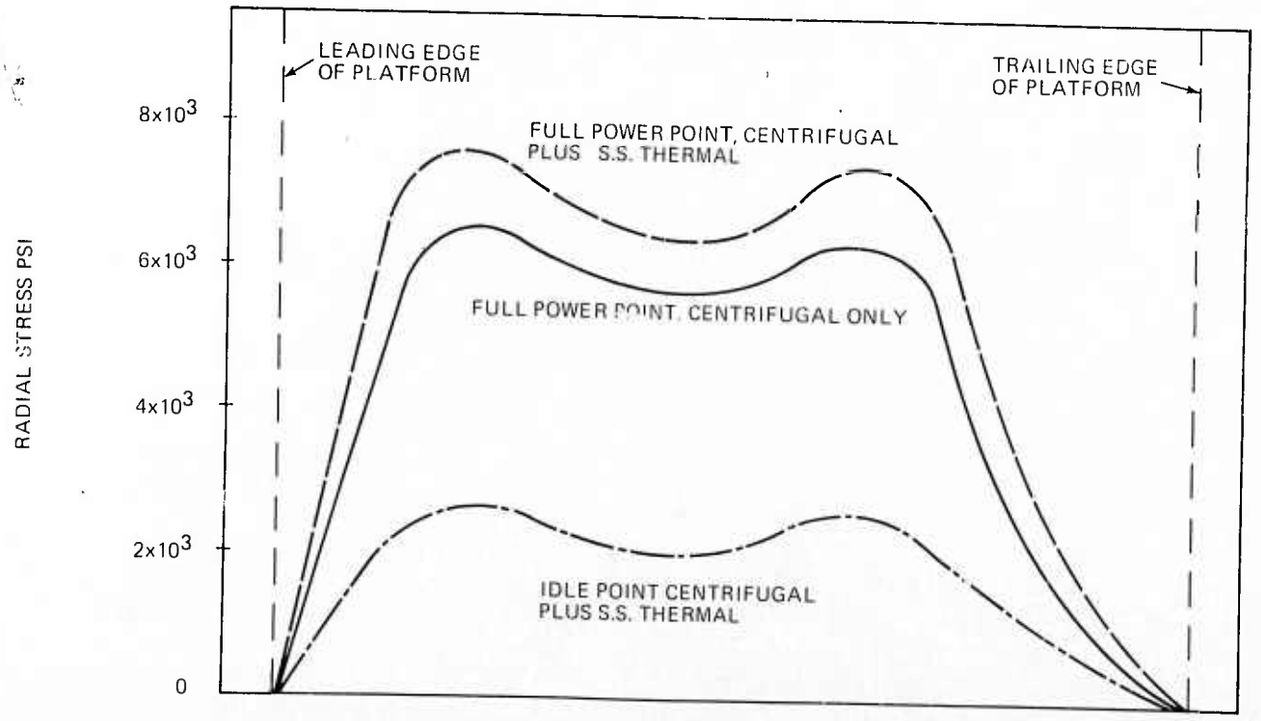


Figure 3.21 Radial Stresses for Second Stage Rotor Joint

Table 3.1 Maximum Bore and Neck Stresses - Duo-Density Rotor - Concept 1.

	FIRST STAGE			SECOND STAGE		
Thermal Condition	Mech. Only	Idle S.S.	Full Speed S.S.	Mech. Only	Idle S.S.	Full Speed S.S.
Rotor Rotational Speed	110%	55%	110%	110%	55%	110%
Bore Stresses	24,000 psi	15,000 psi	35,000 psi	28,000 psi	17,000 psi	37,500 psi
Neck Stresses	30,000	18,000	41,300	27,000	18,000	40,500

3.1.2 MATERIALS AND FABRICATION

Introduction

Previous work[1, 2] on fabricating ceramic turbine rotors has been concerned primarily with two candidate materials; fully dense silicon nitride and fully dense silicon carbide. Work has also been initiated on the duo-density rotor concept, as described in Section 3.1.1, which consists of a ring of molded reaction-sintered silicon nitride blades joined to a hot-pressed silicon nitride disk. In this concept, the high strength of hot-pressed silicon nitride is utilized in the disk region where stresses are greatest but temperatures are moderate and therefore creep problems are minimal. The blade portion, which reaches the highest temperatures, but at lower stress levels, is made from reaction sintered silicon nitride. The reaction-sintered material does not contain densification additives which contribute to creep in the hot pressed material.

Because of difficulties encountered in trying to make a ceramic rotor by the pseudo-isostatic approach previously reported,[1,2] emphasis has shifted to a study of assembling and bonding components for the duo-density concept. Additional fabrication benefits of this approach are apparent. Technology is well-developed[1,2] for injection molding of the complex airfoil shapes of the rotor blades while fabrication of the relatively simple disk shape from hot-pressed material is much closer to current state of the art.

Programs for fabricating monolithic rotors from hot-pressed silicon nitride include (1) ultrasonic impact grinding of blades from disks hot-pressed to the contoured rotor shape and (2) a conformable tool, psuedo-isostatic hot-pressing technique to form the blades without the need for machining.

Programs for fabricating rotors from dense silicon carbide include (1) chemical vapor deposition and (2) electric discharge machining from a disk of hot-pressed silicon carbide.

Pseudo-Isostatic Hot-Press Method

Hot-pressing is the principal method of fully densifying silicon nitride (Si_3N_4) because of its inherent resistance to sintering due to low atomic mobilities and high decomposition pressures at the sintering temperature. Hot-pressing or pressure sintering is the simultaneous application of pressure and temperature to an object usually contained within a graphite die system.

Because of the ability to form complex shapes, the pseudo-isostatic hot-pressing technique is one approach that has been investigated.[1] This approach utilizes a powder bed, usually graphite or boron nitride, which behaves as an isostatic fluid to transmit uniaxially applied pressure isostatically to a preformed part. After considerable effort, two major problems continued to persist. The blade airfoils deformed and fractured

during pressing, and the blades reacted severely with the graphite powder bed to form silicon carbide. The distortion and cracking of the turbine blades was caused by non-uniform flow of the powder media through the blade openings during hot-pressing. Variations in the techniques of loading and applying pressure did not solve the problem. Solid individual graphite inserts were designed to fit between the blades. These inserts greatly reduced the deformation, and allowed some densification of the turbine blades. However, all the blades exhibited some degree of fracture due to bonding between the graphite inserts and the blade airfoils, making the use of inserts impractical.

The severe reaction of Si_3N_4 turbine blades with the graphite powder bed continued to be a problem. The trailing edges of the blades are only 0.020 inch thick and complete conversion to a weak, powdery SiC resulted. The use of boron nitride as a powder media eliminated the reaction to form SiC, but boron nitride densified around the blades making removal of the finished part most difficult.

Because of these problems, the pseudo-isostatic hot-pressing technique has been de-emphasized in favor of more attractive alternatives for the fabrication of ceramic turbine rotors.

Duo-Density Method

The duo-density concept consists of blades of molded reaction-sintered Si_3N_4 joined to a hub section of hot pressed Si_3N_4, producing an integral turbine rotor. This concept is illustrated by a simplified cut-away view, Figure 3.22. The principal advantages of this concept are (1) known technology exists to form the reaction-sintered Si_3N_4 complex blade airfoils[1, 2], (2) reaction-sintered Si_3N_4, whose strength although low does not deteriorate with increasing temperature[1], is utilized for blades where operating stresses are low but temperatures are high, and (3) high-strength hot-pressed Si_3N_4 is utilized in the hub region where stresses are high but operating temperatures are low, minimizing the high-temperature creep characteristic of hot-pressed Si_3N_4.

The reaction-sintered portion of the duo-density turbine rotor consists of a ring of blades. Tooling was obtained for

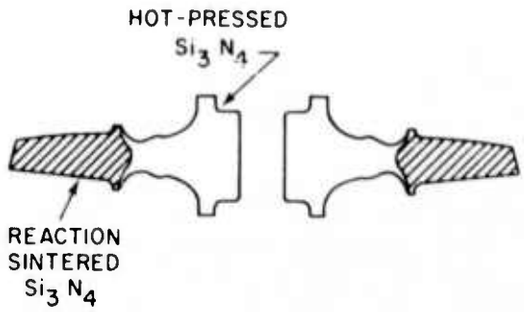


Figure 3.22 Duo-Density Turbine Rotor Concept

the injection molding of this component. Figure 3.23 illustrates two views of the molded blade ring along with the disk-like molding sprue which is subsequently machined off. This entire assembly is injection molded as one piece from silicon metal powder in an organic carrier which is later burned off and the component nitrided to form Si_3N_4. The ring adjacent to the blades can be easily modified to accommodate various design concepts of the reaction-sintered Si_3N_4 hot-pressed Si_3N_4 joint interface.

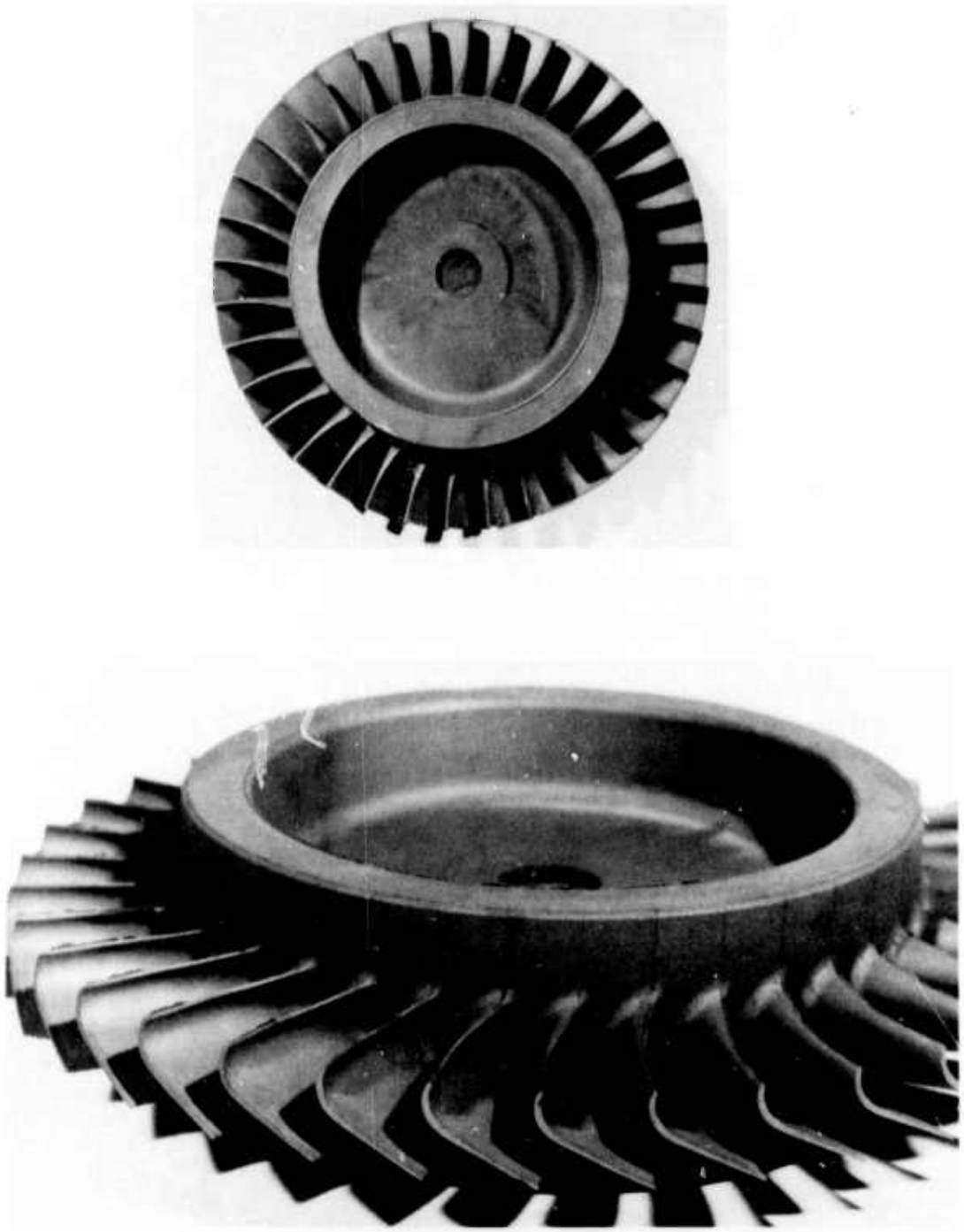


Figure 3.23 Injection Molded Blade Ring for the Duo-Density Rotor

Fabrication techniques for bonding the reaction-sintered Si_3N_4 blade ring to the hot-pressed Si_3N_4 disk are presently being developed. To expedite studies, reaction-sintered Si_3N_4 components of simplified shape which simulates the turbine rotor were used. A reaction-sintered Si_3N_4 ring with a simplified hot-pressed Si_3N_4 hub is illustrated in Figure 3.24. The small cylindrical hot-pressed disk was machined to slip fit within the inner diameter of the reaction-sintered Si_3N_4 disk, while two hot-pressed Si_3N_4 disks are used on the top and bottom of the reaction-sintered disk to form the hub.

The reaction-sintered Si_3N_4 rings were fabricated by cold pressing or slip casting silicon metal, nitriding the rings to form Si_3N_4, and machining the Si_3N_4 ring to the desired dimensions. The Si_3N_4 components for the hub were prepared by hot-pressing alpha-Si_3N_4 powder to theoretical density followed by machining each disk. All bonded surfaces were machined to remove any oxide or reaction surface layer. The components were assembled and re-hot-pressed to bond the parts. A typical simplified duo-density shape which has been bonded in this manner is shown in Figure 3.25.

The bonding between the Si_3N_4 component parts was excellent, as shown by the sectioned assembly in Figure 3.26. A closer view of the joints between the various components is shown in Figure 3.27. The duo-density shape in Figures 3.26 and 3.27 was hot-pressed at 1775°C and 2,000 psi for one hour. A thin Si_3N_4 coating consisting of Si_3N_4 powder dispersed in laquer containing 1 w/o MgO was painted on all bond surfaces to enhance densification and fill any small machining defects which may have been present.

The first few hot-pressed duo-density blanks exhibited radial cracks and severe reaction of the Si_3N_4 with the graphite hot-pressing dies to form SiC. The radial cracking problem was eliminated by using small graphite spacers to prevent the inner graphite sleeves from exerting excessive pressure on the reaction-sintered Si_3N_4 disk during hot pressing.

The severe reaction occurring in the reaction-sintered Si_3N_4, forming SiC, is shown in Figure 3.28. Various barrier materials have been evaluated to eliminate this reaction. Carbon cloth and boron nitride were not effective in reducing the reaction. However, both graphite and molybdenum foils were both very effective. For the latter two barrier materials to be effective, the cavity must be tight and completely lined with the barrier material. A duo-density shape hot-pressed using molybdenum foil as a barrier material is shown in Figure 3.29.

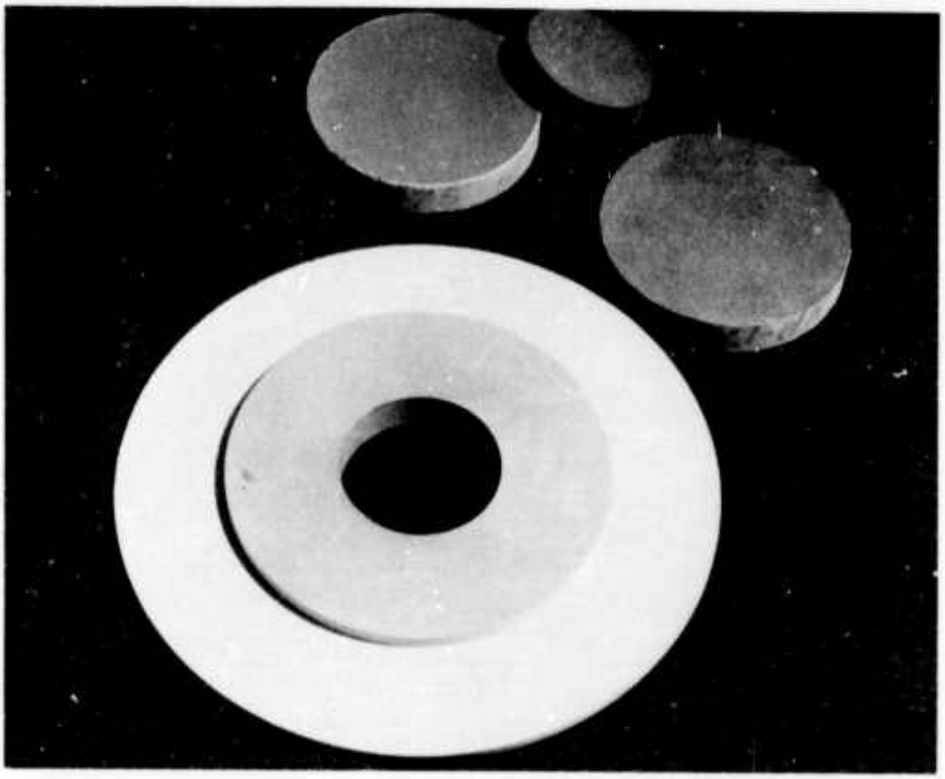


Figure 3.24 Simplified Silicon Nitride Components Used for Bonding Studies

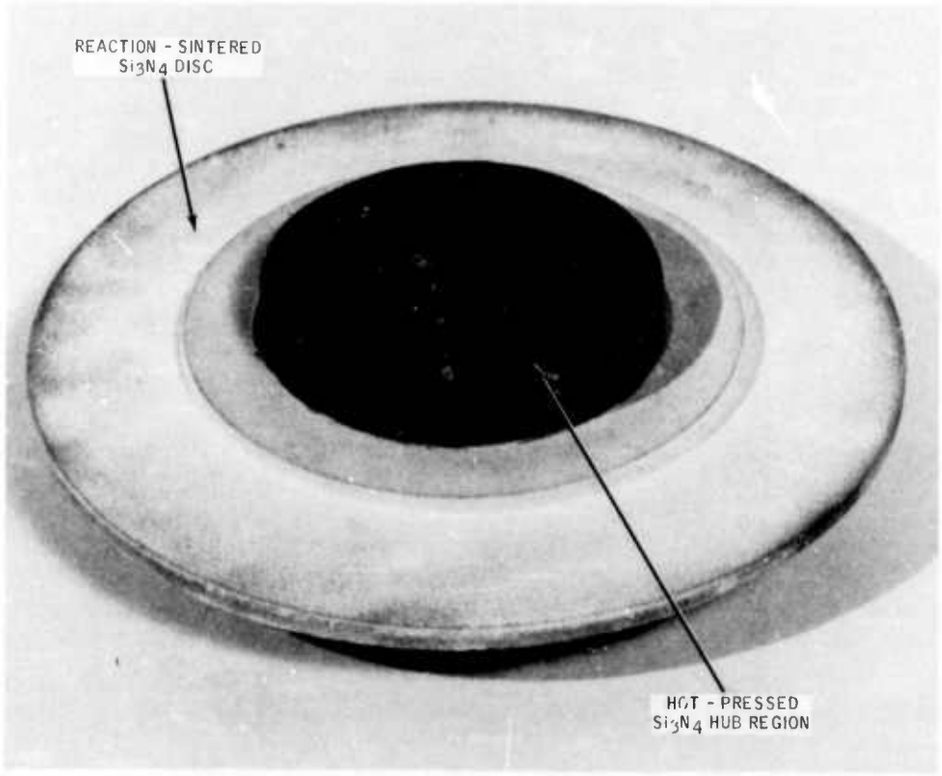


Figure 3.25 Bonded Duo-Density Shape

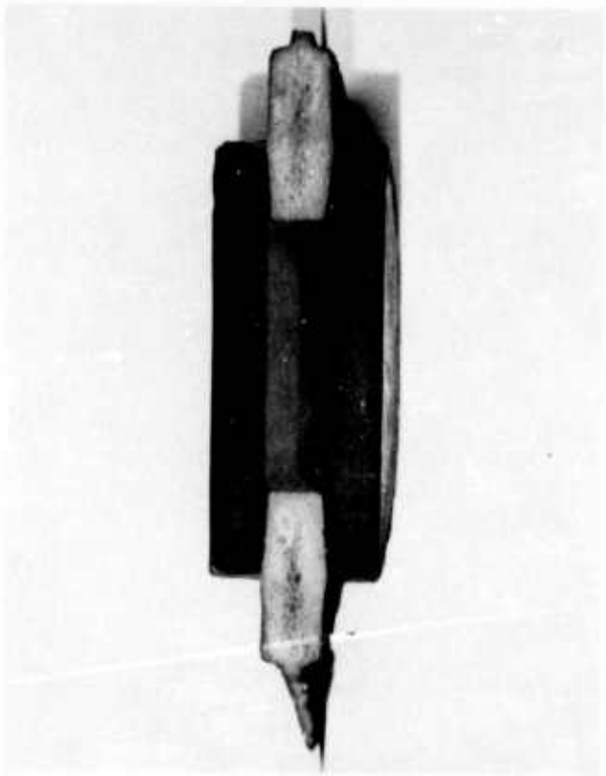


Figure 3.26 Sectioned Duo-Density Shape

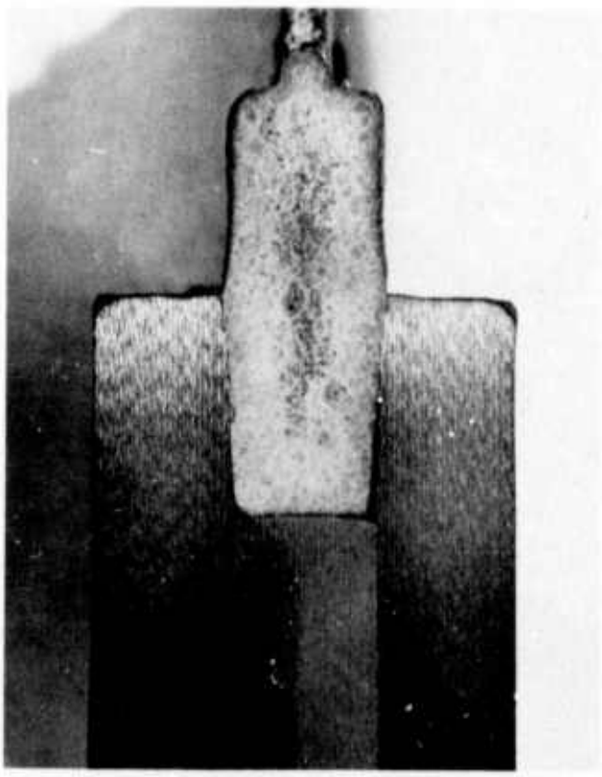


Figure 3.27 Magnified view of Joints in Duo-Density Shapes



Figure 3.28 Effect of Reaction With Graphite on Silicon Nitride

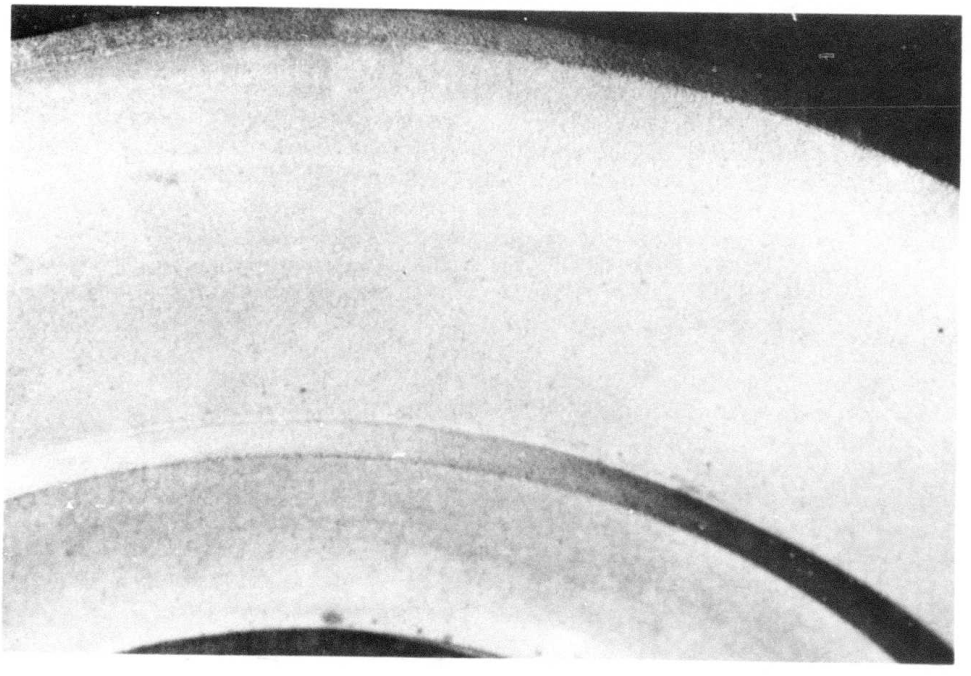


Figure 3.29 Surface of Silicon Nitride After Hot-Pressing with a Molybdemium Foil Barrier to Prevent Reaction

Bonding studies have been initiated to determine the optimum hot-pressing parameters to obtain satisfactory bonding between the Si_3N_4 components. These studies were conducted using 2 inch diameter disks of both materials which were joined by hot-pressing. The reaction-sintered disks were prepared by nitriding preformed silicon disks and the hot-pressed disks were prepared by hot pressing AME α-Si_3N_4 powder. The bonding surfaces of each billet were machined to remove any oxide or reaction surface layer.

The controllable parameters that affect the degree of bonding are temperature, pressure, time, and a bond-promoting material. This added material was a slurry of Si_3N_4 powder dispersed in laquer with varying amounts of MgO ranging from 0 to 5 w/o, which was painted on the bond surfaces of each disk to enhance bonding. The bonded samples were characterized with respect to microstructure and strength.

As an example of microstructure characterization the structure of two bonded samples (HP-162 and HP-165) are shown in Figures 3.30 and 3.31 respectively. The only difference between the processing of the two samples is that HP-162 contained a bond promoting layer of Si_3N_4 containing 2 w/o MgO while HP-165 had nothing added to its bonding surface prior to processing. Both samples were hot pressed at 1775°C under a moderate pressure of 1000 psi and held for only one hour.

The bond for HP-162, shown in Fig. 3.30, appeared poorer then the bond for HP-165, shown in Fig. 3.31. It is probable that the relatively low pressure (1000 psi) and time (1 hour) were insufficient to densify the Si_3N_4 bond promoting layer leaving a region of considerable porosity at the bond. The bond for HP-165, shown in Fig. 3.31, appeared considerably better in that a portion of the reaction sintered Si_3N_4 had undergone significant densification to approximately 5 microns below the original contact surface. This may be due to diffusion of some MgO sintering aid from the hot pressed material into the surface of the reaction sintered material during pressure bonding and appears to improve bonding under these conditions. The small white spots are tungsten, deliberately added to the Si_3N_4 powder to assist in the location of the bond region.

Room temperature flexural strength measurements were made to evaluate the bond strength. The strength measurements were conducted on tests bars (1/8 in. x 1/8 in. x 1-1/8 in. long) in 3 point loading with a 0.75 inch span. The test bars were machined such that one-half of the test bar was composed of each material. The samples were positioned such that the point of maximum tensile stress occurred at the joint. The strength values obtained varied from 23,000 psi to approximately 31,000 psi, and there appeared to be no correlation between strength and the degree of bonding, as judged from the microstructure of various bonds tested.

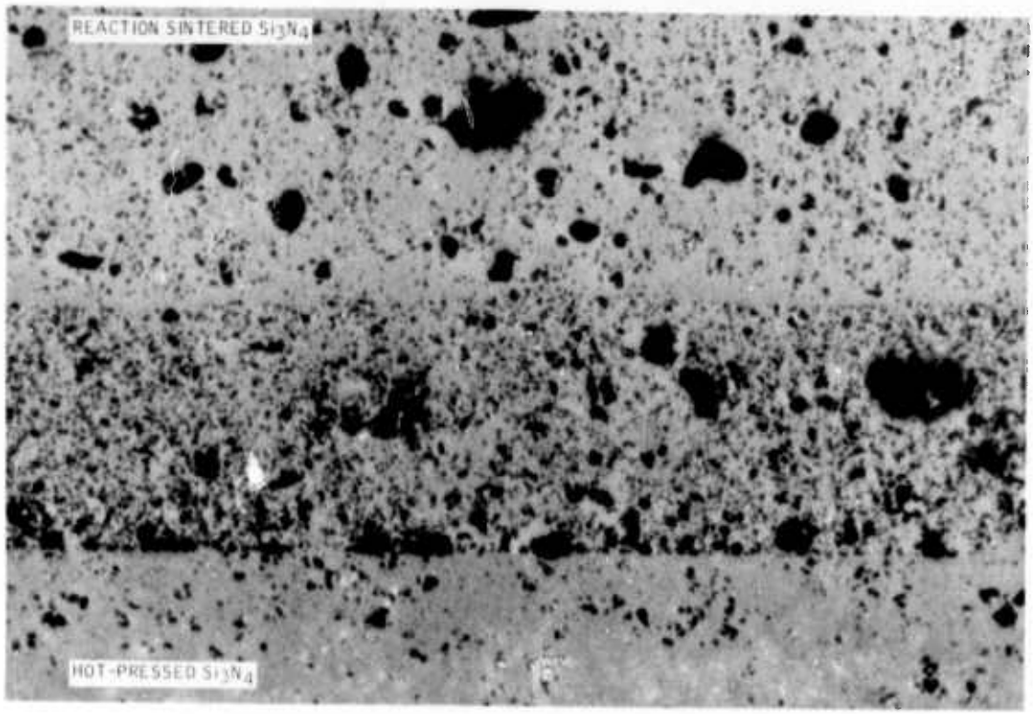


Figure 3.30 Microstructure of Duo-Density Bond, Sample HP-162. 500X

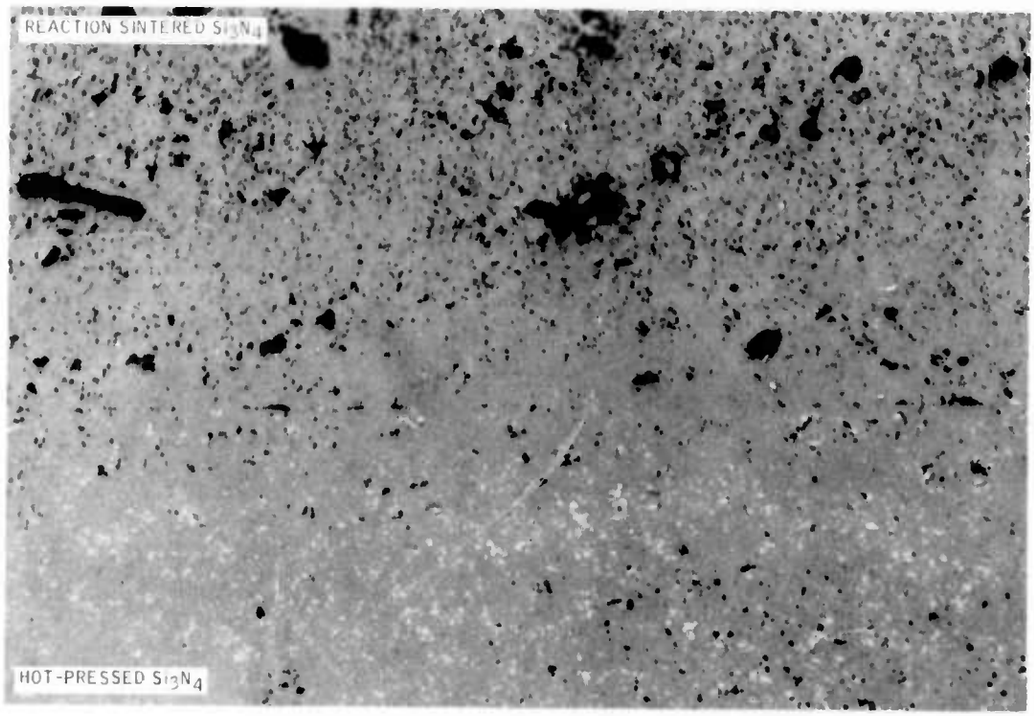


Figure 3.31 Microstructure of Duo-Density Bond, Sample HP-165. 500X

Perhaps of greater importance is the observations of the location of the fractures. Fifty percent of the HP-162 test bars fractured at the bond and fifty percent in the reaction-sintered Si_3N_4, indicating the strength of the bond and reaction-sintered Si_3N_4 are similar. All the HP-165 test bars fractured in the reaction-sintered Si_3N_4 portion and none at the bond, indicating that the bond was stronger than the reaction-sintered Si_3N_4. The strength results therefore reflect the metallographic observations that sample HP-165 was a better bond than sample HP-162.

These results indicate that good bonding can be obtained between reaction-sintered and hot-pressed Si_3N_4. Work is continuing to optimize the fabrication parameters.

Ford/Lucas Silicon Nitride Program

The Joseph Lucas Company, under subcontract to the Ford Motor Company, is engaged in a program to fabricate ceramic turbine rotors from hot-pressed silicon nitride.

The fabrication method starts with well characterized, high alpha phase, reactive silicon nitride powder, from which complex blade shapes are formed individually by injection molding the powder with a suitable vehicle. These will be assembled and densified by a conformable tool method.

Figure 3.32 illustrates this concept. The starting shape, which is larger than the final shape because of the densification occurring during hot-pressing, is delineated by the lighter lines in Fig. 3.32. The heavier lines show the final shape of the finished hot-pressed rotor.

Pending delivery of tooling to fabricate the blade preforms, work is in progress to hot-press the hub section. Using reactive

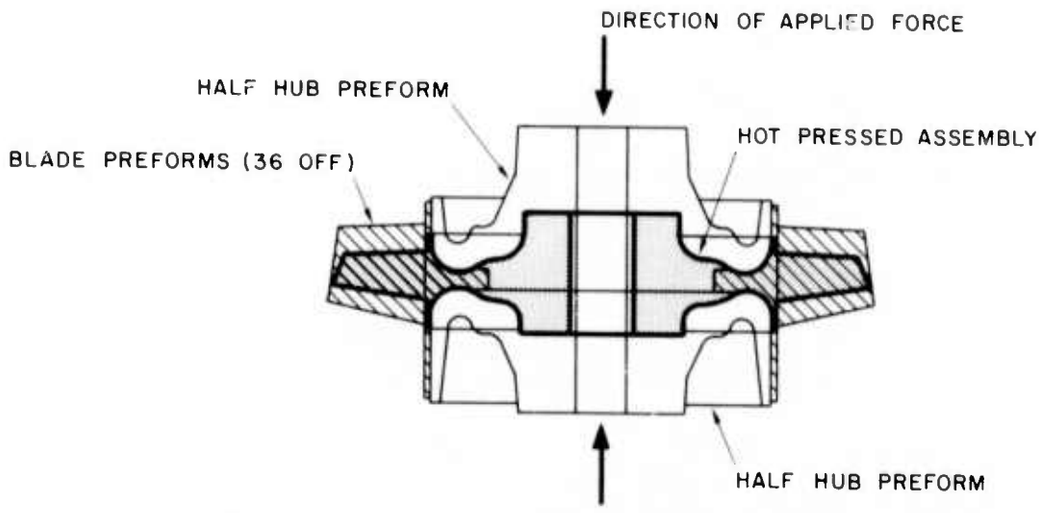


Figure 3.32 Lucas Concept for Hot-Pressing of Silicon Nitride Turbine Rotors

Si_3N_4 powder, which results in hot-pressed material with an average transverse strength of 132,000 psi, initial trials resulted in hot-pressed hubs close to desired dimensions. Some cracking, primarily in the radial direction, has been observed on all hubs. Modifications to the dimensions of the starting preform will allow hot-pressing to the correct final dimensions, and work is in progress to eliminate the cracking problems.

Ford/Energy Research CVD Silicon Carbide

It was previously reported[1, 2] that Energy Research Corporation is developing a process to form turbine rotors by the chemical vapor deposition (CVD) of silicon carbide. It was established[1] that a full size integral rotor shape could be formed in a tungsten mold and released intact as a free standing shape. However, filling of the mold was incomplete, resulting in hollow weak blades and not enough material in the hoop region. In addition, some cracks due to residual stresses were apparent.

Development of the CVD process has continued with emphasis on improvements in these problem areas.

A study is in progress to optimize deposition parameters governing the rate of deposition of silicon carbide within specific regions of the tungsten mold. These include:

- Temperature distribution within the mold.
- Concentration of reactant gases in the carrier gas.
- Flow rate of the gas mixture.
- Deposition time and temperature.

Results to date of this study are illustrated in Fig. 3.33 and Fig. 3.34, which show that blade fill can be achieved while a hoop of sufficient thickness is also formed. Fig. 3.33 also shows the cavity at the base of the blades. More work is required in order to form a homogeneous hoop under the blade roots.

Fig. 3.35 is a macrophotograph of a 1/16 in. thick cross section of CVD SiC as deposited inside a graphite cavity sliced from a 1-1/2 inch by 3/4 inch hollow shape, originally 5 inches long. The flow of gases was normal to the plane of the picture, with deposition proceeding from the periphery of the graphite cavity inward towards the central opening through which the reactant gases were passing. The CVD silicon carbide is translucent, indicating a relatively pure homogeneous deposit. Curved lines from the four sharp corners simulate the way silicon carbide deposits might grow together after bridging a blade root in forming a rotor hoop. Fig. 3.36 is an electron micrograph taken at 7,100X of a translucent portion of that junction. This is

a replica transmission photograph of a polished section etched 6 minutes in a fused mixture of 95.4 grams potassium carbonate and 13.0 grams sodium fluoride, and shows that the two growth regions depositing nearly 90° to each other can be made to knit into a dense product.

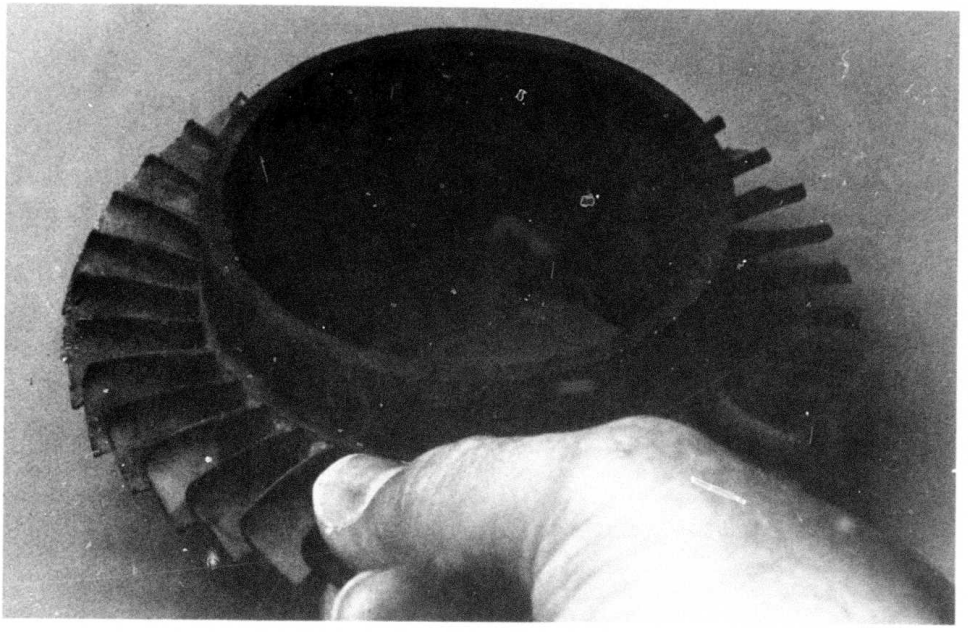


Figure 3.33 CVD Silicon Carbide Rotor

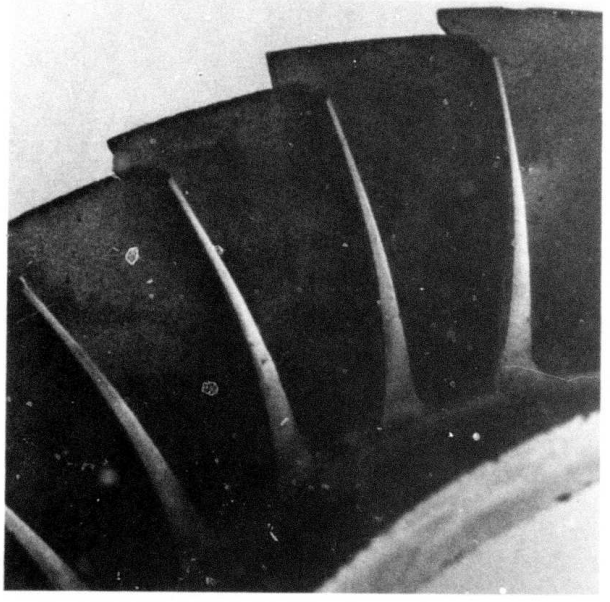


Figure 3.34 CVD Silicon Carbide Rotor Showing Fully Filled Blades

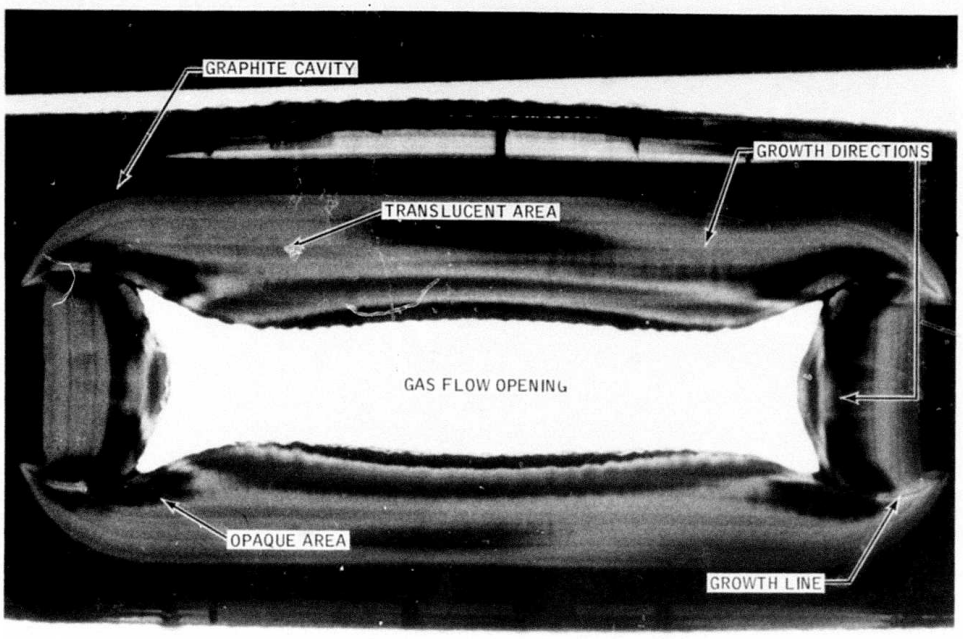


Figure 3.35 Thin Cross Section of CVD Silicon Carbide

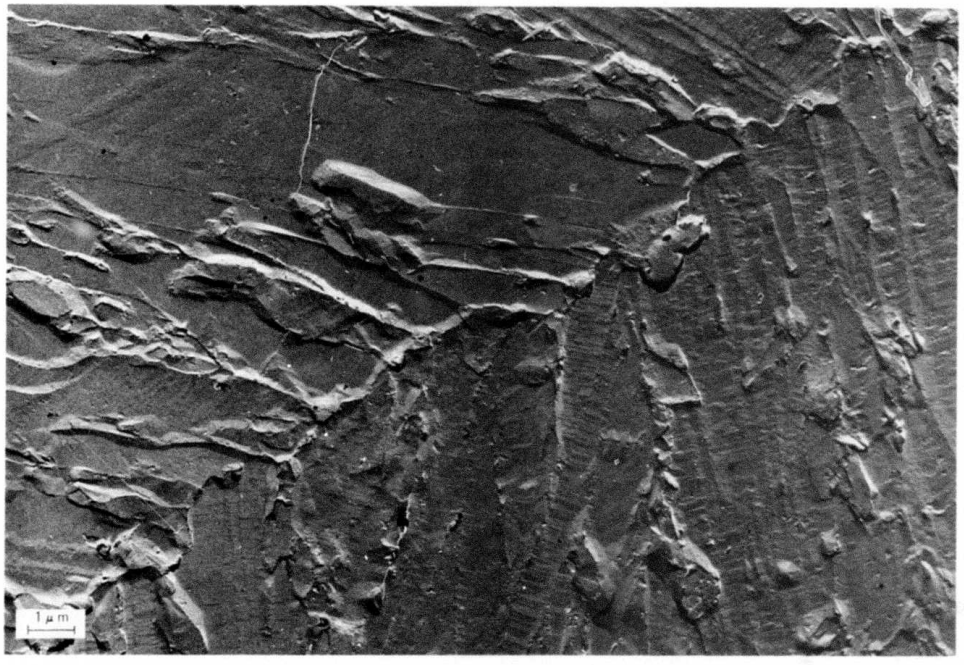


Figure 3.36 Microstructure of CVD Silicon Carbide at Joint of Two Adjacent Regions. 7100X

A few small regions of the macrophotograph, Fig. 3.35, appear opaque and were compared with their neighboring translucent regions. Fig. 3.37 illustrates the microstructure from an opaque region, while Fig. 3.38 shows the microstructure of an adjacent translucent region. These two figures are also transmission replica electron micrographs, and show many small inclusions of impurities occurring in Fig. 3.37 which are absent in Fig. 3.38. These impurities apparently cause the opacity. These photographs are preliminary results of an extensive characterization study which is currently in progress.

Ultrasonic Machining

Because of the long lead time anticipated in the development of fabrication techniques for ceramic turbine rotors, work was initiated aimed at machining of rotors from hot-pressed silicon nitride blanks. Ultrasonic impact grinding has been shown to be a feasible means of machining hot-pressed silicon nitride parts as pointed out in the last report[1]. Two aspects of this work are presented here; fabrication of the silicon nitride blanks and machining of the airfoil blades.

Work continued during this reporting period on the fabrication of contoured turbine rotor blanks for use in developing ultrasonic machining of airfoils. These blanks were made by hot-pressing to approximate contour in pre-shaped graphite dies and then ultrasonic machining to obtain the center bore and accurate contour.



Figure 3.37 Microstructure of CVD Silicon Carbide at Opaque Region. 7100X

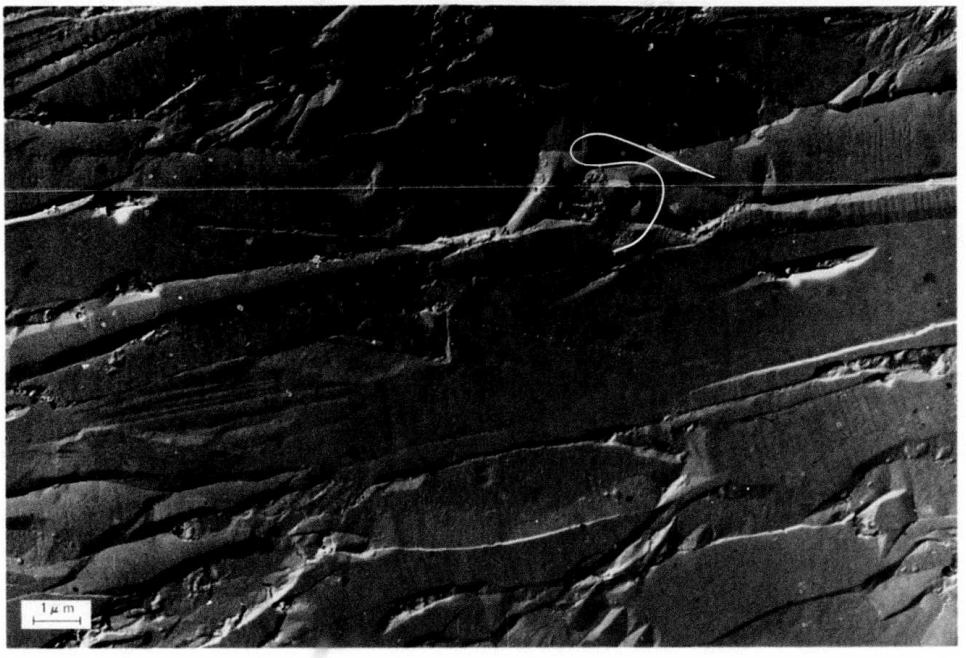


Figure 3.38 Microstructure of CVD Silicon Carbide at Translucent Region. 7100X

Silicon nitride power was ball-milled in rubber lined mills using tungsten carbide balls with a 2 w/o MgO addition as a densification aid. After milling, the Si_3N_4 powder was loaded into a graphite die system with shaped punches for hot-pressing. The shaped graphite punches used to form the contour of the turbine rotor are shown in Fig. 3.39. The rotor blanks were hot-pressed at 1775°C and 4000 psi for 2 hours, achieving 99 percent theoretical density. Flexural strength measurements made on test bars machined from a blank exhibited a strength of 113,000 psi as measured in 3 point bending on 1/8 in. x 1/8 in. x 1-1/8 inch long samples.

A view of a hot-pressed silicon nitride blank is shown in Fig. 3.40. The bore and neck area of this blank was finished by ultrasonic machining to final dimensions. A view of the ultrasonic tools, superimposed on a sketch showing the area machined, is shown in Fig. 3.41. The tools were fabricated from cold rolled steel and fed vertically into the rotating blank. Machining time was two hours per side.

In order to ultrasonically machine airfoil-shaped blades, an ultrasonic machining tool of constant thickness airfoil shape has been developed for rough cutting of rotor blades. This tool, shown in Fig. 3.42, was made from cold rolled steel and brazed onto a mounting block. Each constant airfoil blade can be cut in forty minutes of machining time, using a vacuum applied through the center of the tool to assist in removing debris.

A slurry of 200 grit boron carbide was used in this operation. Tool wear was shown to be a problem; a wear ratio of one part tool to three parts Si_3N_4 was measured. Diamond coating of the tool is being evaluated as a means of reducing this wear, however, a suitable coating has not yet been achieved which will make the diamonds adhere under the ultrasonic loads.

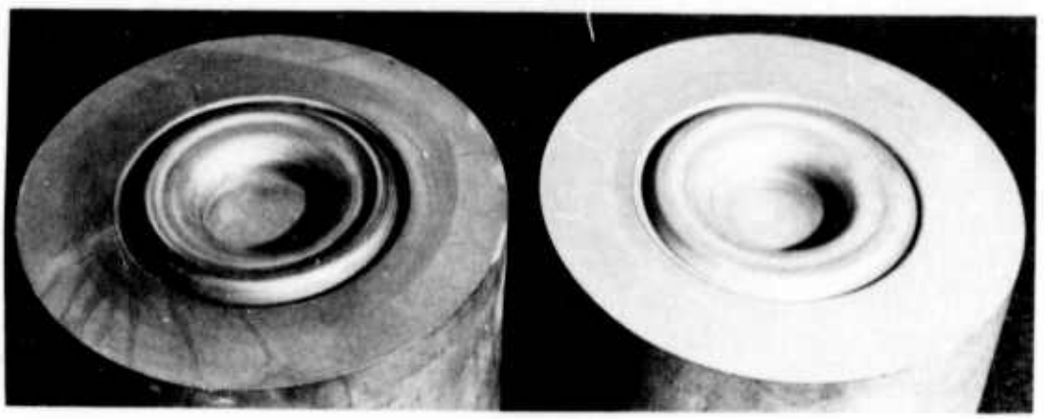


Figure 3.39 Shaped Graphite Punches



Figure 3.40 Hot-Pressed Silicon Nitride Blank

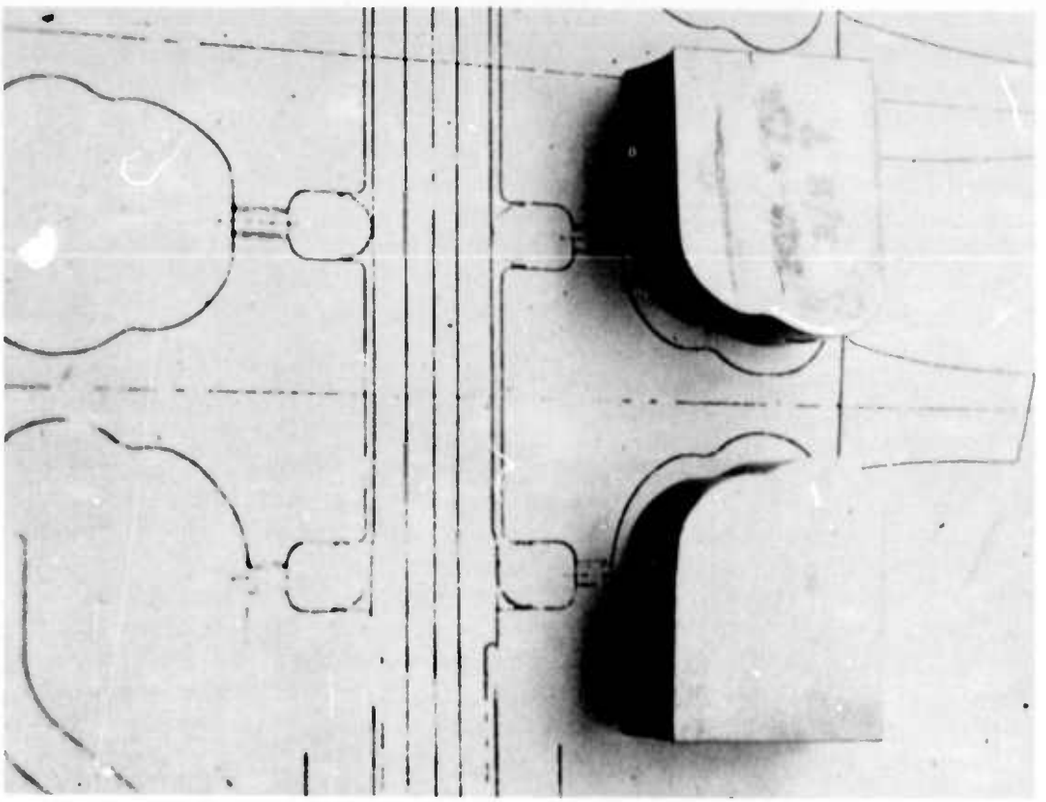


Figure 3.41 Ultrasonic Machining of Neck Area

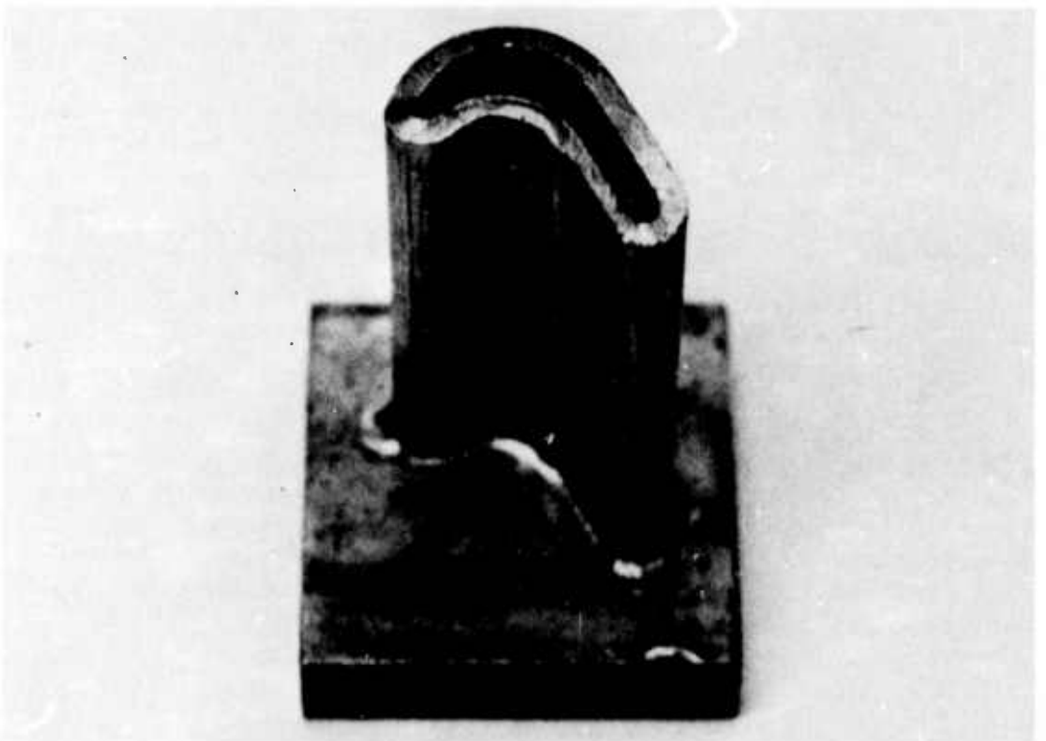


Figure 3.42 Ultrasonic Tool for Machining Constant Thickness Blades

A Bendix 2400 watt Cavitron machine is used for this ultrasonic machining development. The unit is equipped with a device for automatic control of the tool feed rate. A hot-pressed silicon nitride blank is shown on the Cavitron machine in Fig. 3.43; the disk is rigidly mounted on an index plate. The airfoil blade tool is positioned over the disk and automatically fed vertically downward into the disk. The abrasive grit is supplied externally to the tool and drawn under and through the tool by a vacuum. The disk used for evaluating the constant airfoil blade tools is shown in Fig. 3.44, after several blades have been cut.

The constant airfoil blade has been designed as an initial configuration prior to finishing to the final aerodynamic shape. The proper blade orientation must be maintained in this machining operation. The constant airfoil tools were designed to remove the maximum amount of material while allowing sufficient stock for the finished geometry. The design required that the cutting be performed at an eight degree forward tilt and five degree tangential offset. The tool was finished on its end to give the proper blade root radius at the platform. The constant airfoil shape was machined prior to finishing the leading and trailing edge surface in order to maintain the vacuum seal. The stock in this region is removed after all the blades have been machined. Fig. 3.45 shows a section of the test disk with this section removed.

Although ultrasonic machining of hot-pressed Si_3N_4 is a slow process, work will be continued on blade machining and hub contouring. The primary reason for blade machining is to provide ceramic turbine rotors for evaluation; should alternate approaches appear capable of producing rotors in equal or less time, the blade machining work will probably be terminated. Hub contouring will be needed for finishing of rotors formed by other methods, such as the duo-density approach, and will be developed accordingly.

Electric Discharge Machining of Hot Pressed Silicon Carbide

A program is in progress at Ford to establish the feasibility of machining a turbine rotor from a billet of hot-pressed silicon carbide by electric discharge machining (EDM).

Four grades of hot-pressed silicon carbide were evaluated for machinability by this method. Two of the four samples, one from Norton Company and one from Ceradyne Inc., were such good electrical insulators that it was impossible to machine them at all on the available equipment. The other two grades of SiC each required different machining parameters, and exhibited significantly different machining rates and ratios of tool wear to material removal.

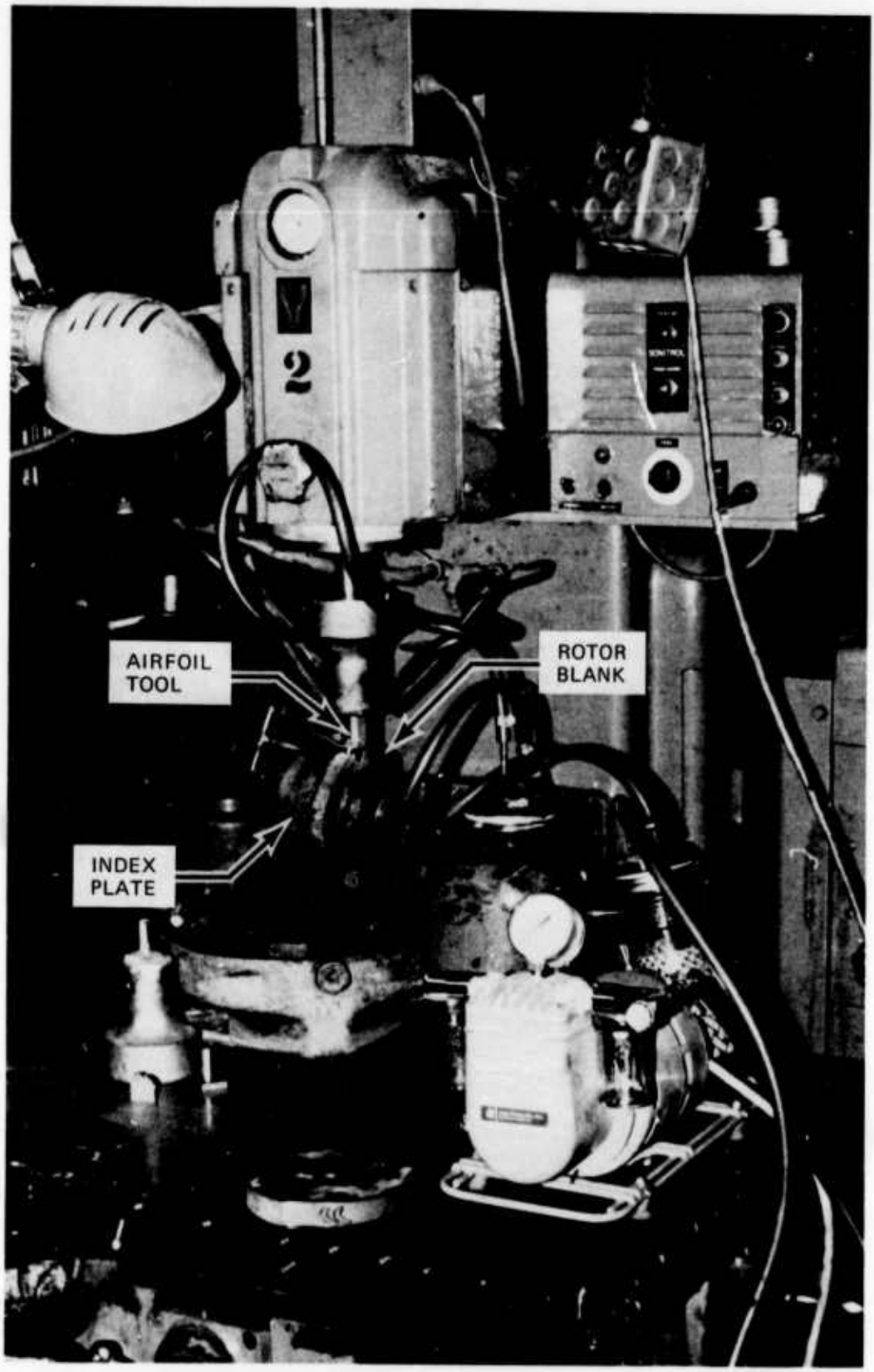


Figure 3.43 Bendix Cavitron Unit Used for Ultrasonic Machining Development

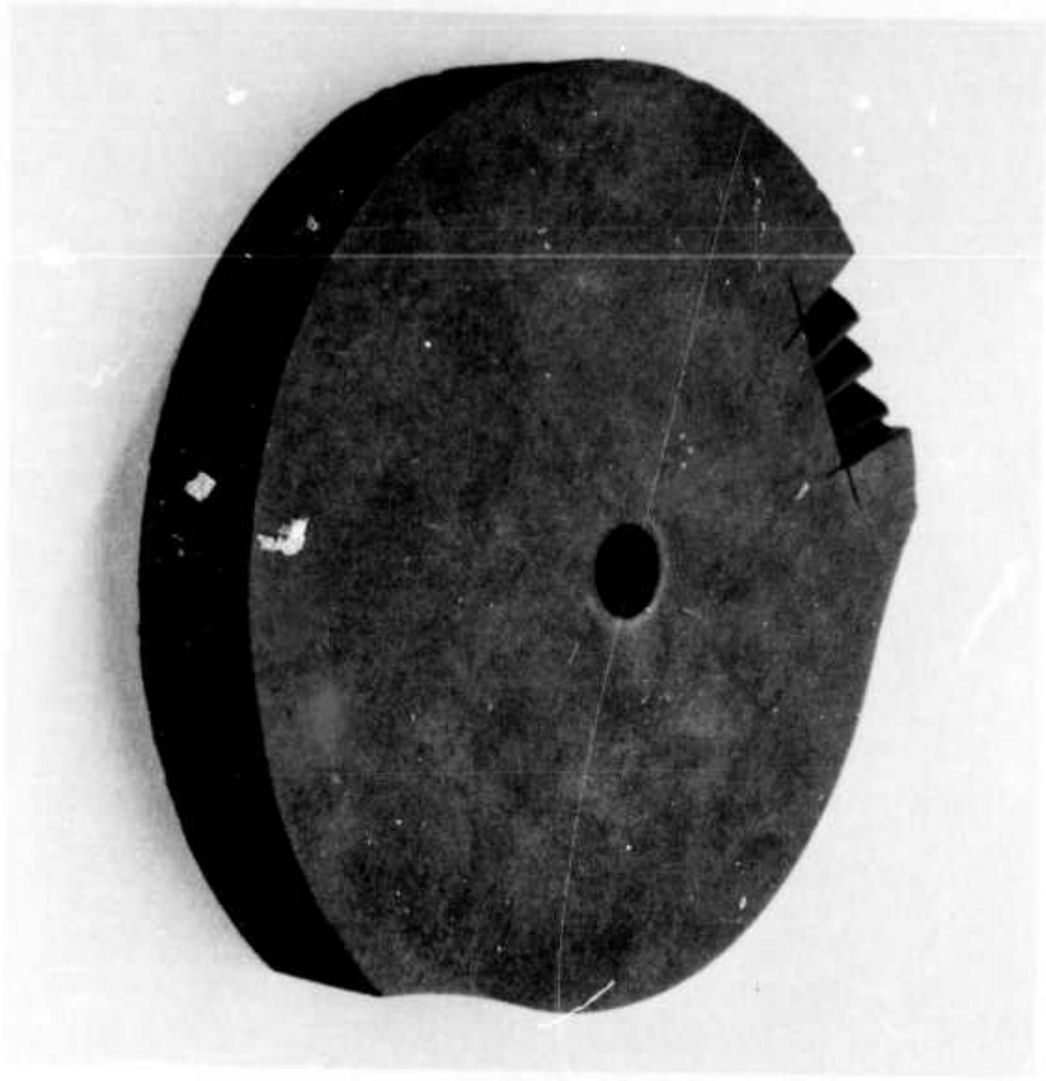


Figure 3.44 Disk of Hot-Pressed Silicon Nitride Showing Several Constant Airfoil Blades

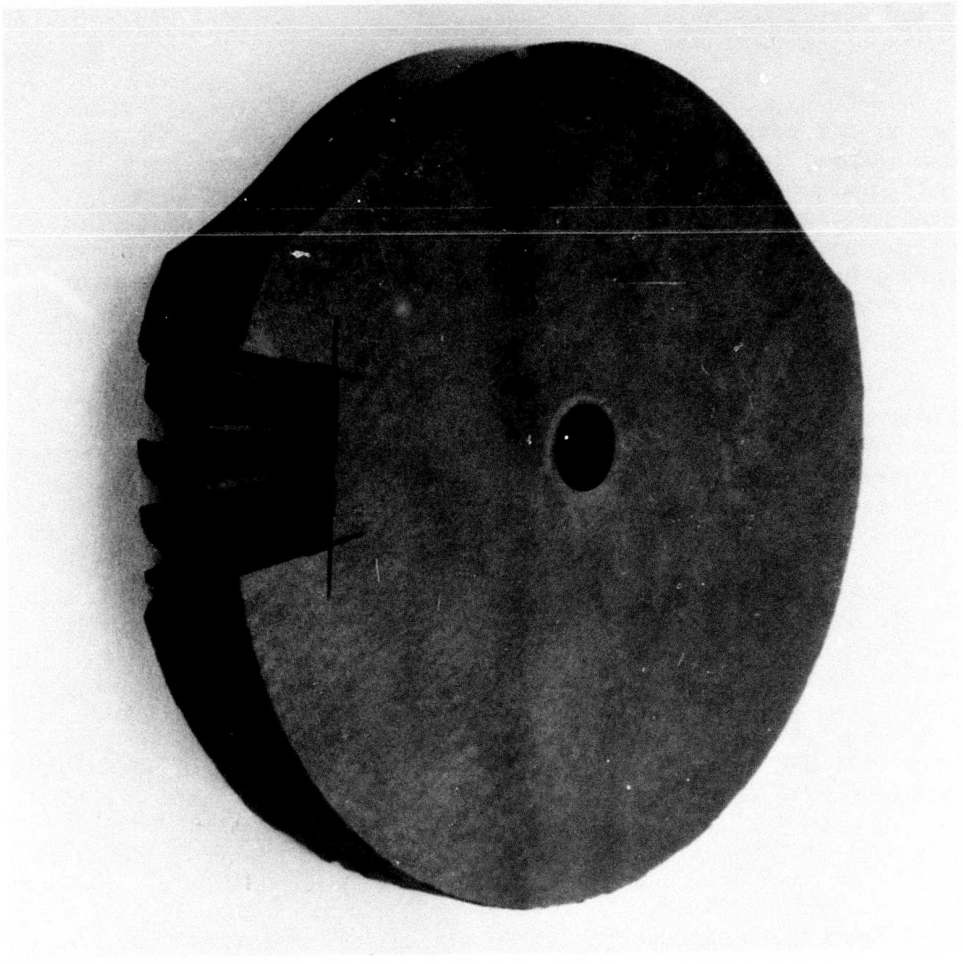


Figure 3.45 Hot-Pressed Disk with Extra Stock Removed

The sample with the highest electrical conductivity was Ceradyne 146A5, which had a surface resistance of 15 ohms as measured between two points one inch apart. A cutting arc from a 1/2 inch square copper tool, using 16 amps at 74 volts D.C., yielded an optimum cutting rate of 0.206 cubic inches per hour with a tool wear-to-material removal ratio of 1 to 9. The next highest conductivity grade Ceradyne 146ALF4 had a resistance of 35 ohms when similarly measured. With this grade, a cutting arc of 13 amps at 80 volts yielded a cutting rate of 0.105 cu. in. per hour and a tool wear to material removal ratio of 1 to 22.

Development work on formed tools to cut actual airfoil shapes is in progress.

3.1.3 TESTING

A Turbine Rotor Test Rig (TRTR) has been designed for use in ceramic rotor development. The TRTR simulates the mechanical and thermal loading conditions which the rotor experiences in the turbine engine. The main function of the TRTR will be to evaluate ceramic rotors over the full range of expected engine operating conditions. The test rig has considerably fewer parts than a complete engine and can be quickly rebuilt after a rotor failure. All rotors will be fully tested in the test rig prior to engine use.

The design of the TRTR is similar to the engine but is considerably simpler. The hot flow path ceramics, rotor attachment and bolt cooling mechanism, high speed shaft, and gear reduction reflect the latest engine hardware. Many of the individual rig components can be interchanged with engine parts. A schematic view of the rig is shown in Fig. 3.46.

As shown in Fig. 3.46, the burst shield completely surrounds the turbine rotors and pilots the hot flow section ceramics. The bore diameter is identical to the engine which allows the use of engine hot flow section components. The burst shield also collects and ducts the hot exhaust gas to the rig outlet port where it blends with the compressor discharge air and is then cooled with a water spray before being dumped into the test facility exhaust system.

The pressure drop across the rotors is controlled by a valve in the exhaust system downstream of the rig.

The first complete set of rotors of any design will be subjected to a 200 hour duty durability cycle which ranges up to 100% rotor speed and 2500°F turbine inlet temperature. During the duty cycle the rotors will be subjected to the same loadings at temperature and speed as experienced in the engine. Testing will be periodically suspended to check for possible creep.

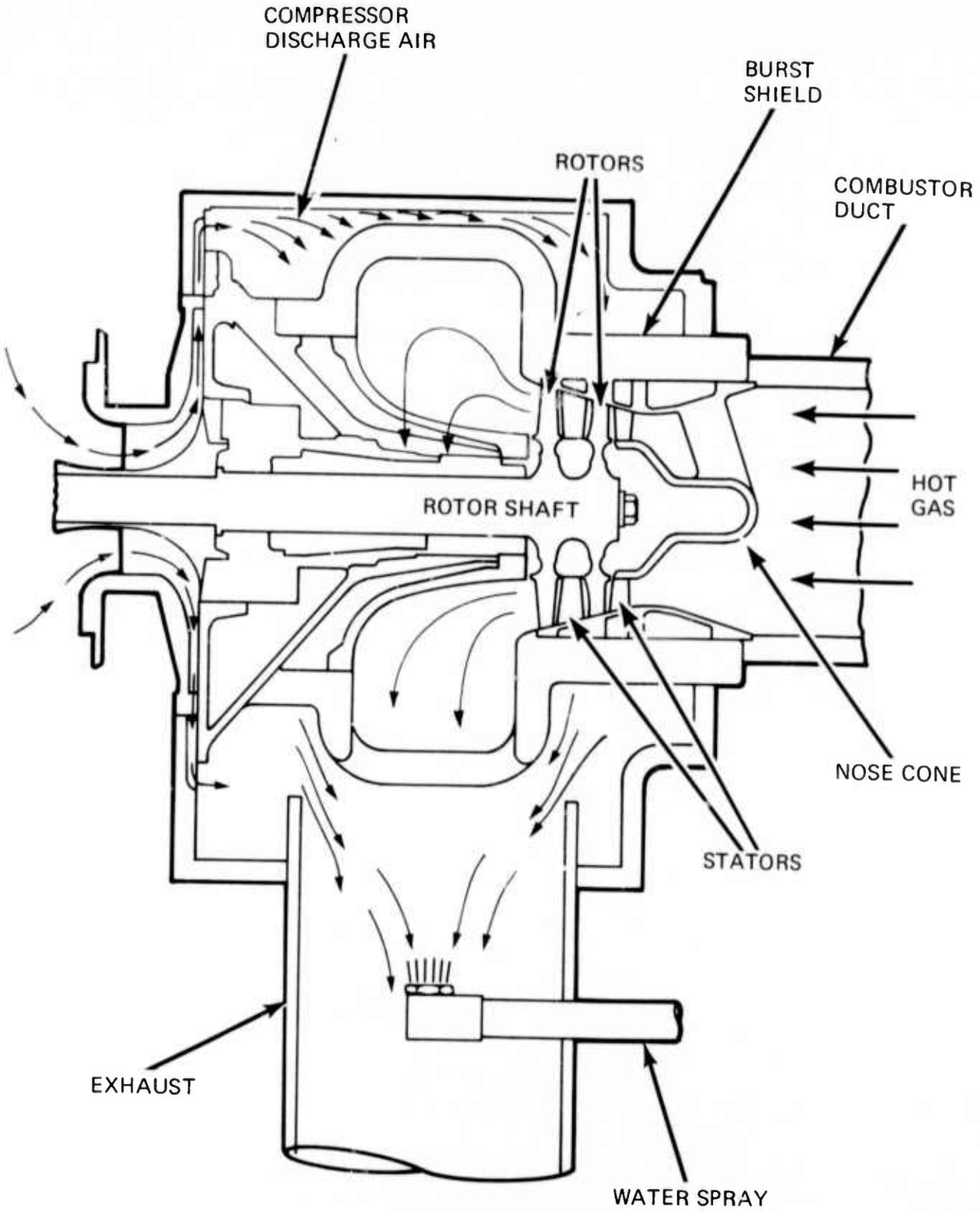


Figure 3.46 Turbine Rotor Test Rig

PRECEDING PAGE BLANK-NOT FILMED

3.2 METAL ROTOR DEVELOPMENT

SUMMARY

A considerable amount of dynamic engine testing is being conducted with metal rotors, pending the development of ceramic rotors. While the use of metal rotors causes the turbine inlet temperature to be limited to 2000°F, much valuable information about stationary ceramic components is being obtained. However, failures of second stage metal rotors have limited the amount of testing. Several of these failures have been identified as having been caused by high cycle fatigue. The cause of these fatigue failures was poor quality castings combined with a resonant condition at 55% engine speed.

New castings, conforming to a tighter specification and subject to a more stringent inspection process, are being obtained. The suspected source of excitation is under investigation. In the meantime, test engines are accelerated through the resonant speed range in order to continue the development of ceramic turbine components.

3.2.1 METAL ROTOR DEVELOPMENT

Introduction

The development of ceramic turbine rotors is the most formidable task in the development of the small ceramic gas turbine engine, due to the high strength required plus the complex shape. In order that the development and testing of the other ceramic components are allowed to continue in parallel, metal turbine rotors are used for dynamic testing. While this limits the turbine inlet temperature to a maximum of 2000°F, a considerable amount of meaningful thermal and aerodynamic testing can be done in order to confirm the design concepts of the other ceramic components. When ceramic rotors are available, they will replace the metal rotors.

Metal turbine rotors are fabricated by investment casting techniques using a nickel-base super-alloy developed by Ford before the start of this contract. This alloy is similar in composition to Mar-M-246. During 1972 several second stage turbine rotor failures occurred, although only one was catastophic and resulted in the destruction of other turbine components. These failures prompted an investigation into the causes of failure.

Materials Investigation

The investigation to determine if metallurgical quality problems contributed to the premature failure of metal turbine rotors necessitated re-evaluating all of the methods utilized in qualifying rotors for engine use. The following course of action was taken:

- All castings were macro-etched and reinspected by visual, fluorescent particle and radiographic means.
- The casting quality criteria was revised to emphasize the regions where maximum quality control was imperative.
- An investigation to identify the failure mechanism was initiated.
- The mechanical properties of rotors with satisfactory service lives were compared to mechanical properties of the failed rotors.

Re-evaluating all available rotors resulted in identifying a hot tear condition in some castings. Hot tears, which initiate early in the casting process and occur at grain boundaries, were detected in several untested castings. They were located, in all instances, in the area which was the location of cracks detected after engine operation. Previous inspection procedures did not detect this condition since the cracks were extremely tight. Smeared metal remaining on the casting surface retarded detection even though very sensitive fluorescent particle inspection procedures were employed.

Attempts were made to determine if hot tears were present in the failed rotors which ultimately led to severe cracking and one case of rotor burst. Identification of hot tears was not possible since the service temperatures were high enough to oxidize any carbides present in the cracks, thus preventing detection of carbides which would have been present in open cracks during solidification of the castings.

Examination of the fracture surfaces of failed rotors by transmission and scanning electron microscopy did not reveal any specific initiation site. Some associated porosity in the fracture surface was observed but its effect upon crack initiation is not known.

The material quality specification for metal rotors covers all aspects necessary for initial acceptance of first and second stage rotor castings. The type of inspection was established for several non-destructive methods. These included visual, radiographic, acid etch and fluorescent particle inspections.

Chemical and mechanical property requirements for casting lot acceptance were stipulated in a previously established specification.

It was necessary to optimize the x-ray procedures used for subsurface defect detection due to the varying thickness of the rotors. A minimum of four exposures for the first stage rotor was established. Once the procedures were optimized, x-ray indications were noted in these rotors at 140 Kv, but not at 1000 Kv. It was noted that these indications intersected the outer diameter of the platform and were oriented radially in each rotor while the number and severity varied considerably between rotors. These indications had a specific block-type morphology and a sharp, defined outline as shown in Fig. 3.47.

Metallurgical examination of a first stage rotor, investigated specifically to identify these subsurface indications, revealed no segregated or grain boundary associated micro-shrinkage of sufficient magnitude to be observed by x-ray radiography. Microspecimens taken from areas with many x-ray indications revealed large dendrites (columnar grains) which constituted a major portion of the section thickness. An incremental, two-plane, metalographic analysis was conducted to determine the extent of dendritic formation and to intersect any subsurface flaws. The plans analyzed were oriented parallel and perpendicular to the rotor axis. These grains were truely dendritic, in that they had the classical tree-like shape and lack of random carbide formation within the grain due to solute rejection during solidification. The absorption of x-rays passing through the rotor, normal to the rotor, depends on the orientation of these grains in specific areas. It was concluded that this effect was creating the subsurface indications noted during radiographic inspection and could impair the detection of actual subsurface flaws.

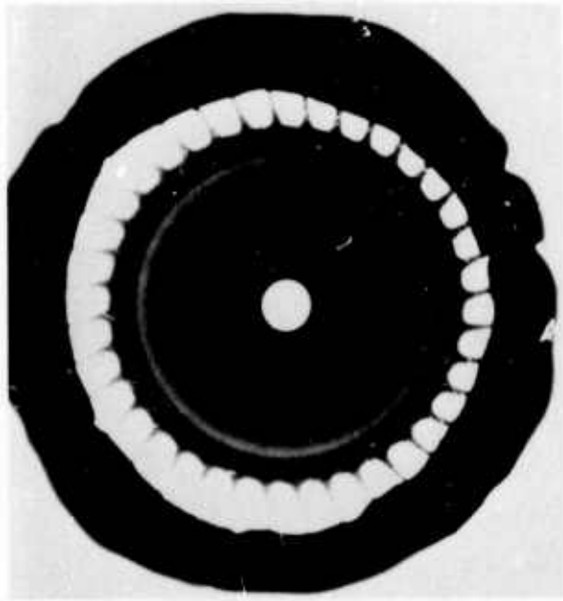


Figure 3.47 Radiographic Reversal Print Showing X-Ray Indications

The failure mode was identified as high cycle fatigue. This was substantiated by scanning electron micrographs which showed the fracture surface, at the initiating side of the rotor, to be crystallographic and typical of fatigue controlled fracture in this alloy.

A rotor with over 100 hours of engine service and a failed rotor were examined metallographically and the mechanical properties determined from test specimens machined from the rotor hub regions. The results appear in Table 3.2.

The 100 hour rotor had finer grain size, higher ultimate tensile strength, comparable yield strength and nearly double the ductility of the failed rotor. The increase in ultimate tensile strength affords added resistance to high cycle fatigue while the significant increase in ductility allows for greater redistribution of localized stresses.

Microstructural analysis showed the carbide morphology to be different in the two rotors. The long life rotor had an angular type while the failed rotor had a script type of carbide morphology as shown in Fig. 3.48 and Fig. 3.49 respectively. In general, these grain boundary carbides are dislocation sources which influence the ductility of the material. The "script" type carbide material typically has a lower ductility than the angular type, which is substantiated by the data in Table 3.2. A significant difference in the interior grain size between the two rotors was also noted as shown in Fig. 3.50.

Based on these results, guidelines have been established to eliminate occurance of this situation in subsequent rotor castings. The vendor has been notified of these findings and is presently involved in casting additional rotors which conform to the specification requirements.

Table 3.2 Property Comparison of Rotor Materials

Prior Rotor History	Grain Size	Ultimate Tensile Strength KSI	Yield Strength 0.2% KSI	Elongation %
Burst Failure	1/8-1/4 in.	127(1)	124	4.3
100 Hours Service	1/32-1/16 in.	139(2)	129	8.2

(1) Average of two test specimens.

(2) Average of four test specimens.

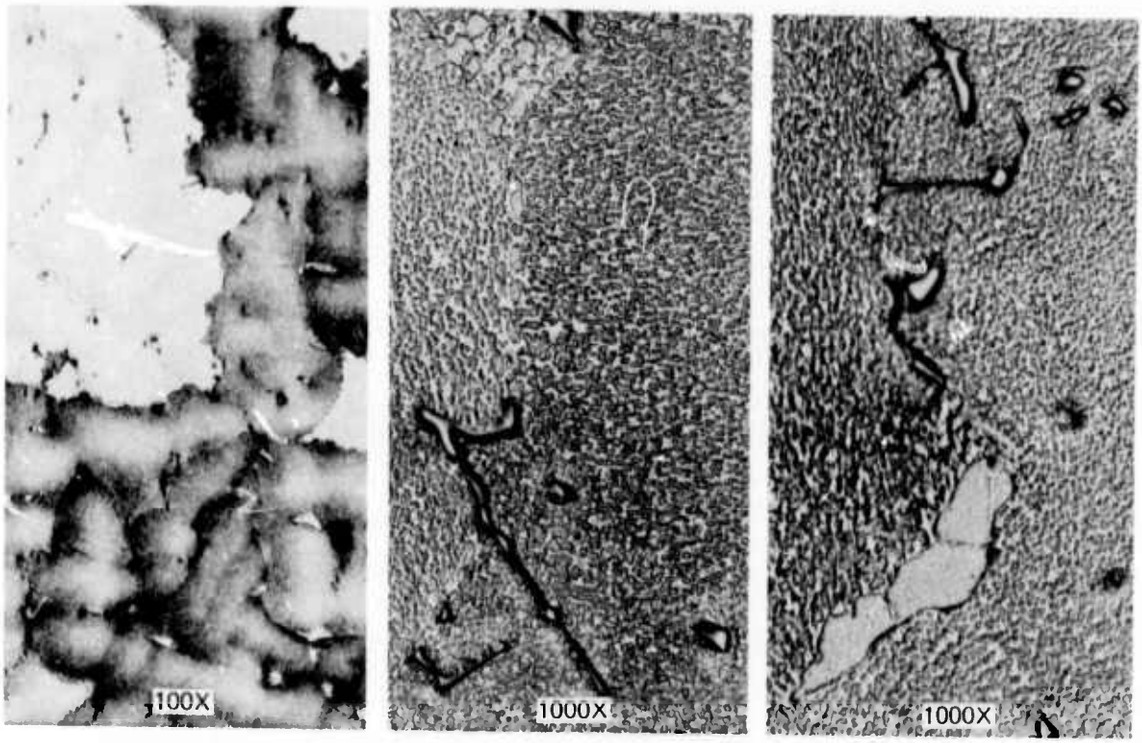


Figure 3.48 Angular Carbide Formation in Long Life Rotor

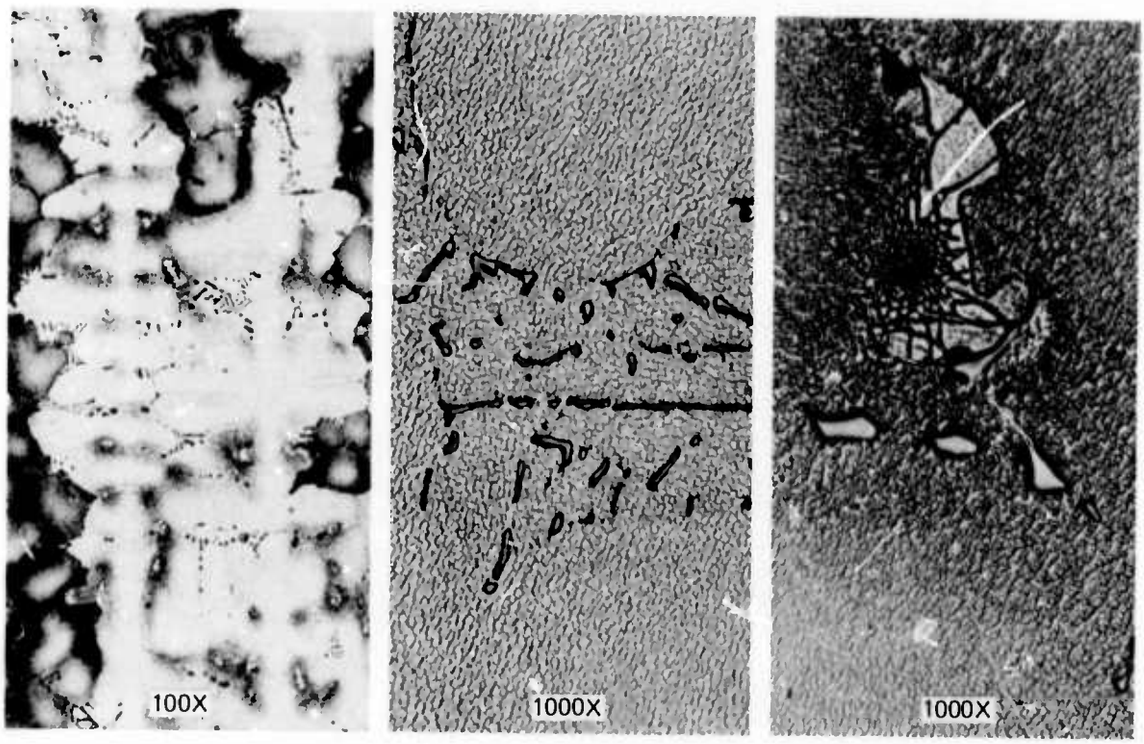


Figure 3.49 Script Type Carbide Formation in Failed Rotor

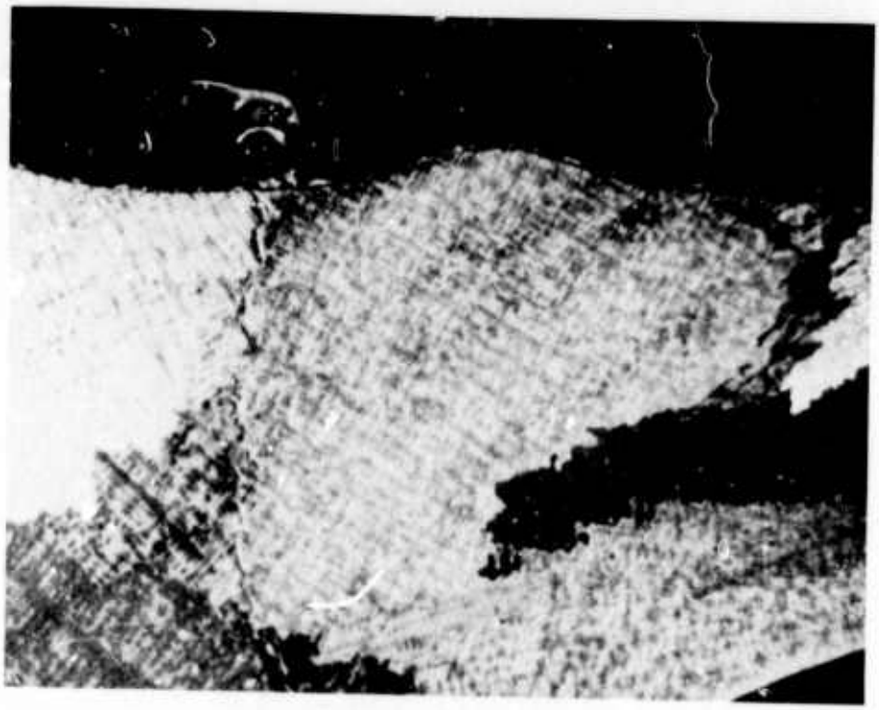


Figure 5.50a Grain Size of Failed Rotor. Grain Size Approximately 1/4 inch



Figure 5.50b Grain Size of Long Life Rotor. Grain Size Approximately 1/16 inch

Figure 3.50 Interior Grain Size Comparison Between Long Life and Failed Rotors

Investigation Into Causes of Metal Rotor Failures

The last report[1] presents information on most of the second stage rotor failures. Three additional failures occurred during this reporting period; cracks were found in the hub area after 45 minutes of engine operation.

A two fold test program was initiated to determine the rotors natural frequencies and the critical engine operating conditions.

The natural frequencies of the rotor were determined by holographic techniques. A second stage rotor was mounted on a vertical angle plate and excited by a magneto-strictive device. The frequency of the exciter was increased until a rotor resonant condition was visually observed. A photograph was taken at this point and the exciter frequency increased until the next resonant condition was determined. Fig. 3.51 and 3.52 show typical mode shapes. The room temperature natural frequencies identified are shown in Table 3.3.

The determination of critical engine operating conditions was concentrated on the effect of engine rotor speed. A second stage turbine rotor was run at 55% speed and inspected after 5 minutes, 35 minutes, 1-1/2 hours, 2-1/2 hours, 3-1/2 hours and 4 hours and 39 minutes. The final inspection revealed a small (approximately 1/4" long), tight, circumferential crack in the hub region - the same area as previous cracks and rotor fractures occurred. Another rotor was subjected to the same

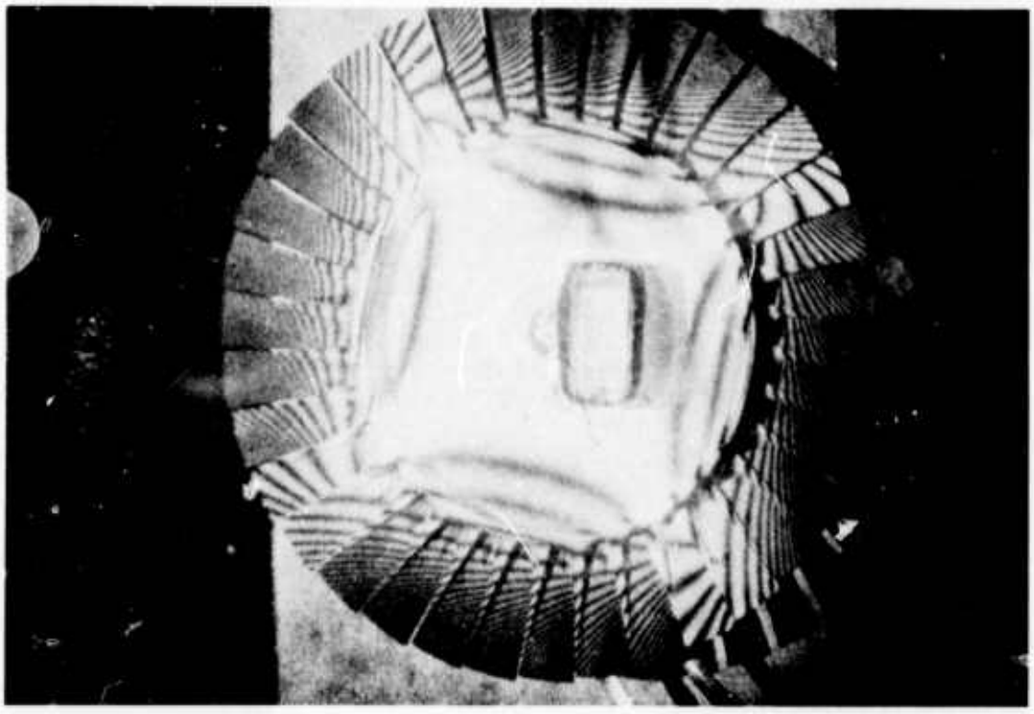


Figure 3.51 Two Diameter Mode Shape. 3383 Cycles Per Second

procedure with more frequent inspections and cracks developed after 3 hours hot running time. These tests indicated that 55% engine speed was the critical speed. Two rotors were than tested at 60% speed, inspected frequently, and have accumulated 26-1/2 hours without hub cracks, giving further indication that 55% speed was indeed the critical point.

Since the critical operating speed was now apparently identified, the excitation orders and possible sources of excitation could be determined. Table 3.3 showed the room temperature natural frequencies which can be analytically adjusted to account for the effect of temperature changes on the dynamic modulus of elasticity. Table 3.4 shows the measured and adjusted natural frequencies and the most probable excitation orders. An investigation into the possible sources of excitation is underway.

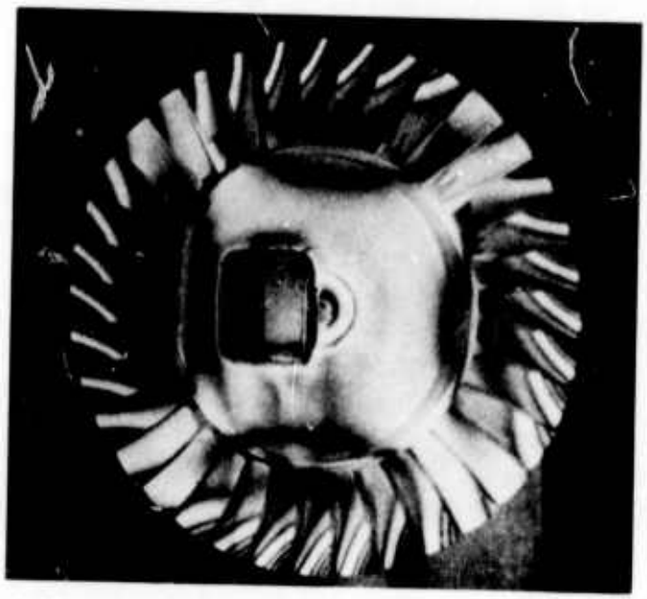


Figure 3.52 Two Diameter Plus One Radial Mode Shape 4925 Cycles Per Second.

TABLE 3.3

SECOND STAGE TURBINE ROTOR NATURAL FREQUENCIES

Mode Shape	Room Temperature Natural Frequency (cycles per second)
Two diameter	3383
One radial	4158
Two diameter plus one radial	4925
Four diameter plus one radial	9600

TABLE 3.4

SECOND STAGE ROTOR EXCITATION ORDERS

Mode Number	Natural Frequency At Room Temperature	Natural Frequency At Operating Temperature	Excitation Order
1	3383	2950	5.0
2	4158	3620	6.2
3	4925	4290	7.3
4	9600	8350	14.0

3.3 CERAMIC STATORS, SHROUDS, AND NOSE CONES

PRECEDING PAGE BLANK-NOT FILMED

SUMMARY

The stationary ceramic components in the hot flow path of the vehicular turbine engine are the inlet nose cone which directs the hot gases from the combustor to the first stage stator, two stator stages to direct these gases to the turbine rotors, and shroud rings which form the tip shrouds for each of the two rotors.

Two sources of silicon raw materials were evaluated for injection molding hot flow path components. These studies revealed slight differences in silicon particle size distribution and particle surface area; however, the differences had little effect on density and strength of molded silicon nitride test samples.

Tooling design changes were effected which permitted better radial and circumferential positioning of the first stage stator segments into the assembly fixture. The bond strength of second stage stator segments was substantially improved through the use of a high strength slip-cast Si_3N_4 back-up ring, with the stator vanes bonded to this ring.

Engine testing has concentrated on evaluating Design 'B' stationary components. Two types of tests were used; the first is a hot test without turbine rotors (hot static test), and the second is a hot test using metal turbine rotors (hot dynamic test). Over 140 hours of hot dynamic testing, including over 500 lights, have been accumulated in this reporting period despite a problem with the second stage metal turbine rotor cracking. Six first stage stator assemblies each accumulated over 25 hours of hot running before retirement, primarily because of vane cracking.

The cracking of first stage stator vanes was simulated on a thermal shock test rig. This rig provided rapid evaluation of vane modifications, and allowed valuable visual observation of the parts being tested, which is impossible in the turbine engine. A modified vane design was developed which survived rig testing with no cracking, whereas control group of unmodified vane design experienced 100% failure under the same conditions. Limited engine testing of the modified first stage stators has been very encouraging; no cracks have developed thus far.

A reaction-sintered silicon nitride second stage stator has accumulated 61 hours of hot running, 58 of which was hot dynamic; another has withstood 28 hours of hot testing, 25 of which was hot dynamic, and yet another 24 hours of hot testing, all without failure. A silicon carbide nose cone has been hot static tested for 680 hours and 166 lights and is still serviceable. The design modification to the inner body of the silicon nitride nose cone has eliminated the circumferential cracking problem. Second stage shrouds have been free of primary failures; one has accumulated 95 hours with 84 lights and another 47 hours with 404 lights.

3.3.1 MATERIALS AND FABRICATION

Introduction

The inlet nose cone of the vehicular turbine engine, currently made of reaction-sintered silicon nitride, directs the hot gases from the combustor to the first stage stator. The nose cone is a very complex shape, and lends itself to fabrication by injection molding techniques. Other methods of fabricating nose cones require a great deal more time and necessitate bonding together of various segments.

The hot gases of the vehicular turbine are ducted through the nose cone onto the first stage stator which in turn directs the hot gases to the first stage rotor. After passing the first stage rotor, the second stage stator directs the hot gases to the second stage rotor. Currently, stators are made by injection molding of individual stator segments with subsequent assembling into rings by use of a second injection molding operation to bond the segments into an integral component.

Other stationary components, such as reaction-sintered Si_3N_4 shroud rings which form the tip shrouds for each of the two rotors, have been fabricated by dry pressing and by slip casting of silicon metal powder.

Figure 3.53 shows a view of the various ceramic engine components discussed in this section. These are Design B versions of these parts, which are currently being fabricated and evaluated.

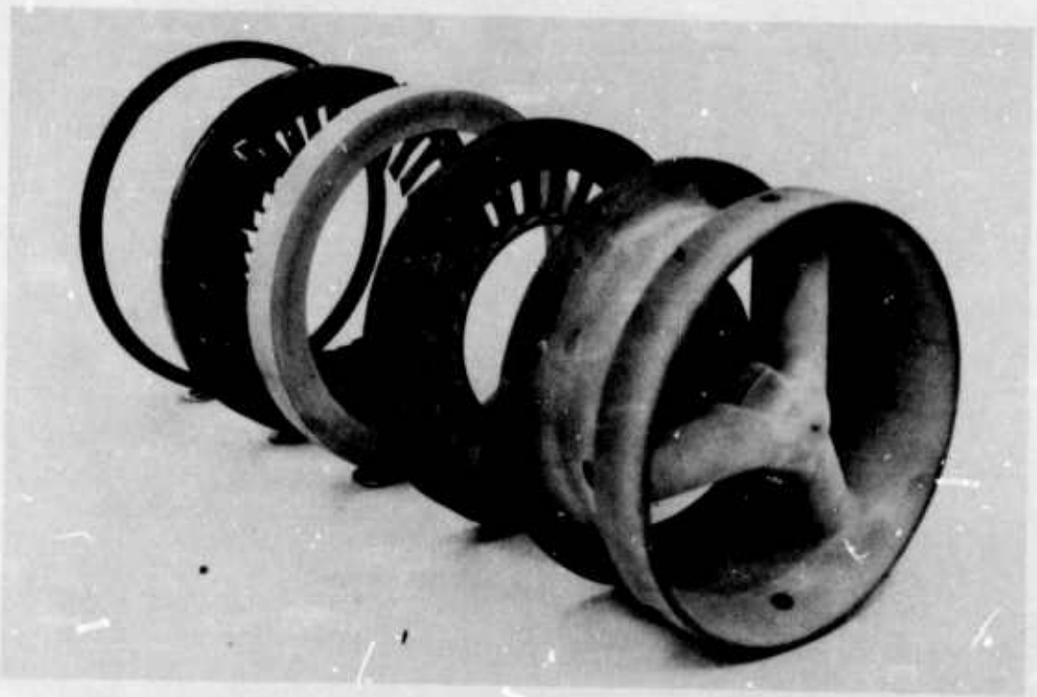


Figure 3.53 Design B Ceramic Nose Cone, Stators and Shrouds

Raw Material Studies

Silicon metal powder, which is the raw material for the fabrication of silicon nitride gas turbine engine components, is a difficult material to obtain with reproducible characteristics. To date, only one supplier has been able to consistently supply silicon metal powder for injection molding within specifications. Analysis of this material shows 98.5% silicon with major impurities consisting of 0.5% aluminum and 0.75% iron. The maximum particle size is less than 74 microns, with an average particle size ranging between 10 to 13 microns. The overall particle size distribution of this material from lot to lot has been consistent, and has proven suitable for injection molding.

Studies have been conducted to define an ideal particle size distribution for the silicon powder used in the injection molding process, since particle size distribution can be critical to both fabrication processes and final physical properties.

The size distribution from two sources of material are compared in Fig. 3.54. The MSA sedimentation technique was used for determining these particle size distributions. The distribution curve for material from vendor A is the silicon powder described earlier. Material from vendor A is a finer grade of silicon than that from vendor B; this was also verified by surface area measurements. Material from source A had a

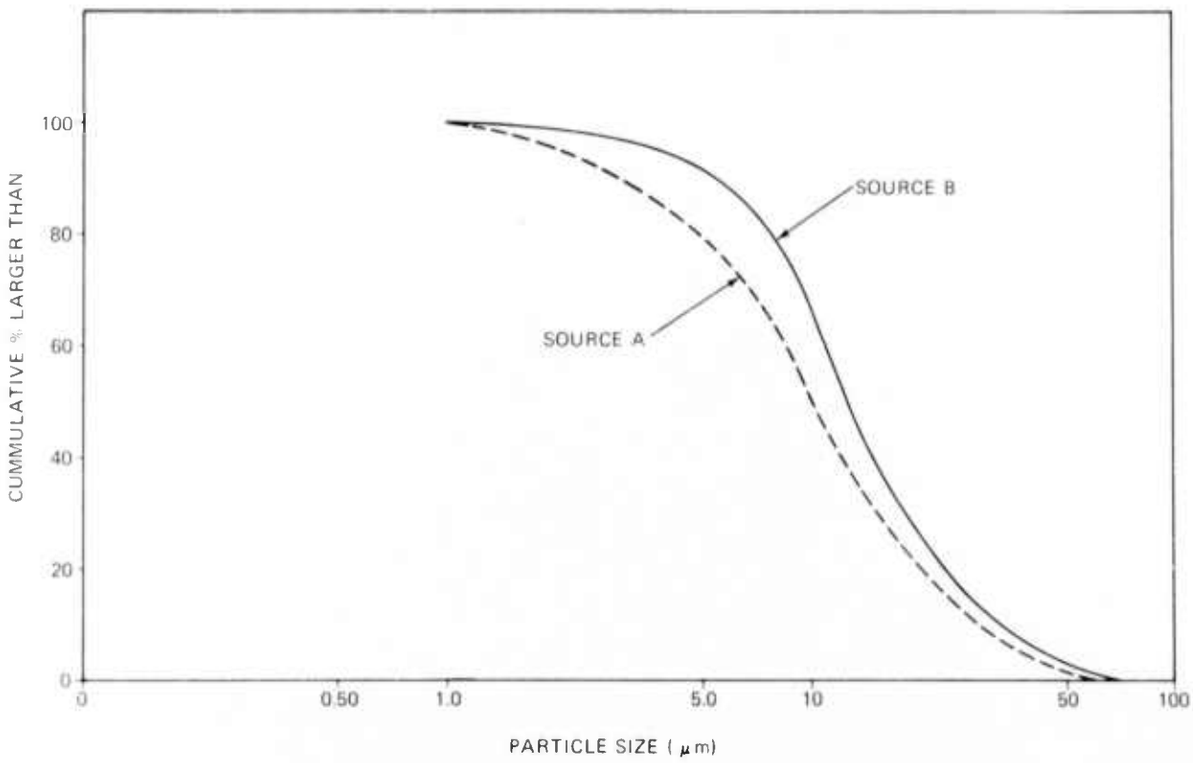


Figure 3.54 Particle Size Distribution of Silicon Metal Powder

B.E.T. surface area of 1.0 M^2/g while material from source B had a B.E.T. surface area of only 0.4 M^2/g.

Test specimens of each material were processed using identical injection molding parameters, after which room temperature physical properties were measured. Results showed no differences in density or strength for the two materials tested, indicating that the injection molding process is not dependent on a critical particle size distribution. A band of particle size distributions appears to be acceptable. Determination of the extent of this band is the subject of work now in progress.

Stator Assembly Development

The procedure for assembling stator segments into rings has consisted of placing the individual injection molded segments into a fixture containing locating piloting surfaces. The use of piloting surfaces alone proved to be inadequate for the consistent manufacture of accurate rings, because of inadequate radial and circumferential positioning upon assembly. Consequently, a method for independent positive blade location was devised.

Tooling changes were made so that each molded blade segment contained two locating tabs, one at the inner tip shroud and one at the base of the outer shroud. (See Fig. 3.55). In addition, modifications were made to the assembly fixture to provide for accurate circumferential and radial location by a positioning point on each blade. These changes should provide independent positive locating necessary for proper and consistent assembly. Fabrication and assembly of prototype stators is now in progress.

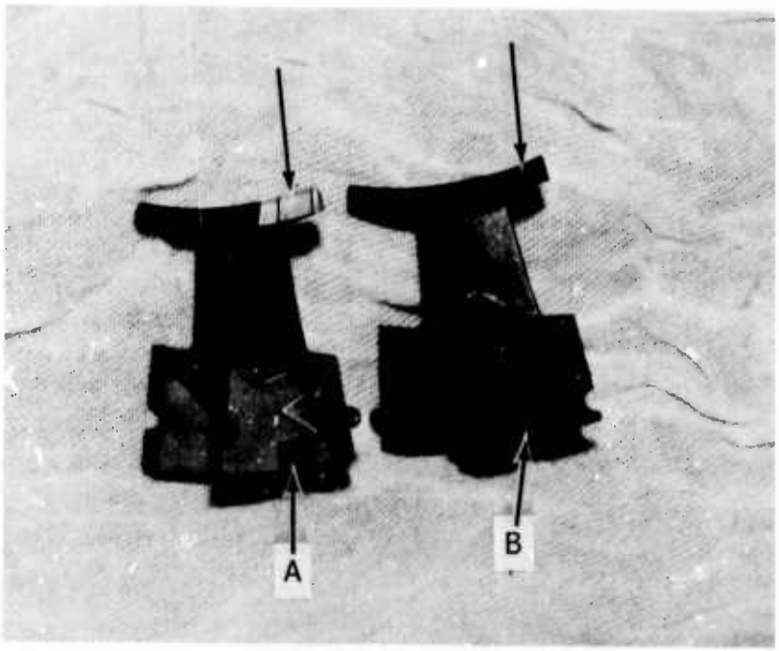


Figure 3.55 First Stage Stator Segments Showing Locating Tabs on Revised Design. A - Revised Design, B - Old Design

Once the stator segments are placed into the assembly fixture, they are bonded into a integral unit by injection molding with a silicon metal-polymer mixture into the U-shape outer shroud channels. The material has a reduced viscosity, which is necessary in order to reduce molding pressure to avoid breakage of the stator segments. The viscosity is reduced by adding additional polymeric materials to the molding batch at the expense of silicon. This modified material is of lower density and hence lower strength after nitriding.

This bonding material has cracked rather frequently in engine testing, particularly in the second stage stator, allowing segments to become loose. Consequently, alternate means for stator assembly were needed to permit the use of much stronger backing materials to eliminate the cracking.

One alternate method being developed entails the bonding of pre-sintered silicon stator segments onto a pre-sintered slip cast backing ring, as shown in Fig. 3.56. The slip-cast Si_3N_4 material has a transverse strength of 40-50,000 psi, providing a considerable strength increase over the injection molded Si_3N_4 (17-20,000 psi). Bonding of the slip cast ring and stator segments was accomplished by application of a fine silicon metal slip onto the mating parts, followed by sintering in nitrogen to convert the entire assembly into silicon nitride. Fig. 3.57 illustrates the nature of the bond achieved by this process, in this case showing the joint between adjacent stator segments. Several prototype stators are being assembled by this method for engine evaluation.

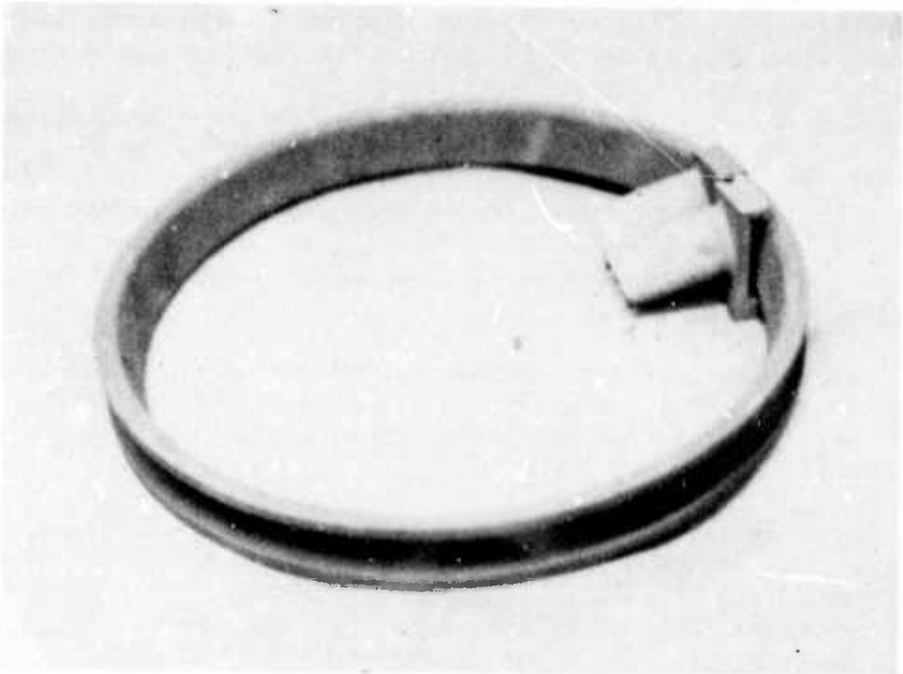


Figure 3.56 Second Stage Stator Illustrating Experimental Assembly Method



Figure 3.57 Microstructure of Joint Between Injection Molded Stator Segments. 150X

Shrouds

The rotor shroud rings (Fig. 3.53) used for much of the engine testing to date have been made from reaction-sintered Si_3N_4 formed by a cold-pressing process. Cracking of these components during engine operation indicated the need for a stronger material. A slip-casting technique was developed which does yield stronger Si_3N_4. Both fabrication methods are discussed in this section.

Silicon metal powder blended with binders and granulated using a Patterson Kelley V-Blender was cold pressed at 10,000 psi into cylindrical blanks approximately 1" high. After burnout of the binders, the cylinders were pre-nitrided, machined into shroud rings and then completely nitrided. Cold pressing produced Si_3N_4 with a fired density of 2.2 gm/cc and a transverse strength of 12,000 psi (4 point).

Slip casting of fine-grained silicon metal in an aqueous media produces Si_3N_4 with densities ranging from 2.35 gm/cc to 2.75 gm/cc with corresponding transverse strengths of 24,000 psi to 40,000 psi (4 point).

The slip casting process consists essentially of the following steps:

Nominal 325 mesh silicon metal is comminuted by ball milling for a pre-determined length of time. In most cases the bulk of the powder is in the particle size range of .5 to 20μ, with a mean particle size between 4.0 and 5.5μ. Contamination due to ball milling is considered minimal.

- A slurry is prepared of the milled silicon metal powder and distilled water.

- Deflocculating agents are added to prevent the settling of the powdered particles, and to create the desired viscosity and pH of the slip.

- The slip is thoroughly mixed and cast into a plaster mold. The water is absorbed into the pores of the mold through capillary action, causing the casting to solidify.

- The cast part is removed from the mold, dried and pre-nitrided.

Shroud rings are fabricated by drain casting of six inch high hollow cylinders. These are sliced into rings, nitrided, and diamond machined to final dimensions.

3.3.2 TESTING

Introduction

The inlet nose cone, stators, and shrouds are classified as the hot gas flow path stationary components. These components, located directly downstream from the combustor, must be developed to withstand (a) thermal shock upon start up and shutdown, (b) aerodynamic loading at engine operating conditions, and (c) mechanical and vibratory loads transmitted from the surrounding structure. Testing of these ceramic components is carried out primarily in engines or engine test rigs. A supplemental form of testing using a thermal shock rig has also been employed in the search for solutions to stator blade cracking problems, because experimental components can be evaluated quickly with repeatable and easily observable test conditions.

Thermal Shock Rig Testing

The expense and time required to evaluate prototype ceramic components can be significantly reduced as compared to engine testing by utilizing a mechanized test rig. Candidate materials can also be screened in simple bar form and often, as in the case of ceramic stators, segments of components rather than an entire component can be used to evaluate design variations. The thermal shock test rig apparatus can be controlled more readily and precisely than a test engine, therefore causes of failures are more easily determined.

The thermal shock test rig is shown in Fig. 3.58. Eight samples (A), are clamped to the air operated mechanical index table (B). Asbestos coupons or glass tape are used to isolate the test pieces from the metal clamping fixtures. The table cycle time, 0 to 4 minutes, is controlled by an electric timer (C) which actuates a double solenoid valve controlling the table index air supply. Revolutions of the table are recorded on an electric digital counter (D). Cooling air, used to accentuate thermal gradients by cooling the stator shrouds, is supplied by eight tubes (E), which have an orifice behind each clamp. Cool air to quench the test piece as it indexes out of the flame from the burner (G), is supplied through tubes (F) which direct the airflow upwards. The air from the first tube quenches the test piece as it leaves the flame; the subsequent streams of air continue to cool the warm piece to ambient temperature before it re-enters the flame.

Two mixing burners (G), using natural gas mixed with oxygen, have the capability for supplying a concentrated pencil flame or a more diffuse larger flame. Flame temperatures are pre-set using a thermocouple located in the test sample position. Safety equipment (H) monitors gas and oxygen pressures while sensing ultraviolet light from the flames.

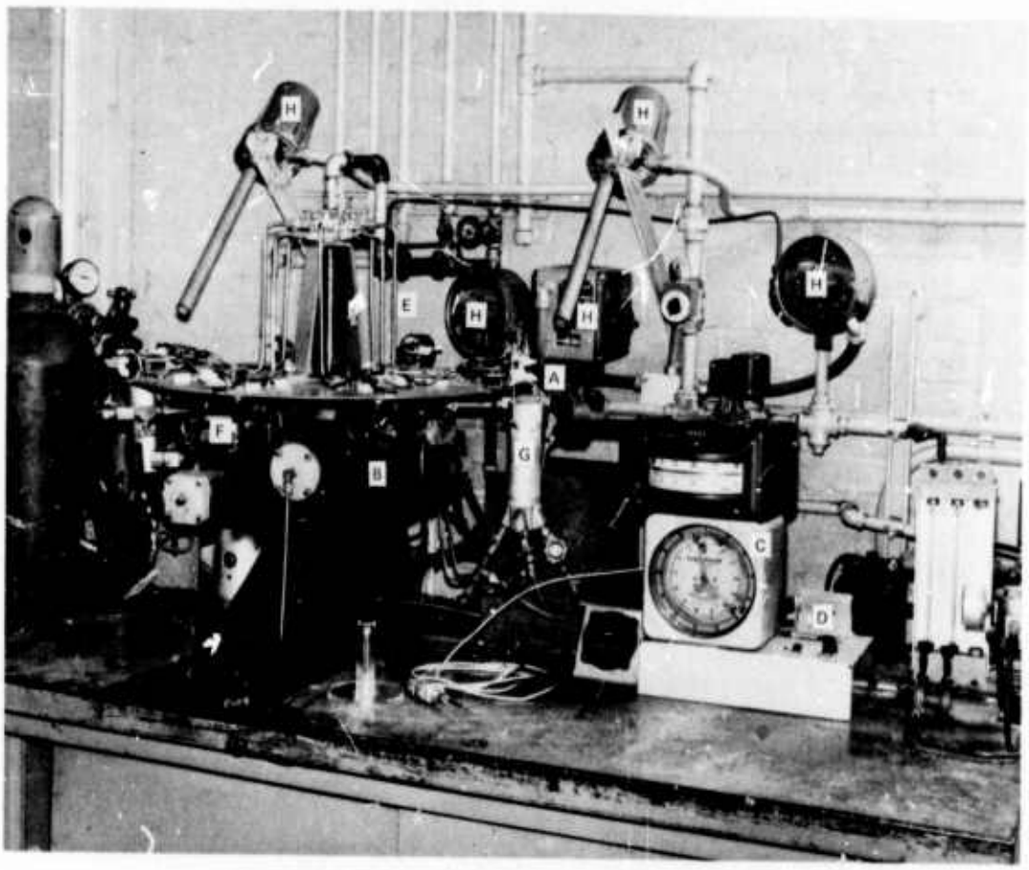


Figure 3.58 Thermal Shock Test Rig

The thermal shock test rig was used to investigate blade cracking failures of first stage ceramic stators which occurred during engine operation. These stators have three basic failure modes which were diagnosed as being caused by thermal stresses. A midspan vane failure was noted on a large percentage of first stage stator assemblies after both static and dynamic testing. This midspan crack characteristically originated at the trailing edge of the vane, propagated forward toward the leading edge during continued service, and ultimately resulted in vane failure. A second type of failure noted during operation can be characterized as a root failure. In this case the crack originates in the fillet radius at the trailing edge junction of the vane and outer shroud during static or dynamic operation. The third type of failure, cracking of the outer shroud, is at present less critical than the vane cracking and has not yet been included in the thermal shock test program.

Several variations of the design B first stage stators were subjected to 1000 cycles with flame temperatures of 3000°F and corresponding test piece temperatures of 2300-2500°F. Cooling air flows for shocking the hot components and cooling the outer shroud of the stator segments were set at 100 and 50 cubic feet per hour respectively.

Normal Design B first stage stator segments (Fig. 3.59), consisting of two to four vanes per segment, were tested to establish a baseline. These segments had visible vane cracks in several vanes after only a few cycles; after 1000 cycles all vanes were cracked.

The next configuration evaluated was the Design B second stage stator (Fig. 3.60). Alternate stations (4 of 8) were loaded with these segments while the remaining stations were loaded with normal Design B first stage stator segments as a control group. At the conclusion of the 1000 cycle test, the failure rate of the Design B second stage stator vanes was only 8.3% while the failure rate of the control group was 100%.

First stage stator vanes of Design 'A' configuration with added stock to double the trailing edge thickness, as shown in Fig. 3.61, were tested to 1000 cycles with a control group. The failure rate of the control group was again 100% while these modified Design 'A' vanes experienced no failures.

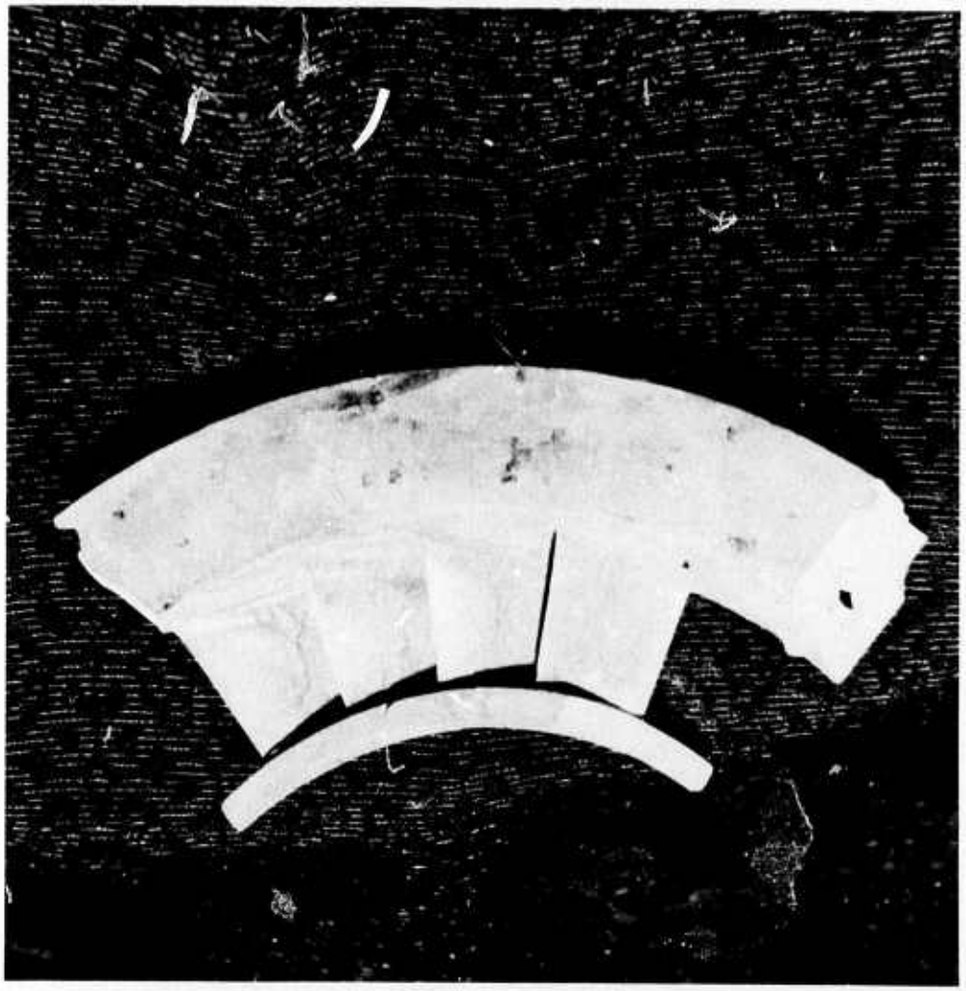


Figure 3.59 First Stage Stator Segments, Normal Design B

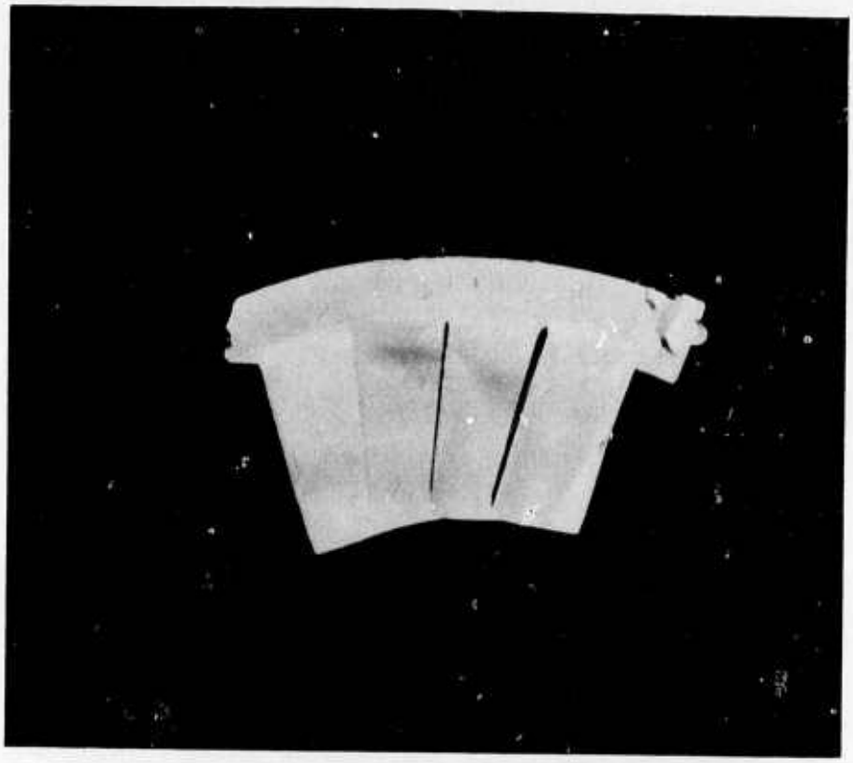


Figure 3.60 Second Stage Stator Segments, Normal Design B

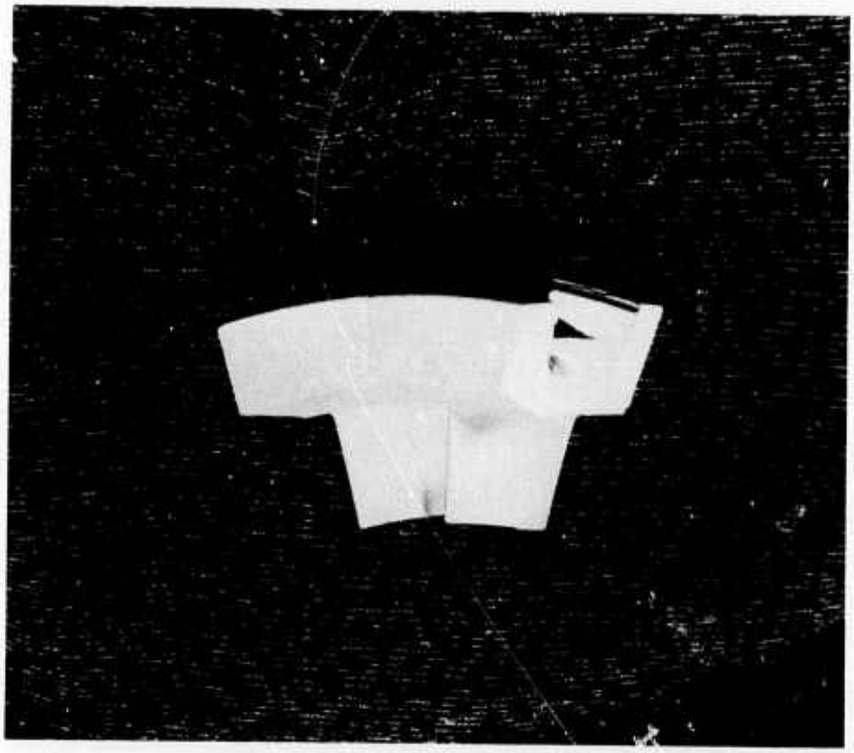


Figure 3.61 First Stage Stator Segments with Thicker Trailing Edges, Design A

There were two probable causes for the vane failures observed during this evaluation. There was a possible tip shroud interference problem in which the designed expansion gap between tip shroud segments was not maintained during fabrication. The absence of this gap would result in an interference of the tip shrouds during thermal cycling which could fail the vanes. The other possible cause of failure was the localized thermal response of the trailing edge of the vanes. It was noted during the previous testing that the trailing edges of normal Design 'B' first stage stator vanes were much hotter to the eye than the trailing edges of the other designs tested. The cause of the very hot area observed is attributed to the wide chord plus the rather large area of this material at the trailing edge of the vane. The Design 'A' vanes and Design 'B' second stage vanes previously tested both have a more uniform cross-section than the normal Design 'B' first stage stator vanes.

Two more thermal shock test runs were designed to check-out these two possible causes of failure. A control group of four sets of Design 'B' first stage stator segments with normal inner shroud gaps plus four segments with essentially no gaps were thermal shock tested. The vanes with no gap failed almost immediately while the control group failure rate was much slower. The conclusion reached was that an inner shroud gap was necessary to prevent immediate failures. The second test consisted of a group of Design 'B' first stage stator segments with a portion of the trailing edge removed. This change, shown in Fig. 3.62,

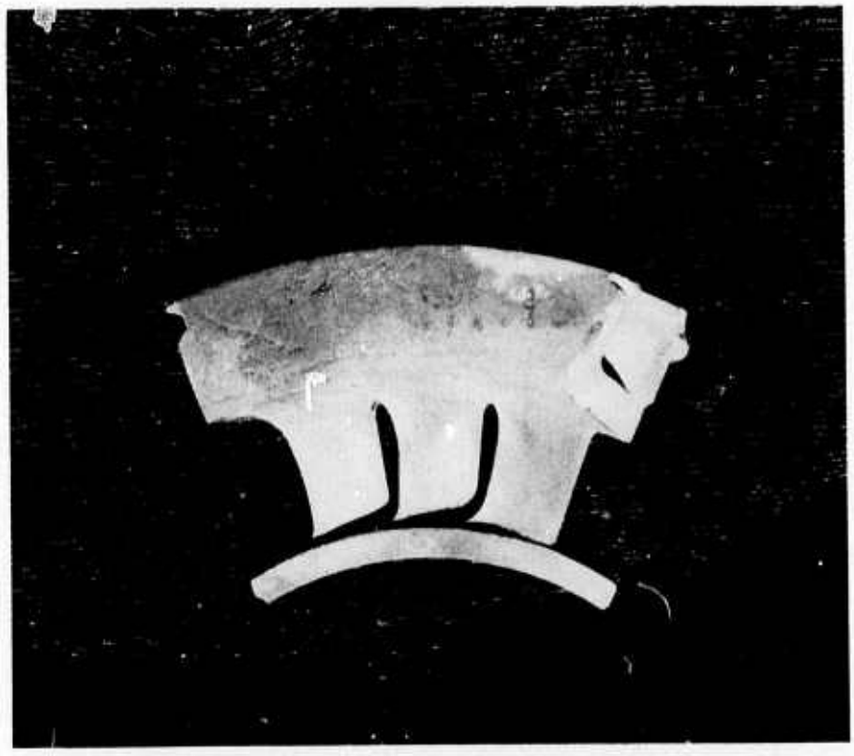


Figure 3.62 First Stage Stator Segments of Reduced Chord, Design C

removed much of the thin area and resulted in a thicker trailing edge. No failures were observed on the modified design vanes after 1000 cycles whereas the control group failure rate was 100%. It was also noted that the aforementioned hot areas were no longer visually observed in the modified vanes. The entire vane area reached a much more homogeneous maximum temperature. The number of cycles was increased to 3000 and the test was repeated with the same results.

This design modification was incorporated for two prototype first stage stators, which are currently being evaluated by engine testing.

Hot Static and Dynamic Testing of Stators, Shrouds and Nose Cones

The ceramic stators, shrouds and nose cones are qualified in an engine test rig prior to incorporation in a complete engine for continued testing and development.

Component qualification consists of the following:

(1) 25 static light cycles

(2) 3 hours of static testing, and

(3) 25 hours of dynamic testing

Testing without rotors is referred to as static testing whereas testing with rotors is referred to as dynamic testing. The various test conditions under which the ceramic stators, nose cones, and shrouds are qualified are as follows:

- Static testing - 55% engine speed with turbine inlet temperature limited to 1800°F.
- Dynamic testing - 55% speed with turbine inlet temperature limited to 2000°F.
- Cyclic testing (static or dynamic) - a sequence of (1) light-off and acceleration to 55% speed, and (2) shutdown (zero fuel) and speed reduction back to light-off condition. This condition is held until the turbine inlet temperature falls to 1000°F, whereupon the sequence is repeated for the desired number of cycles. One of these cycles is termed the one light test.

The evaluation of Design 'B' nose cones, stators, and shrouds was accomplished in engine test rigs, and the results are summarized in Table 3.5. This table is an update of test information noted in the last report[1]. In each case the component was manufactured from reaction-sintered silicon nitride, except for nose cone serial number G4, which was made of Norton "Crystar" silicon nitride.

Table 3.5 Summary of Testing of Ceramic Nose Cones Stators and Shrouds

COMPONENT	COMPONENT SERIAL NUMBER																	TOTALS
First Stage Stator	208	214	215	216	219	232	244	247	248	250	259	260[3]	266	268	286	322	331[3]	
.Hot Static Hrs.	7	3	3	3	29	3		3	3	19	3	3	.5	3	4		5	91.5
.Hot Dynamic Hrs.	12	25	34	3	8	2	4.5	25	25	7					20		9	174.5
Total Hot Hrs.	19	28	37	6	37	5	4.5	28	28	26	3	3	.5	3	24		14	266
Total Lites	58	48	126	144	68	52	11	32	33	64	28	27	25	51	53	2	44	866
Status	F,X	F,V	F,V	F,V	F,V	F,X	F,V	F,V	F,V	F,V	F,V	S,C	F,V	F,V	F,V	F,V	S,C	
Second Stage Stator	222	271	274	275	288	292	295	298	301	303	305	309	317	324	326[4]	327[4]	328[4]	
.Hot Static Hrs.	10			24	3		3	3	8	12	4	3	4	3	4	3		84
.Hot Dynamic Hrs.	2	8	5	.5	2	2	25	58	26	.5	13				20			162
Total Hot Hrs.	12	8	5	24.5	5	2	28	61	34	12.5	17	3	4	2	24	3		246
Total Lites	53	4	2	69	28	9	30	43	124	170	35	26	32	27	63	25	2	742
Status	F,X	F,X	F,V	S,C	F,X	F,X	S,C	S,C	F,V	F,X	S,C	S,C	S,C	S,C	F,V	F,V	F,V	
First Stage Shroud	2	4	5	6	7	8A	8B	9	10A	10B	11	12						
.Hot Static Hrs.		38				3	6	9		4	3							63
.Hot Dyanmic Hrs.	9	31	2	2	83	.5	6	28										161.5
Total Hot Hrs.	9	69	2	2	83	3.5	12	37		4	3							224.5
Total Lites	7	259	2	9	41	146	53	74	1	32	27	2						653
Status	F,X	S	F,X	F,X	F,C	F,C	S	S	F,C	S	S	F,X						
Second Stage Shroud	1	2	3	5	6	9	10	12	14	16	17	18	19					
.Hot Static Hrs.		28		.5		7	15	9	3	3	4	3						72.5
.Hot Dynamic Hrs.	2	.5	2		9	.5	32	86		32								164.
Total Hot Hrs.	2	28.5	2	.5	9	7.5	47	95	3	35	4	3						236.5
Total Lites	9	73	2	25	7	178	404	84	51	14	32	27	2					908
Status	F,X	S	F,X	S	F,X	F,X	S	S	S	S	S	S	F,X					
Nose Cones	G4[2]	11	14	15	16	17	19	23	30	31	32[5]	33[5]	34	35[5]	40[5]	42[5]		
.Hot Static Hrs.	680	20	12	28	12	6		3		4		8		30	3	7		813
.Hot Dynamic Hrs.			8	1	6	4.5	3	2	6	13	46	47	19	3				158.5
Total Hot Hrs.	680	20	20	29	18	10.5	3	5	6	17	46	55	19	33	3	7		971.5
Total Lites	166	5	133	176	56	62	10	119	1	37	29	95	8	166	29	30		1122
Status	S	S	F,B	F,B	F,B	F,B	F,B	S	F,B	F,B	F,C	S	F,B	S	S,C	S		

1
Status Legend
B - Inner Body Crack
C - Cracked Shroud
F - Failed
S - Serviceable; at present nose cones are considered serviceable if outer shroud has only axial cracks - ceramic stators are considered serviceable if outer shroud is cracked.
V - Cracked or Broken Vane(s)
X - Results of other component failure

2
Silicon Carbide Material (Nose cone G4 and 4 in last report are acutally the same one)

3
Design 'C'

4
Modified Outer Shroud

5
Modified Bell Section

The first stage stators which are serviceable, i.e., without broken or cracked vanes, have the modified airfoil blade described earlier in this section. One assembly, serial number 331, has accumulated 44 lights and 14 hours of hot engine testing without any vane cracks. Two of the failed first stage stator assemblies were the result of other component failures, while the remaining unmodified assemblies developed cracked or broken vanes which rendered them unserviceable.

Table 3.5 shows that second stage stators had a lower failure rate - 7 out of 17 are still serviceable. It should be noted that 50% of the failed assemblies were caused by other component failures. Three of the remaining failures were primarily the result of an experimental shroud design while the remaining two

were attributed to fabrication flaws. The serviceable second stage stators have several shroud bonding cracks. Parts are presently being fabricated with a shroud incorporating a one piece ring, described earlier which may eliminate this form of cracking.

The first stage shroud has had a failure rate of seven out of twelve. However, four of these failures were due to other component failures and the remaining three were parts of questionable quality material.

Two first stage shrouds (Nos. 10B and 11) and two second stage shrouds (Nos. 17 and 18) were made of higher strength slipcast Si_3N_4; these parts have not cracked after limited testing. The remaining second stage shrouds have performed satisfactorily. All noted failures were caused by other component failures.

Hot static and dynamic testing of ceramic nose cones has produced nine failures in sixteen components. Eight of the failed units developed a circumferential crack in the nose cone inner body, shown in Fig. 3.63A. This cracking problem has been eliminated by removing the cylindrical portion of the inner bell section as shown in Fig. 3.63B. Five nose cones with this modified bell have been tested and none have developed an inner body crack. The remaining nose cone failure occurred when an axial crack in the outer shroud turned circumferentially and thus jeopardized the integrity of the part. Axial cracks in the outer shroud of the nose cone occur frequently but have not rendered the parts unserviceable. However, in order to prevent these cracks from turning circumferentially, and to control the random nature of the cracks, a nose cone with a pre-notched outer shroud is being evaluated.

Figure 3.63A

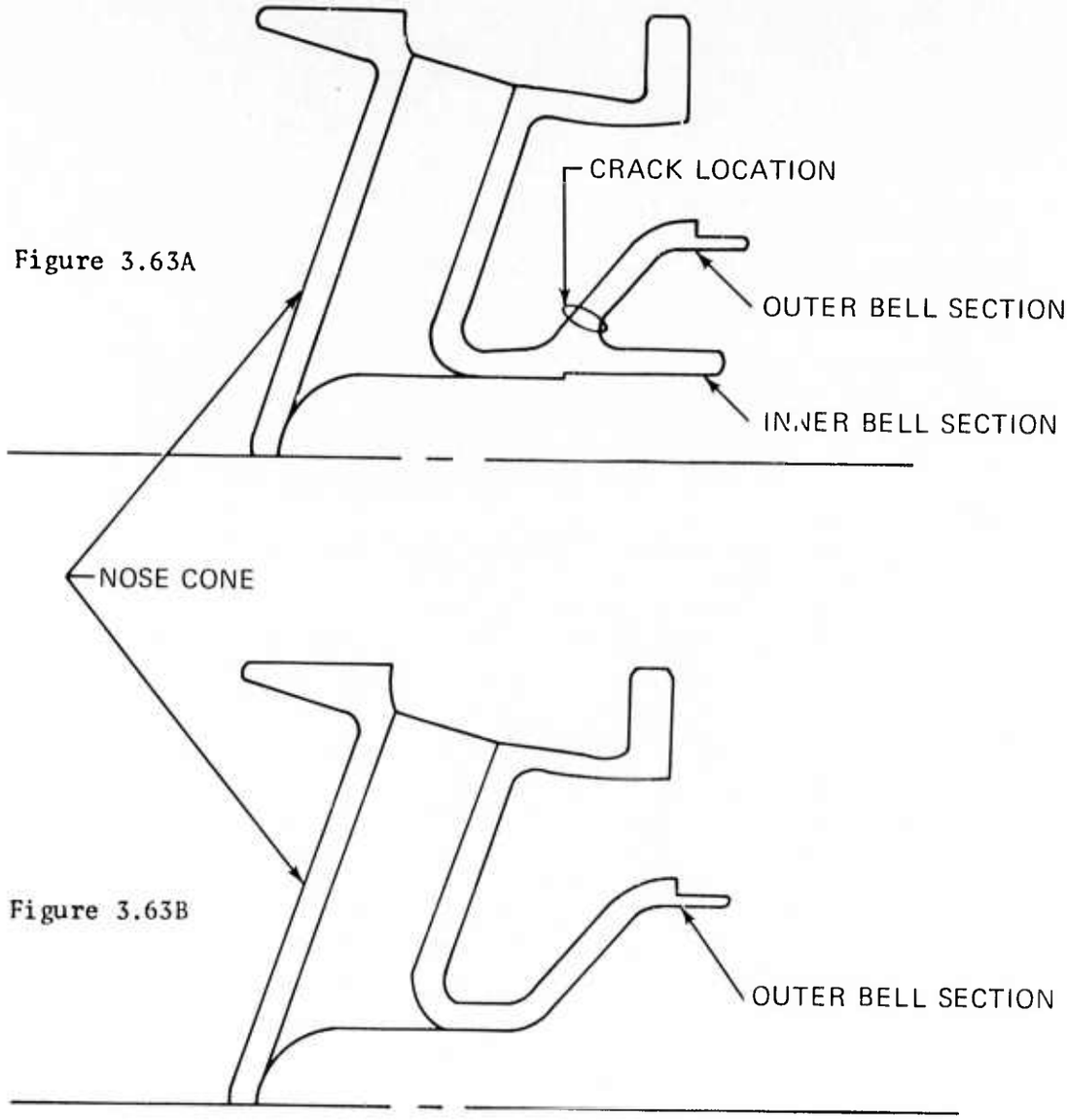


Figure 3.63B

Figure 3.63 Design B Nose Cone Modification

4.0 PROGRESS ON THE STATIONARY TURBINE PROJECT

4.1 STATOR VANE DEVELOPMENT

SUMMARY

A full scale kinematic model of the 3 piece ceramic stator vane assembly with all elements of the spring loaded support structure was built to demonstrate the design, illustrate the static rig test configuration and demonstrate assembly behavior under simulated conditions of differentially expanding inner and outer support rings. Maximum transient thermal stresses in the airfoil section are expected to reach 41,000 psi based upon engineering property data for Norton HS-130 silicion nitride. The steady state thermal stresses and contact stress maxima of 21,200 psi and 9600 psi, respectively, were calculated for the grooved, rectangular end caps.

The Norton Company has produced 40 silicon nitride billets from which 20 stator vane assemblies have been partially machined. Three billets of high-strength, hot-pressed silicon carbide have also been received for physical property characterization.

A static rig has been designed for the testing of ceramic stator vane assemblies up to 2500°F. Construction, installation and check out must be accomplished before static rig tests at 2200°F can begin in August 1973.

The design and analyses phases of the stationary gas turbine projects are in accord with the program schedule. Results to date indicate that the project goals lie within the material's capability to survive in a turbine environment. Only in the area of transient thermal stress under emergency conditions do anticipated tensile stresses approach critical material property values. These stresses are distributed across small volumes of material in the vanes, however, and are of extremely short time duration. Silicon nitride does creep above 1800°F. Creep resistance, therefore, may limit vane applications to temperature below 2300°F. Under operating conditions and normal conditions for start up and shut down, silicon nitride, and presumably, silicon carbide are expected to function satisfactorily in stator vane applications.

Delivery of silicon nitride stator vane assemblies from Norton is approximately six months late. This delay is not expected to affect the start of static rig testing in August, 1973.

By anticipating the program requirements for rotating rig testing now, Westinghouse does not expect the total program goals to be affected seriously by the static rig test delays.

Introduction

A three piece ceramic stator vane assembly has been proposed for test and demonstration in the 30 Mw stationary gas turbine illustrated in Fig. 4.1. Silicon nitride or silicon carbide stator guide vanes are intended to increase the service temperature from 1955 to 2500°F without cooling the first stage stator row.

The large size of the Westinghouse turbine permits the use of the three piece vane design, which is better suited to brittle materials rather than the conventional metal geometry where the airfoil section with integral platform or end plates is a single component part. This design innovation reduces thermal stresses to their minimum by total elimination of the transition zone. Each segment presents a relatively uniform cross section and mass to its specific temperature regime. The temperature extremes experienced by either the individual end caps or the airfoils are much smaller than those encountered in an integral vane design. The airfoil segment, for example, will operate at a somewhat higher but more uniform temperature because heat losses are minimized at the interface with the end caps. Radial and longitudinal thermal gradients in the end caps are influenced by gas temperatures at the wall rather than by peak temperatures in mid-stream, except for minimum heat transfer from the airfoil across the contact interface.

There are economic advantages to producing segmented vane components because of the simplicity of individual parts. Although, at the present time end caps and airfoils are machined from hot pressed billets, conventional uniaxial techniques can be employed to hot press end caps with grooves and airfoil blanks to shape. Diamond grinding will be required as a finishing operation only.

In order to assure that the best vane design has been considered for brittle materials, the recently developed 3 dimensional finite element analysis is being used to re-evaluate the magnitude of stresses encountered in an integral vane.

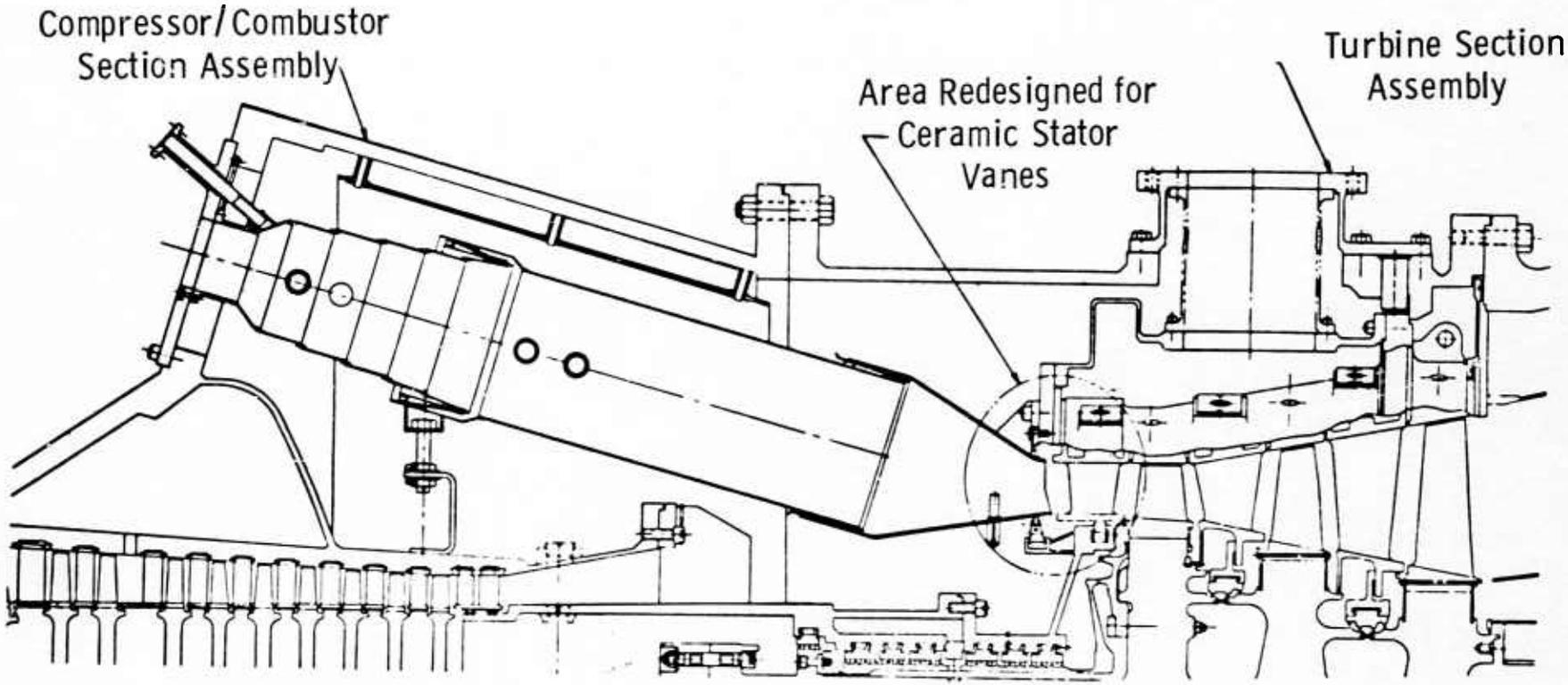


Figure 4.1 — Schematic of 30 Mw Test Turbine Flow Path

4.1.1 DESIGN

Emphasis was placed exclusively on the mechanical aspects of stator vane design in an effort to establish a brittle material's capacity for survival in a high temperature gas turbine environment. Tolerances were carefully selected to avoid making contact between the airfoil tenon area and the edge of the end cap groove. Generous radii have been provided throughout to eliminate possible areas of stress concentration.

The unique feature of the three piece design is a freedom of motion to compensate for differential thermal expansion of the inner and outer support rings without imposing residual stresses on the airfoils. This is demonstrated in the full scale kinematic model illustrated in Fig. 4.2. An adjustment screw and scale permit controlled axial movement of the inner support. The assembly can be moved 0.50 inches or five times the maximum displacement expected in turbine operation without disturbing the integrity of the design.

The ten vane segment configuration used in the kinematic model represents the first generation Si_3N_4 airfoil and end cap assembly scheduled for initial static rig testing. It is obvious from the large gaps which appear at the trailing edges of the non-tapered, non-twisted airfoil sections that aerodynamic performance was not of primary concern in this first generation design. Vane geometry will be optimized with respect to all performance parameters in a second generation structure.

As the hardware for the static rig and eventually the rotating rig tests become available, the model will serve as a convenient assembly checkout device.

Every attempt will be made in the second generation design iteration to eliminate the aerodynamic deficiencies apparent in the first generation vane assembly design. Special attention will be given to:

(1) The longitudinal slots created by the removal of sharp edges from adjacent end caps. These do not run parallel to the gas flow through the vanes.

(2) The large perturbations in the wall produced by those portions of the end cap grooves left unfilled by the tenons at both ends of the airfoil.

(3) The excessive clearances provided at both the leading and trailing edges of the airfoil to avoid any possibility of stress due to contact with the wall. These were exaggerated as a result of the radius used to blend the tenon into the airfoil.

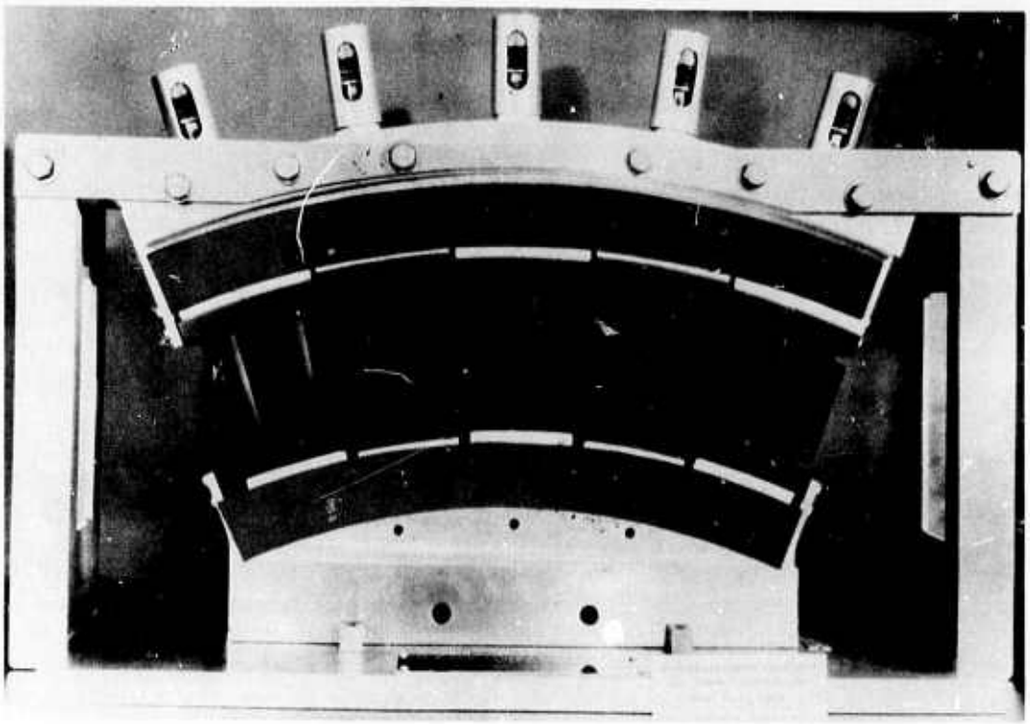


Figure 4.2 Kinematic Model of 3 Piece Ceramic Vane Design with Support Structure

4.1.2 STRESS ANALYSIS

Airfoil Transient Thermal Stress

Property data from the literature was originally used to determine the maximum out of plane transient thermal stresses occurring in a half size Si_3N_4 stator vane under emergency shut down conditions from 2500°F. The time vs stress plot (Fig. 4.3) indicates that a tensile stress of 31,000 psi is developed at the leading edge approximately 11 seconds after cooldown is initiated. Two dimensional finite element and finite difference programs have been used to recalculate these maximum transient thermal stresses based upon reliable engineering property data for Norton HS-130 silicon nitride.

Results of this recent analysis show that the maximum transient thermal stress at the leading edge of a silicon nitride vane approaches 41,000 psi, 12 seconds after shut down from 2500°F (Fig. 4.4). The 25% increase in calculated stress compared to earlier analysis is mainly a result of the use of recently updated material property data (Table 4.1). This seemingly higher stress appears realistic since both the finite element and finite difference techniques independently yield similar results as shown by temperature decay, temperature and stress profiles in Figs. 4.5-4.7, respectively.

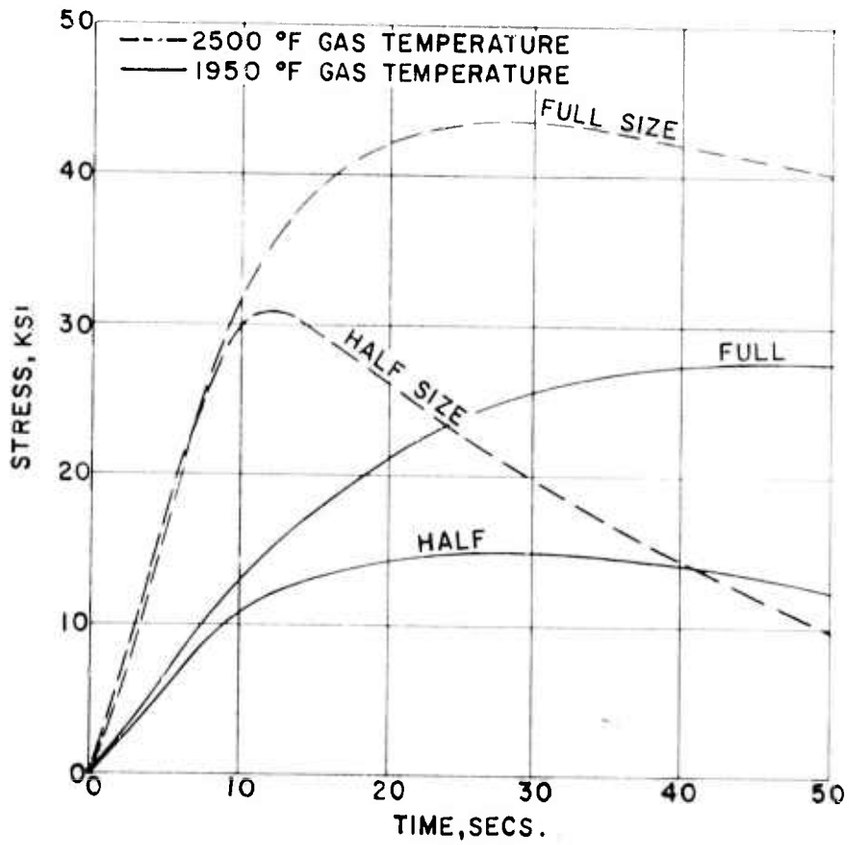


Figure 4.3 Stress History for Silicon Nitride Airfoils from 1950°F and 2500°F

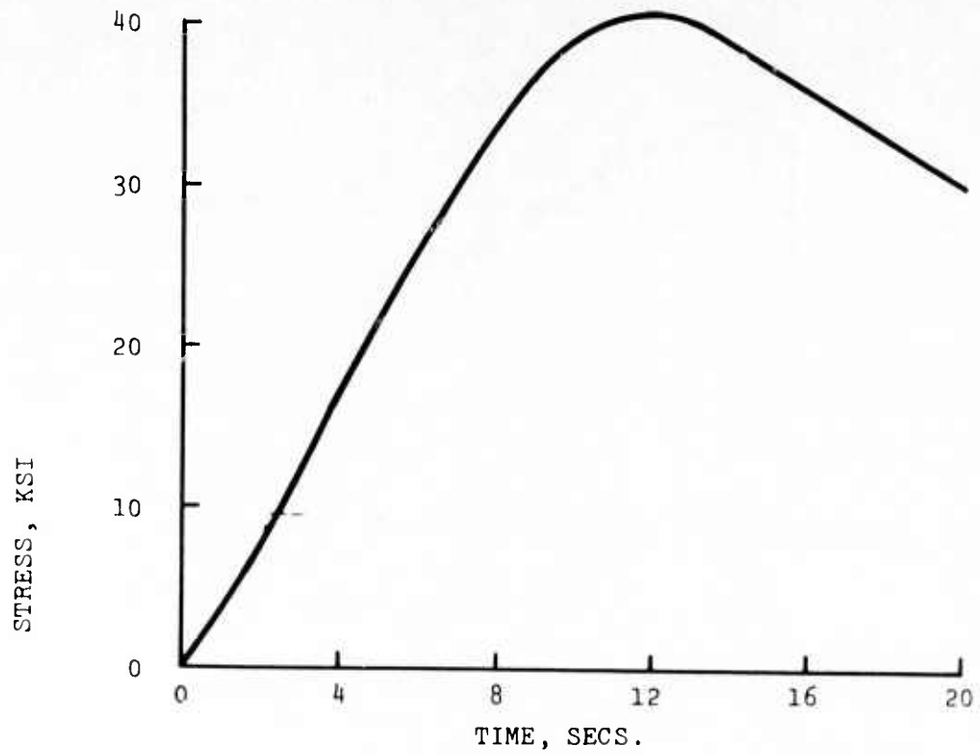


Figure 4.4 Maximum Transient Thermal Stress at the Leading Edge of a Silicon Nitride Vane under Emergency Shut Down from 2500°F

TABLE 4.1

Comparison of Si_3N_4 Property Data

Temperature °F	Thermal Conductivity BTU/hr-°F-ft.		Modulus of Elasticity x 10^{+6} psi		Coef. of Expansion x 10^{-6} in/in-F°		Specific Heat BTU/lb-F°	
	Old	New	Old	New	Old	New	Old	New
80°	13.5	18.7	41.2	44.9	1.7	0.60	.16	.16
200°	14.0	18.0	41.0	44.7	1.75	.78	.18	.18
400°	12.0	16.7	40.8	44.3	1.78	1.07	.21	.21
600°	11.0	15.7	40.5	44.0	1.80	1.25	.24	.24
800°	10.5	14.7	40.3	43.8	1.85	1.36	.25	.25
1000°	10.0	13.7	40.1	43.3	1.87	1.46	.26	.26
1200°	9.3	12.7	40.0	42.7	1.90	1.55	.27	.27
1400°	8.8	12.0	39.8	42.0	1.95	1.67	.28	.28
1600°	8.5	11.0	39.5	41.3	1.97	1.85	.29	.29
1800°	8.2	10.5	39.3	40.0	2.00	1.93	.30	.30
2200°	7.7	9.0	39.	37.5	2.05	2.37	.31	.31
2500°	7.5	8.3	38.7	29.0	2.15	2.40	.32	.32

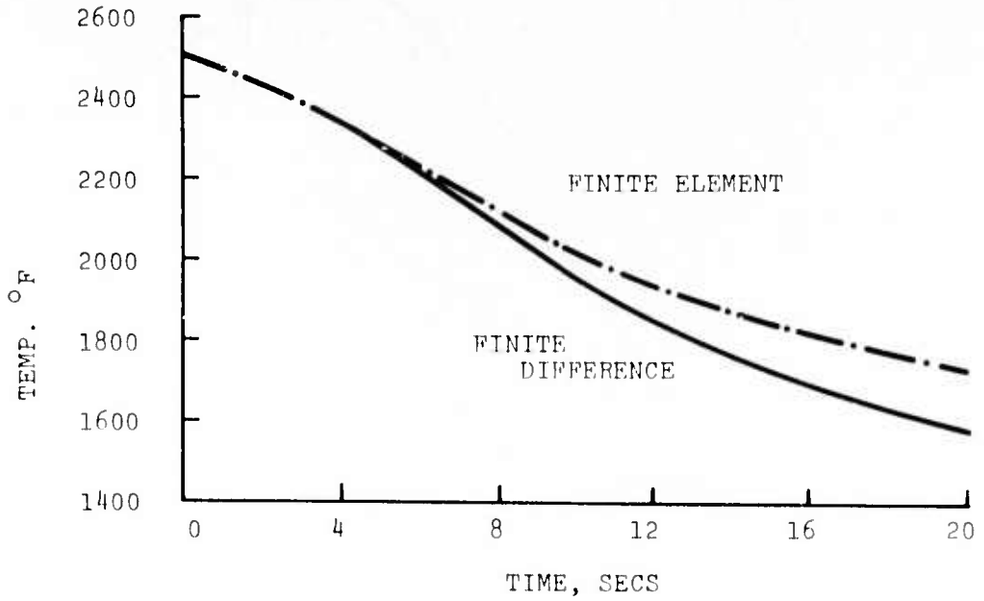
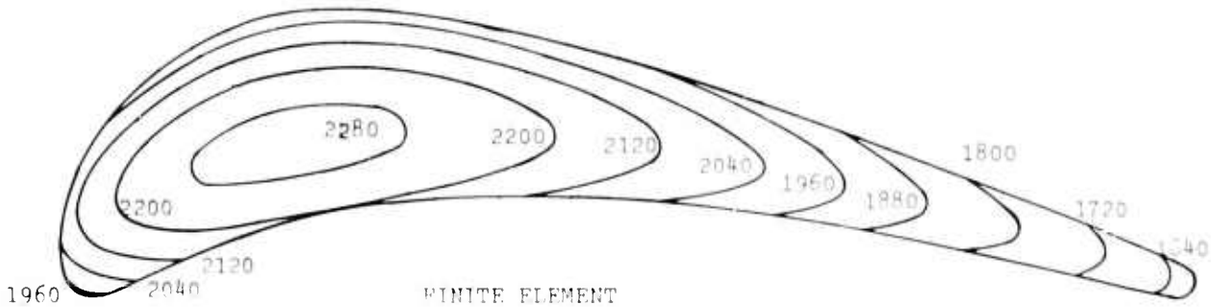


Figure 4.5 Temperature Decay Curve for Ceramic Vane under Emergency Shut Down from 2500°F



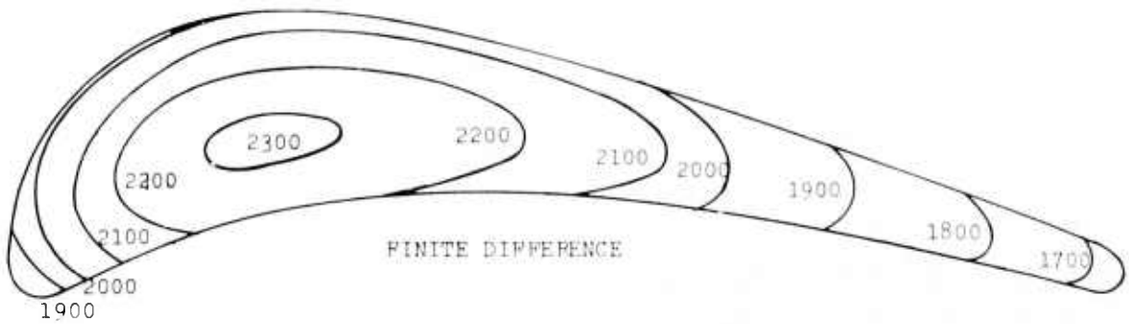


Figure 4.6 Temperature Contours in Solid Half Size Silicon Nitride Airfoils

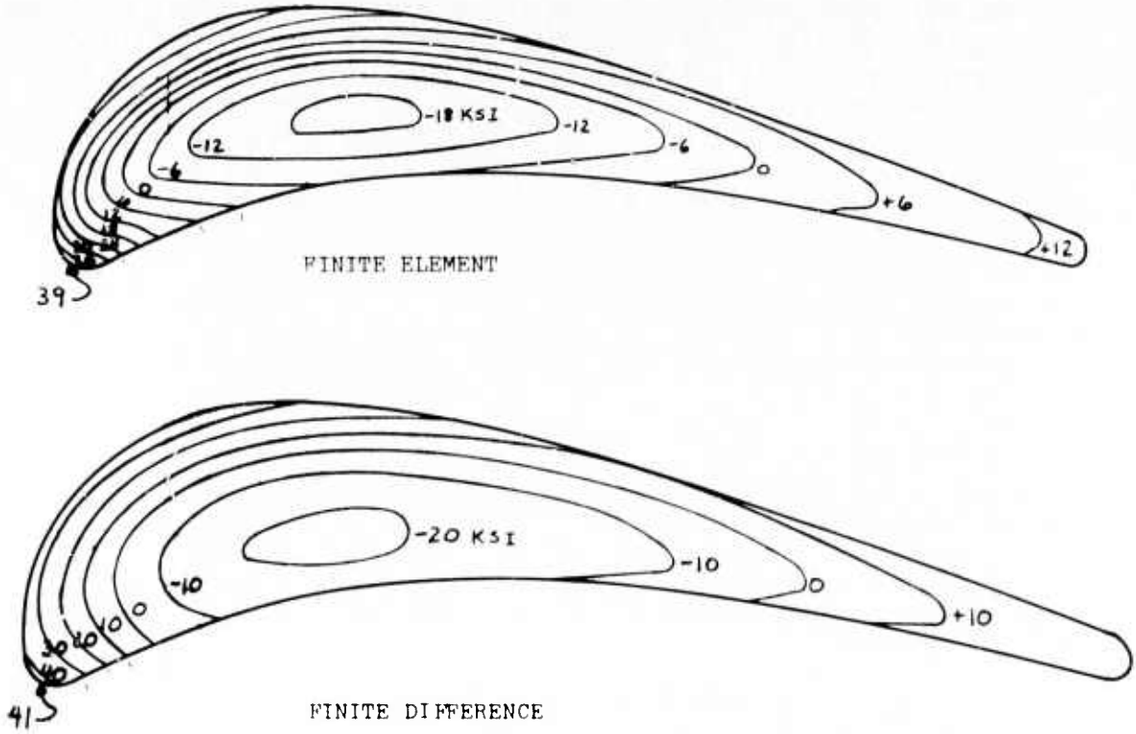


Figure 4.7 Stress Contours in Solid Half Size Silicon Nitride Airfoils

A plane stress finite element program is being used to calculate end effects in the current airfoil design. The model shown in Fig. 4.8 takes contact stresses and thermal gradients into account. Variations in thickness along the cord and the effect of various end configurations are also considered. The contact stresses result from spring loaded end caps. The gas temperature profile imposes radial thermal gradients in the area designated the hub and tip. Figure 4.9 represents the finite element mesh generated for this particular model. The mesh is made finer where high stress gradients are encountered.

An airfoil with a different trailing edge relief, a new airfoil-tenon design, and a partially shrouded airfoil will be subjected to analyses.

Contact Stress for Ceramic Vane Interface System

Ceramic interfaces are inherently present in any three-piece design. Since Si_3N_4 exhibits no significant plastic response prior to fracture, it is necessary to define explicitly the maximum tensile stress at the contact so that a reasonable safety factor can be applied to avoid the generation and catastrophic propagation of localized cracks.

The entire sandwiched assembly of the present design is subjected to four load types as shown in Fig. 4.10. The first of these, the radially compressive spring load, is a design parameter that remains

effectively constant over the cycle of operation. The other loads are components of the gas load which rise to peak values during operation after short transients. The pressure force against the vane is one component which acts at 28° from axial or 66° from the major axes of the vane end and end-cap groove. Another gas load component acts as a radially compressive force against the metal shoe. This force is displaced somewhat from the center line. The fourth relevant load is a small twisting moment about the radial axis. It is important to realize that all of the interface types associated with the design (Fig. 4.10) represent an interdependent system with respect to both radial and friction-reacted tangential loads. This condition complicates the optimum choice of geometry, surface finish, and the applied spring load.

Curved surfaces are in area contact at the airfoil-end cap interface. The contact stress field here may be analyzed by superimposing the two stress fields derived from normal and tangential loads. These fields are defined with respect to the interface. Stresses due to normal loads are calculated easily, using standard formulae from the theory of elasticity. Stresses due to tangential loads are calculated by the cylindrical analogy method, developed by extending the analysis for simple cylindrical contacts to the actual situation. The contact stress field is implied from a knowledge of the material properties, the geometry, and the loads. For a realistic range of parameters appropriate to this interface system, tensile stresses due to friction-reacted loads far exceed those due to the standard Hertzian normal loads. If it were possible to design the interfaces to convert tangential (friction-reacted) loads to normal loads, an overall reduction of stress would result. This is accomplished with curved interfaces where geometry is chosen as a function of friction.

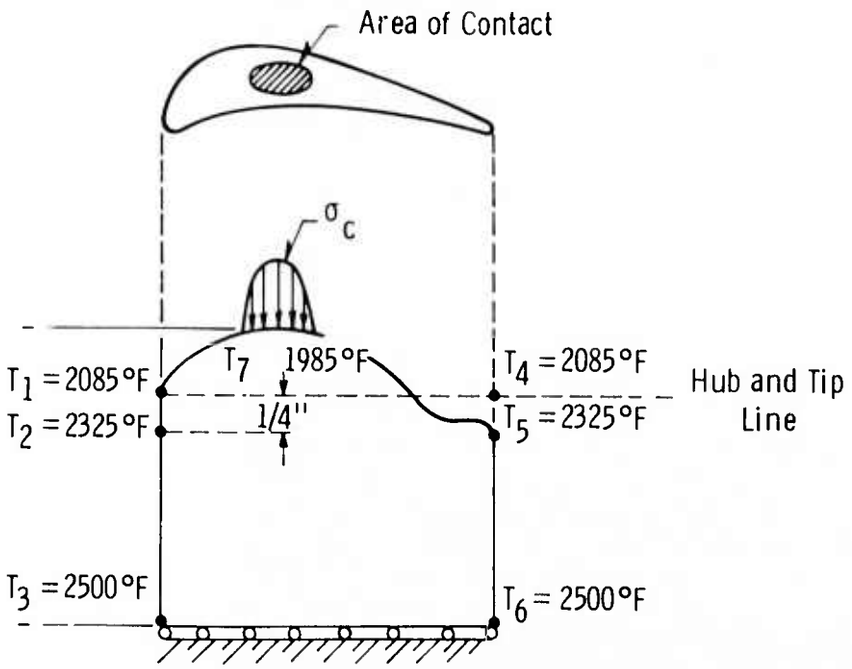


Figure 4.8 Airfoil End Effects Model

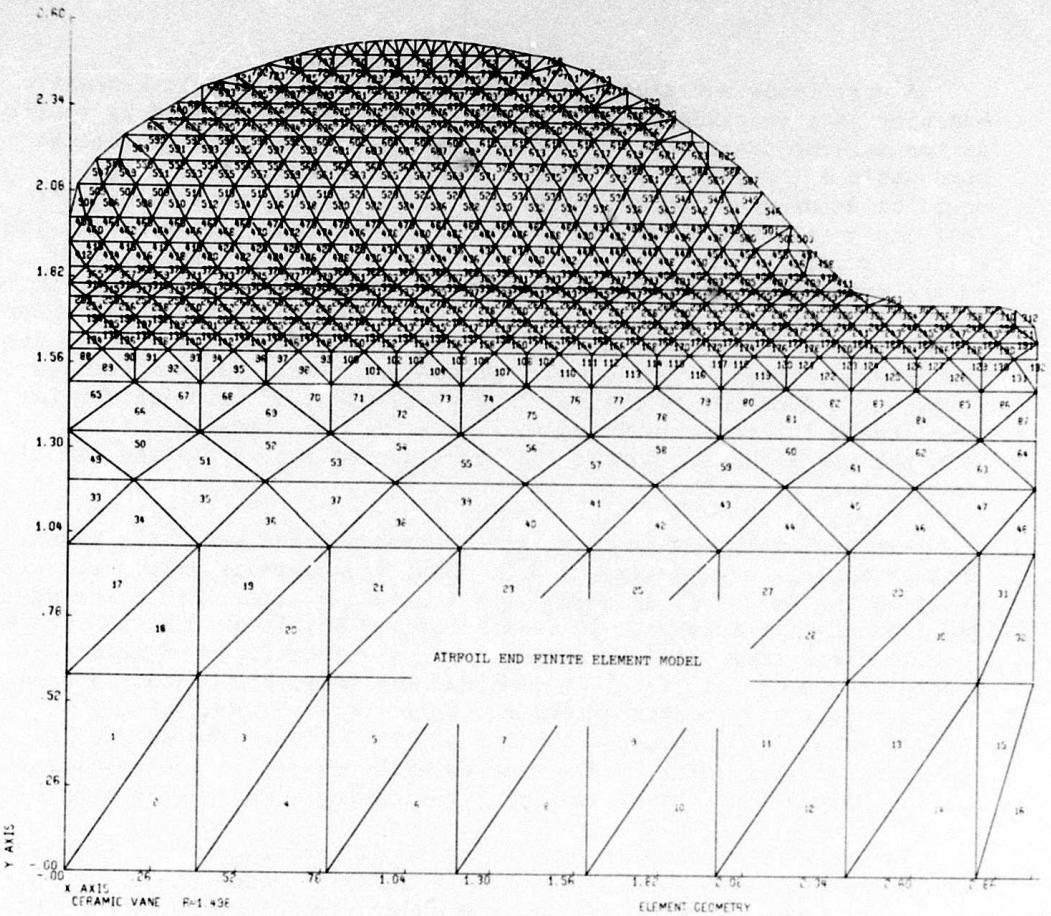


Figure 4.9 Airfoil End Finite Element Model

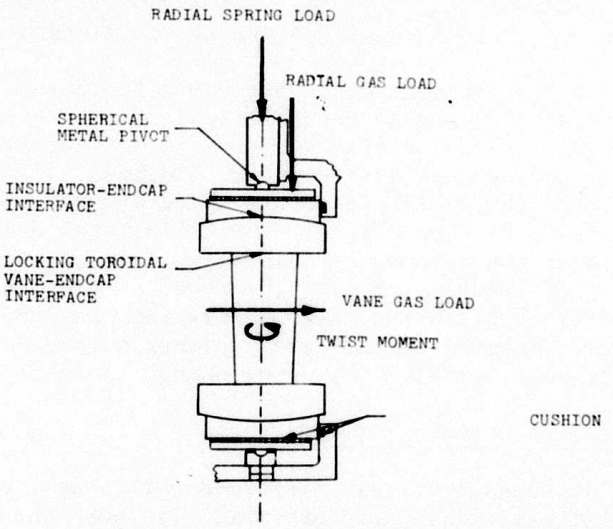


Figure 4.10 Loads and Interfaces Defined with Respect to Ceramic Vane Assembly

A very important aspect of curved interfaces is their kinematic behavior as a function of load and friction. When gas load is applied as the machine starts up, the center of the contact rotates through some angle ϕ. Figure 4.11 shows a simple one-dimensional force equilibrium diagram for the situation corresponding to a turbine at rest and just after start up. R refers to the radial compressive loads while G refers to the vane gas load. The subscripts $_T$ and $_N$ refer to the tangential and normal components, respectively, defined with respect to the interface. From the diagram, the net normal load on the interface is $G_N + R_N$, while the net tangential load is $\mu l\ (G_N + R_N)$. These are the relevant loads in the contact stress formulae. Maximum tensile stress as a function of the start-up coefficient of friction for the vane-endcap interface is shown in Fig. 4.12. The tensile maximum is 9600 psi for a 420 lb. spring load considering the worst case friction coefficient, $\mu = 0.25$.

The endcap-insulator interface transmits loads more like planar contact because of the large radii. That is, there is little curvature to allow the trade-off of normal and tangential load. Since the vane gas load at this interface is reacted almost solely by friction, this requirement establishes the spring load as a function of friction at the endcap-insulator interface. A combined kinematic and contact stress analysis is nearly completed for the inter-related group of two insulators and four endcaps. This analysis includes the effects of circumferential sliding of the endcaps with respect to the insulators as well as the most severe case of edge-loading when interlocking occurs.

The metal pivots represent the terminal resistance to the entire circumferential component of the vane gas load. Under the worst case of tolerance and loading, the maximum shear stress due to pivot contact is 18,700 psi.

Two other locations of contact are the insulator to shoe and insulator to housing ring. Since these areas are cushioned by metal weave material, stresses equal P/A and are considered negligible.

One final area of concern in the contact problem is the magnitude of stresses generated during thermal transient periods. The only interface of dissimilar materials, which is not cushioned by a metal weave, is the endcap-insulator contact. Because of the difference in values of thermal expansion coefficients, a considerable tractive shear force can develop on the surface. The cylindrical analogy can be used to place an upper bound on this shear. It can also define the maximum value of tensile stress. The bound is proportional to the friction coefficient and the maximum Hertzian pressure developed at the interface. Because of the nearly planar nature of this interface, the latter is quite small. The upper bound, therefore, is also small.

Thermal Stress in Ceramic Endcaps

Steady state analysis was performed utilizing a plane-wise symmetric finite element plate program. The mesh and loading are shown in Fig. 4.13. Although the endcap actually has radial sides and a groove with a fourth order surface perimeter, it is modeled as

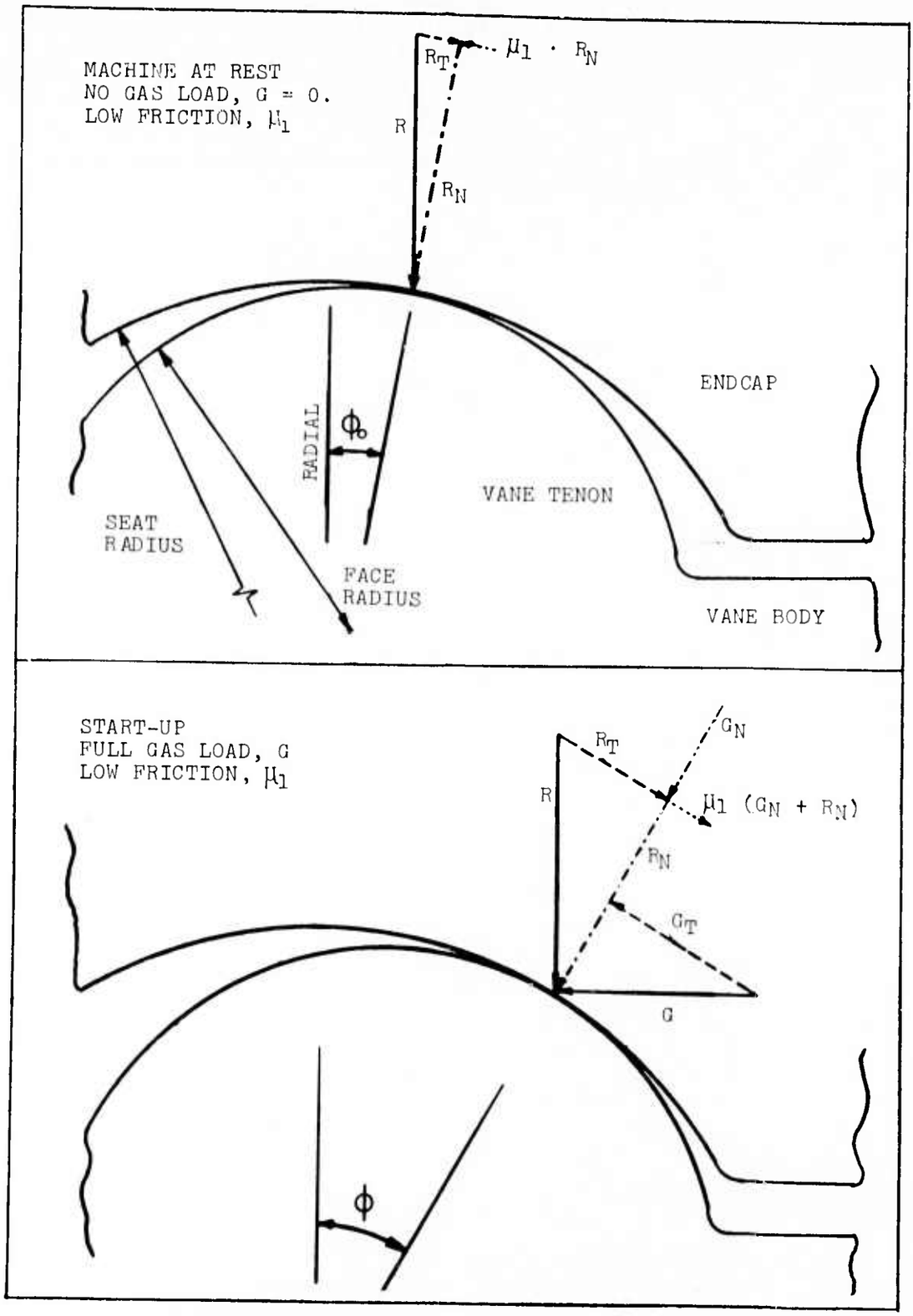


Figure 4.11 One-Dimensional Force Equilibrium Diagram for Airfoil-End Cap Interface

a rectangular block with an ellipsoidal groove. This model was chosen to approximate both the inner and outer endcaps and also the various geometries that occur as the result of varying the groove depth. The endcap is loaded thermally with radial gradients ranging from 200 to 300 degrees which are skewed with respect to the sides so as to present the worst case. The endcap is simply supported at 3 corners and free at the fourth. It is restrained from thermal bending by a uniform pressure of 8000 psi corresponding to the total radial compressive load distributed evenly over the contact area.

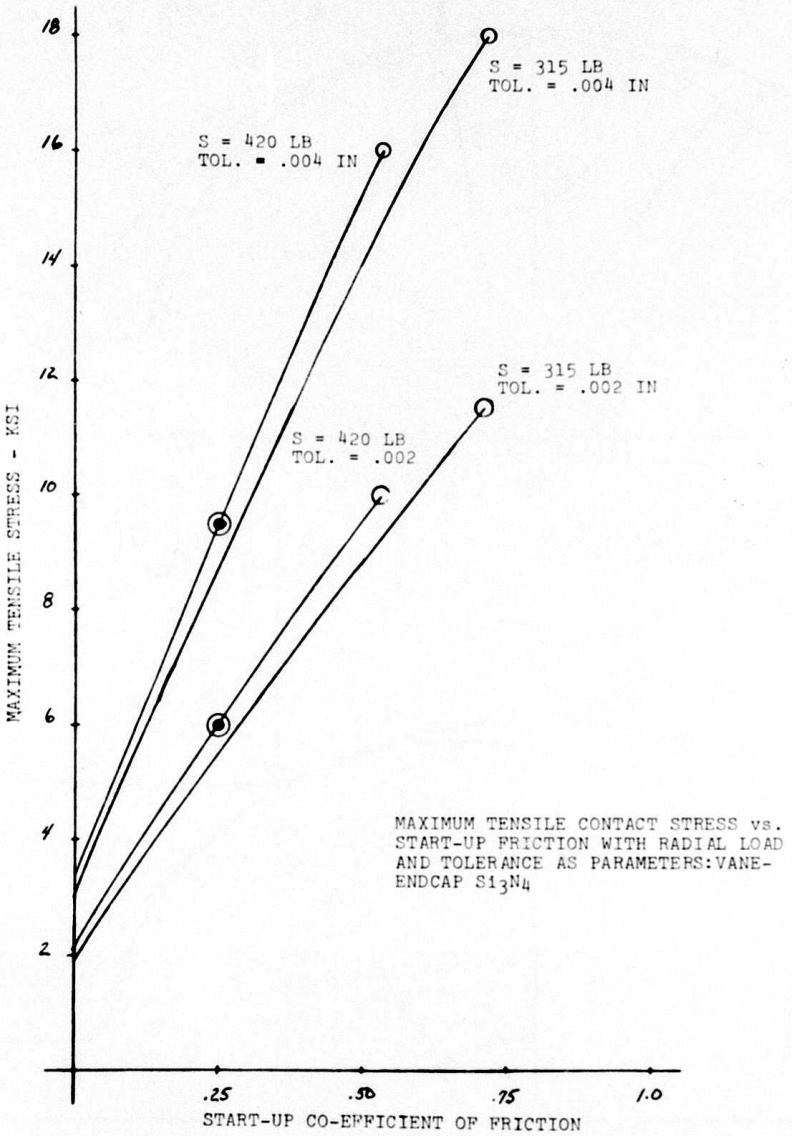


Figure 4.12 The Effect of Friction on Maximum Contact Stress at the Vane-End Cap Interface

Six individual stress analyses were performed. The first three attempted to isolate the effect of reducing the depth of the endcap groove. The maximum principal stress dropped very significantly as the limit of a simple rectangular block was approached. Figure 4.14 indicates this reduction, where the maximum tensile stress at the center of the groove is plotted vs the thickness of the endcap at that point. Since the model used was symmetric, a correction factor was applied to the finite element results to account for the actual asymmetry. This correction factor is simply the ratio of stress concentration factors for flat plates in bending which are grooved completely as shown in Fig. 4.14. The effect is actually more pronounced since the analysis

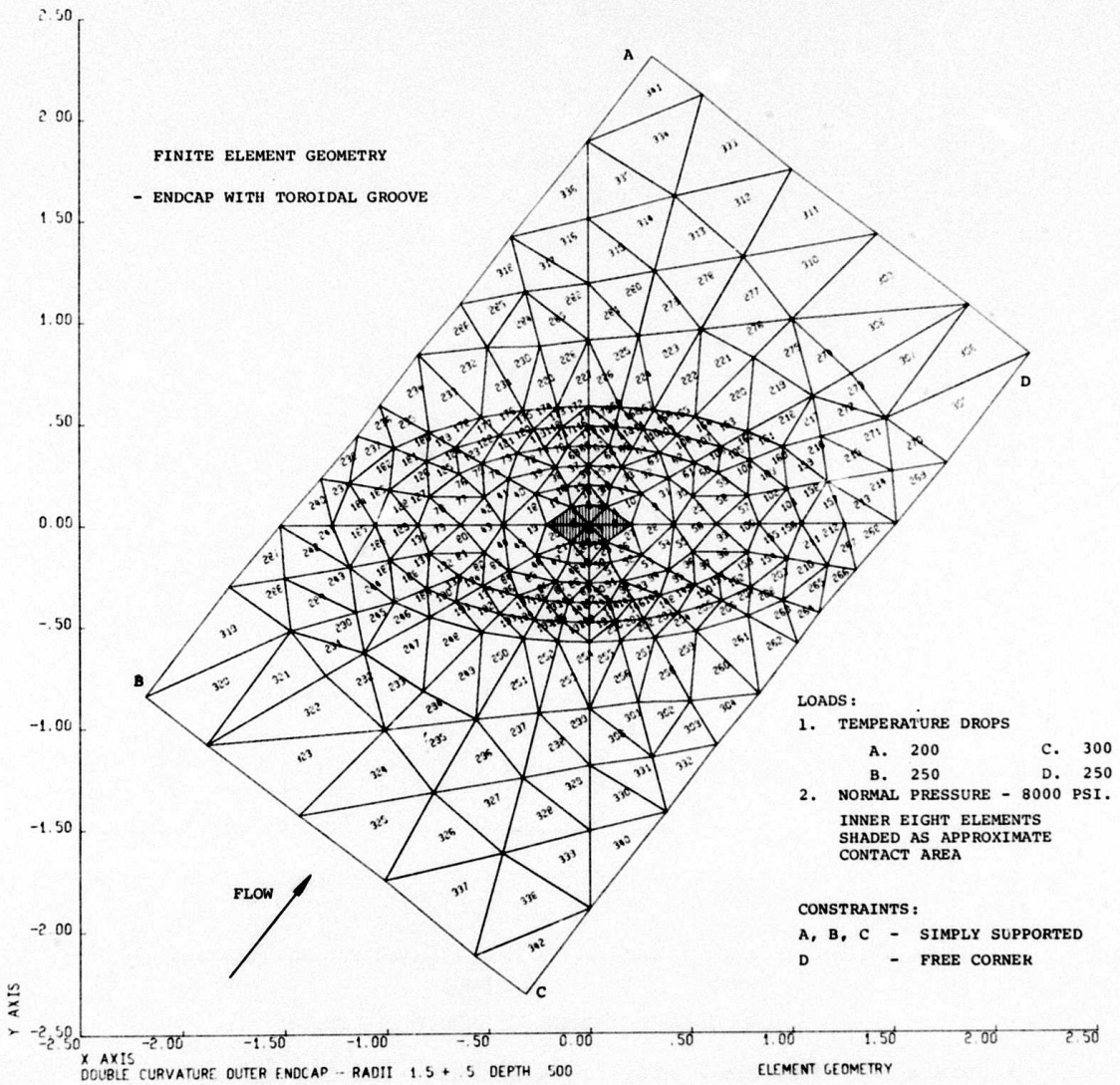


Figure 4.13 Finite Element Geometry - End Cap with Toroidal Groove

uses the same temperature gradient regardless of thickness. From the standpoint of steady state thermally derived plate stress, reducing the depth of the groove from 1/2 inch to 3/8 inch is clearly desirable. This reduction would require an increase in the spring load and in the contact stresses. The net effect of such a change would be beneficial.

The fourth case modeled the stress state in adjacent endcaps, under the same insulator, which have a temperature loading that is the mirror image of that previously shown.

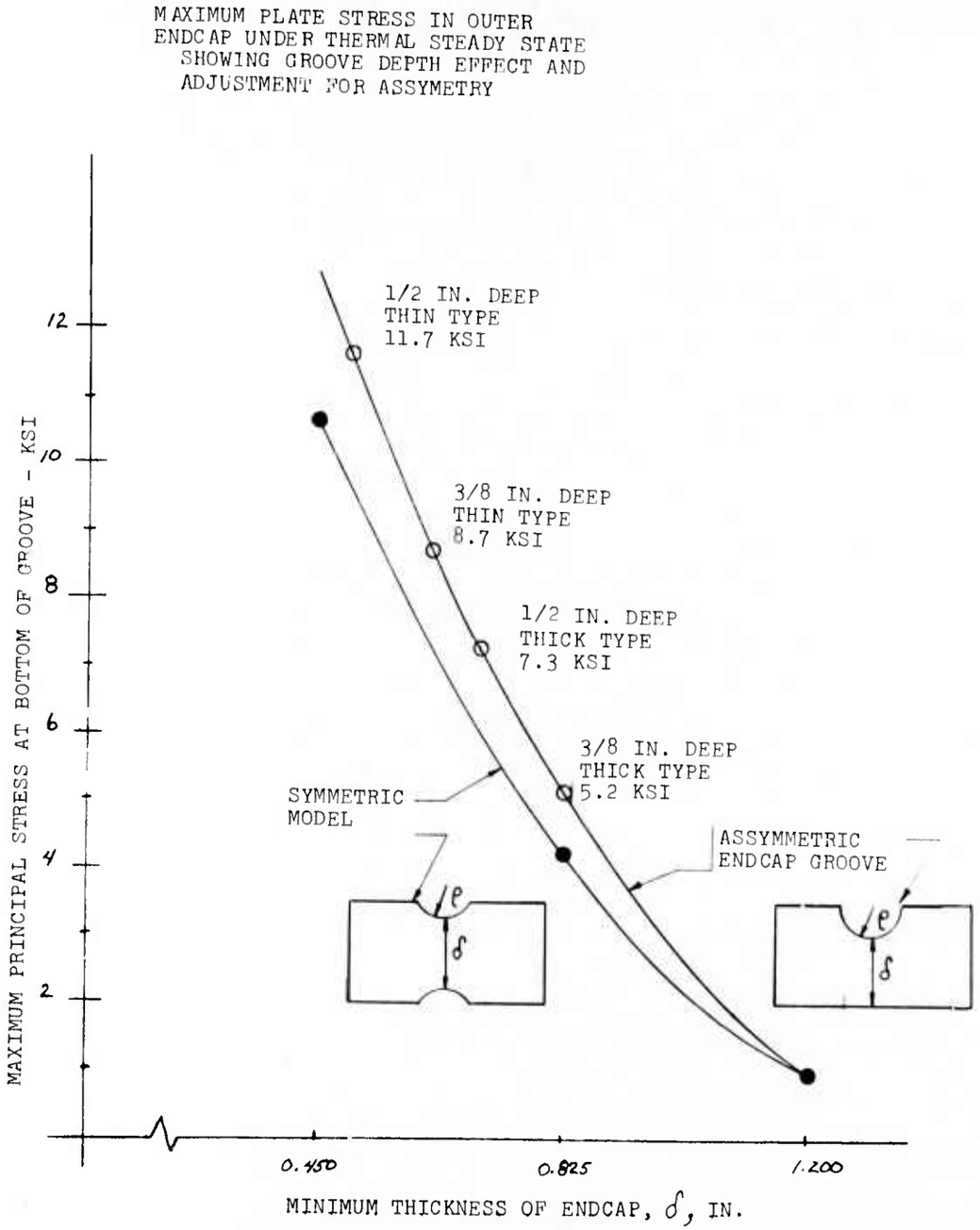


Figure 4.14 Maximum Plate Stress in Outer End Cap under Thermal Steady State Showing Groove Depth Effect and Adjustment for Assymetry

The fifth case studied the effect of reducing the spring load constraint to thermal bending. The results of these runs showed endcap position and spring load to be insignificant as design parameters. Stress reductions of only several hundred psi were realized.

The sixth case compared the stress at the groove bottom to the stress at the thin portion of the endcaps defined by the groove perimeter and the endcap edge. Without the groove the maximum tensile stress occurs at the outer periphery of the endcap. Adding a groove decreases this stress as a function of groove depth but a new maximum stress occurs at the groove bottom. This new tensile stress is generally four times the peripheral stress for useful groove depths, thus peripheral stresses do not greatly influence the choice of groove depth.

In the area of transient thermal stress analysis, efforts are progressing to determine the required cooling flows, inherent leakages and their effect on the convection coefficients. The design process is iterative, in that a set of plausible inputs is formulated to produce a temperature-time profile. If the cooling flow inputs are adjusted to produce a new temperature field which is less severe, the flow adjustments are considered beneficial. The heat transfer problem for a ring segment is being solved with the aide of an axisymmetric finite element program. The temperature fields of interest will be substituted into the finite element plate program described earlier to evaluate transient thermal in-plane stresses.

The analysis has been carried to a sufficient extent to be able to determine the maximum tensile stress in steady state. The combined contact and thermal stresses yield maximum values of 21,200 psi (tension) for the 1.0 inch thick endcap and 16,700 psi (tension) for the 1.2 inch thick endcap. The stress maxima occur near the center of the bottom of the groove. Stress levels of 21 and 17 ksi are acceptable. However, transient conditions are expected to be more severe.

Thermal Stress Tests

Thermal shock tests were conducted in a gas test passage, closely resembling the environment of a gas turbine. These tests were performed for the following reasons:

(1) To subject Si_3N_4 specimens to a thermal shock condition in a gas turbine environment which simulates emergency shutdown.

(2) To obtain information on shape and size effects for Si_3N_4 material under thermal stress.

(3) To correlate computer design codes with experimental data.

Si_3N_4 cylinders (1 inch diameter x 2 inches high) were heated to a steady state temperature of 2000°F, then immediately quenched in a blast of relatively cool compressor air. The thermal environment in the test passage during a shutdown cycle is shown in Fig. 4.15.

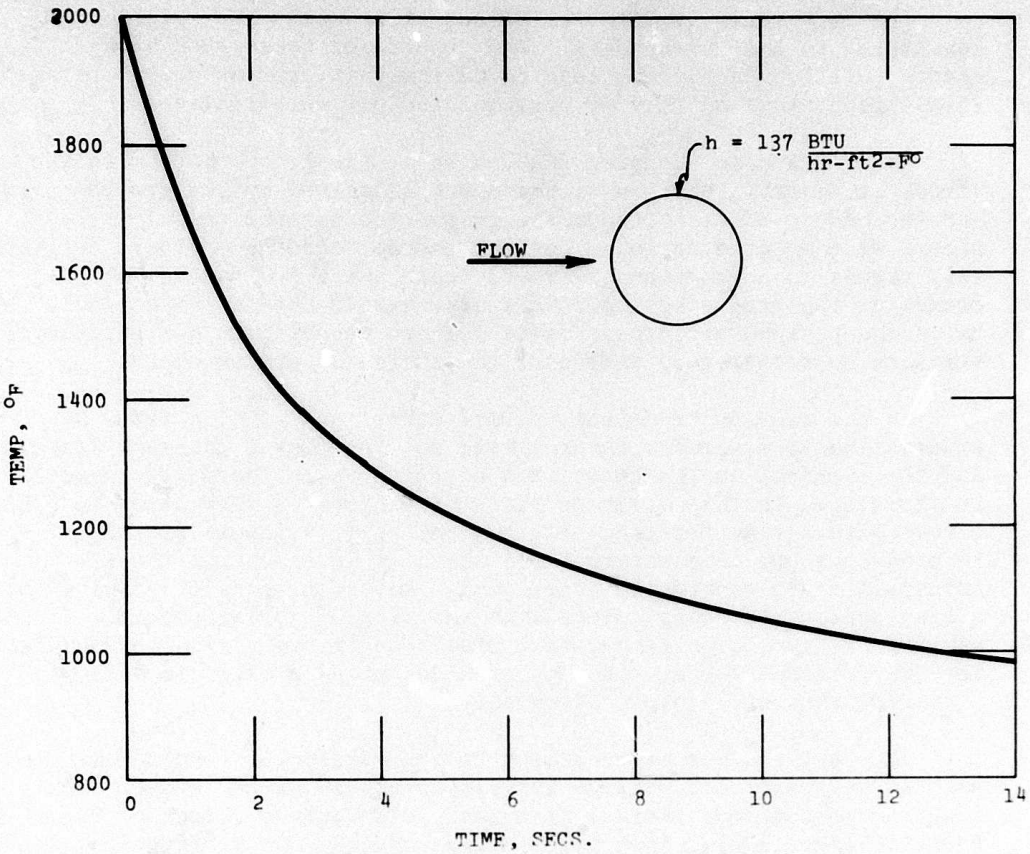


Figure 4.15 Boundary Conditions Gas Temperature and Film Coefficient

The film convection coefficient, h, for the shutdown was calculated from the gas properties, mass flow and physical dimensions of the test passage and cylinder.

Tests in the passage indicated that the quenching is fairly uniform around the cylinder, i.e., within a 10°F deviation around the circumference of the cylinder. Hence, an axisymmetric analysis can be used to calculate the transient temperatures and stresses in the cylinder.

Two analytical techniques were used to evaluate and compare the experimental data. An axisymmetric finite element model has the capability of treating the non-uniform cooling along the axis of the cylinder. A finite difference model was employed to treat non-uniform cooling around the circumference of the cylinder. Figure 4.16 shows the cylinder geometry tested along the computer models used in the analysis. The axisymmetric finite element model employed to calculate transient temperatures and stresses is given in the bottom view of the model on the left hand side of Fig. 4.16. The top view shows the mesh

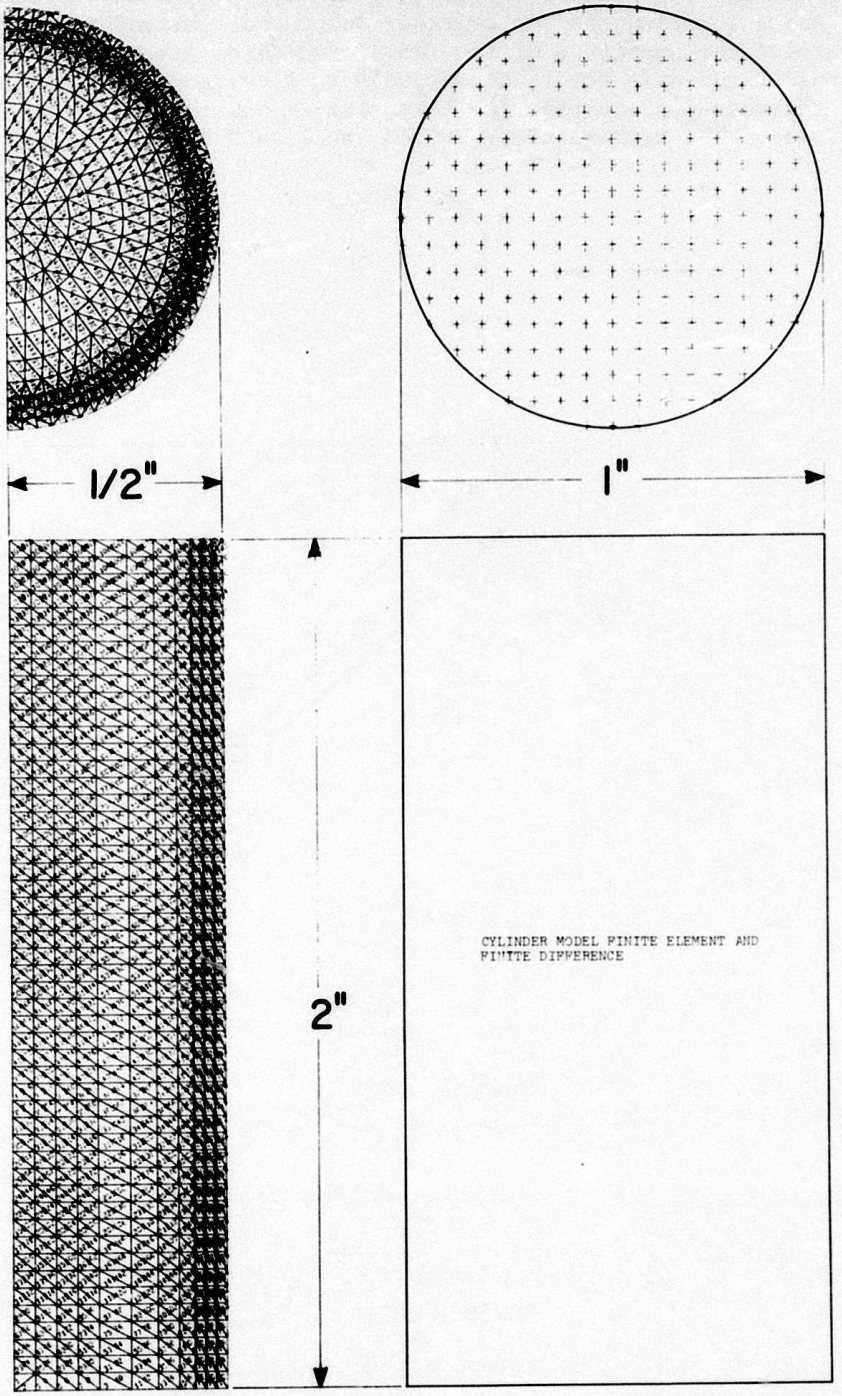


Figure 4.16 Cylinder Models (Finite Element and Finite Difference)

used in the generalized plane strain program. This model was used to verify the axisymmetric thermal stresses and to calculate non-axisymmetric stresses where required. Thermocouples were placed at various radial and axial locations in the cylinder to monitor thermal response and determine the magnitude of the radial and axial temperature gradients. A typical response for a thermocouple in a cylinder is plotted in Fig. 4.17. The thermocouple location for this case is just below the surface of the cylinder. The temperatures at this location as predicted by both the

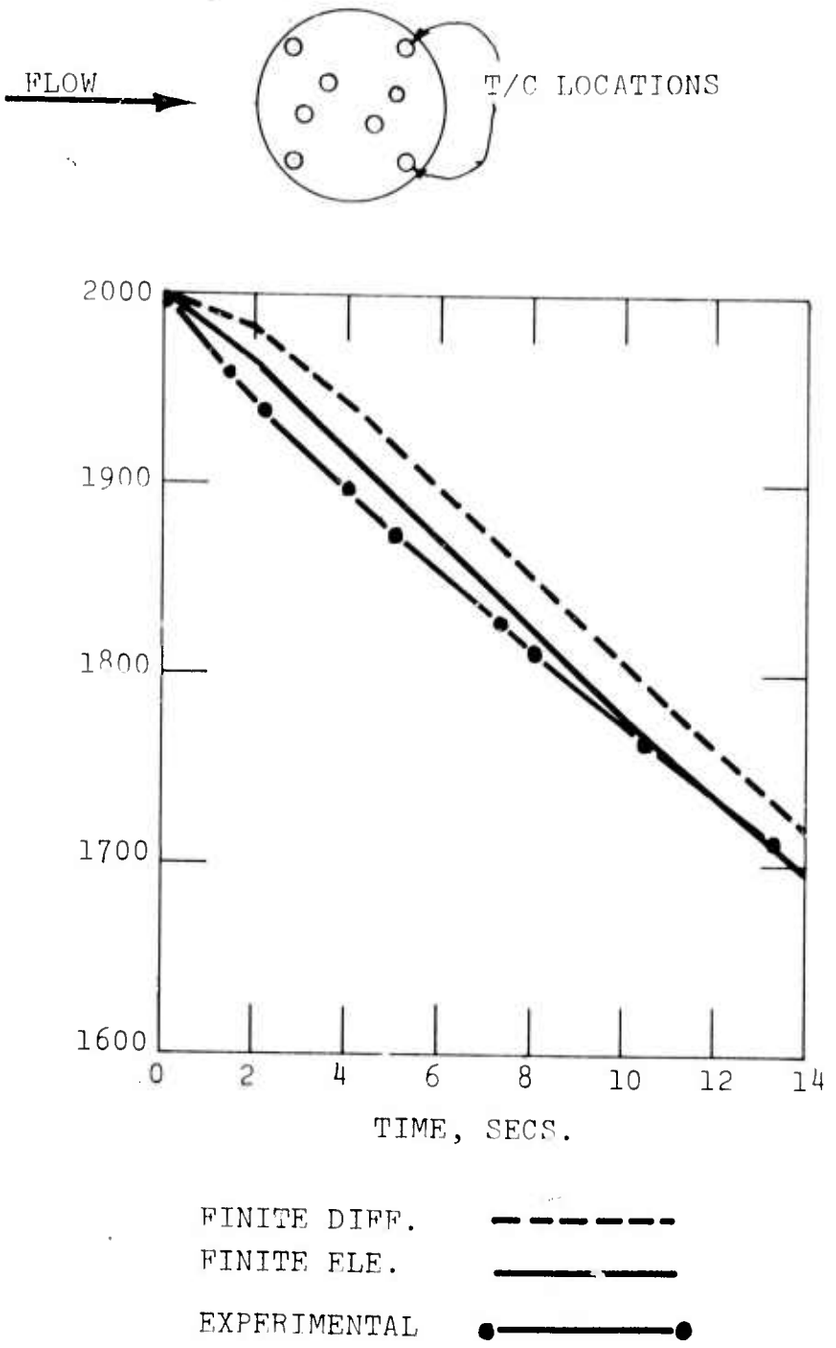


Figure 4.17 Effect of Time on Temperature for Cylinder Thermal Quench Test

finite element and finite difference computer codes are also indicated. Both methods predict the measured temperature response quite well. The finite element method yields slightly better correlation.

The maximum tensile stress history generated by this thermal shock is given in Fig. 4.18. This tensile stress occurs on the surface of the cylinder because of differential thermal contraction caused by the relatively cool gas which washes over it during shutdown. The maximum tensile stress reaches a value of 12.8 ksi, well below the rupture strength of the material. Fourteen tests were run on two cylinders, one of which was drilled for thermocouple holes. No cracks were observed either by visual or X-ray inspection in any of the cylinders. Since the cylinder tests were conducted at the limit of the thermal shock capacity of the test passage, a decision was made to change the specimen to an airfoil shape in an effort to generate higher stresses which cause failure. A simple teardrop shape airfoil is currently being tested.

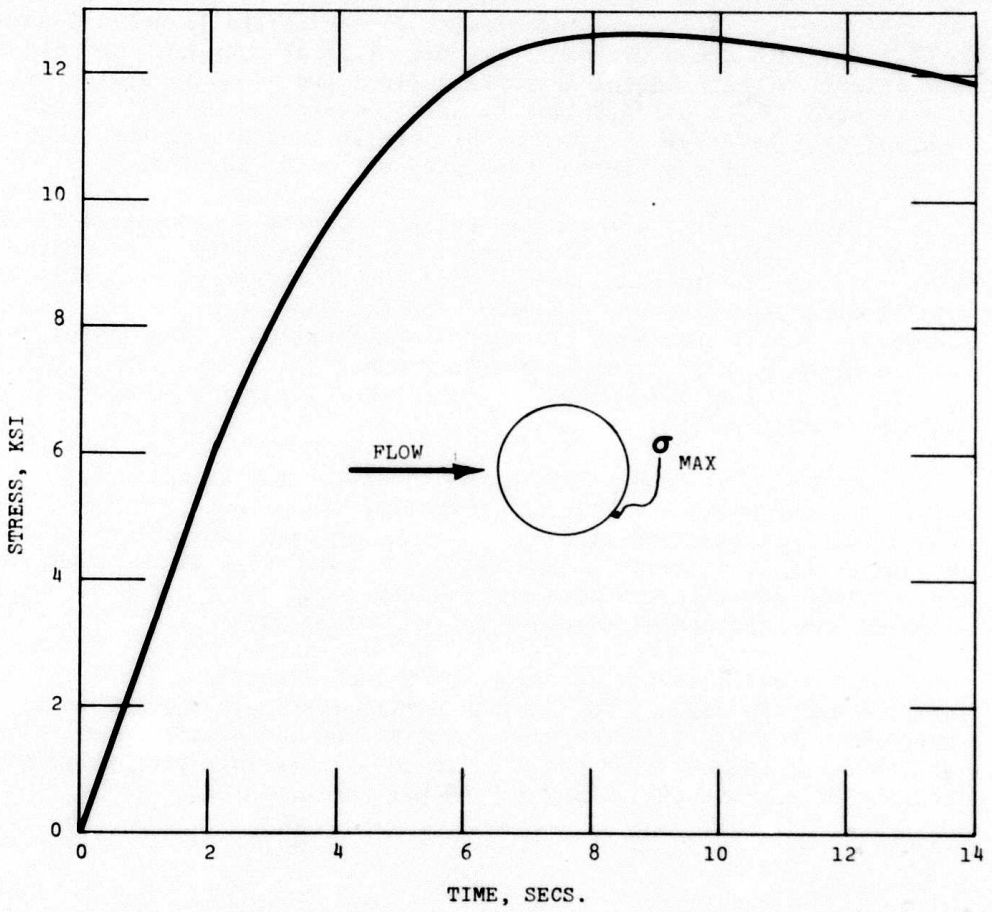


Figure 4.18 Development of Stress in Cylinder Thermal Quench Tests

4.1.3 VANE FABRICATION

The Norton Company was selected to manufacture stator vane assemblies of high-strength, hot-pressed silicon nitride.

In addition to the hardware requirements, Norton was required to supply representative room temperature property data and sufficient quantities of this material for evaluation and statistical property characterization. Norton's high-density, hot-pressed silicon carbide has been purchased for initial evaluation as a candidate turbine material.

The Norton subcontract has been extended to include hot pressed silicon carbide and additional HS-130 silicon nitride material. These materials will be used to fabricate stator vane assemblies to a second generation design specification.

Norton data to certify the last 17 Si_3N_4 billets (Norton HS-130 material)are reported in Table 4.2. Densities range from 3.14 to 3.21 gm/cc, well above the minimum 3.10 gm/cc originally specified. The specification, however, was recently revised to reject billets of density below 3.15 gm/cc. The results of bend tests (3 point loading over a 3/4 inch span) indicate that the material continues to meet the specification that modulus of rupture (less two standard deviations) must exceed 90,000 psi. Billet to billet variation as well as the scatter of data within individual billets is much higher than that representative of a uniformly processed material, however.

Finished airfoil and end cap sections of the 3 piece stator vane assembly are shown in Fig. 4.19 and 4.20, respectively. Processing steps are also indicated. Delivery of the 20 first generation nitride stator vane assemblies is now scheduled for January 31, 1973. Fifteen airfoil sections have been ground to specification. Five airfoil blanks have already been accepted by Westinghouse. Two finished airfoils are being subjected to a dimensional check. Forty endcaps have been partially machined.

Norton's preliminary inspection indicates the finished end cap cavities were ground up to 0.005 inch oversize on both the large and small radii as measured at the end of the groove. The out of tolerance situation is less severe at the bottom of the groove in the area where the airfoil actually contacts the end cap. Norton has proposed hand lapping specific pieces together to insure the best fit.

Norton delivered three prototype 9 inch diameter x 1.3 in. thick silicon carbide billets to Westinghouse in July. This material is described in Table 4.3 from data submitted by the manufacturer. Density values range between 3.28 and 3.31 gm/cc. An average room temperature modulus of rupture of 112,500 ± 9700 psi was reported.

TABLE 4.2

Summary of Westinghouse Contract Billets
HS-130 Si_3N_4

Phase II

Billet Number	Density	Average* MOR	Standard Deviation	Range	# of Tests
060372A	3.19	122,200	11,100	136,900 / 96,500	20
060572A	3.19	121,500	8,800	132,700 / 95,500	20
060672A	3.18	124,600	9,500	136,200 / 102,000	21
060872A	3.17	112,700	11,000	129,000 / 85,000	21
060872B	3.18	128,500	10,900	143,200 / 100,000	20
060972A	3.21	142,800	9,300	156,900 / 119,800	20
052472A	3.14	114,926	12,157	138,332 / 98,641	20
061272A	3.18	116,916	9,245	137,512 / 99,896	20
061472A	3.20	125,426	10,838	146,852 / 104,976	20
061672A	3.20	133,249	20,998	158,630 / 58,751	20
061972A	3.20	135,896	10,047	148,145 / 112,872	20
061972B	3.21	130,701	9,492	146,051 / 112,072	20
062072A	3.18	124,895	9,134	139,560 / 103,487	20
062072B	3.20	135,202	10,273	149,628 / 109,687	20
062172A	3.18	124,607	8,877	137,279 / 102,666	20
062172B	3.19	130,403	10,245	143,770 / 101,620	20
062772B	3.16	117,591	7,344	128,194 / 104,232	20

*Data obtained by 3 pt. loading over 3/4 in. span on specimens of 1/8" x 1/8" cross section, loading rate 0.01 in/in/min.

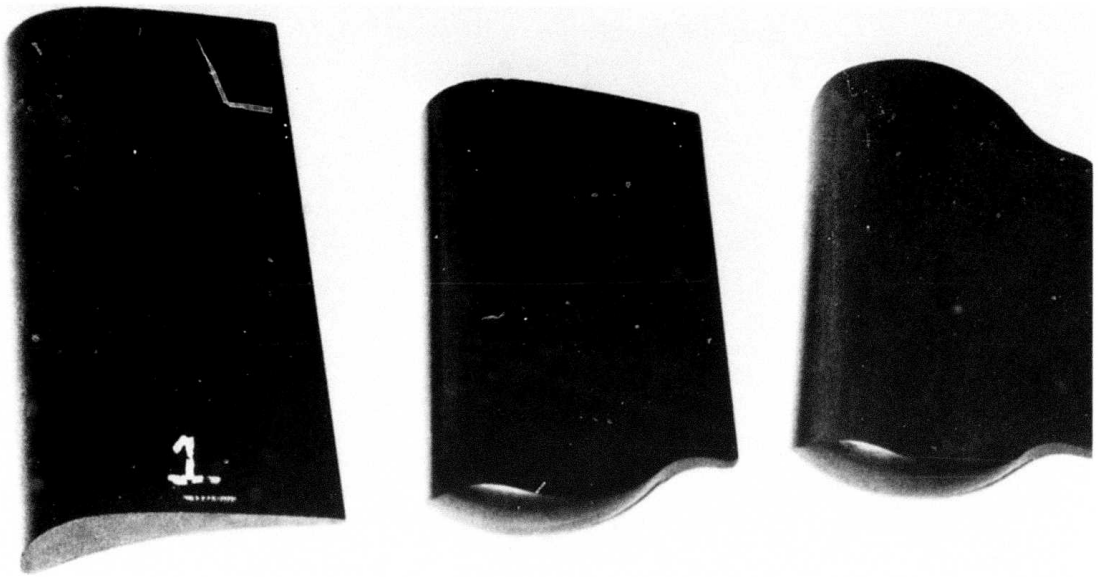


Figure 4.19 Major Steps in the Machining of the Airfoil

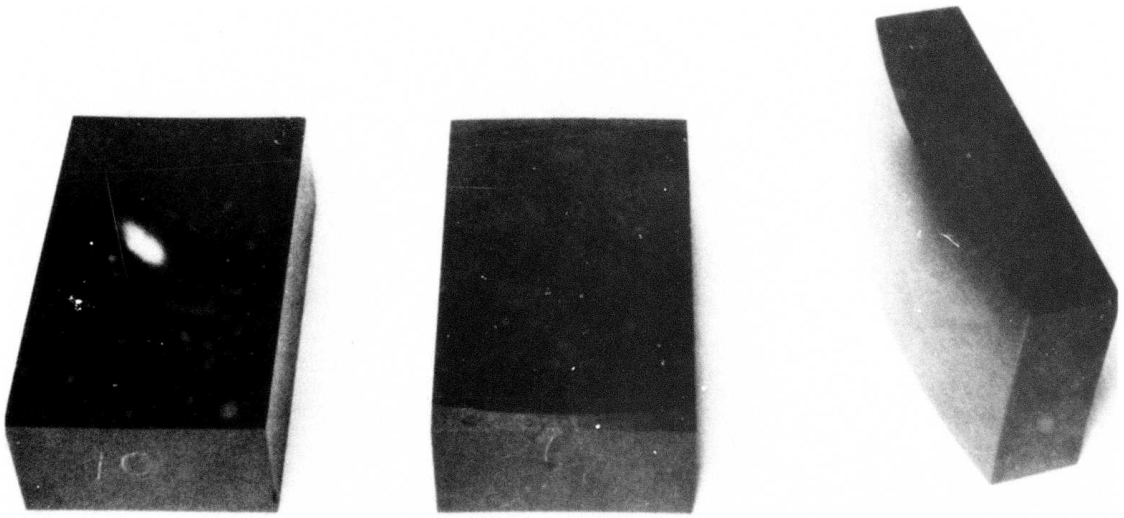


Figure 4.20 Steps in the Grinding of an End Cap

TABLE 4.3

Properties of Norton Hot Pressed Silicon Carbide

Billet No. "7"

Density	3.28
Average MOR	112,214
Std Deviation	12,184
Range	130,068
	88,020

Test No.	MOR *	Test No.	MOR *
1	99794	8	117734
2	88020	9	126705
3	95309	10	130068
4	117734	11	109325
5	114931	12	115492
6	114902	13	122220
7	106522		

Billet No. "8"

Density	3.28
Average MOR	109,850
Std Deviation	7,010
Range	117,174
	94,188

Test No.	MOR *	Test No.	MOR *
1	108204	9	116613
2	116052	10	109913
3	106522	11	114931
4	102006	12	94188
5	102036	13	116052
6	109325	14	114931
7	109301	15	117174
8	113810	16	115492

*Data obtained by 3 pt. loading over 3/4 in. span on specimens of 1/8" x 1/8" cross section, loading rate 0.01/in/in/min.

TABLE 4.3(cont'd)

Properties of Norton Hot Pressed Silicon Carbide

Billet No. "2"

Density	3.31
Average MOR	115,472
Std Deviation	10,034
Range	129,478
	94,456

Test No.	MOR	Test No.	MOR
1	119902	12	109626
2	127468	13	118248
3	125140	14	129478
4	108843	15	128060
5	96213	16	112012
6	116939	17	123871
7	106817	18	95456
8	111437	19	113499
9	124139	20	98366
10	113169	21	123394
11	121252	22	117574

Norton will supply the following materials and components to complete FY 73 requirements:

(1) 38 HS-130 Si_3N_4 billets for the machining of 15 second generation stator vane assemblies.

(2) 38 hot pressed SiC billets for up to 15 first generation stator vane assemblies and sufficient material for statistical characterization by Westinghouse.

(3) Machining of up to 15 first generation stator vane assemblies.

(4) 38 hot pressed SiC billets for the machining of 15 second generation stator vane assemblies.

The Norton Company is making every effort to improve the quality and uniformity of both silicon nitride and silicon carbide. They have constructed clean room facilities for Si_3N_4 powder handling and processing. Separate hot press facilities have been installed. Two methods have been developed to eliminate or minimize the inclusions in Si_3N_4 as follows:

(1) Modifications to the processing prcoedure to eliminate the source of inclusions.

(2) The addition of an inclusions removal step in the powder handling process.

The calcium level in HS-130 silicon nitride appears to be solely a function of starting material purity according to Norton. The calcium content of additives used contributes approximately 15 ppm to the total billet concentration. Norton claims to have found sources of low calcium silicon powder but has not identified them.

4.1.4 Static Rig Testing

The static rig for the testing of ceramic stator vane assemblies and their spring loaded support structures up to 2500°F is represented schematically in Fig. 4.21. Final design drawings for the rig were completed in December. The basic, high pressure shell is scheduled for delivery in late February.

The high temperature exhaust duct will be built from a one inch thick molded silicon carbide refractory wall insulated by three inches of low density alumina castable which is wrapped within a Fiberfrax blanket. The insulated duct assembly will be encased in a stainless steel jacket. Heat transfer across the duct may still require cooling air flow in the space between the duct and the outer shell. Delivery is expected in April.

Instrumentation for 2200°F operation will consist of Chromel-alumel thermocouple in Hastelloy X aspirated probes. These will be available in February. Silicon nitride rakes with Platinum-Platinum, Rhodium thermocouples for 2500°F must be developed.

Drawing to show the layout and details of all the parts required to support the ceramic vanes in the static rig have been completed. This hardware together with air inlet piping, combustors and transition ducts have been ordered.

The present arrangement will test 8 ceramic vanes and their associated ceramic end caps with insulators. The left and right sides of the ceramic passage are formed from modified full-size metal vanes through which high pressure cooling air flows. The metal end vanes have been ordered in the as-cast condition. A vendor has been found to carry out the welding modification, machining and heat treating required with the X-45 cobalt base alloy.

All the rig parts and test hardware for 2200°F testing should be on site by June. About eight weeks will be required for installation and operational checks. Testing of first generation silicon nitride and silicon carbide stator vane assemblies will start in August 1973.

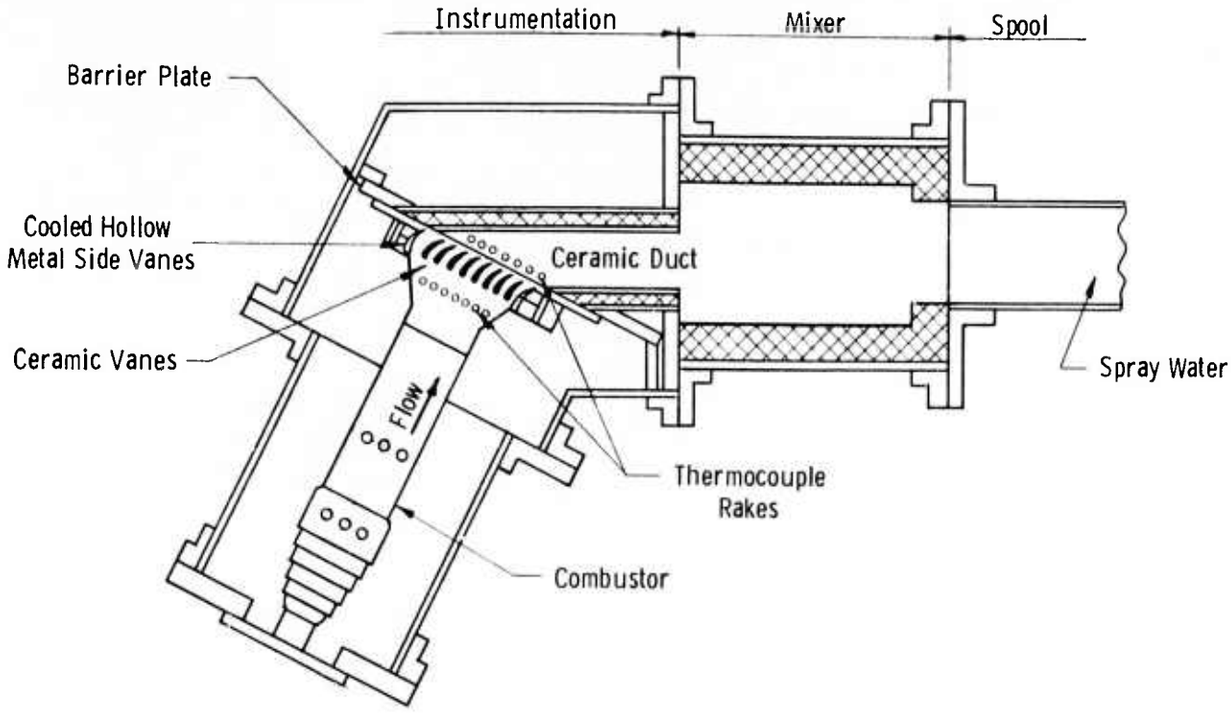


Figure 4.21 Static Rig for 2500°F Test of Ceramic Vanes

4.2 ROTOR BLADE DEVELOPMENT

PRECEDING PAGE BLANK-NOT FILMED

SUMMARY

Westinghouse has completed three dimensional finite element programs for the isotropic elastic stress and heat transfer analysis of solids. Supplementary programs are being developed to handle anisotropic and temperature dependent materials properties. A data transfer system is used to form an interface between the heat conduction and stress analysis portions of the overall program.

Development of the 3D finite element design code has progressed to the point where ceramics rotor blade design and analysis are in progress.

The location and magnitude stresses were determined for a tentative ceramic rotor blade design subjected to centrifugal loading (3600 rpm) at room temperature. Tensile stresses reached at maximum of 23,00 psi in the dovetail attachment area. Steady state gas bending and transient thermal stresses must be superimposed upon these mechanical stresses in order to complete the preliminary evaluation of this particular rotor blade configuration.

4.2.1 THREE DIMENSIONAL FINITE ELEMENT STRESS ANALYSIS

The finite element program for three dimensional elastic stress analysis has been completed, checked out and demonstrated on a number of practical problems. Development of the program is continuing to produce a version for the analysis of problems with anisotropic materials. The computer program also contains a sub-routine which produces data for plotting the geometry of finite element models based on the elements used in the program.

The theoretical development for the steady state and transient heat conduction has been completed. This program contains numerical procedures which allow anisotropic and temperature dependent material properties to be evaluated.

Three of four computer program overlays have been completed. The fourth is being written. In addition, programming for a data transfer system is in progress. This will serve as an interface between the heat conduction and stress analysis portions of the overall three dimensional finite element program.

The heat conduction program uses the same elements as the stress analysis program; namely:

(1) Eight node elements (linear temperature variation)

(2) Twenty node elements (quadratic temperature variation)

(3) Thirty-two node elements (cubic temperature variation)

(4) Mixed elements.

The mixed element is the most versatile since it allows the user to vary the number of nodes. It also facilitates the generation of graduated element networks to account for regions where large temperature gradients are anticipated.

The following boundary conditions and thermal loads can be handled by the program:

(1) Prescribed temperatures

(2) Prescribed heat flux

(3) Heat generation

(4) Forced convection

(5) Material convection

(6) Radiation.

4.2.2 Stress Analysis of Blades

The preliminary design concept of a ceramic rotating blade has been identified. The blade has a conventional airfoil attached to a dovetail root. The root geometry was estimated based on state of the art experience with cermet and ceramic rotating blades.

The state of the art condition shows that brittle turbine blades frequently fail in the root area. Therefore, an optimization study of the root area is in progress. A two dimensional model of the root geometry for this study is shown in Fig. 4.22. This model is being used to study the effect of various root parameters on the stresses induced in the root by a centrifugal force F_c shown in Fig. 4.22. This force is resisted by the normal and shear contact forces, F_N and F_S, as indicated.

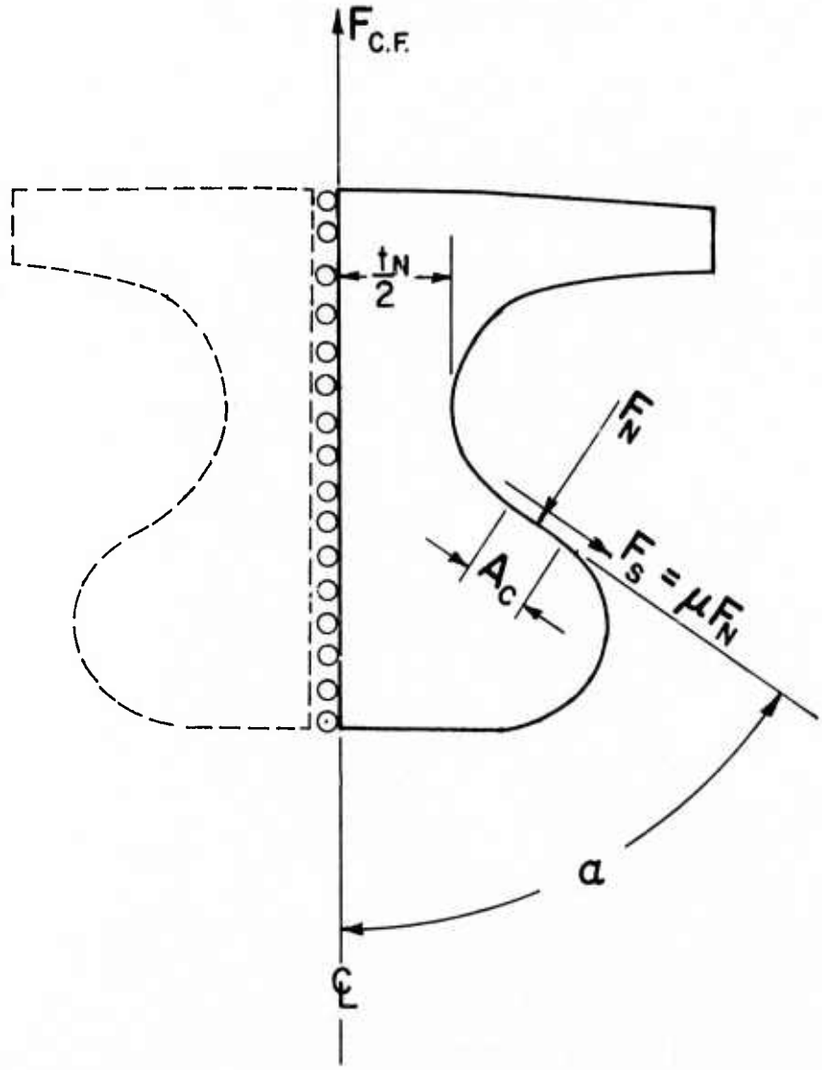


Figure 4.22 Root Model

The root parameters currently under consideration are the root necks, t_N, the included angle α, and the area of contact A_c. This model assumes symmetry along the centerline of the root. Variations of these parameters are currently being studied with a finite element model in order to minimize the stresses in the blade root. Two finite element models with different included angles are currently being analyzed. These appear in Fig. 4.23. A generalized plane strain analysis of each root is in progress.

The root geometry will first be obtained under a centrifugal force field which represents the primary load; it will be analyzed for anticipated thermal loads. If the design appears to be adequate under both centrifugal force and thermal loads, contact analysis will be performed to consider the actual deformation of the disc or rotor which holds the blade.

The elastic stress portion of the three dimensional finite element program has been used in an analysis of a ceramic rotating turbine blade attached to a platform and dovetail root.

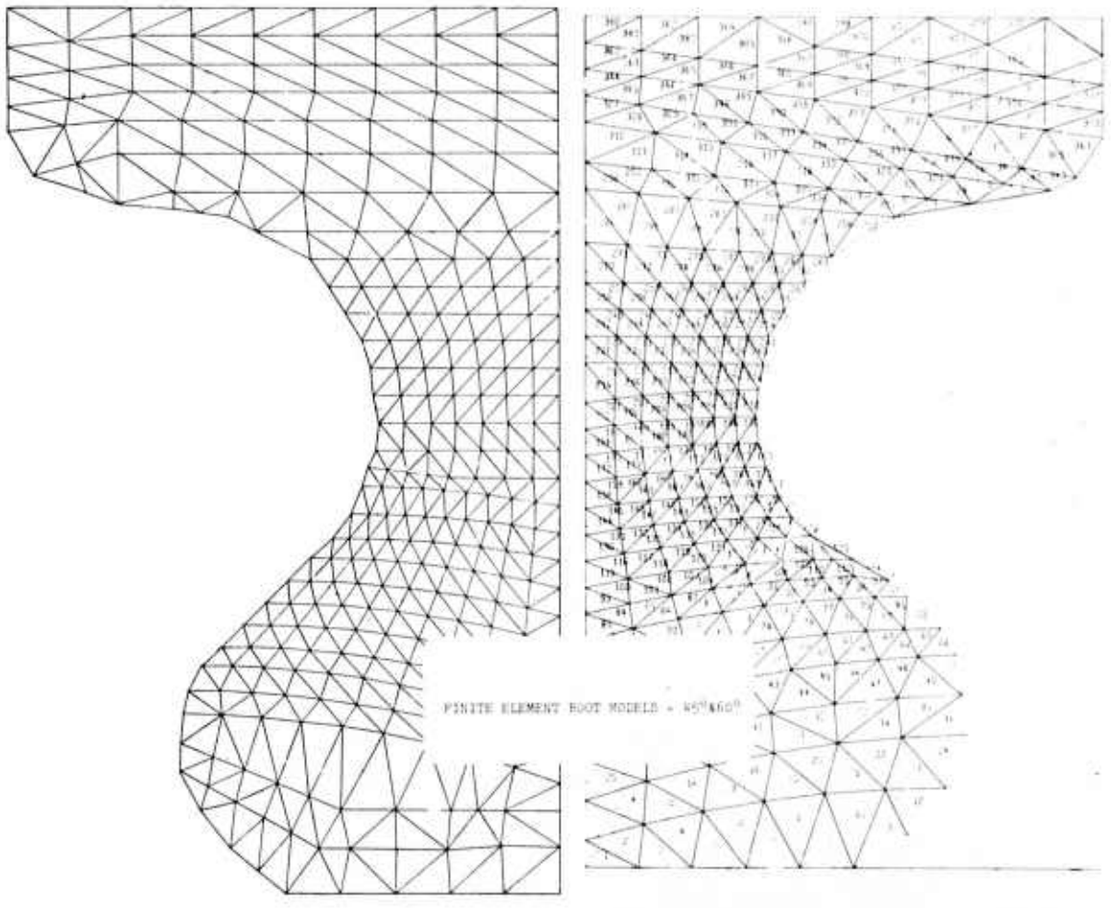


Figure 4.23 Finite Element Root Models - 45° and 60°

A computer plot of the finite element blade model is shown in Fig. 4.24. The model consists of 132 elements. Quadratic elements are used in the airfoil section, the platform and the root. The fillet between the airfoil and the platform is modeled with mixed elements which have cubic edges along the fillet and parabolic edges elsewhere. A total number of 949 nodal points in the model gives 2847 possible degrees of freedom. However, some degrees of freedom are removed by the boundary conditions imposed. The maximum wave front for this problem is 237 degrees of freedom. The analyses are performed as if the blade and root are supported by knife edges at the intersection of section 11000 and the root boundary surface.

The blade and root were loaded by centrifugal forces caused by the maximum rotational speed of 3600 rpm.

The material properties used are as follows:

(a) Modulus of Elasticity 45×10^6 psi

(b) Poisson's Ratio 0.23

(c) Density 0.115 lb/cu inch

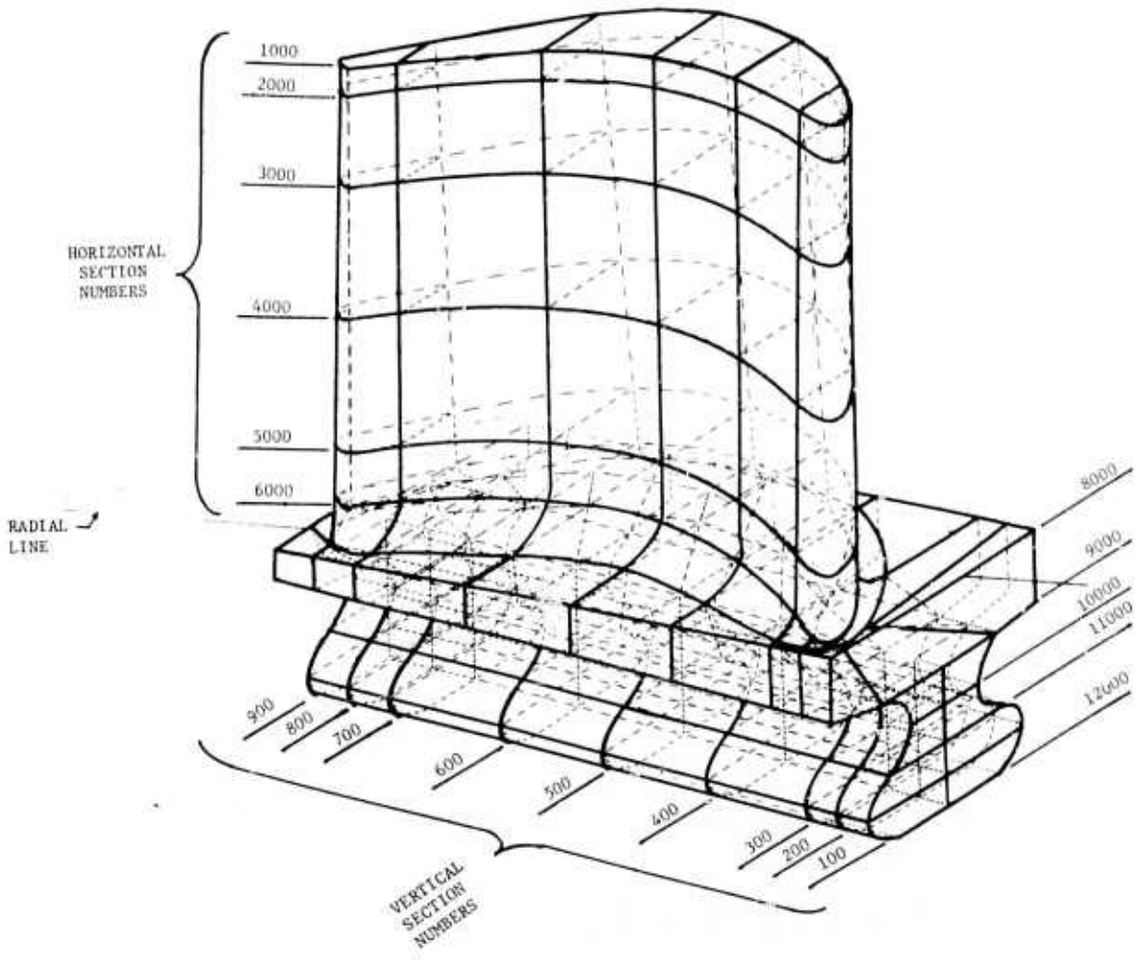


Figure 4.24 Computer Plot of Ceramic Rotor Blade

Figures 4.25 through 4.29 show computer plots of segments of the finite element model. These plots enable the engineer to check the model in detail before the final computer run is made. The figures clearly show the complexity of the model and difficult connection between the fillet section and the platform on the one hand and between the platform and the root on the other. These connections were such that incompatible element conditions were required. For example, some midside nodes of the platform are connected to corner nodes of the root section (see Figs. 4.24-4.26).

The results of the analysis are shown in the plots of Figs. 4.30 through 4.36. The contours of the radial stresses in the airfoil are shown in Figs. 4.30 through 4.32 for the convex boundary surface, the middle surface of the airfoil and the concave boundary surface, respectively. The results suggest that only a small amount of bending takes place in the upper portion of the airfoil since the stresses are almost uniform. The stresses on the three surfaces are quite different in the lower portion of the airfoil for indicating the effects of the fillet and platform.

Figures 4.33 through 4.36 represent the contours of the σ_z stresses in the vertical cross-sections 300, 400, 500 and 700. The location of the knife edge supports are also shown. The high stresses at the knife edge supports are not considered realistic since the actual support will be spread over a finite area. Maximum tensile stresses of 22,787 psi occurs in the root area (see Fig. 4.33). The stresses in the lower part of the airfoil vary considerably. This is expected since the airfoil sections also varies greatly and the fillet and platform have a considerable effect on the deformation and stresses in this part of the airfoil.

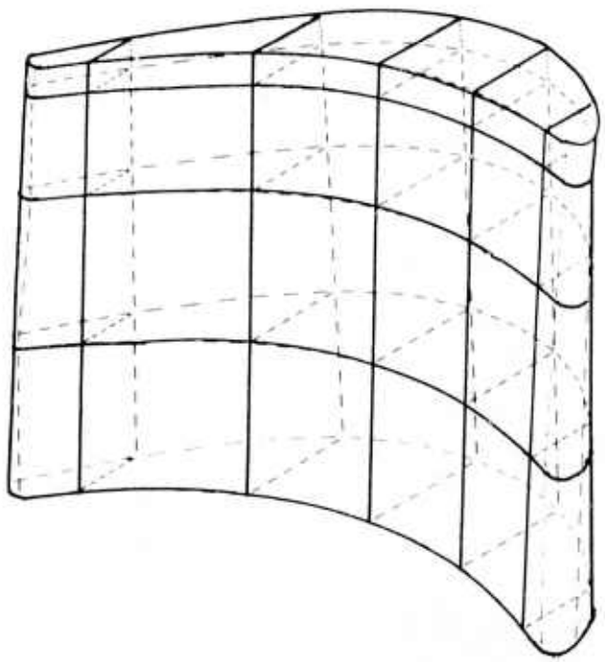


Figure 4.25 Airfoil, Slice Between Vertical Sections 1000 and 5000

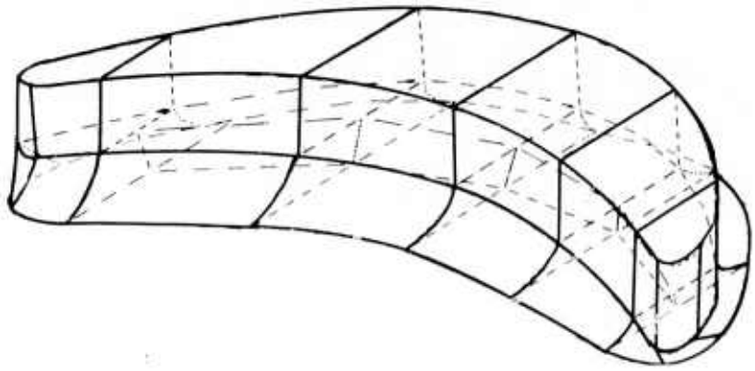


Figure 4.26 Airfoil, Slice Between Horizontal Sections 5000 and 8000

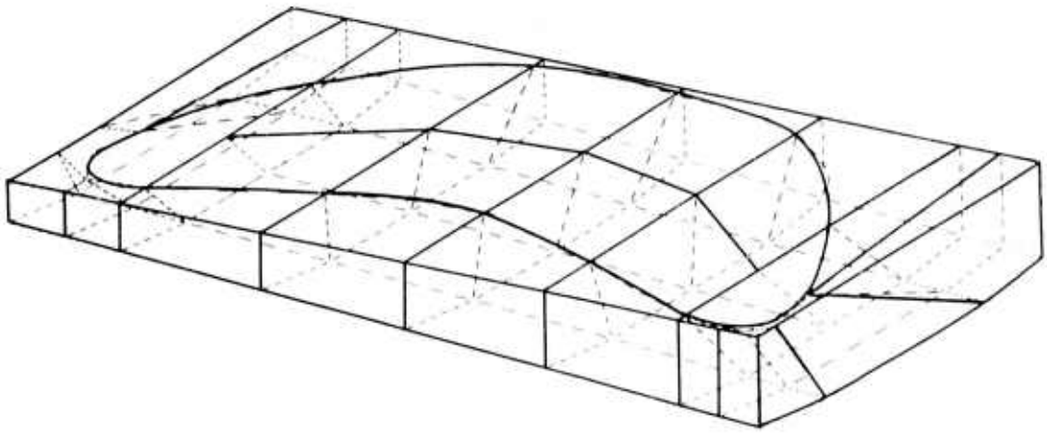


Figure 4.27 Platform, Slice Between Sections 8000 and 9000

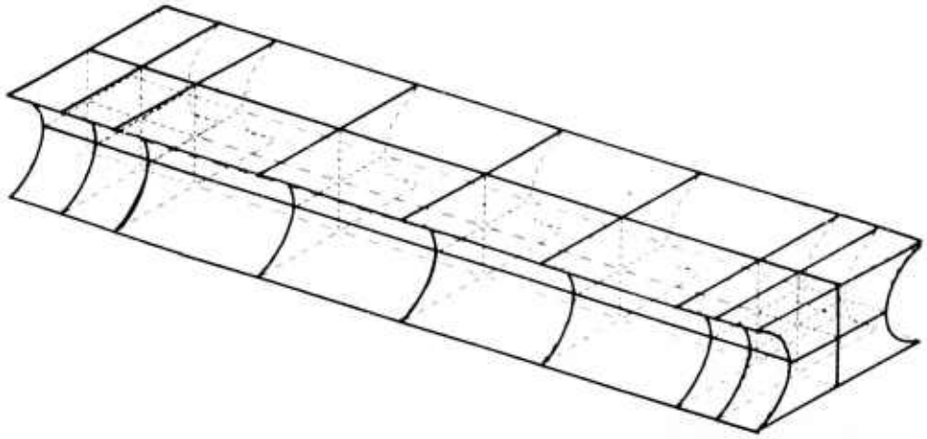


Figure 4.28 Platform, Slice Between Horizontal Sections 9000 and 11,000

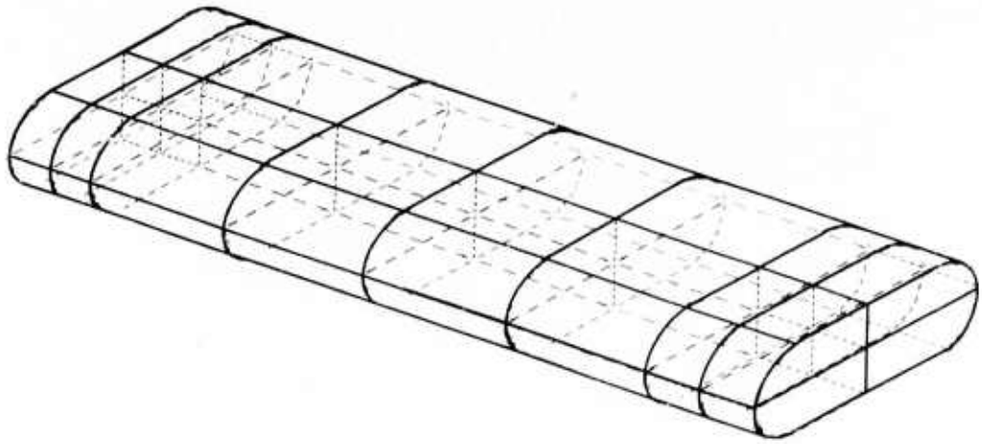


Figure 4.29 Platform, Slice Between Horizontal Sections 11,000 and 12,000

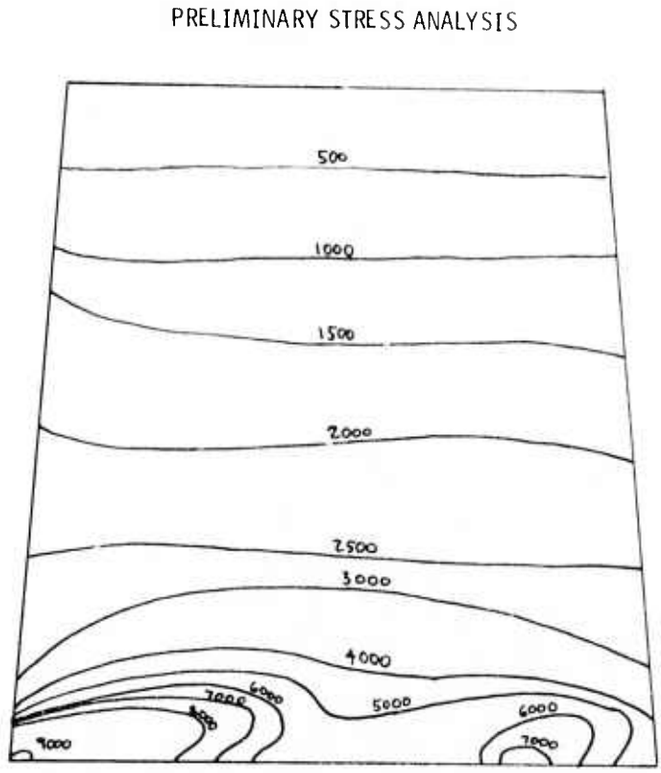


Figure 4.30 Radial Stress Contours (psi) for Airfoil Convex Surface

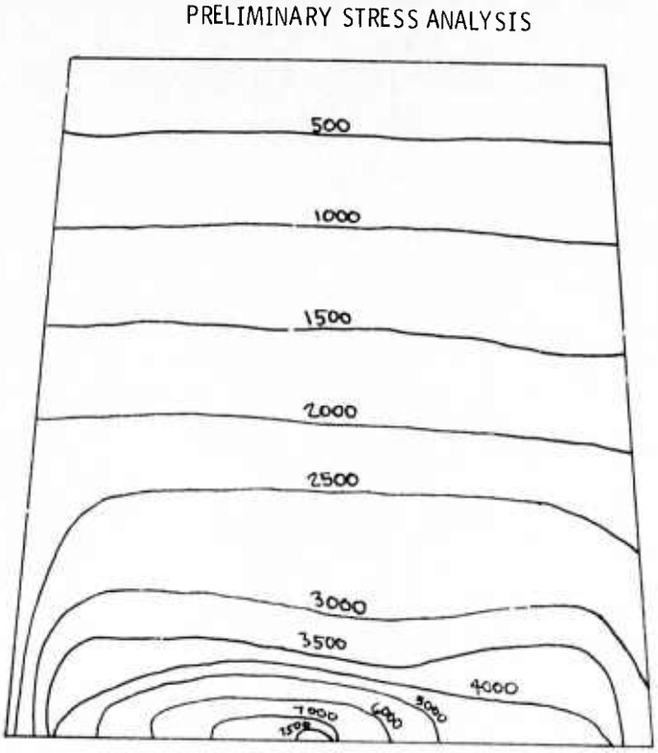


Figure 4.31 Radial Stress Contours (psi) for Airfoil Middle Surface

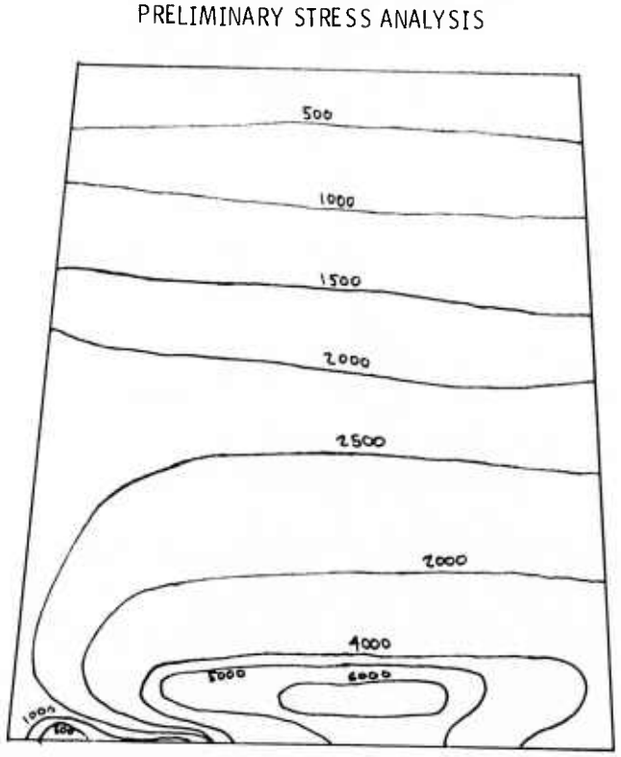


Figure 4.32 Radial Stress Airfoil (psi for Concave Surface

PRELIMINARY ANALYSIS ROTATING BLADE

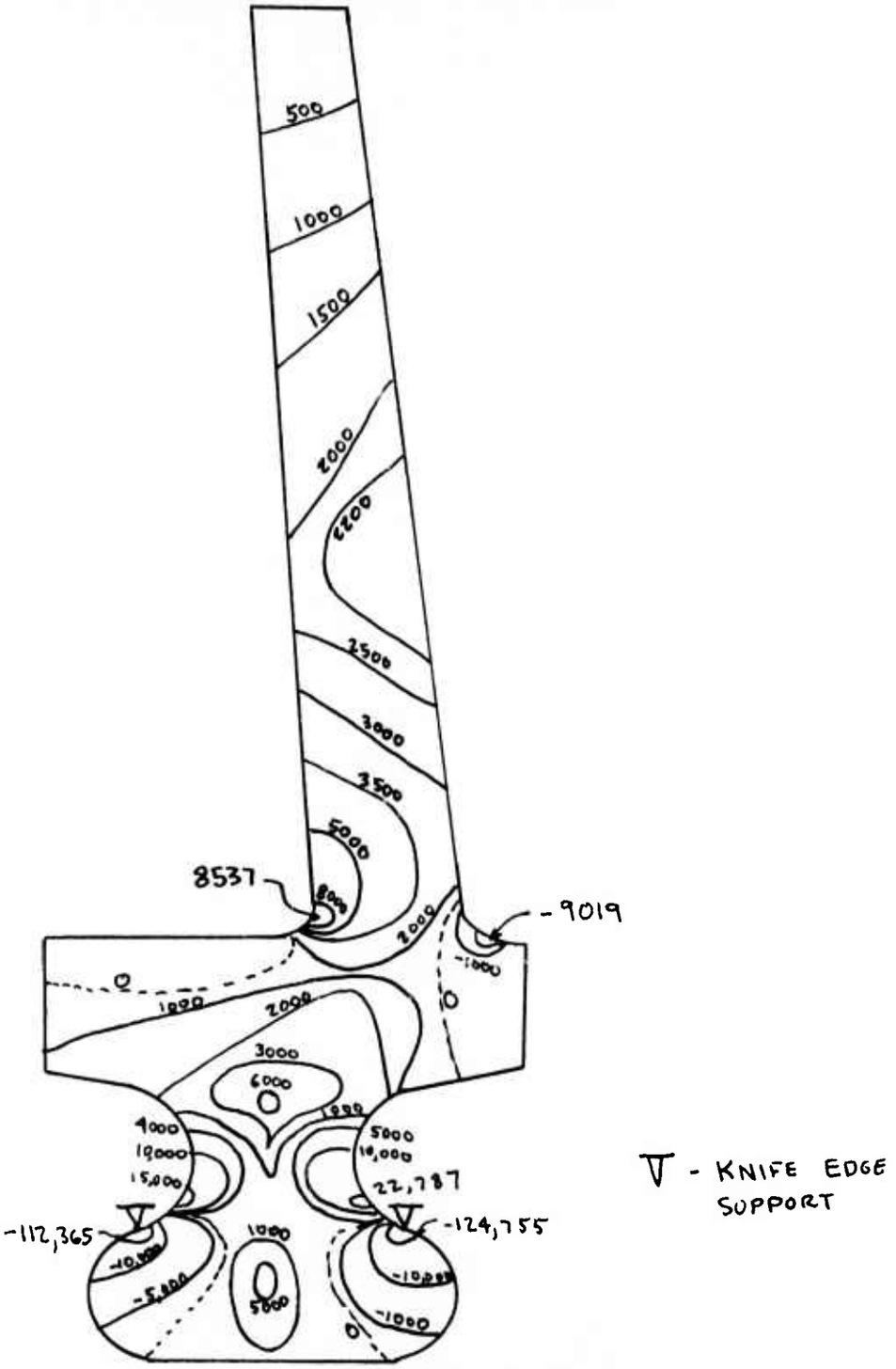


Figure 4.33 Vertical Cross Section 300, σ_z Stress Contours (psi)

PRELIMINARY ANALYSIS ROTATING BLADE

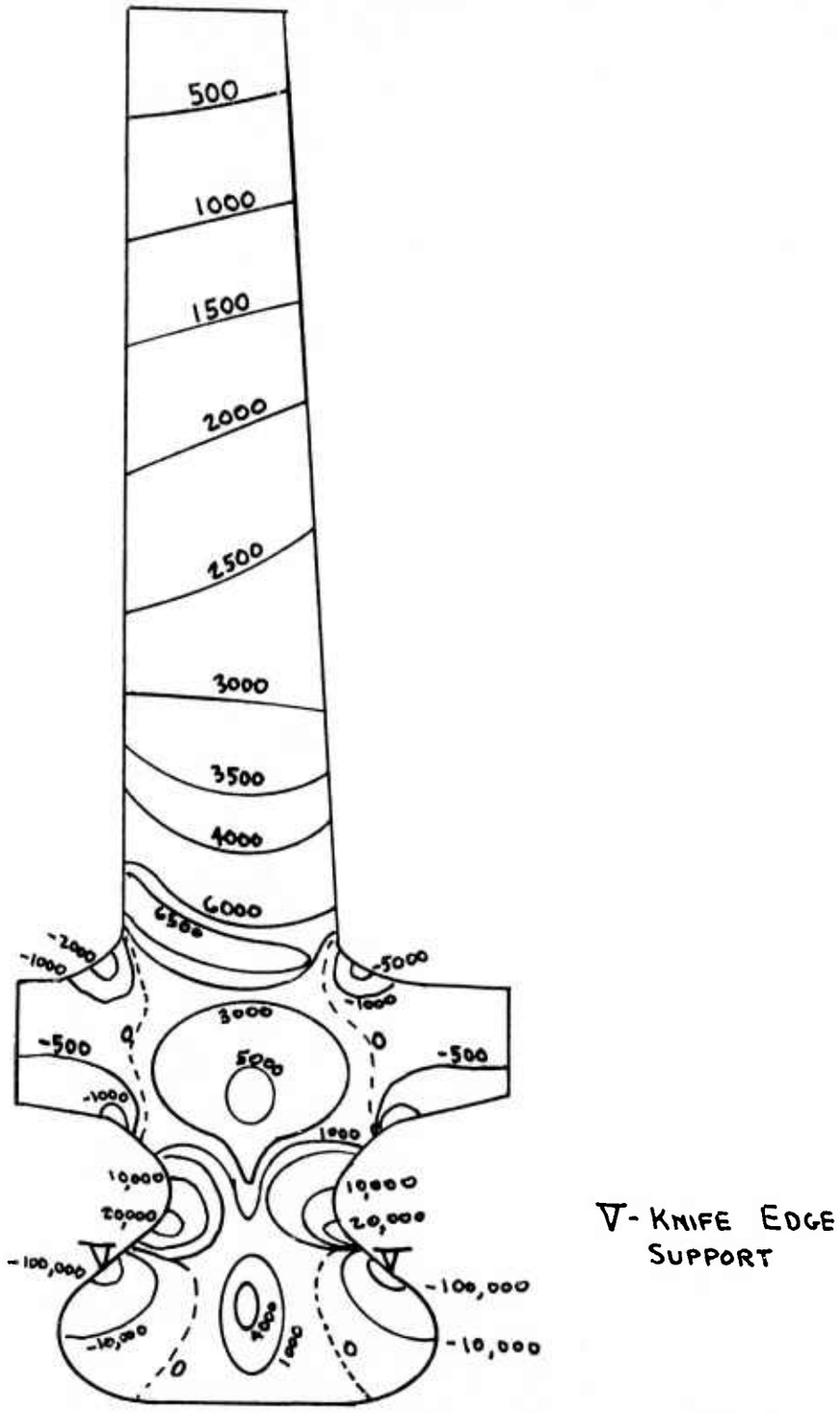


Figure 4.34 Vertical Cross Section 400, σ_z Stress Contours (psi)

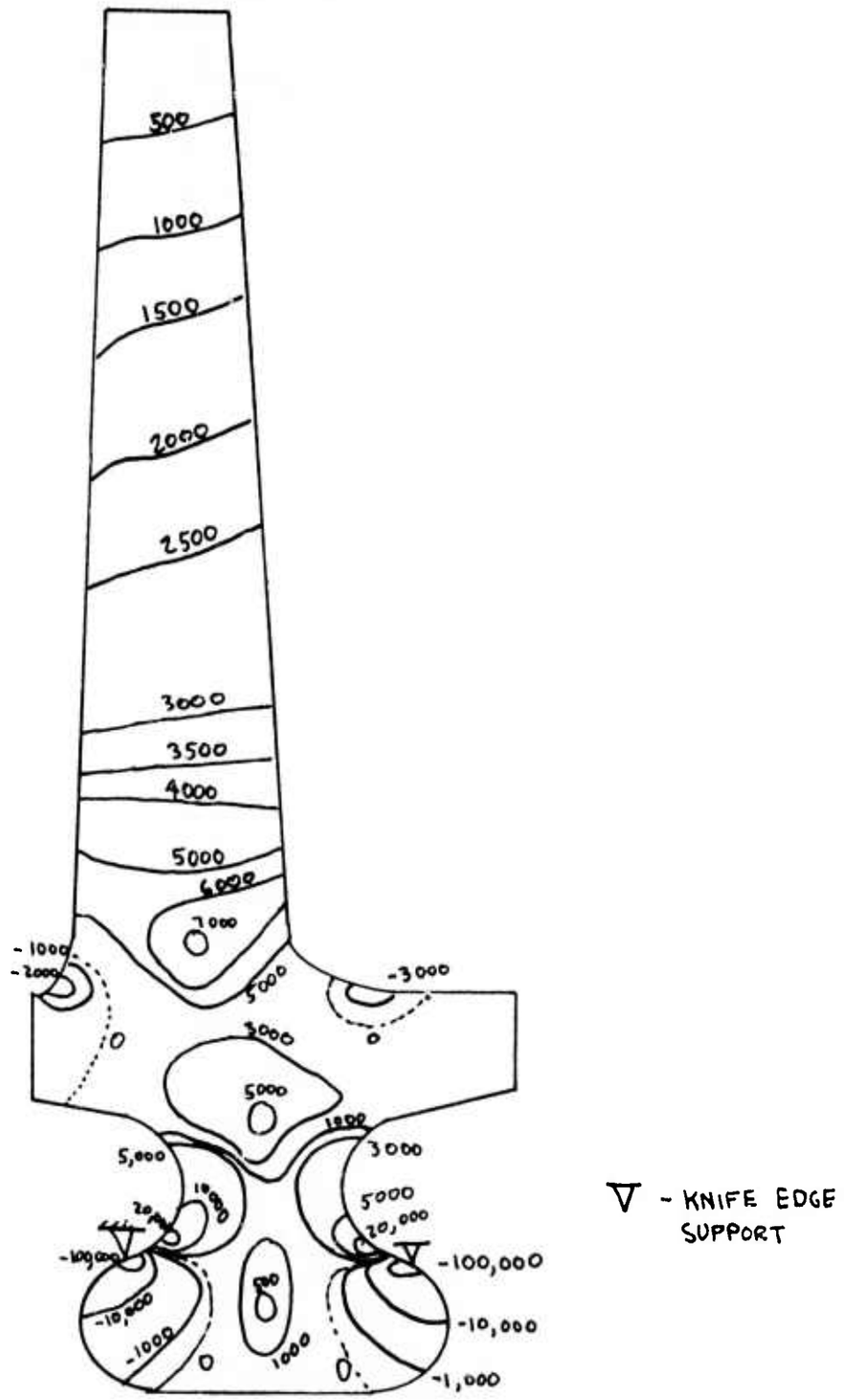


Figure 4.35 Vertical Cross Section 500, σ_z Stress Contours (psi)

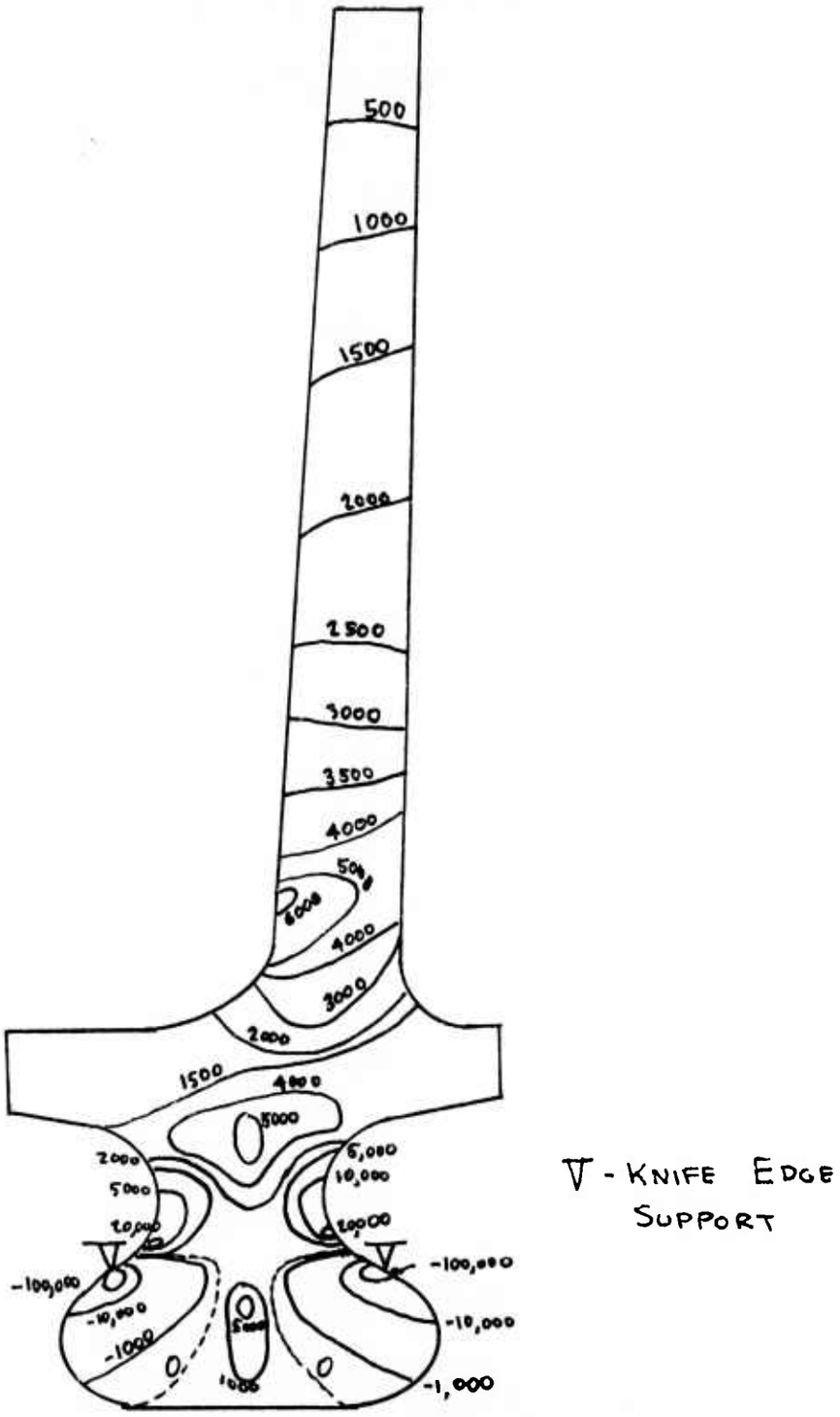


Figure 4.36 Vertical Cross Section 700, σ_z Stress Contours (psi)

5. PROGRESS ON MATERIALS TECHNOLOGY - VEHICULAR AND STATIONARY PROJECTS

5.1 MATERIALS ENGINEERING DATA

PRECEDING PAGE BLANK-NOT FILMED

SUMMARY

Design technology is highly dependent upon physical properties of the materials being used. This section deals with work performed during the reporting period on the acquisition of physical property information. Many of the materials being investigated are in the development stage and improvements in properties are anticipated; this will require that some, if not all, of the physical properties must from time to time be re-determined. Therefore, property characterization of the ceramic materials for turbine engine use is a task which will continue throughout the life span of the contract.

A comprehensive program to evaluate mechanical properties of candidate ceramic materials is underway. Flexural strength, compressive strength, and tensile fatique resistance are being determined; these tests will yield fundamental information leading to the understanding of these materials, as well as data for design purposes. Initial results of flexural strength testing indicate that reaction-sintered SiC (Refel) is similar in strength to hot-pressed materials.

Elastic properties of candidate ceramic materials are also being determined and techniques are being developed for measurements at elevated temperatures. Shear modulii vs temperature were determined for hot-pressed SiC and Si_3N_4, as well as lithium-aluminum-silicate.

The characterization of Norton HS-130 hot-pressed Si_3N_4 has progressed to the point where reliable engineering estimates of material properties have been provided. Sufficient data are available to permit statistical treatment. Additional tensile testing at elevated temperatures show some dependance upon strain rate with a general decrease in strength as temperature increases. Stress-rupture testing shows that creep deformation is apparently controlled by a grain-boundary sliding mechanism. Hot-pressed Si_3N_4 of lower purity then HS-130 displayed significantly less creep strength.

Flexural strength testing of HS-130 material at various temperatures and loading rates were performed. While some effect of load rate was noted, additional statistically significant data are needed to clarify the load rate dependence. Thermal properties of HS-130 silicon nitride were determined and reported.

Dynamic corrosion-erosion tests in the turbine passage were conducted to determine the effect of fuel contaminants on HS-130 Si_3N_4 and Norton hot pressed SiC. Average weight losses for Si_3N_4 increased from 4 to 13 mg/cm^2 after 250 hours at 2000°F when Na, S, Mg, and V were added to the fuel. Results for SiC indicated losses of 17 mg/cm^2 for contaminated as well as clean diesel fuel under similar conditions.

5.1.1 PHYSICAL PROPERTIES OF CERAMIC MATERIALS

Introduction

The comprehensive program to evaluate the mechanical and thermal properties of many varieties of silicon nitride, silicon carbide, and lithium aluminum silicate in gas turbine applications is continuing. These data not only contribute valuable fundamental information about the materials but also are considered essential to an optimum design with brittle materials in order to provide the maximum safety factor. All of the candidate materials have been improved significantly. Since the potential for greater improvement exists, the Material Engineering task is expected to continue for the full term of the turbine project.

The characterization of Norton HS-130 silicon nitride has progressed to the point where reliable engineering estimates of both the mechanical and thermal properties of the material have been provided for stator vane design and stress analysis. Sufficient data are now available to permit initial statistical treatment. The application of Weibull theory, and an analysis of variance as related to size effects and billet variability are discussed.

Preliminary physical property data for Norton hot pressed silicon carbide are reported.

Statistical Aspects of Mechanical Responses

The flexural strength of silicon nitride measured in 4-point bending, is twice that of the tensile strength under similar conditions of temperature and loading rate. This difference may be due to the mode of testing or it may indicate that strength is dependent upon the actual area or volume under tensile stress as predicted by Weibull statistics. The stationary turbine program relies heavily upon flexural tests to provide strength data for design and stress anslysis. Tensile tests, however, are used to verify the predicted results. In the event that the Weibull theory does not apply, sufficient data points are provided in the test program to analytically correlate tensile with flexural strength.

The statistical test plan was adopted to provide property data at a 0.95 confidence level from a minimum of 10 specimens per condition. All pertinent physical and thermal properties, including tensile, flexural, compression, shear, thermal expansion and conductivity together with creep and high and low cycle (thermal) fatigue will be determined across 10 billets to characterize 4C. Billet to billet variations and property variations across particular billets are being determined with respect to flexural strength only. Specimen size, strain rates, directionality, and temperatures were selected to provide a minimum of 30 degrees of freedom within each test matrix. Even with this, additional testing may be required to achieve the level of significance desired. A statistical evaluation of all accumulated data is expected to define data deficiencies.

The test matrices for flexural and tensile strength determinations are included as Tables 5.1 and 5.2, respectively, to illustrate the testing philosophy. The 20 specimens per test condition occasionally observed in flexural testing permitted computation of Weibull modulus for Si_3N_4 early in the test program.

A large number of flexural samples are required to determine the Weibull parameters at 1800 and 2300°F. These tests will also be used to establish the failure mode and the effect of impurities. Specimens are taken from at least 10 billets to assure that billet to billet

Table 5.1

Flexural Failure Tests/Billet

Temperature, (°F)	Specimens/Condition: Cross Rate (in/minute) 0.02[1]	0.002	0.0002[1]	Directions
RT	5	20[2]	5	2[3]
1000		10		strong
1800	5	10	5	2
2100		10		strong
2300	5	20[2]	5	2
2500		10		

1. Strain rate effects to be determined on 3 billets only
2. To provide Weibull modulus for 1st billet at .90 confidence level
3. Strong direction $\perp$ to hot press, weak $\parallel$ to hot press direction

NOTE: Weibull modulus in both directions will be determined across 10 billets from data provided at 0.99 confidence level

variations are determined. The Weibull characterization of the risk of failure with respect to volume given by

$$\int \left(\frac{\sigma-\sigma_u}{\sigma_o}\right)^m dV$$

has been utilized with σ_u set equal to zero. Weibull modulus is m, σ_o is the normalizing stress and σ_u is a value of stress below which no failures are expected. All three are material constants which should not vary with the mode of test. To determine the dependence of strength upon area, the integral with respect to volume is replaced by an integral with respect to area.

Table 5.2

Tensile Tests

(Samples Randomly Selected from 10 Billets)

	Specimens[1]/Condition		
	Strain Rate (in/in/minute)		
Temperature °F	0.01	0.001	0.0002
RT	5	10	5
1000		10	
1800	5	10	5
2100		10	
2300	5	10	5
2500		10	

1. Strong direction only (specimen cannot be prepared for weak direction from 1.25 in. thick billets)

NOTE: Elastic modulus determined from strain measurements.

The area and volume dependent probabilities are plotted in Figs. 5.1 and 5.2, respectively. Once the area or volume under critical stress is determined for the stator vane, it will be possible to predict the survival probability under emergency shutdown conditions from the appropriate curves. Available data indicate that the Weibull area integral is more appropriate for predicting tensile strength at room temperature, while the volume integral appears to be more accurate at 2500°F.

Tensile Strength

The tensile strength of Si_3N_4 was measured using specimens of different sizes (Fig. 5.3). Twenty two tests were conducted in helium using graphite grips and load train. Tests at 1800, 2100 and 2300°F used 3 inch specimens with 1.50 in. gauge length of 0.147 in. diameter cross section so that the 750 lbs capacity of the load train would not be exceeded. Specimens for tests at 2500°F were similar except for the cross section of the gauge length which increased to 0.25 in. diameter. Some of these specimens were tested at 2300°F for comparative purposes. A cross head rate of 0.001 in/in/min was employed for the most part. Strain rate sensitivity was studied by testing at .00018 and .010 in/in/min at 1800 and 2300°F.

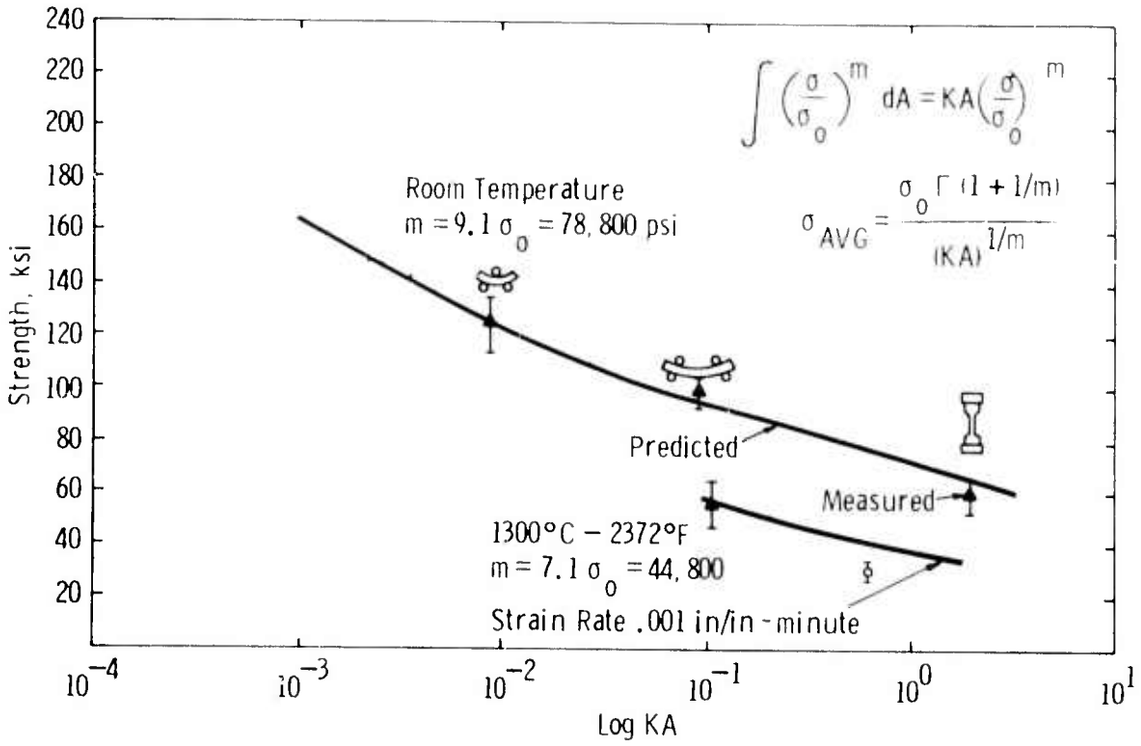


Figure 5.1 Predicted and Measured Failure Stress of Hot Pressed Silicon Nitride for Various Test Modes (Two Parameter Weibull Theory Based on Area)

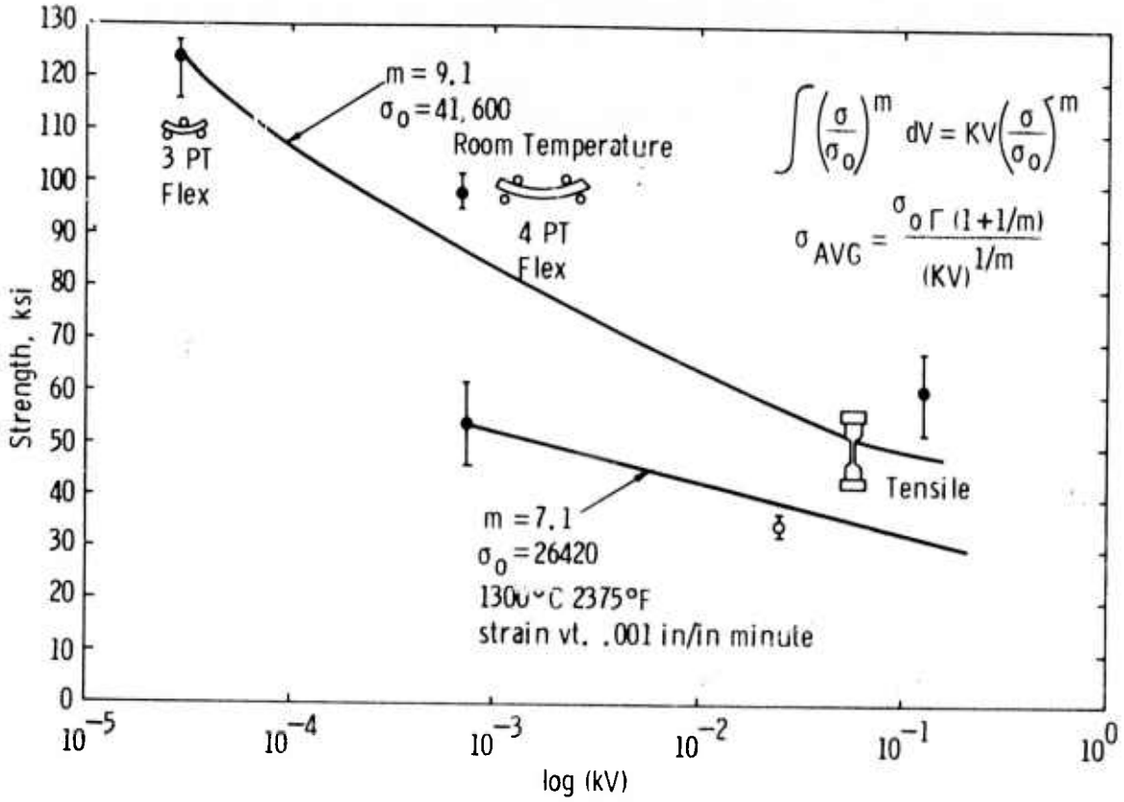


Figure 5.2 Average Failure Stress for Hot Pressed Silicon Nitride for Various Test Modes as Predicted by Two Parameter Weibull Theory Based on Volume

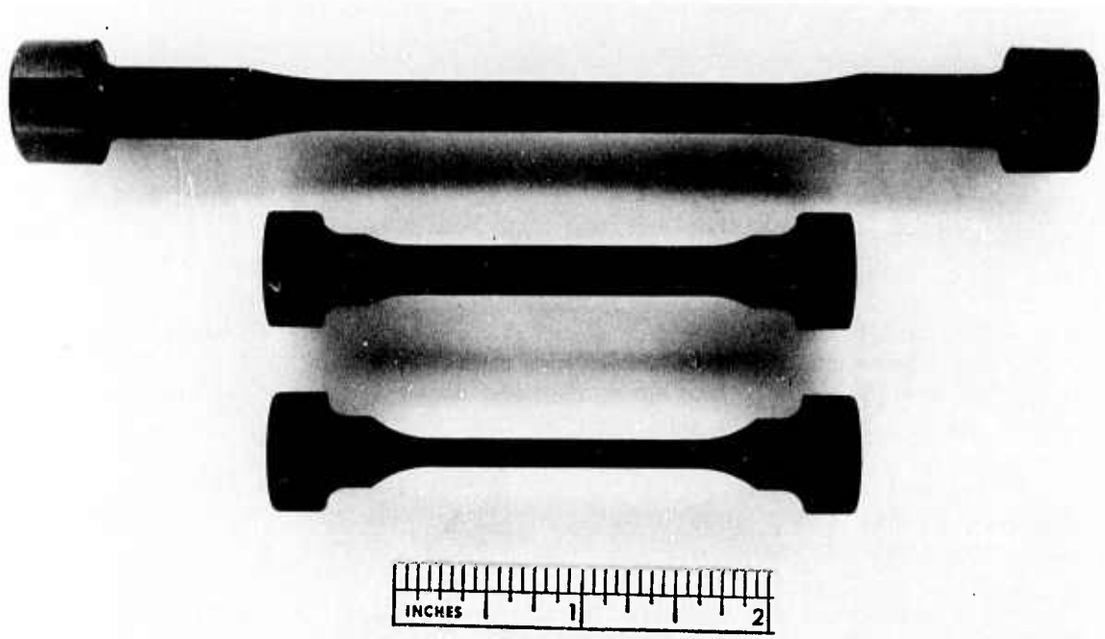


Figure 5.3 Tensile Specimens

Tensile tests were also conducted in air. In this case, a KT silicon carbide load train with HS-110 Si_3N_4 grips was used, with a specimen of 5.5 inch length with 2.50 in. gauge length and 0.25 in. diameter. Comparative tests were made using the 3 in. specimen with a 0.25 in. diameter.

The results are plotted independently in Fig. 5.4. While some strain rate sensitivity was observed, the effects of atmosphere and specimen size are considered negligible. Upon cooling a vane from 2500°F, a maximum transient thermal stress of 41,000 psi is expected to develop at 1800°F with a strain rate approaching 0.001 in/in/min. The reported strength of 42,500 psi under these conditions lies marginally above the requirement.

The modulus of elasticity was also measured as part of the tensile test program. Figure 5.5 shows Young's Modulus versus temperature measured by several methods. The highest values were determined ultrasonically by Corning and reported by Ford. Since the middle curve reflects the .001 in/in/min strain rate, it is considered to be the most appropriate for the gas turbine condition.

Preliminary data indicate that the tensile strength of Norton hot pressed silicon carbide is 26,200 psi at 2300°F (0.001 in/in/min strain rate).

Creep of Hot Pressed Si_3N_4

Stress rupture tests were made on Norton HS-110 Si_3N_4 at 2100°F, and Norton HS-130 Si_3N_4 at 2300° and 2500°F, respectively. These tests were conducted in a helium atmosphere using cylindrical specimens, 2-3/4 in. long with 1/4 in. gauge diameter and 1-3/4 in. gauge length. Gripping is accomplished by a ball-and-socket arrangement, where all parts are made of graphite. The specimens were placed in an induction furnace capable of providing a uniform 3 in. long hot zone at the maximum test temperature of 2500°F. The furnace and specimen assembly were placed in an Instron machine, where a constant load is maintained automatically. Specimen elongation was measured by an LVDT attached to the bottom ram of the machine. Good agreement was obtained for all samples tested between the elongation measured on the machine and that measured from the fractured specimens.

The results of the stress rupture tests are plotted in Fig. 5.6. Although these data are not yet considered statistically significant; they relate in the following manner to the operating requirements of vanes in the stationary gas turbine:

(1) Under design conditions of 5000 psi steady state gas bending stress and 10,000 hours operating schedule, HS-130 grade Si_3N_4 does not have adequate creep strength at 2500°F.

(2) For the same load and time conditions, HS-130 grade Si_3N_4 does have the required creep strength at 2300°F.

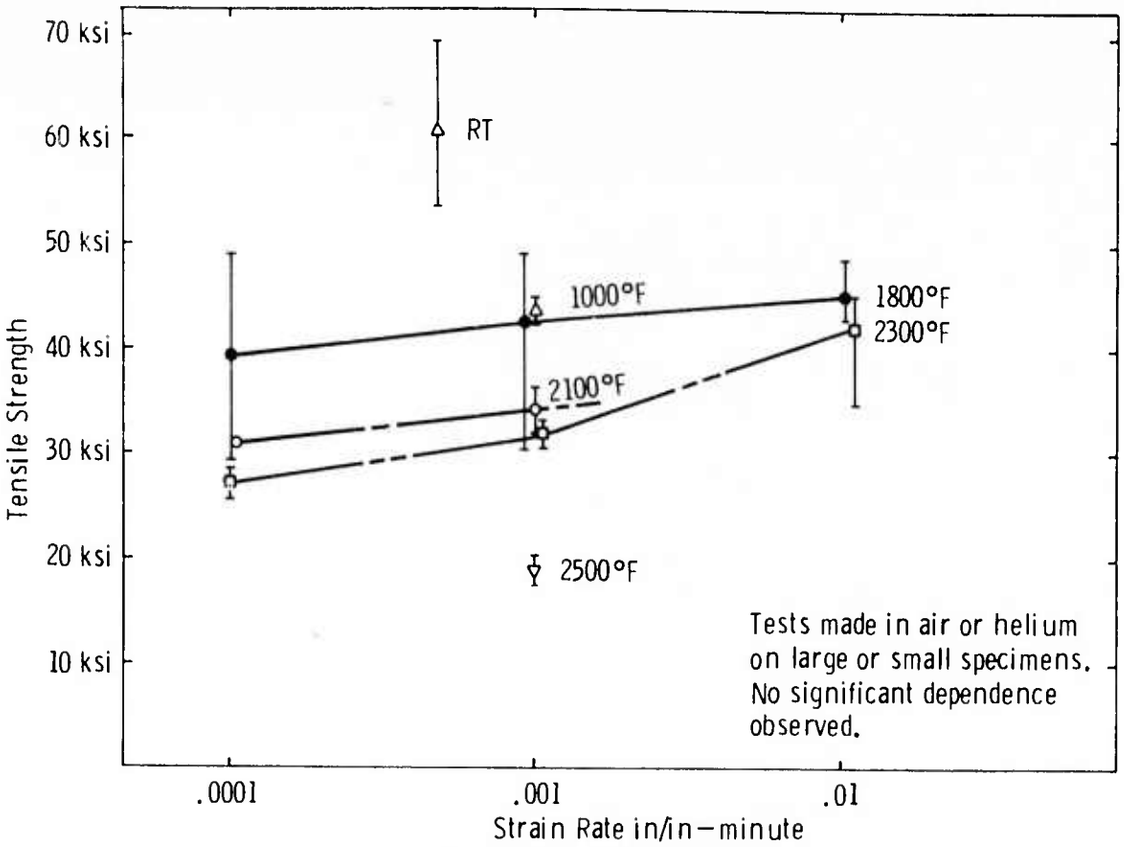


Figure 5.4 Tensile Strength as a Function Temperature and Strain Rate for Hot Pressed Silicon Nitride

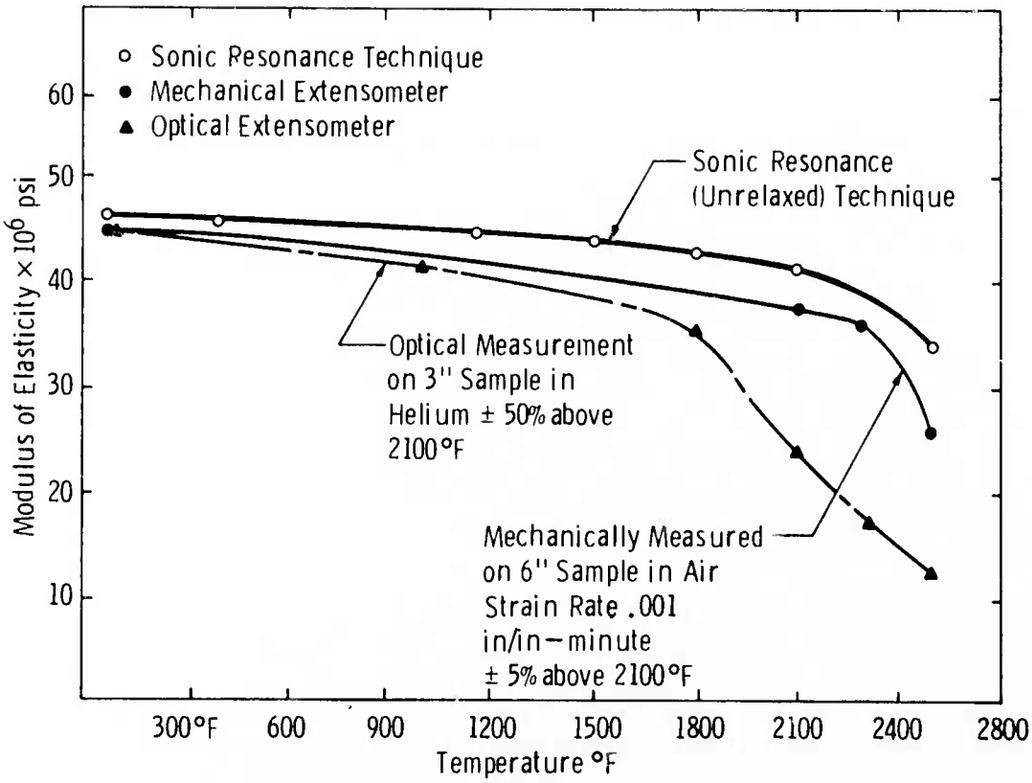


Figure 5.5 Young's Modulus as a Function of Temperature for Silicon Nitride by Various Methods

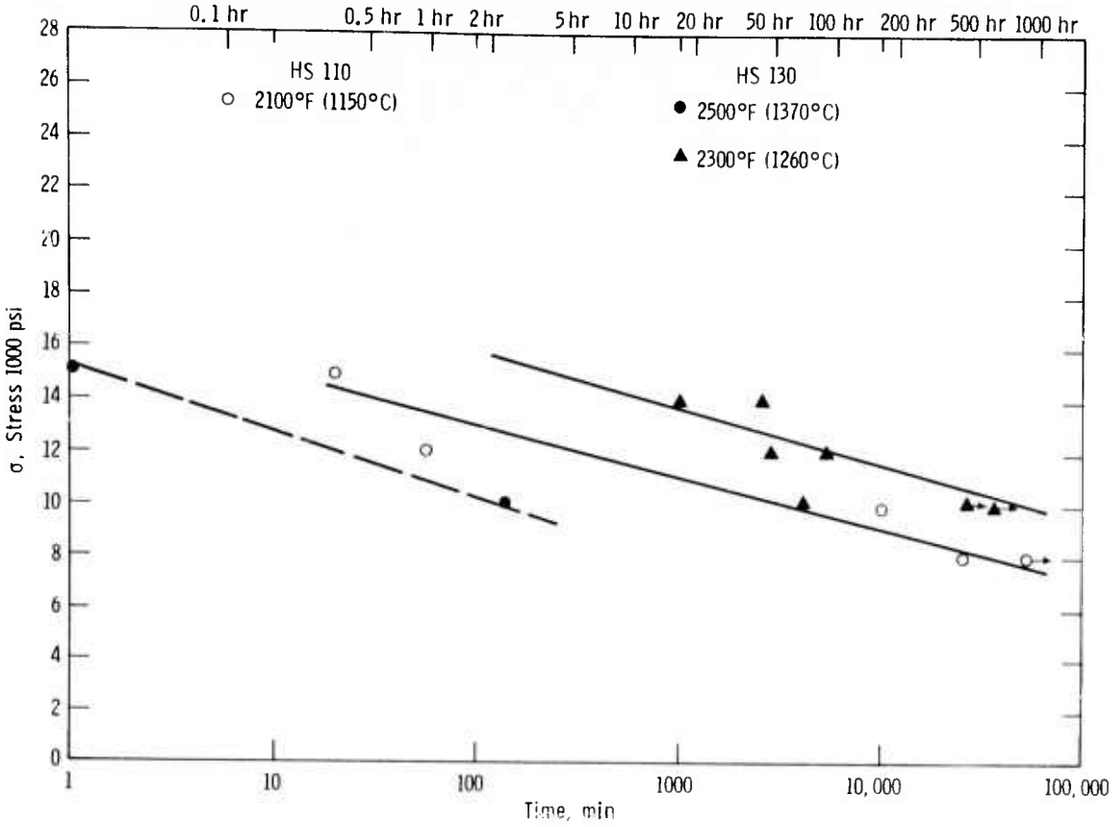


Figure 5.6 Stress-Rupture Properties of Silicon Nitride He Atmosphere

In addition, it may be seen that the impurity level (particularly Ca) has a major effect on the creep strength of Si_3N_4. Figure 5.6 shows that the creep strength of the HS-110 material at 2100°F is lower than the creep strength of the HS-130 material at 2300°F. The steady state creep rate of Si_3N_4 is plotted as a function of inverse temperature for three impurity levels (Fig. 5.7). Assuming the steady state creep rate can be expressed by a generalized Arrhenius equation, similar to the well established practice in metallic materials, activation energies for creep (ΔH)can be obtained.

Figure 5.7 shows ΔH = 150 Kcal/mole for HS-130 Si_3N_4 at 10,000 psi within the range of 2300°F and 2500°F; and ΔH = 130 Kcal/mole for the HS-110 material at 10,000 psi in the temperature range of 2050°F to 2150°F.

Creep deformation in hot pressed Si_3N_4 is apparently controlled by a grain-boundary sliding mechanism. The viscosity of the boundary glassy phase is a dominating factor when the mechanical strength of the material is considered, particularly at elevated temperatures. The activation energy data are consistent with these observations.

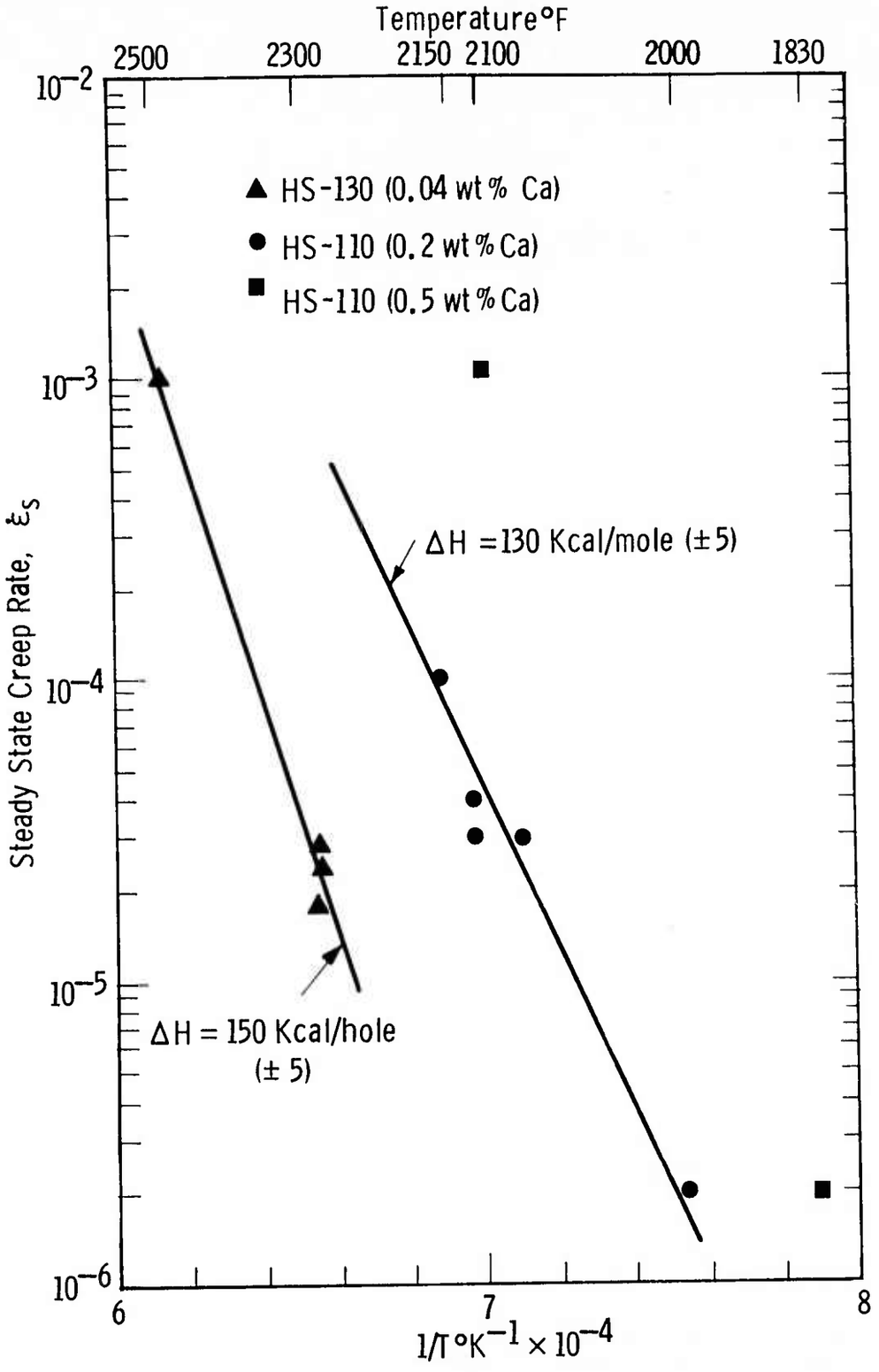


Figure 5.7 Steady State Creep Rate vs 1/T at, 10,000 psi, in He Atmosphere

Rosin, et al.[3] measured the viscosities and the activation energies for viscous flow of SiO_2, and of CaO and Al_2O_3 doped SiO_2. Their data on the activation energies for viscous flow of pure SiO_2 are shown in curve A, Fig. 5.8. As discussed in Section 5.2.2, of this report, the boundary glass phase in HS-130 Si_3N_4 contains about

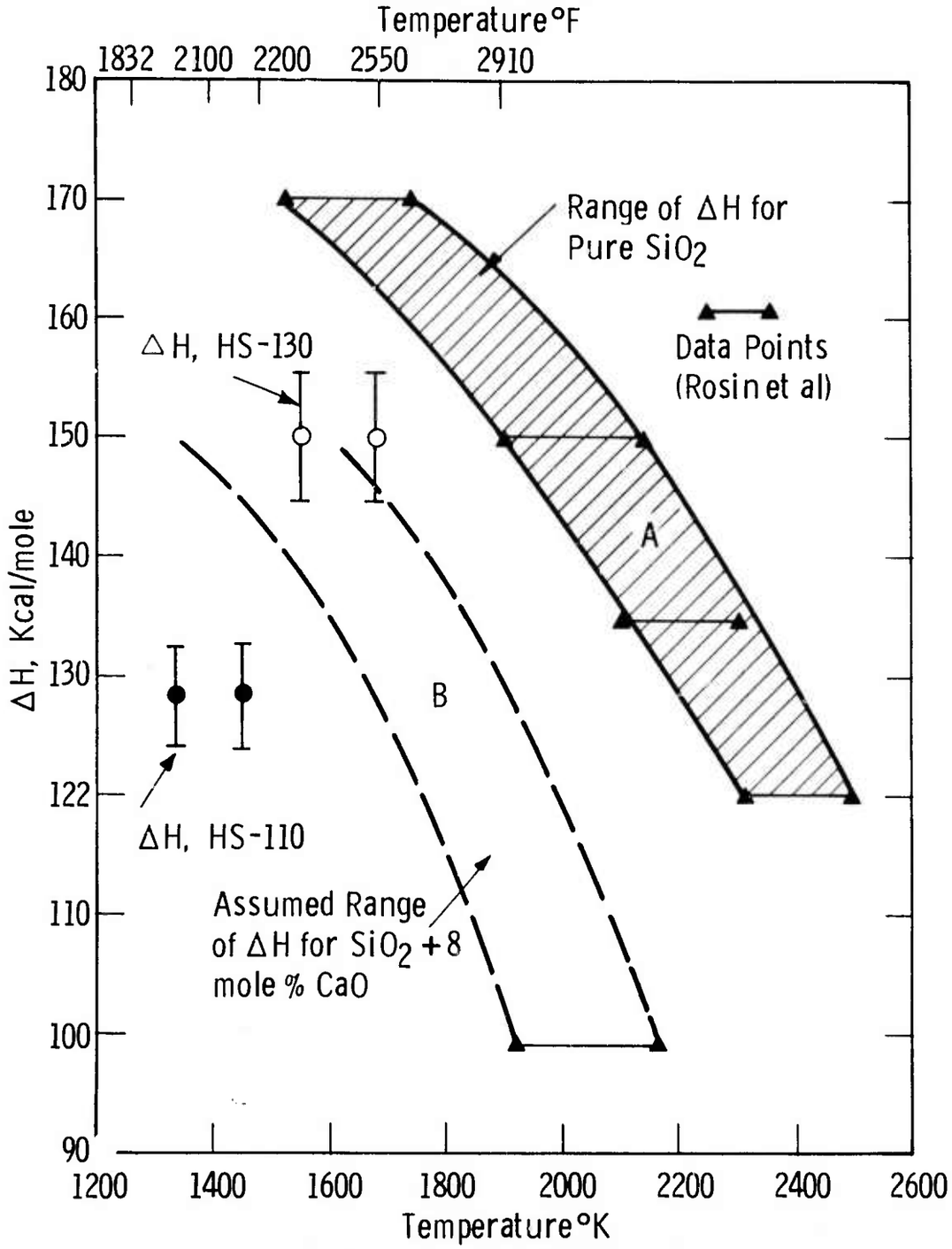


Figure 5.8 Activation Energy for Viscous Flow (for SiO_2, and CaO Doped SiO_2)

12 mole % CaO. If the temperature dependence of ΔH for viscous flow of SiO_2 plus 8 mole % CaO is assumed to be similar to that of pure SiO_2, curve B of Fig. 5.8 can be constructed from the single data point given by Rosin, et al., for this glass composition at the temperature range of 1900 to 2200°K. It now becomes apparent that there is good agreement between the activation energies for creep of Si_3N_4 and the activation energy for viscous flow of a CaO doped SiO_2. This agreement, and the very strong effect of Ca on the creep rate under given conditions of temperature and stress suggest that the creep behavior of Si_3N_4 is controlled mainly by the properties of the boundary glass phase.

Flexural Strength

The flexural strength of Norton HS-130 hot pressed silicon nitride was measured at Westinghouse in 4-point loading (outer span = 0.875 in., inner span = 0.375 in.) with a fixture made of hot pressed silicon nitride. The specimen dimensions were 0.125 x 0.250 x 1.25 inches long. All samples were ground parallel to length on four sides with a 320 grit wheel to insure a uniform surface finish. All tests were conducted in air.

The results of 150 flexural strength tests under conditions of 4-point loading are reported in Figs. 5.9 and 5.10. These tests were designed to establish the strength of silicon nitride, and also to determine the effect of loading rate, temperature, and direction. As

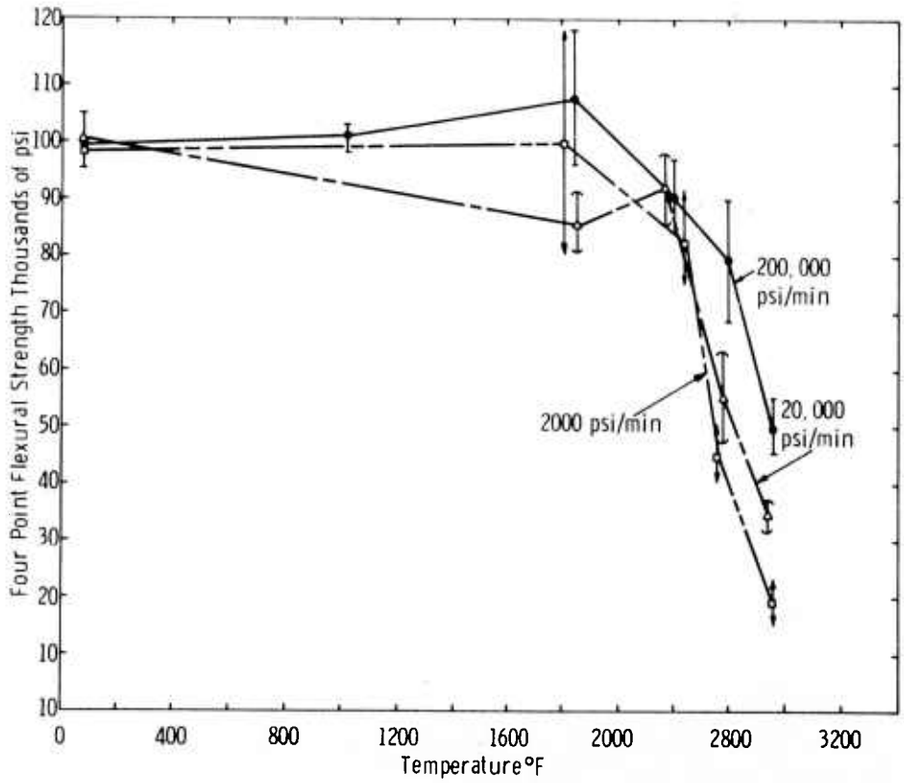


Figure 5.9 Four Point Flexural Strength of Hot Pressed Silicon Nitride vs Temperature for Various Average Loading Rates

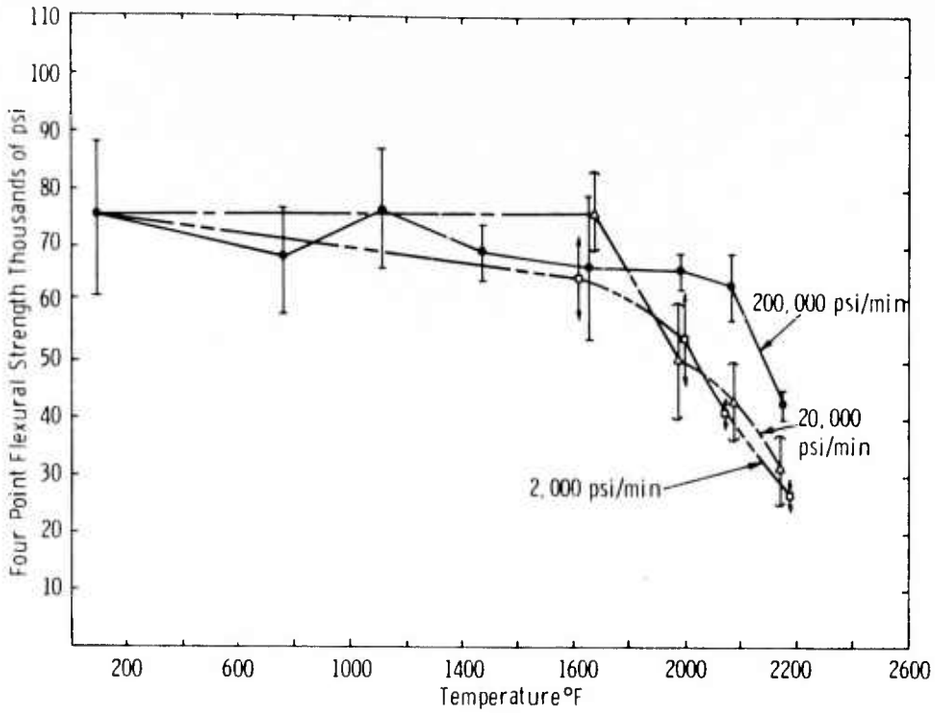


Figure 5.10 Four Point Flexural Strength of Hot Pressed Silicon Nitride Temperature for Various Average Loading Rates

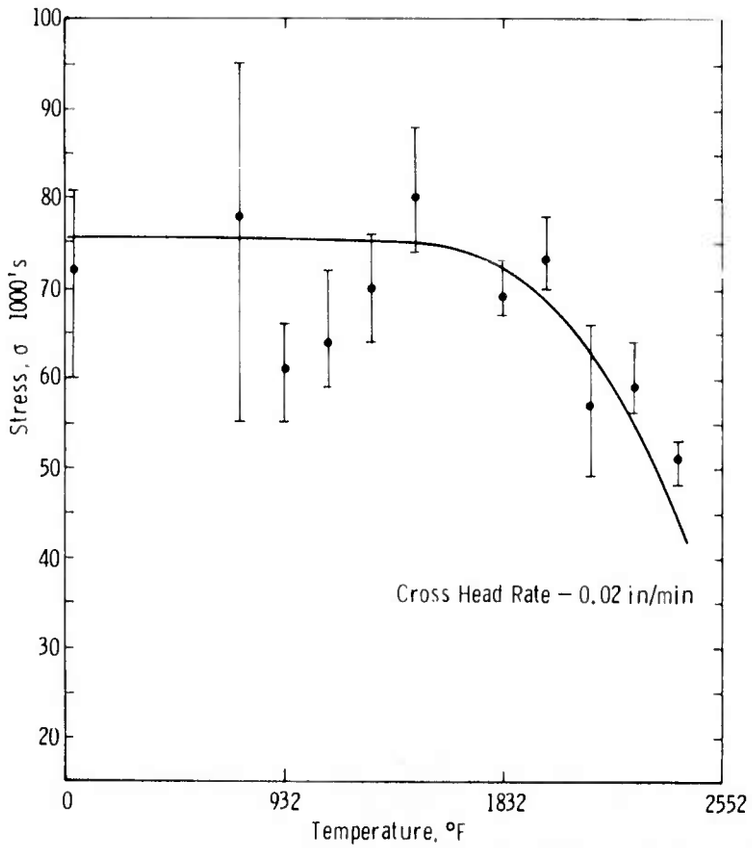


Figure 5.11 Flexural Strength of Hot Pressed Silicon Carbide

statistically significant data become available, the load rate dependence will become clearer. A minimum of 10 samples are used for each set of conditions. A minimum of 360 tests are required to evaluate three loading rates at six temperatures for ten billets of Si_3N_4.

Preliminary data for Norton hot pressed silicon carbide are reported in Fig. 5.11. The large scatter in these flexural strengths make it difficult to establish whether this material shows anisotropic properties or a strain rate sensitivity. In general, its strength appears to be roughly equivalent to HS-130 silicon nitride.

Additional work on determining the flexural strength of SiC and Si_3N_4 was performed at Ford up to 1800°F. The design of the test samples and the loading method is shown in Fig. 5.12. Comparison of the results of this work with those previously reported[1] are found for Norton HS-130 silicon nitride in Fig. 5.13 and for Norton hot-pressed silicon carbide and the "Refel" silicon carbide in Fig. 5.14. "Refel" SiC is being evaluated as a candidate turbine material; test samples were obtained from the United Kingdom Atomic Energy Authority, Springfields, England.

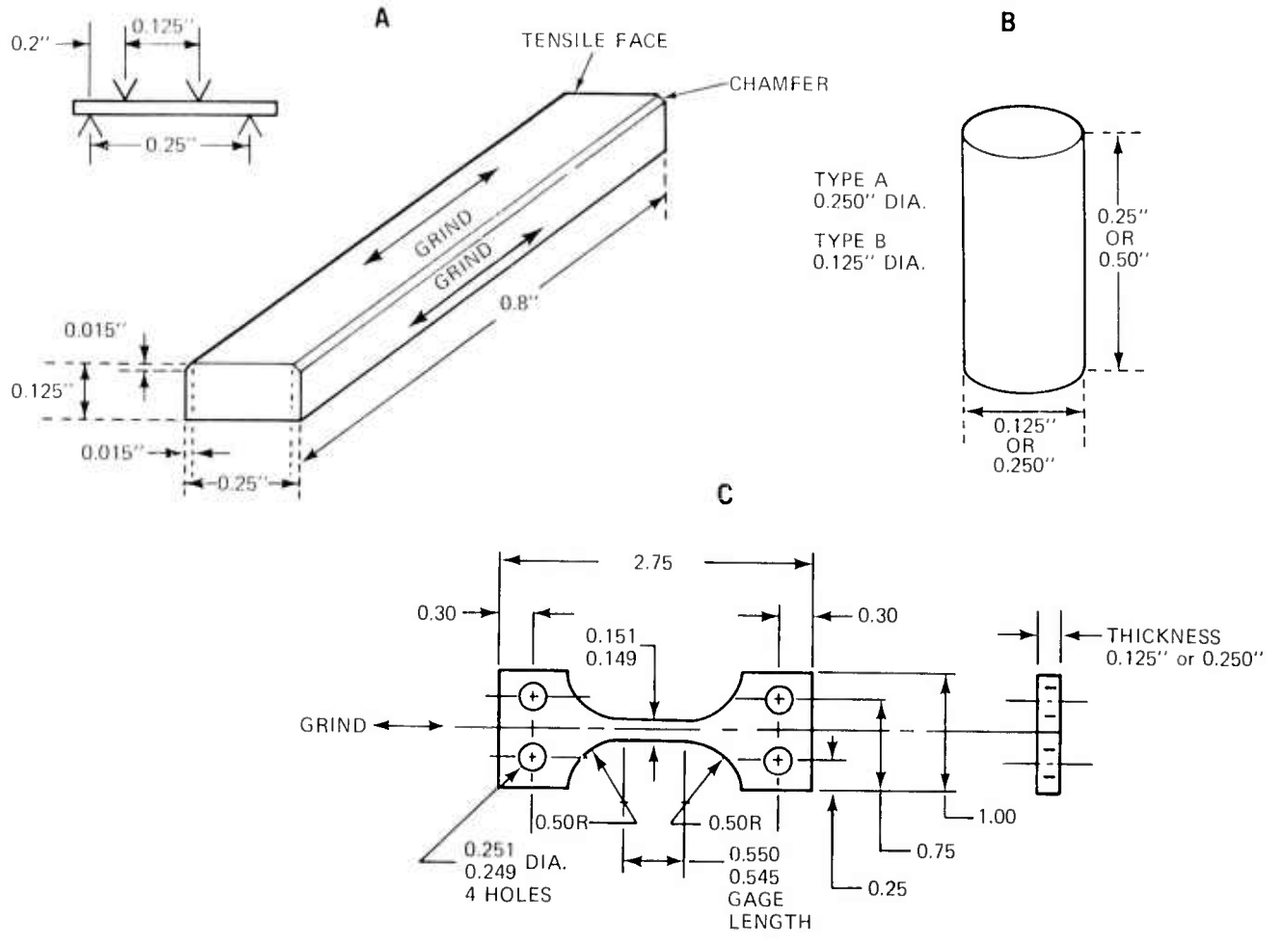


Figure 5.12 All Ground Surfaces Finished with 220 Grit

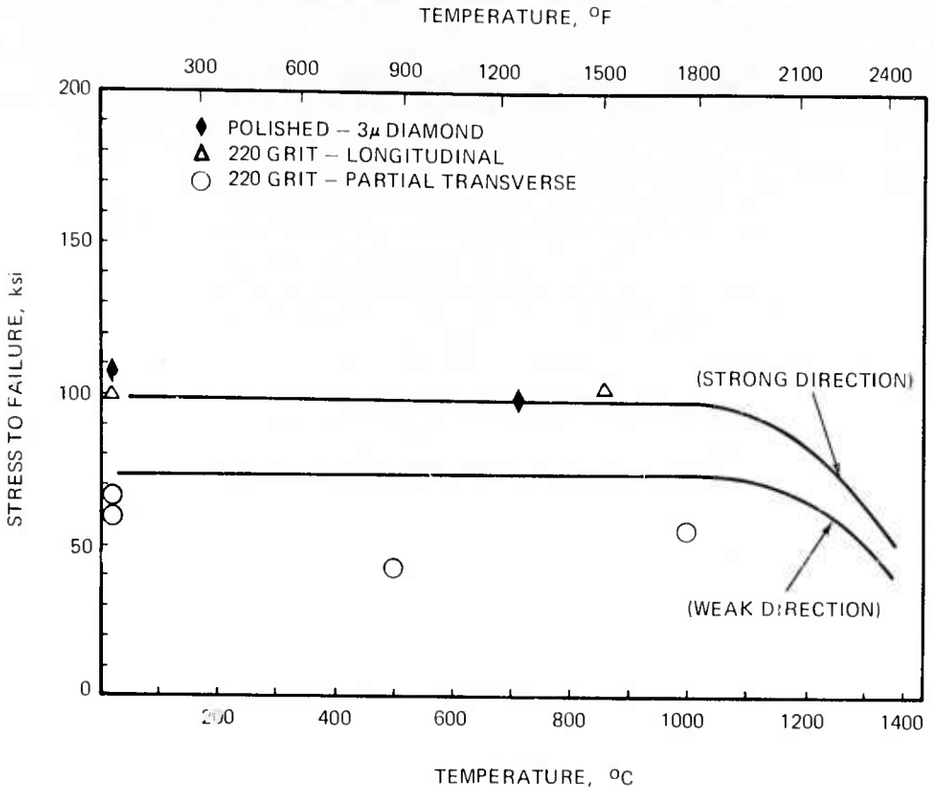


Figure 5.13 Flexural Strength of Hot Pressed Silicon Nitride

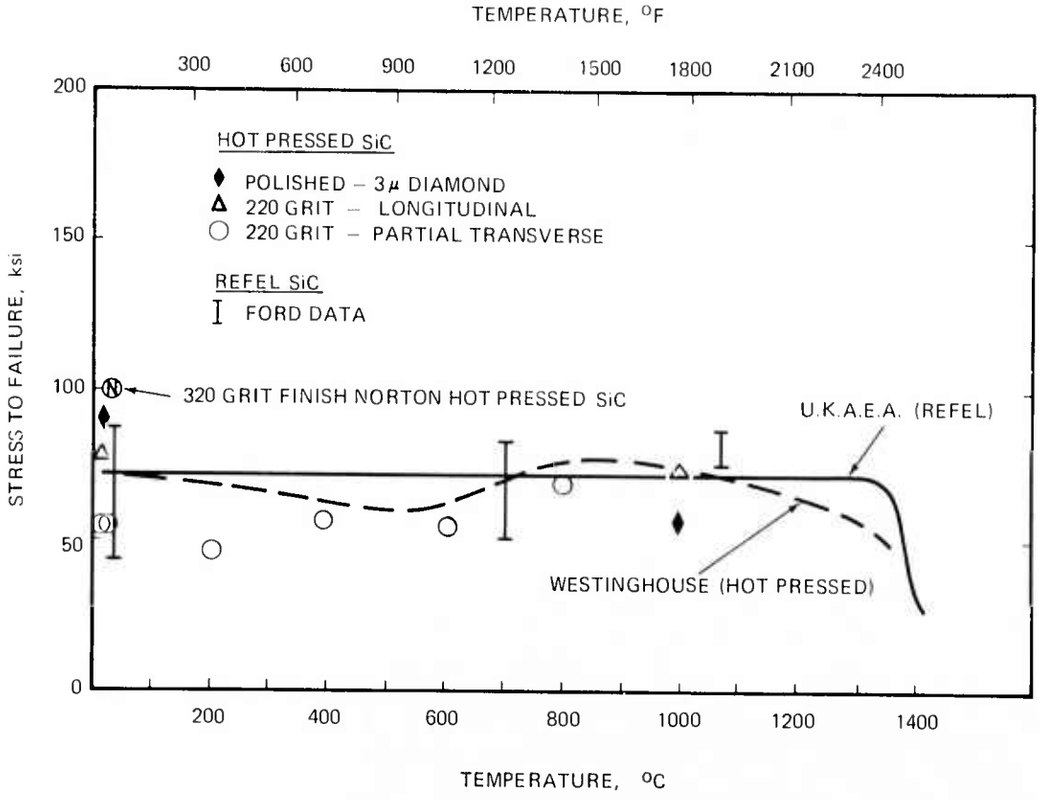


Figure 5.14 Flexural Strength of Silicon Carbide

The significance of the comparison is two-fold. First, where the surface preparation of the bend specimens was as good as (surface ground longitudinal with 220 grit diamond) or better than (polished with 3 μ diamond) the specimens with which the comparison is made, the values of flexural strength compare closely with the data of others and attest to the validity of the specimen design and to the usefulness of comparisons to be made in the future. Second, in the cases where some transverse scratches (220 grit) were introduced by grinding in the chamfered part of the bend specimen, the flexural strengths were correspondingly lower. However, the effect of these scratches was more marked in the case of silicon nitride. When observing the silicon nitride results, it is important to note that the specimens were always cut from the hot pressed material so that the longitudinal axis was perpendicular to the pressing direction (designated the strong direction[1]. In all cases, the lines representing the work of other investigators[1,4] should include an error band of usually no less than ± 10 ksi. The hot-pressed silicon carbide data and the initial results on the "Refel" silicon carbide indicate that the "Refel" process is capable of producing a material which is competitive with the hot-pressed material. While flexural strengths clearly tend to improve with surface finish, the relative sensitivity of the carbide as compared to the nitride is worth further consideration. Continued investigation will no doubt reveal in what way scratches are related to the crack propagation process which was observed to be typically intergranular in the hot-pressed silicon nitride and transgranular in the hot-pressed silicon carbide.

Compressive Strength

Compressive strength of Si_3N_4 exceeds 450,000 psi at room temperature as measured on a standard load frame using 1 inch long x 3/8 inch diameter specimens loaded between KT silicon carbide platens. A compressive creep test at 100,000 psi and 2300°F was run on the same apparatus. Results indicated less than 1/2% strain after 500 hours. The strain vs time curve is shown in Fig. 5.15.

Thermal Properties

The thermal conductivity, diffusivity and expansion measurements of Si_3N_4 as a function of temperature and hot pressing direction were completed at the Battelle Memorial Institute using the flash diffusivity and optical methods described in the last report.[1] The results are presented in Figs. 5.16 through 5.21. Preliminary data for hot pressed SiC (heat flow parallel to the hot press direction) are given in Fig. 5.22. Further tests are underway to measure these properties in the perpendicular direction.

Thermal stresses large enough to fail a specimen under well controlled conditions are being investigated. A centrally heated hollow cylinder with a notch for a stress riser (Fig. 5.23) is undergoing analysis using finite element computer codes. The stress for a measured temperature gradient was computed and the correlation between geometry, thermal gradient, and strength was determined. A Weibull statistical treatment will also be applied to these data.

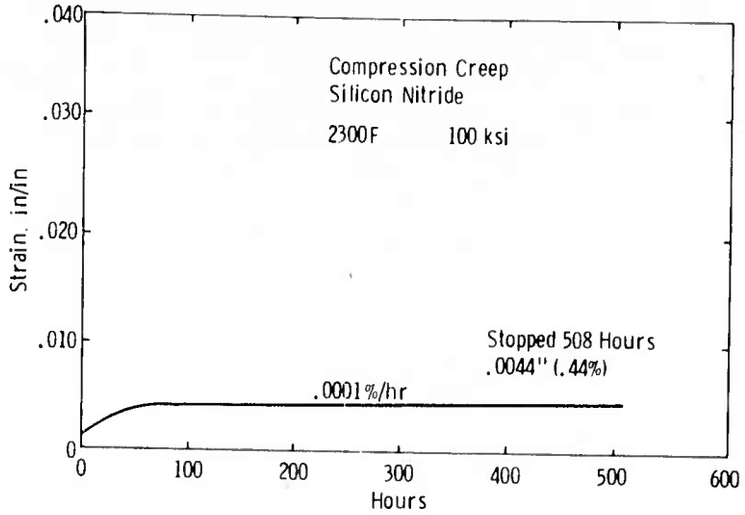


Figure 5.15 Compressive Creep of Silicon Nitride

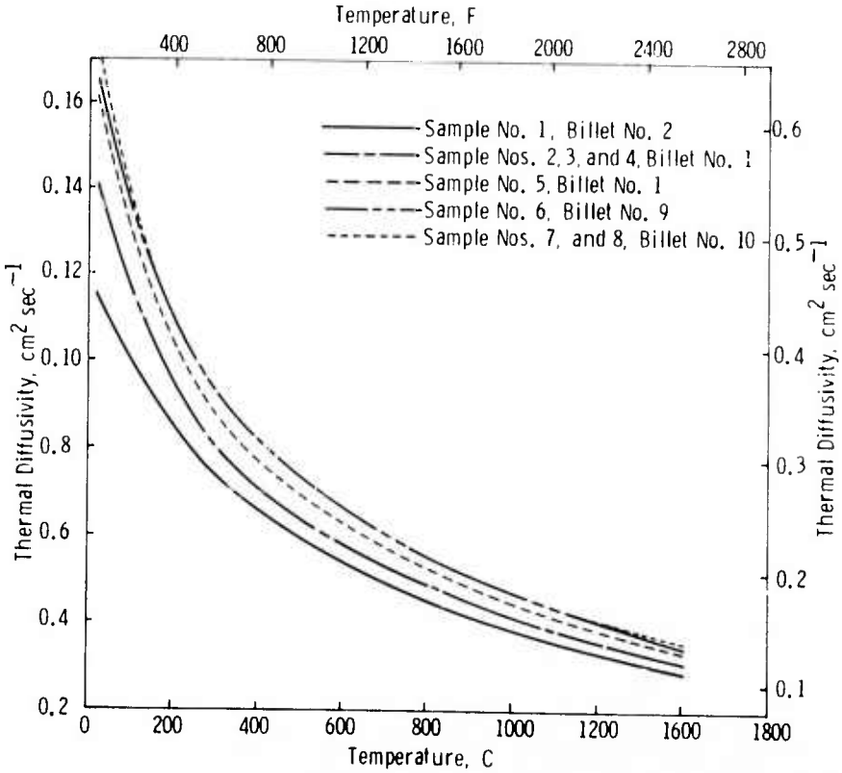


Figure 5.16 Comparison of Thermal Diffusivity Values for Heat Conducted Parallel to the Hot Pressing Direction in Silicon Nitride

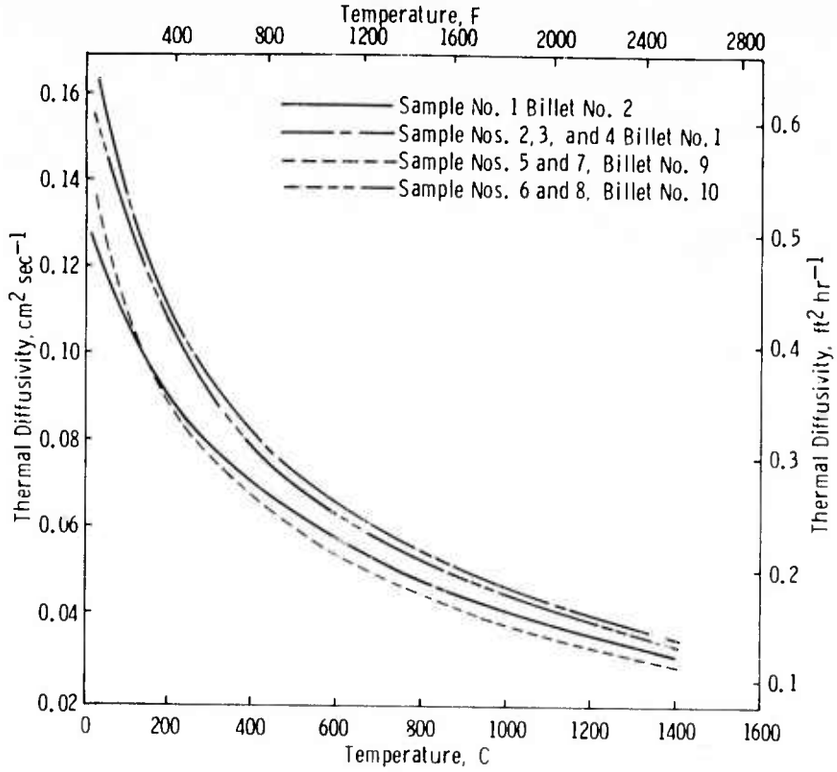


Figure 5.17 Comparison of Thermal Diffusivity Values for Heat Conducted Perpendicular to the Hot Pressing Direction in Silicon Nitride

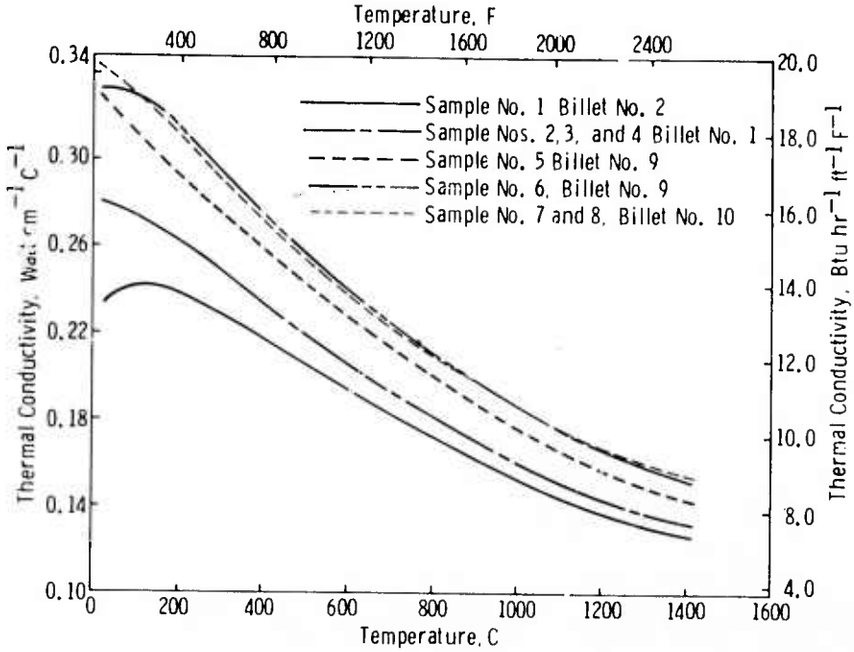


Figure 5.18 Comparison of Thermal Conductivity Values for Heat Conducted Parallel to the Hot Pressing Direction in Silicon Nitride

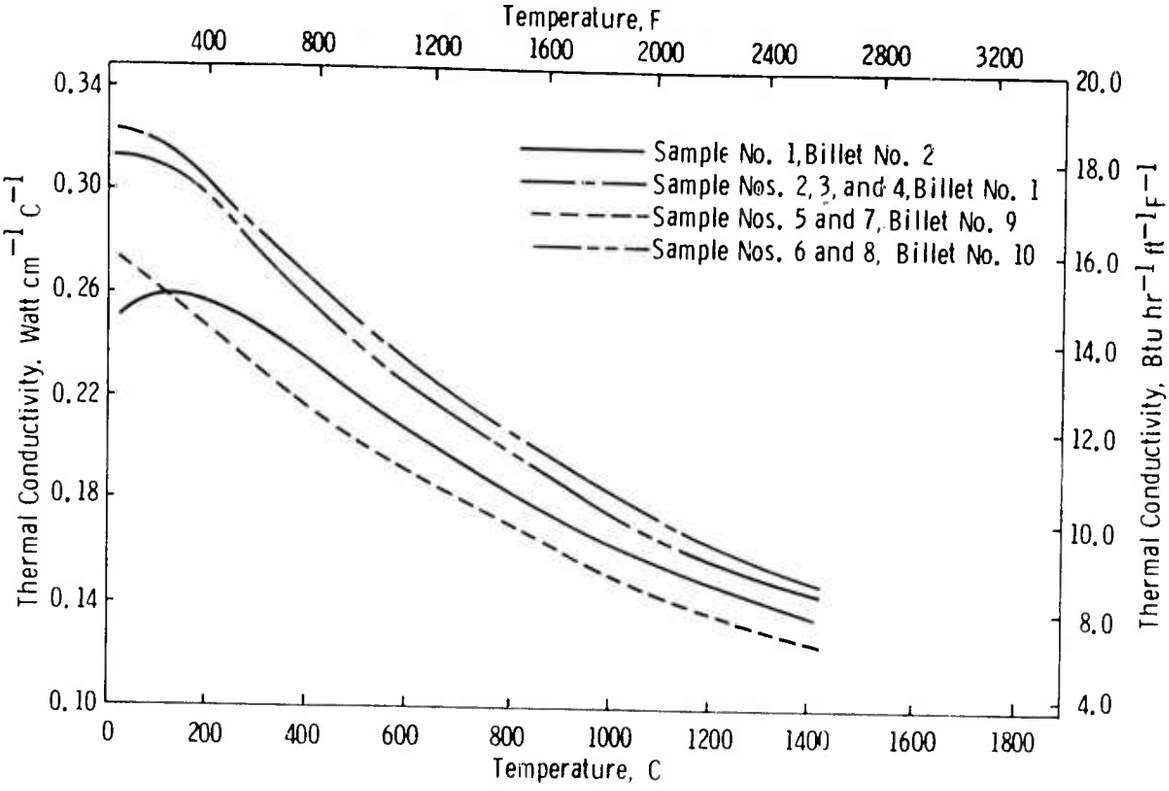


Figure 5.19 Comparison of Thermal Conductivity Values for Heat Conducted Perpendicular to the Hot Pressing Direction in Silicon Nitride

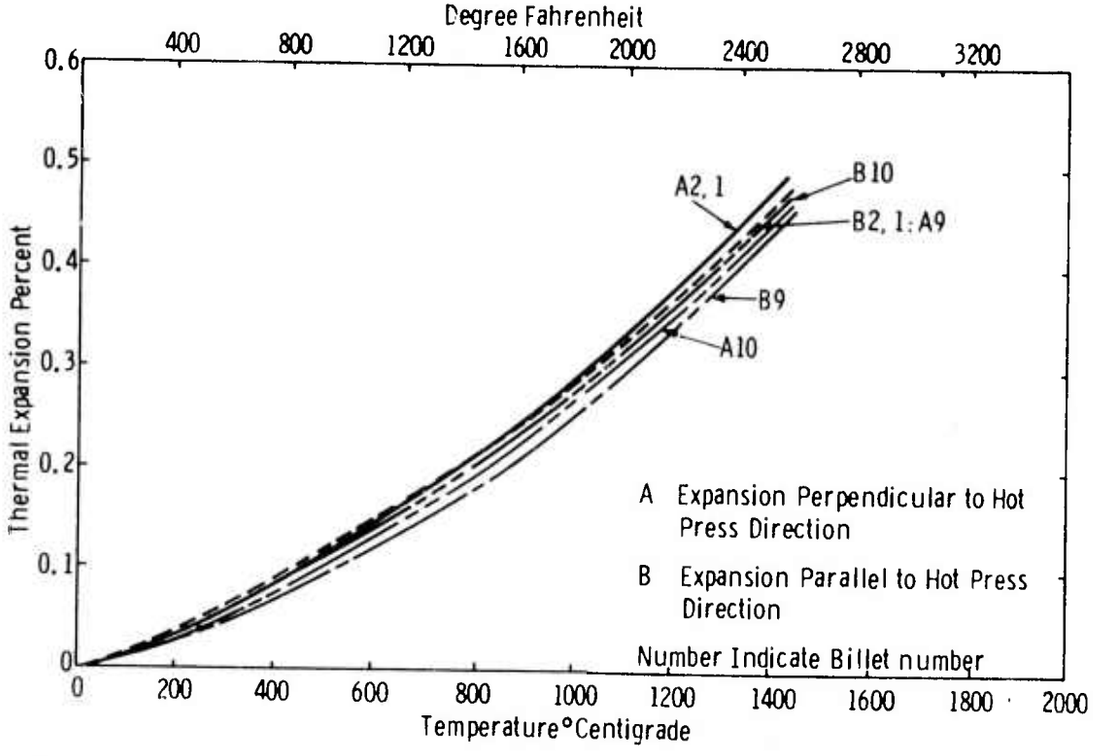


Figure 5.20 Thermal Expansion of Hot Pressed Silicon Nitride as a Function of Temperature

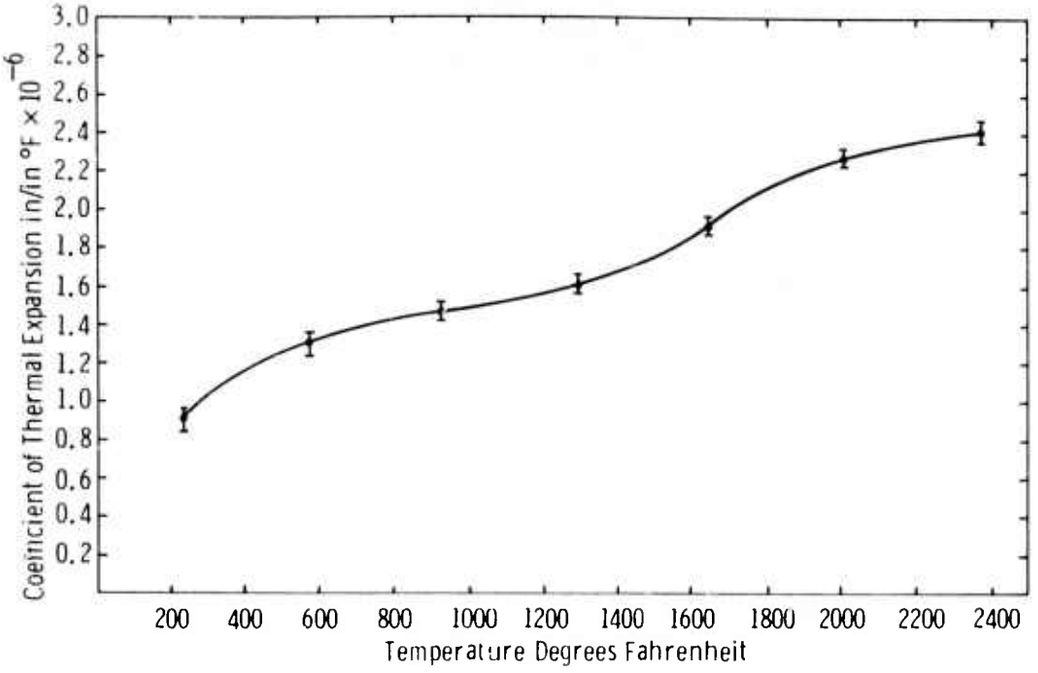


Figure 5.21 Average Coefficient of Thermal Expansion for Norton HS-130 Si_3N_4

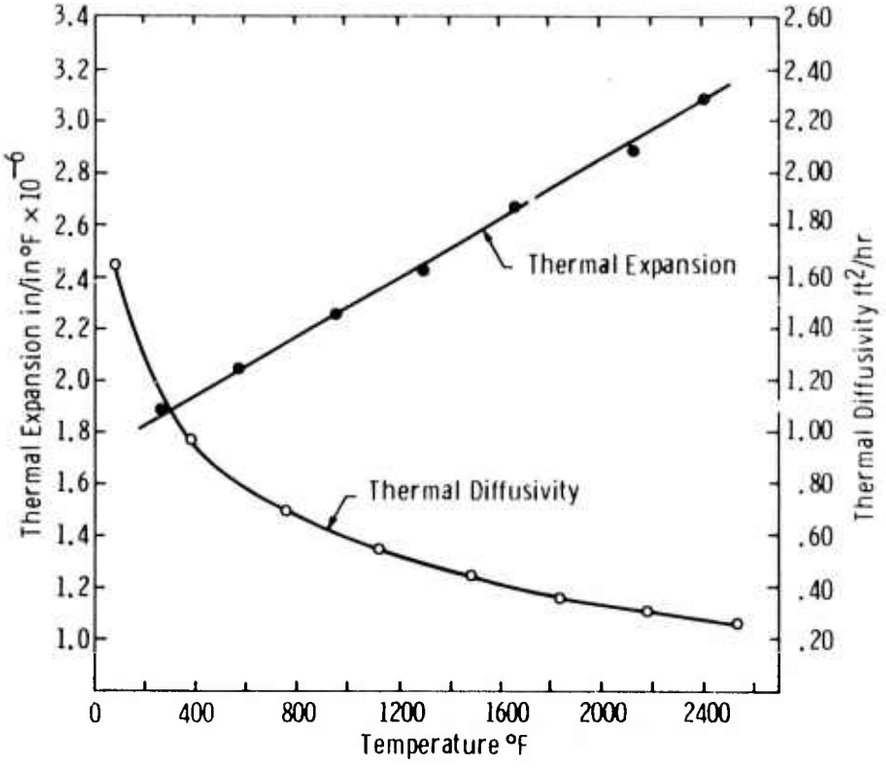


Figure 5.22 Hot Pressed Silicon Carbide Thermal Diffusivity and Expansion

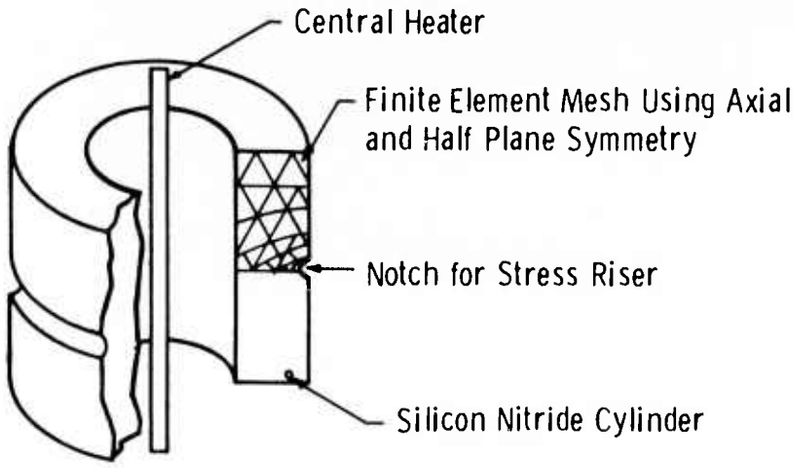


Figure 5.23 Notched Cylinder of Silicon Nitride for Thermal Fracture Showing Orientation of Finite Element Mesh

Shear Modulus

Shear modulus data have been obtained for hot-pressed silicon nitride, hot-pressed silicon carbide, and lithium-aluminum-silicate (used in turbine regenerators) in the temperature range of 660 to 1800°C. Where high temperature shear modulus data are available for the material of interest, the data are compared with the results of others.

Data were obtained using a pulse-echo method; the apparatus is shown schematically in Fig. 5.24. An oxcillator emits 1 μs duration pulses of 10 MHz energy which are converted into ultra-sound by a Y-cut (shear wave) quartz transducer. The pulses of ultrasound are introduced into one end of a fused silica delay line, the other end of which is bonded to the sample in the furnace. The time separation of sound pulses which undergo repeated reflection at the parallel faces of the sample is found from the video display. The speed of shear sound waves, V, is calculated using this separation and the known sample length. The shear modulus is calculated by ρV^2, ρ being the sample density. The quality of the high temperature cement joint limits both the temperature range over which data can be secured and the accuracy of these data. In the present experiment the delay line was bonded to the sample with Ferro Frit XG-142, Ferro Corporation, Cleveland, Ohio to which approximately 5 weight percent PbO was added. This type of cement joint, fired at about 1200°F on initial sample warmup, was satisfactory for use at higher temperatures. Experimental reproducibility of velocity values for successive runs is ± 10%, which yields ± 2% uncertainty in modulus.

Shear modulus data were also obtained at room temperature where the quartz transducer was cemented directly to the sample with phenyl salicylate.

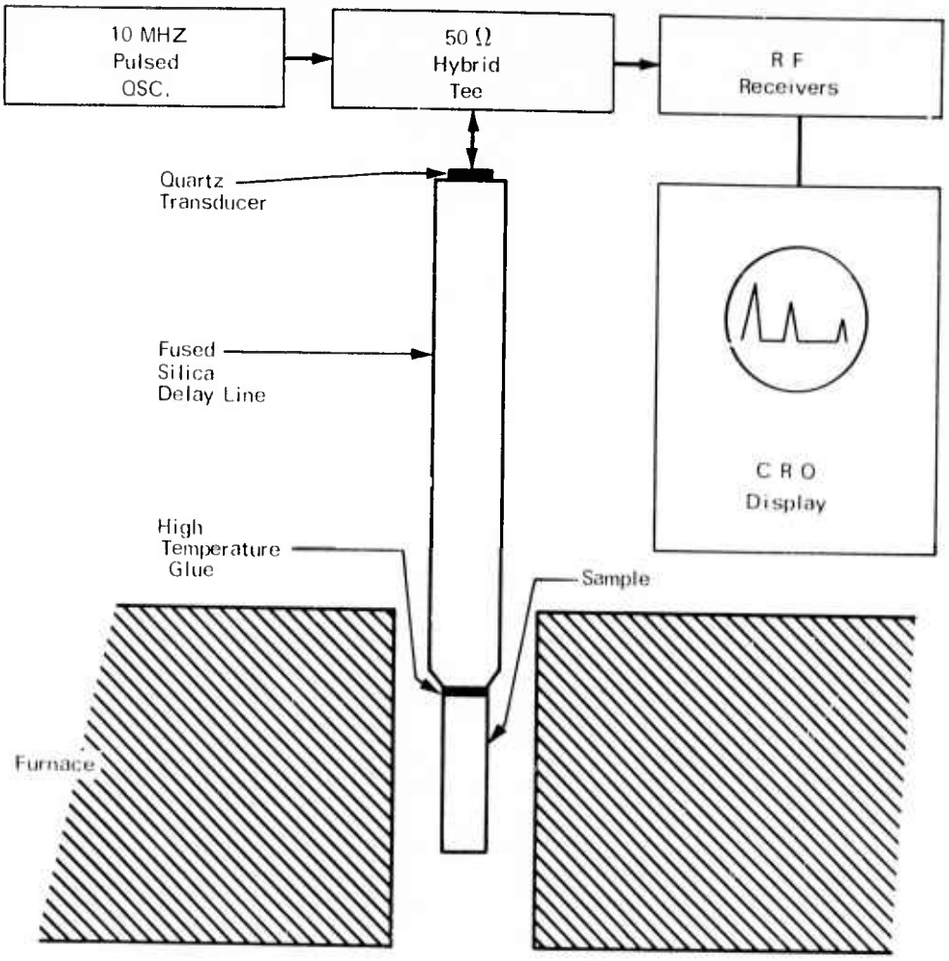


Figure 5.24 Schematic Diagram of Ultrasonic Equipment

Experimental data for silicon nitride, silicon carbide and lithium-aluminum-silicate are shown in Fig. 5.25, 5.26, and 5.27. Numerical data for the three materials at selected temperatures, taken from smooth curves drawn through the experimental points, are given in Table 5.3. A detailed description of the data follows.

High temperature data were obtained on two samples of hot pressed Si_3N_4 with dimensions 1/4 in x 1/8 in x 1-3/4 in long. These are designated as samples no. 1 and 3, (see Fig. 5.25). The shear modulus was found to be a smoothly decreasing function of temperature between 660 and 1800°F. Room temperature measurements on these samples, however, gave a shear modulus about 5% lower than the value at 660°F. The room temperature measurement was repeated on another sample with dimensions 3/8 in x 3/8 in x 6 in cut from a different billet of material. This measurement also yielded a room temperature modulus somewhat lower than the 660°F value.

The room temperature shear modulus of HS-130 material has recently been measured at Corning Research Laboratories using standing wave resonance techniques in the kHz frequency range. A room temperature shear modulus of 17.6×10^6 psi was reported, which compares well with the value of 18.0×10^6 psi determined mechanically at Westinghouse.

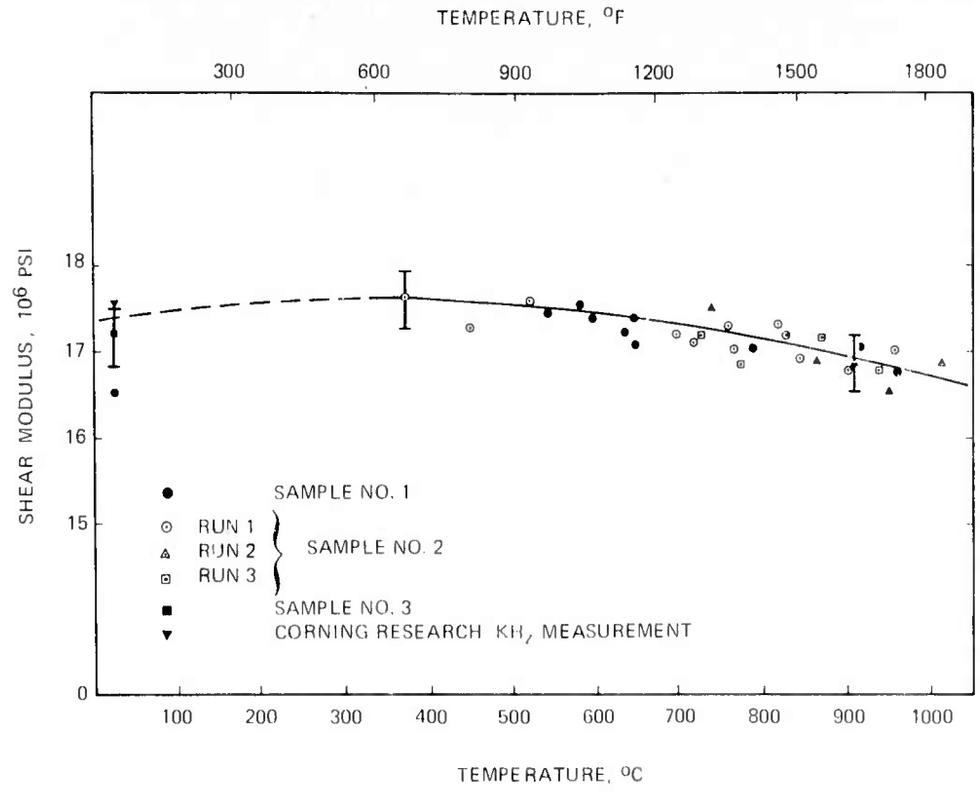


Figure 5.25 Shear Modulus of Hot-Pressed Silicon Nitride

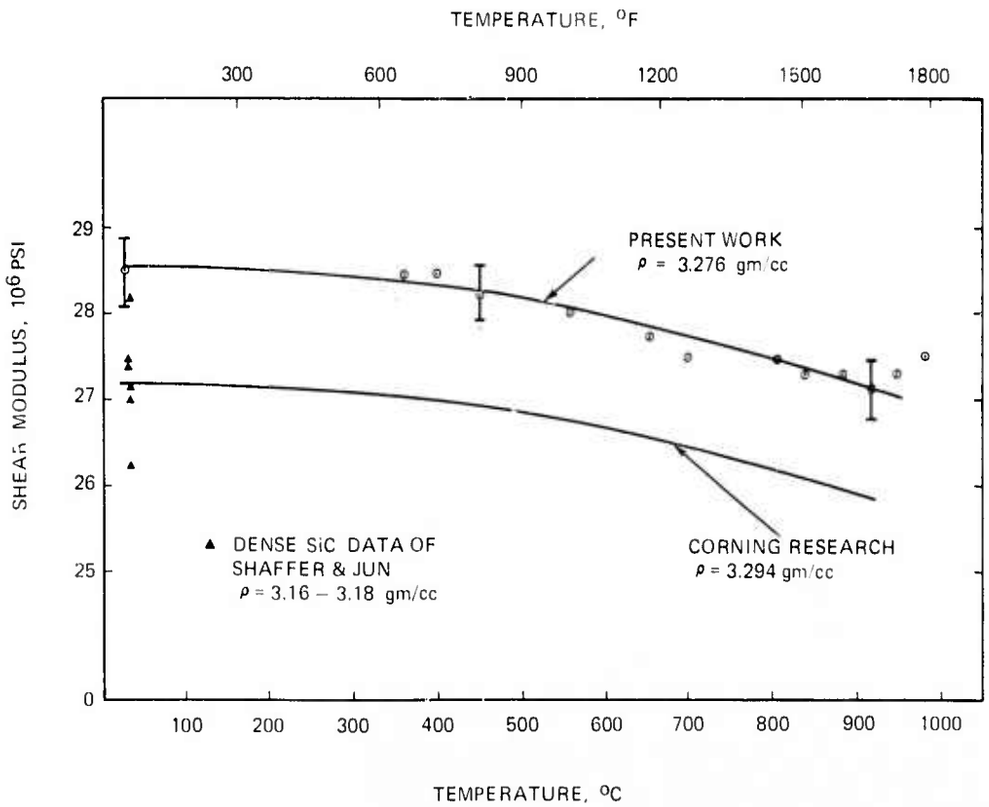


Figure 5.26 Shear Modulus of Hot-Pressed Silicon Carbide

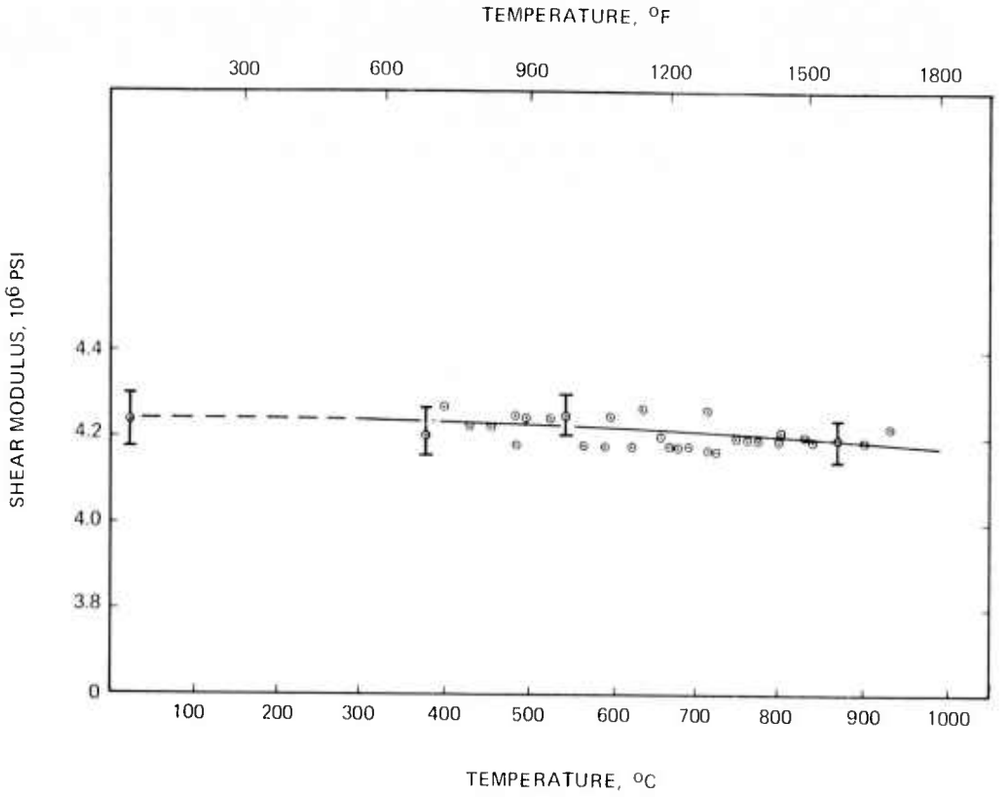


Figure 5.27 Shear Modulus of Lithium-Aluminum-Silicate

TABLE 5.3

SHEAR MODULI OF SILICON NITRIDE, SILICON CARBIDE
AND LITHIUM ALUMINUM SILICATE FOR VARIOUS TEMPERATURES

MATERIAL	SAMPLE DENSITY gm/cm^3	SHEAR MODULUS (10^6 PSI) 350°C	550°C	750°C	950°C
Si_3N_4 (Norton HS-130)	3.18	17.6	17.5	17.2	16.8
SiC (Norton Hot-Pressed)	3.28	28.4	28.1	27.6	27.0
LAS (Corning 9458 753-22)	2.24	4.24	4.23	4.21	4.18

High temperature data, shown in Fig. 5.25, were taken on one sample of Norton hot pressed silicon carbide with dimensions 3/8 in. x 3/8 in. x 3 in. cut from a billet. The measured sample density of 3.276 gm/cm^3 exceeds theoretical density by about 2%. Spectrographic analysis of a sample cut from the same billet showed substantial amounts of iron and aluminum, with trace amounts of nickel and copper.

Shown also in Fig. 5.26 is the curve of shear modulus vs temperature reported by Corning Research Laboratories(1) for another sample of Norton hot-pressed SiC (reported density of 3.294 gm/cm^3). The measured shear moduli typically exceed these kHz frequency range results by about 4%. The temperature dependence given by the two experiments is nearly identical.

Recently Shaffer and Jun(5) have reported kHz frequency range room temperature shear modulus measurements of transparent, high density, high purity silicon carbide grown by vapor deposition methods. For the seven samples investigated the modulus values spread over a 6% range. These same authors claim that small amounts of impurity, in the form of a second phase, can considerably alter the elastic properties of silicon carbide. The difference between the present results and those reported by Corning may be due to differences in impurity content.

Measurements were made on one sample of lithium-aluminum-silicate (Corning 9458) with dimensions 1/2 in. x 1/2 in. x 3/4 in. long. Initial room temperature measurements gave the speed of ultrasonic shear waves as 3.47 x 10^5 cm/sec. After repeated thermal cycling between 570 and 1800°F, a requirement for high temperature data runs the speed of the ultrasonic shear waveset was found to be 3.60 x 10^5 cm/sec. The reason for this change is not understood but may be connected with changes in the structure of the material upon thermal cycling near 1470°F. This study was confined to the evaluation of a thermally cycled specimen, data for which are shown in Fig. 5.27. Within the estimated accuracy of the measurements, the shear modulus remains constant between 660 and 1760°F, although a slight decrease seems to occur at the higher temperatures.

Independent room temperature measurements(1) in this material yield shear wave velocities in the range 3.25 to 3.41 x 10^5 cm/sec, as compared with the value of 3.47 x 10^5 cm/sec as measured before thermal cycling.

Corrosion Testing of Silicon Nitride

Corrosion testing in the turbine passage has been performed using diesel oil containing 0.5 wt % sulfur, 5 ppm sodium, 2 ppm vanadium and 0.6 ppm Mg. These contaminants were introduced into the gas stream by mixing in appropriate amounts of various compounds with the fuel oil as follows:

Sulfur:	dietertiary butyl disulfide
Sodium:	sodium napthenate
Vanadium:	vanadium carboxylate
Magnesium:	magnesium napthenate

This level of impurities corresponds to ASTM specifications for maximum allowable impurities in GT-3 fuel. The degree of corrosion attack was determined by changes in the weight of the test specimens without removing any surface deposits.

The turbine passage is described in detail in the First Semi-Annual Progress Report.[2] However, its operation may be summarized as follows: Air is compressed to 45 psi, preheated to 600°F and fed directly into the inlet end of a thick walled stainless steel tube 6 in. inside diameter which serves as the pressurized gas passage. The combustor is of standard design approximately 4 in. diameter by 30 in. long. Diesel oil is injected into the primary combustion zone through a pressurized fuel nozzle located in the dome shaped front portion of the combustor. Combustion gases and secondary cooling air exit axially with a gas mixer section provided to insure uniform gas temperature in a rectangular test section 2 in. x 4 in. The gas flow is accelerated past a staggered double array of 4 - 2 in. x 1/4 in. x 1/4 in. test specimens in a silicon nitride holder to enter the exhaust duct. Pressure is maintained by a water cooled barrier plate acting as a variable pressure valve. Exhaust gases are vented to the atmosphere through an extensive muffler system to reduce noise to acceptable levels.

Figure 5.28 shows the front and back surfaces of a HS-130 silicon nitride specimen which has been exposed for 250 hours at 2000°F and 3 atmospheres pressure to combustor gases containing 0.5 wt % sulfur, 5 ppm Na, 2 ppm V, and 0.6 ppm Mg. The front surfaces of the specimens, first encountered by the oncoming hot combustion gases, are relatively clean and covered with a uniform layer of barium silicate ($BaO \cdot 2SiO_2$). This results from an impurity of 0.4 ppm barium which is present in the fuel. In contrast, there are large glassy deposits on the back surfaces of the specimens. X-ray diffraction analyses of these deposits gave an amorphous pattern, confirming their glassy nature. Emission spectrography and wet chemical analysis are presently being used to analyze the glass composition.

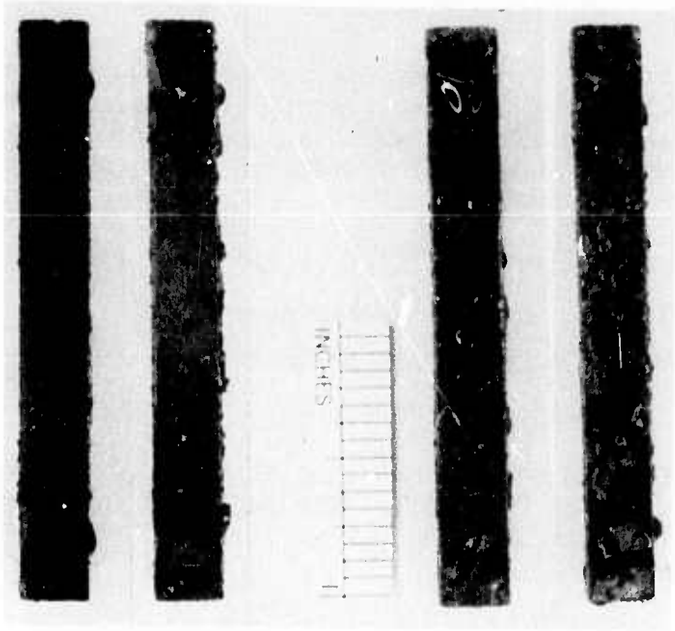


Figure 5.28 Surface Appearance of a Silicon Nitride Test Specimen after 250 Hours of Exposure at 2000°F to Combustor Gases Containing 0.5 wt % S, 5 ppm Na, 2 ppm V and 0.6 ppm Mg

Figure 5.29 shows the average weight change as a function of corrosion time for 5 silicon nitride specimens exposed in the test passage at 2000°F to combustor gases containing 0.5 wt % S, 5 ppm Na, 2 ppm V and 0.6 ppm Mg. Corrosion data for silicon nitride in clean Gulf #2 diesel fuel and in diesel fuel with 0.5 wt % sulfur are included for comparison. Corrosion appears to increase with fuel contamination. Since the scatter in these data, however, exceeds the width of the band generated by the three curves, it is difficult to describe the differences as significant. The specimens initially gained weight, which is almost entirely due to the deposits formed on the specimen surfaces. These surface deposits are formed by the condensation of impurities in the fuel and the air, and from the erosion of the stainless steel liner used in the test passage. As corrosion progresses, the volume of surface deposits increases until it becomes excessive and is swept away by the high velocity combustion stream taking with it some surface silica. The specimens then begin to lose weight.

Minor erosion of the leading edges was also observed, when testing in the contaminated fuel. These initially sharp edges became smoothed and somewhat convex after 250 hours of exposure to the combustion gases. Erosion of this nature also caused some loss in the weight of the specimens. In addition, a small weight loss may be expected due to the possible formation of volatile silicon sulfide in sulfur-containing fuels. However, the difference in the weight changes in Si_3N_4 specimens tested in different fuel compositions, as shown in Fig. 5.29, is very small. This is not considered significant because of the large scatter in the data.

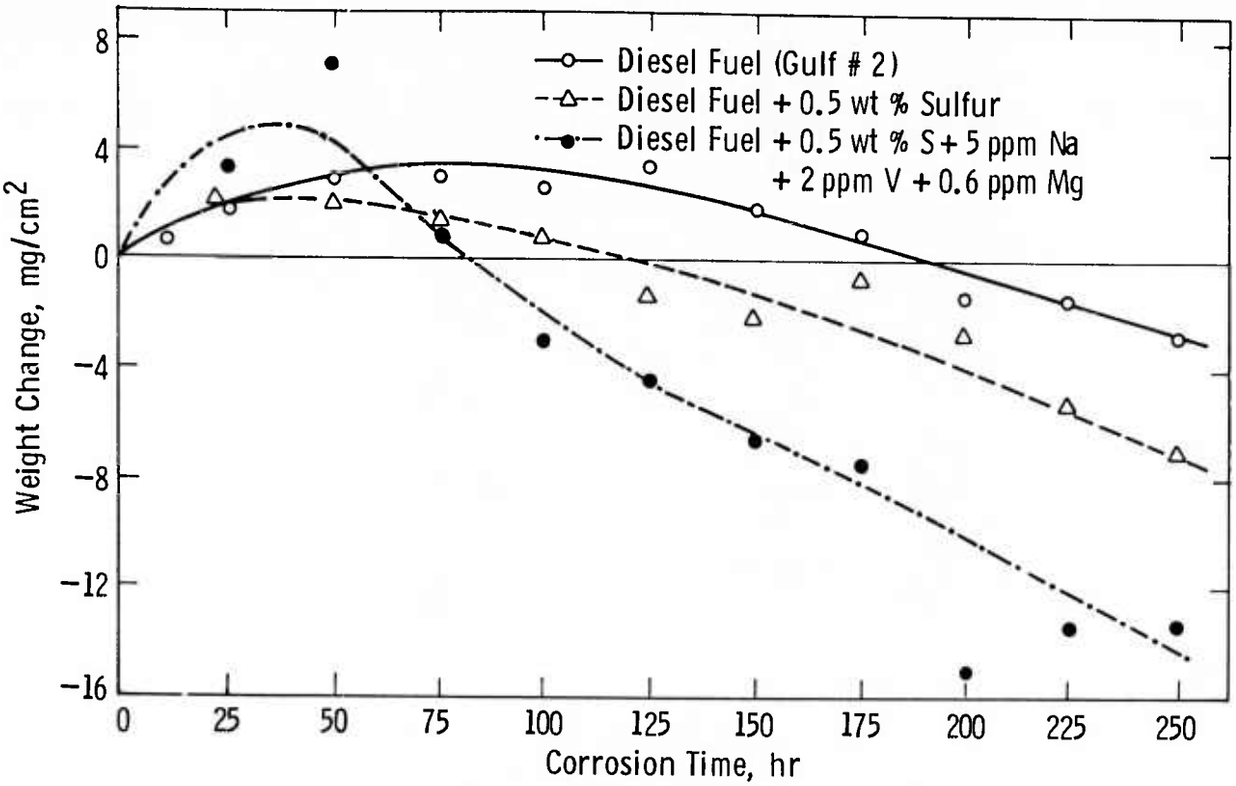


Figure 5.29 Effect of Fuel Contaminants on the Corrosion of Hot Pressed Silicon Nitride in Turbine Test Passage at 2000°F and 3 atm Pressure

The sulfur, sodium, and vanadium in the fuel do not cause any catastrophic accelerated hot-corrosion of Si_3N_4 at 2000°F, as observed for various nickel-base superalloys at temperatures up to 1800°F. This is not totally unexpected since Na_2SO_4, which forms by the reaction between NaCl(g), SO_2(g) and H_2O(g) in the combustion gases, and is believed to cause the hot-corrosion attack on superalloys, cannot condense above about 1900°F in gas turbine environments.

Corrosion Testing of Silicon Carbide

Similar corrosion-erosion experiments were carried out on Norton hot pressed silicon carbide, using both clean Gulf #2 diesel fuel and diesel fuel with 0.5 wt % S, 5 ppm Na, 2 ppm V and 0.6 ppm Mg added, at 2000°F and 3 atmospheres pressure. The surfaces of a silicon carbide specimen after 250 hours of exposure in the contaminated fuel were identical to those of Si_3N_4 specimens, as shown in Fig. 5.30. Again, the front surfaces are uniformly covered with barium silicate and the back surfaces with voluminous shiny glass deposits.

The weight changes in the SiC specimens after exposure in the turbine test passage are shown in Fig. 5.31 as a function of corrosion time. The weight change vs time curves for SiC follow the pattern observed for Si_3N_4, both in the clean and the contaminated fuel. However, in the case of silicon carbide specimens, the top and bottom edges appeared slightly chipped as a result of thermal shock. This caused a small loss in weight in addition to losses due to corrosion and erosion.

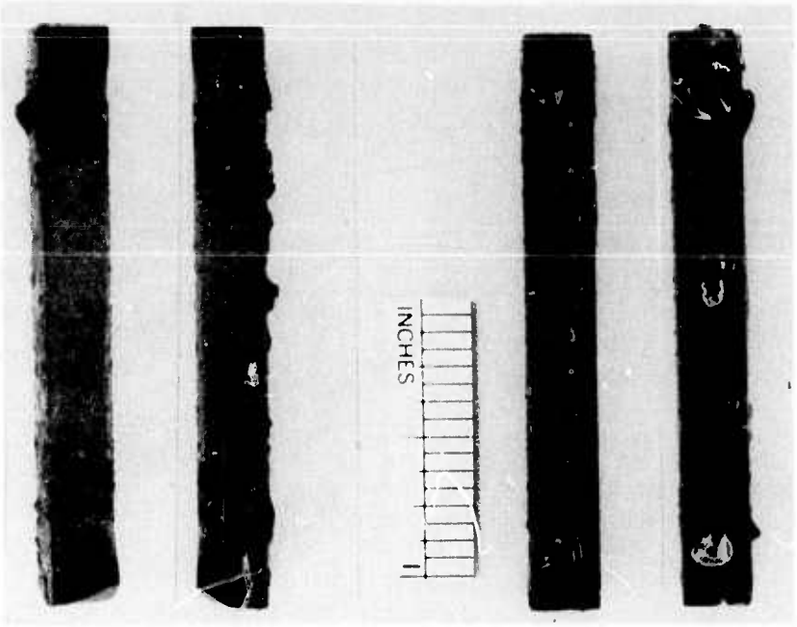


Figure 5.30 Surface Appearance of a SiC Test Specimen after 250 Hours of Exposure at 2000°F to Combustor Gases Containing 0.5 wt % S, 5 ppm Na, 2 ppm V and 0.6 ppm Mg

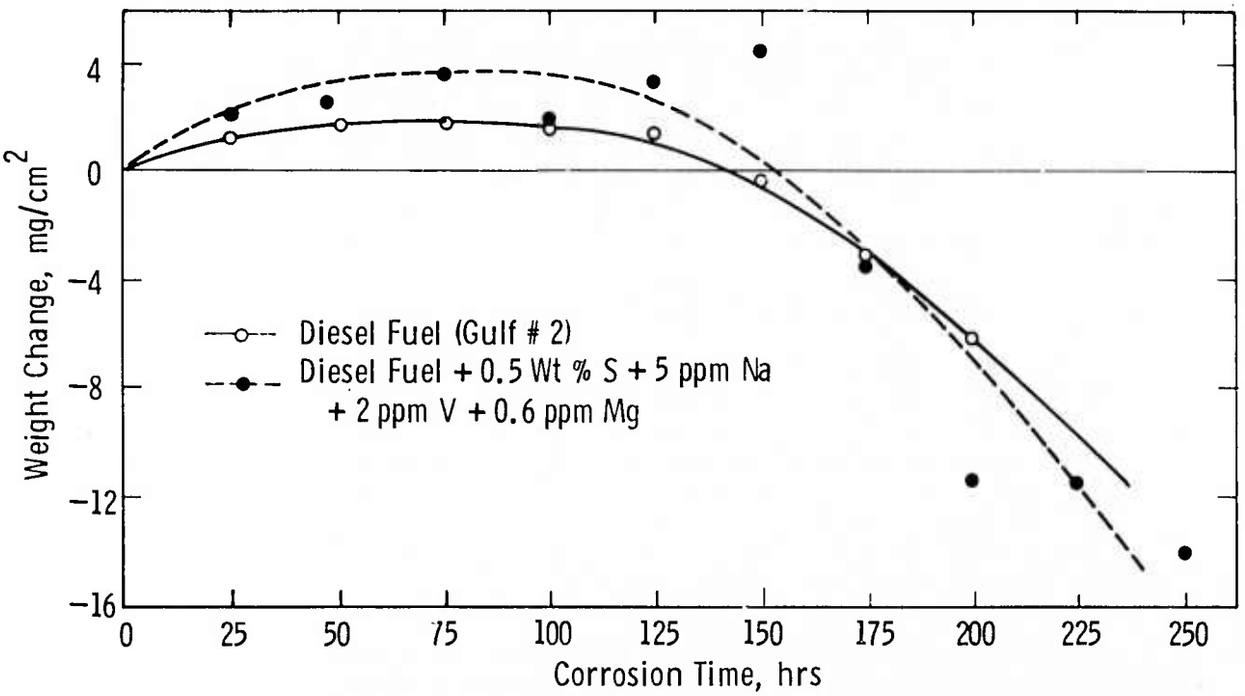


Figure 5.31 Effect of Fuel Contaminants on the Corrosion of Hot Pressed SiC in Turbine Test Passage at 2000°F and 3 atm Pressure

The corrosion-erosion behavior of hot pressed Si_3N_4 and SiC is compared to that of commonly used superalloys, X-45 and Udimet-500 in Fig. 5.32. The magnitude of the weight loss for both Si_3N_4 and SiC exposed to 2000°F combustion gases containing S, Na, V, and Mg at 2000°F is much smaller than that for X-45 and Udimet-500 exposed at the much lower temperature of 1650°F. Moreover, the corrosion of Si_3N_4 in the pressurized turbine test passage does not cause any appreciable degradation in strength.(1)

Low Cycle Fatigue (Thermal Fatigue)

Low cycle fatigue experiments, to model repeated emergency shutdown conditions in a gas turbine, indicate that Si_3N_4 is able to survive 100 cycles at 2300°F, when loaded from 5000 to 20,000 psi in the flexural mode. The samples were the same as the flexural strength samples -- .125 x .25 x 1.25 inches long finished parallel to the long dimension with a 220 grit diamond wheel. Four point loading was employed using inner and outer span distances of 0.375 inch and 0.875 inches, respectively. Silicon carbide dowel pins were used for bearing surfaces on the silicon nitride test fixture. Load was applied without reversal to avoid alignment problems and because compressive creep is not a problem. Further tests in both the flexural and tensile mode are planned following the schedule shown in Fig. 5.33.

Friction

The three piece vane design for the stationary gas turbine permits some freedom of motion between the stator vane airfoil and its restraining end caps. End cap pairs may slide with respect to their associated insulator within the structural column. Because motion at any of the interfaces is possible to some degree, both static and dynamic coefficients of friction as well as wear characteristics must be measured for high density silicon nitride or silicon carbide against themselves and various other materials used to support the vane assembly.

The procedure and apparatus for measuring friction were described in the first semi-annual report.(2) Silicon nitride was tested against materials with different surface finishes. The results are reported in Fig. 5.34 and Table 5.4. Lithium aluminum silicate is the insulating material that is specified to back up the end caps in the vane assembly.

Wear and Fret

Wear and fret tests are being used to supplement the friction data and to simulate the affect of motion at the end cap airfoil interface. The specimen geometry and test fixture is shown in Fig. 5.35.

Silicon nitride vs silicon nitride was tested at 2300°F for one hour (3600 cycles) at 11.0 lbs load, and for 1/2 hour (1800 cycles) at 19.8 lbs load. Fretting increased markedly at the higher load as shown in Figs. 5.36. The white deposit appears to be powdered silicon nitride with some silicon dioxide. Preliminary measurements

indicate that the coefficient of friction, as measured in the friction and wear apparatus, decreases from approximately 1.0 to 0.8 as wear increases with time at 2300°F.

These results may signal a potential problem in the contact area between the airfoil and end cap in the 3 piece vane design if contact and thermal stresses cause crack propagation from the chipped areas. However, the motion imposed in this test exceeds that expected in the part by a factor of 5 and each cycle represent a single turbine start.

Shear Strength

The shear strength and shear modulus of silicon nitride was measured at room temperature and 1832°F using a specimen 5.5 inches long with a 0.75 inch gauge diameter over a 2.50 inch gauge length. Square ends were used to grip the specimen. The strain was measured mechanically by means of linear voltage differential transducers operated against push rods compensated for thermal expansion.

At room temperature, the shear strength and modulus were 68,600 psi and 18.0 x 10^6 psi/in/in, respectively. These values did not change much at 1832°F where a shear strength of 70,300 psi and shear modulus of 16.9 x 10^6 psi/in/in were determined.

A torsion test apparatus capable of 2500°F is currently under construction. A schematic view is shown in Fig. 5.37.

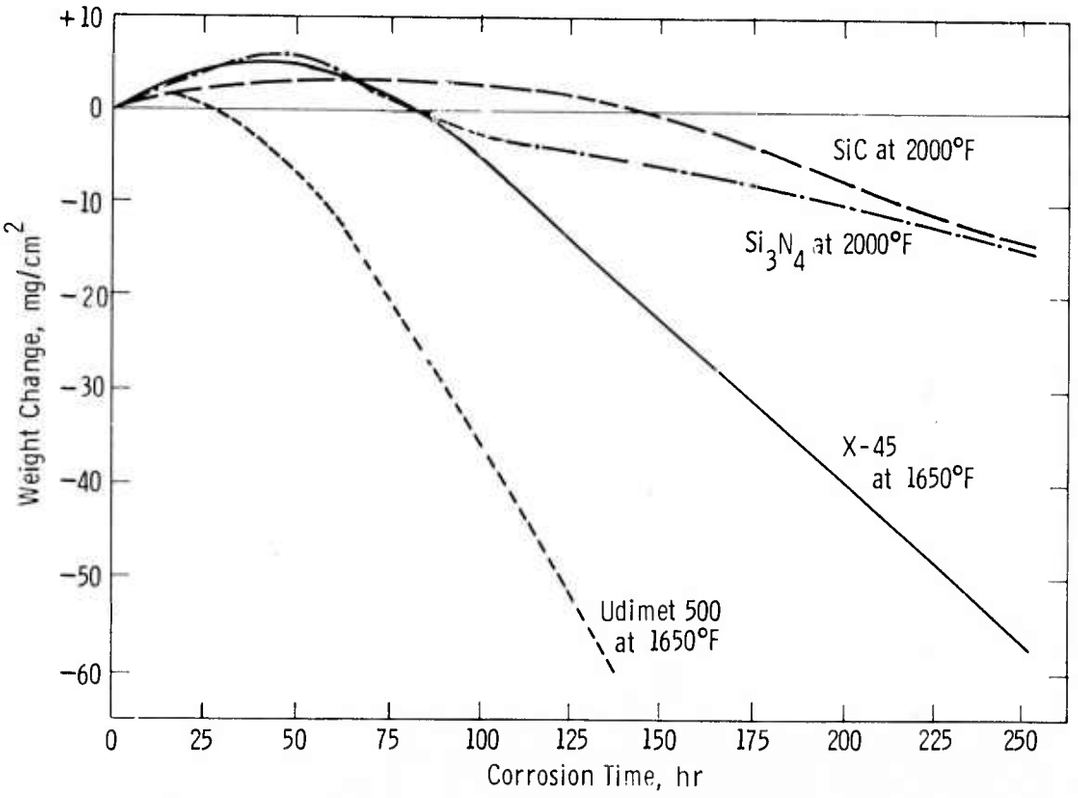


Figure 5.32 Corrosion of Various Materials in Turbine Test Passage, Exposed to Combustor Gases Contaminated with 0.5% S, 5 ppm Na, 2 ppm V and 0.6 ppm Mg.

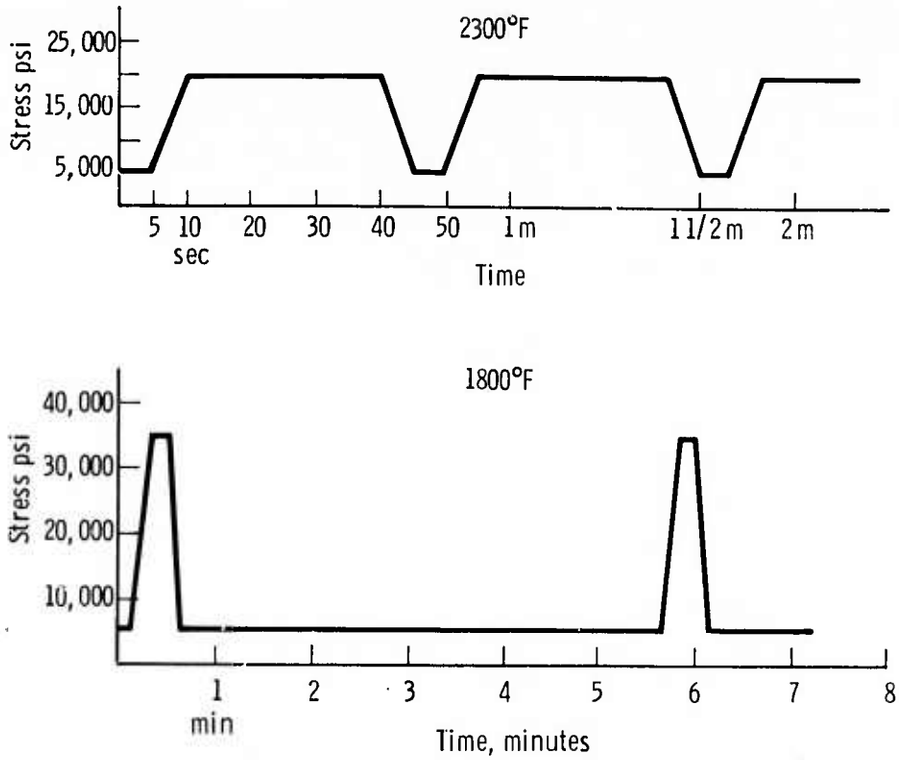


Figure 5.33 Low Cycle Fatigue Testing Schedule at 1800°F and 2300°F

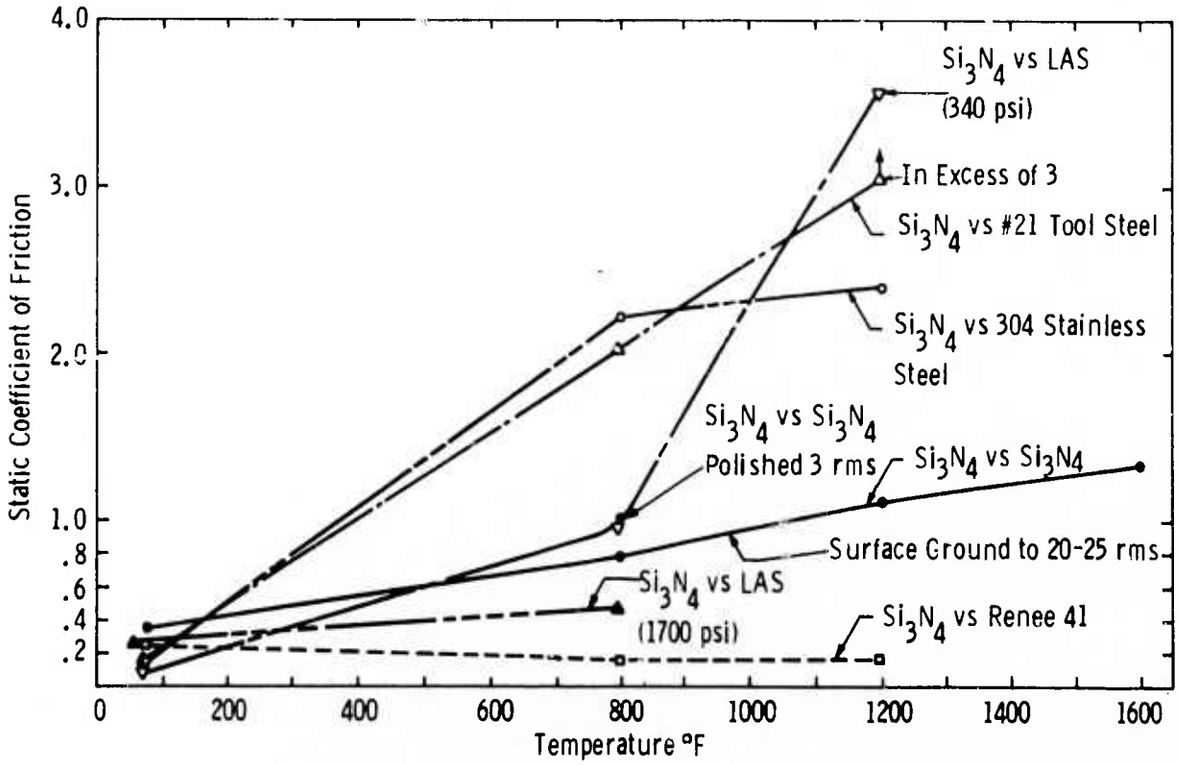


Figure 5.34 Static Coefficient of Friction for Hot Pressed Silicon Nitride vs Various Materials

Table 5.4

COEFFICIENTS OF FRICTION FOR Si_3N_4 vs VARIOUS MATERIALS

Tip		Plate	Load/psi	Temp°F	Static-lbs	Static Coef.	Dynamic*
Si_3N_4 (polished 2-3 rms)	vs.	LAS(Ground Parallel)	340	RT	.11	.11	S.S.
Si_3N_4 (polished 20-25 rms)	vs.	LAS(Ground Parallel)	340	RT	.09	.09	S.S.
Si_3N_4 (polished 2-3 rms)	vs.	LAS(Ground Perpendicular)	340	RT	.10	.10	S.S.
Si_3N_4 (polished 20-25 rms)	vs.	LAS(Ground Perpeniduclar)	340	RT	.11	.11	S.S.
Si_3N_4 (polished 2-3 rms)	vs.	LAS(Ground Parallel)	1700	RT	1.07	.21	S.S.
Si_3N_4 (polished 20-25 rms)	vs.	LAS(Ground Parallel)	1700	RT	1.3	.26	S.S.
Si_3N_4 (polished 2-3 rms)	vs.	LAS(Ground Perpendicular)	1700	RT	1.23	.24	S.S.
Si_3N_4 (polished 20-25 rms)	vs.	LAS(Ground Perpendicular)	1700	RT	1.3	.26	S.S.
Si_3N_4 (polished 2-3 rms)	vs.	LAS(Ground Parallel)	340	600	.76	.76	S.S.
Si_3N_4 (polished 20-25 rms)	vs.	LAS(Ground Parallel)	340	600	.79	.79	S.S.
Si_3N_4 (polished 2-3 rms)	vs.	LAS(Ground Perpendicular)	340	600	.72	.72	S.S.
Si_3N_4 (polished 20-25 rms)	vs.	LAS(Ground Perpendicular)	340	600	.52	.52	S.S.
Si_3N_4 (polished 2-3 rms)	vs.	LAS(Ground Parallel)	1700	600	1.53	.31	S.S.
Si_3N_4 (polished 20-25 rms)	vs.	LAS(Ground Parallel)	1700	600	1.59	.33	S.S.
Si_3N_4 (polished 2-3 rms)	vs.	LAS(Ground Perpendicular)	1700	600	2.65	.53	S.S.
Si_3N_4 (polished 20-25 rms)	vs.	LAS(Ground Perpendicular)	1700	600	2.8	.56	S.S.
Si_3N_4 (polished 2-3 rms)	vs.	LAS(Ground Parallel)	340	1200	----SAMPLE CRACKED----------		
Si_3N_4 (polished 20-25 rms)	vs.	LAS(Ground Parallel)	340	1200	3.67	3.67	S.S.
Si_3N_4 (polished 2-3 rms)	vs.	LAS(Ground Perpendicular)	340	1200	4.31	4.31	S.S.
Si_3N_4 (polished 20-25 rms)	vs.	LAS(Ground Perpendicular)	340	1200	2.67	2.67	S.S.

* Stick-slip

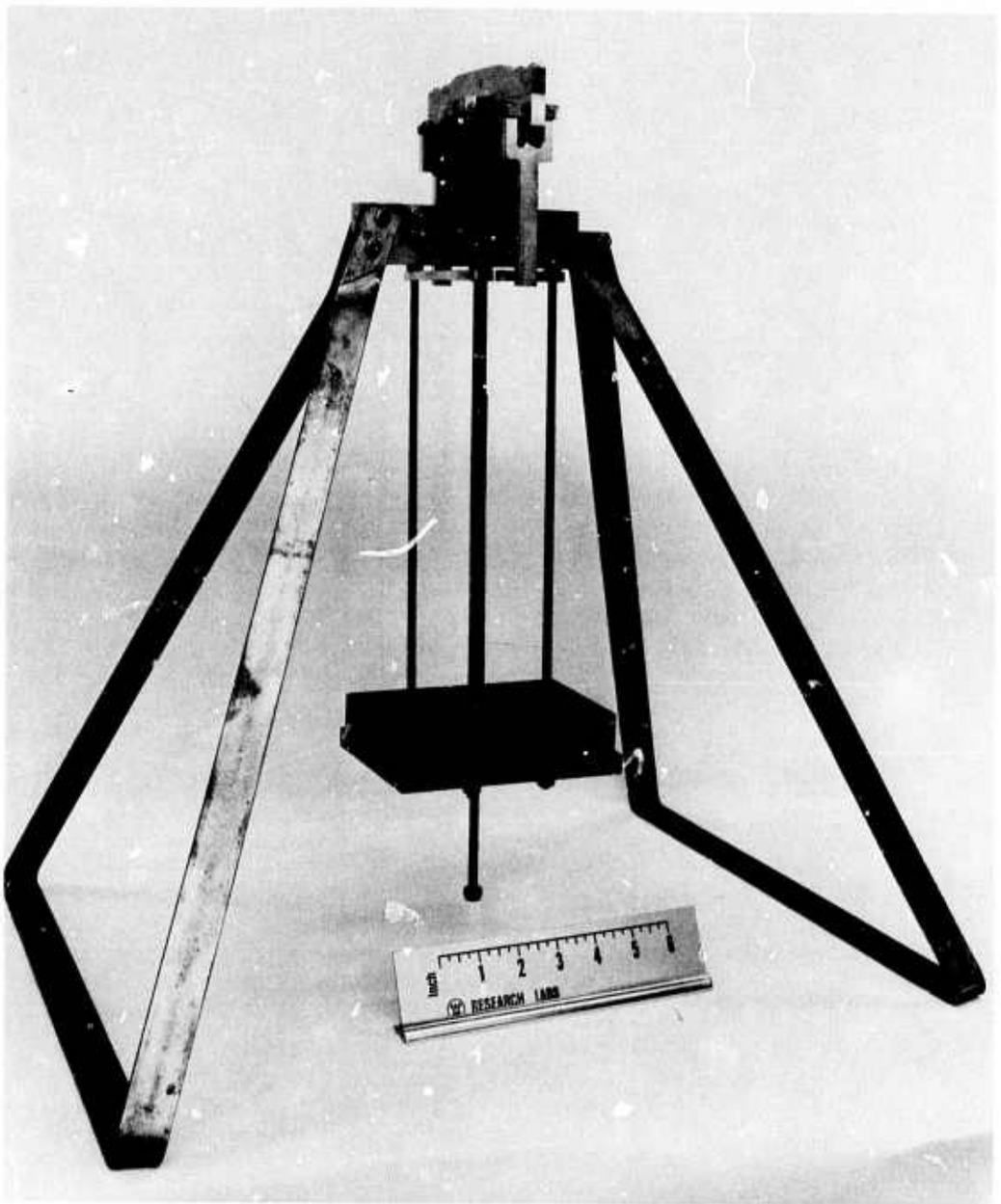
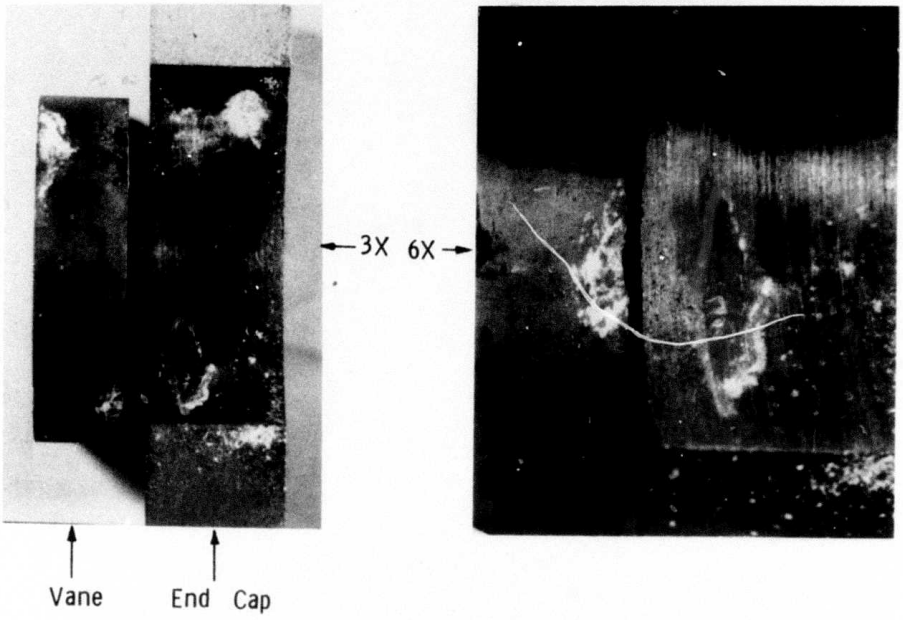
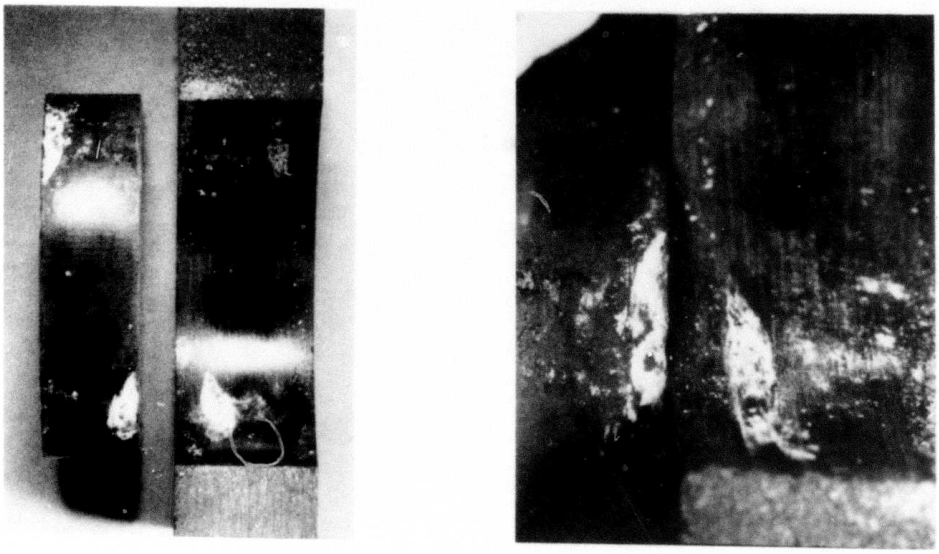


Figure 5.35 Wear and Fret Test Apparatus (Rocking Motion is in the Plane of Ruler)



Model of vane and end cap
after 3600 cycles at
11 lbs load 2300°F



Same surfaces after an additional
1800 cycles at 19.8 lbs, 2300°F

Figure 5.36 Surface of Wear and Fret Specimens of Hot Pressed Silicon Nitride

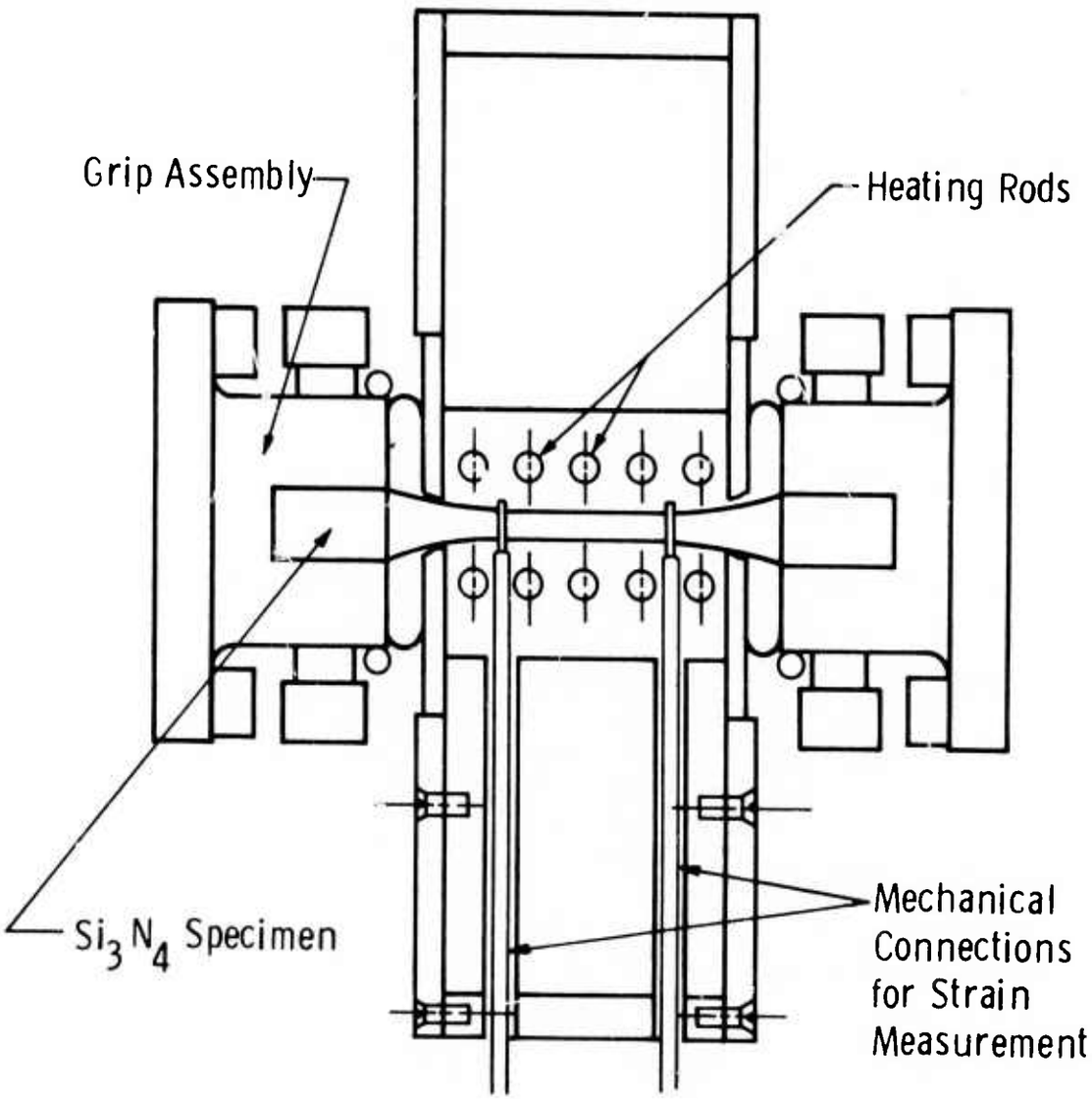


Figure 5.37 Cut Away View of Torsion Test Facility Showing Furnace Grips and Stain Readout

PRECEDING PAGE BLANK-NOT FILMED

SUMMARY

The purpose of detailed investigations into material sciences is to develop an understanding of material behavior which will lead to improved material through better control of composition, processing, and fabrication. This is of particular importance since the ceramic materials being utilized in the turbine engines are relatively new and appear capable of considerable improvement. Various phases of the material sciences investigation will be continued throughout the life of the program.

The effect of some processing parameters upon the properties of reaction-sintered Si_3N_4 was determined. The effect of varying the α/β ratio upon properties was determined. It was found that density, strength, and elastic modulus were essentially constant from 0 to 65% α Si_3N_4; above 65% α, these properties all decreased; however, this decrease may have been caused by additives. Oxidation studies of reaction-sintered material showed that oxidation rates can be considerably slowed if a surface coating is first formed by oxidizing at relatively high temperature. Oxidation proceeds rapidly at lower temperatures in the absence of this coating. The kinetics of oxidation were found to best fit the parabolic oxidation law.

Studies of the effect of impurities upon high temperature strength of reaction-sintered Si_3N_4 have shown that iron was not especially harmful, but calcium does significantly reduce strength, especially at 2400°F and higher.

The effect of variations in the nitriding cycle upon the strength of reaction-sintered Si_3N_4 was studied. While preliminary, results thus far indicate that higher strengths are obtained by reducing the nitriding time at the higher temperature. Baseline transverse strength levels of 15.5 ksi were increased to 20.3 ksi by reducing the time at 2660°F from 24 to 4 hours. Microstructural examination shows the material nitrided for 4 hours to have considerably fewer large crystals of Si_3N_4.

Microstructural studies of hot-pressed Si_3N_4 and SiC were continued. Particular attention was paid to the distribution of impurities in hot-pressed Si_3N_4, and revealed that calcium and oxygen in particular are concentrated at the grain boundaries. The glass composition at the grain boundaries was predicted for both HS-130 and HS-110 grades of Si_3N_4, and appear to account for the differences in high temperature creep strength between these two materials. Analyses of hot-pressed SiC reveals that

Al and W are the major impurities. The structure consists of equiaxed grains varying in size from 1 to 10 microns. The fracture mode was observed to change from predominately cleavage to predominately intergranular fracture with increasing temperature. Grain boundaries appear to have been molten at some point during hot-pressing.

Gas-solid reaction studies were extended to include hot-pressed silicon carbide. Weight gained during static oxidation below 2200°F was insignificant. Above this temperature, weight gain is parabolic. The oxide films formed were found to consist of cristobalite; at temperatures of 2400 and 2500°F small traces of Al_2O_3 were also observed.

5.2.1 CHARACTERIZATION OF REACTION-SINTERED SILICON NITRIDE

Introduction

Processing variables exert a great influence on the properties of ceramic materials. The goal of this work was to systematically determine the effect of processing variables upon the properties of injection molded, reaction-sintered silicon nitride. The variables examined during this reporting period were alpha/beta ratio and nitriding cycles. These variables were examined for the purpose of optimizing the properties of the silicon nitride as they pertain to operation in the vehicular turbine engine. While some phases of this study are still incomplete, the results of this work indicate direction for future effort.

Effect of Alpha/Beta Ratios on Physical Properties of Reaction-Sintered Silicon Nitride

In a previous report[1], it was noted that the alpha/beta ratio of silicon nitride could be varied over a wide range by changing the nitrogen flow conditions. The purpose of this study was to determine the effect of phase composition (% alpha and % beta Si_3N_4) on the physical properties of injection molded Si_3N_4. This property data would be used to define the optimum phase composition and consequently the proper nitriding conditions.

In this study, the density, transverse strength (MOR), modulus of elasticity (MOE), and thermal expansion of samples of Si_3N_4 were determined as a function of the phase composition. The test bars were injection molded and sintered using standard nitriding procedures (24 hours at 2150°F followed by 24 hours at 2660°F). The range of alpha/beta ratios were obtained by varying nitrogen flow conditions within the furnace. To obtain the 95% α 5% β composition, Li_2CO_3 was added to the molding batch[1].

The MOR values were measured in 4 point bending on an Instron test machine. Four inch long by 1/4 inch diameter samples were used with a fixture geometry of 1 inch top span and 3 inch bottom span and a cross-head speed of 0.10 inches/min. The density was determined using a water immersion technique and the MOE determined using a resonance technique. The thermal expansion was measured using a differential dilatometer. The phase composition was determined by x-ray diffraction and expressed as weight percent.

Figure 5.38 shows density variation as a function of % alpha Si_3N_4. As can be seen, the density remains constant up to the 65% alpha region. The curve is then shown to decrease to include the 95% alpha data point. The lower density may be due to the fact that Li_2CO_3 was substituted in the injection molding batch in order to obtain the 95% alpha Si_3N_4 composition.

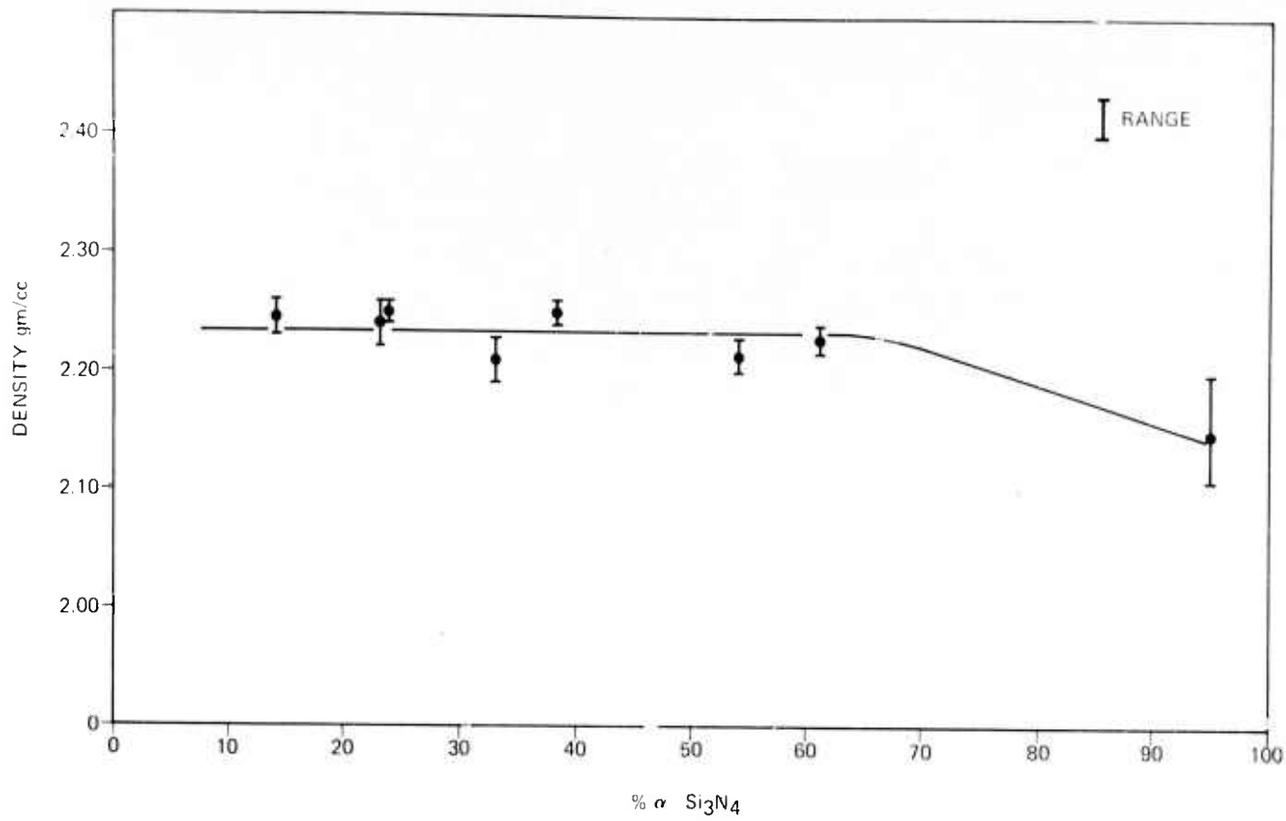


Figure 5.38 The Effect of Alpha-Beta Ratio on the Density of Silicon Nitride

Figure 5.39 shows the MOR as a function of % alpha Si_3N_4. Again no change is noted in strength up to 65% alpha. A decrease is noted at phase compositions greater than 65% alpha.

Fig. 5.40 shows a curve of strength vs density, and was obtained by cross plotting the data from Figs. 5.38 and 5.39. This shows that strength is dependent upon the final density of the material. From this data, it is concluded that the loss in strength at compositions of 65% and greater α Si_3N_4 is a density controlled effect. Fig. 5.41 shows the curve of MOE vs % alpha Si_3N_4. Again a decrease is noted starting at the 65% alpha region. As before, this could be attributed to a density effect.

Fig. 5.42 shows the thermal expansion for two phase compositions. The high alpha phase has a slightly higher expansion (125 ppm at 850°C). This data is consistent with the literature,[6] however it is questionable whether this difference is statistically significant.

Table 5.5 summarizes the physical properties of the injection molded Si_3N_4 for the region 14% to 65% alpha Si_3N_4. In the region greater than 65% alpha, the strength and MOE decreases are probably density controlled.

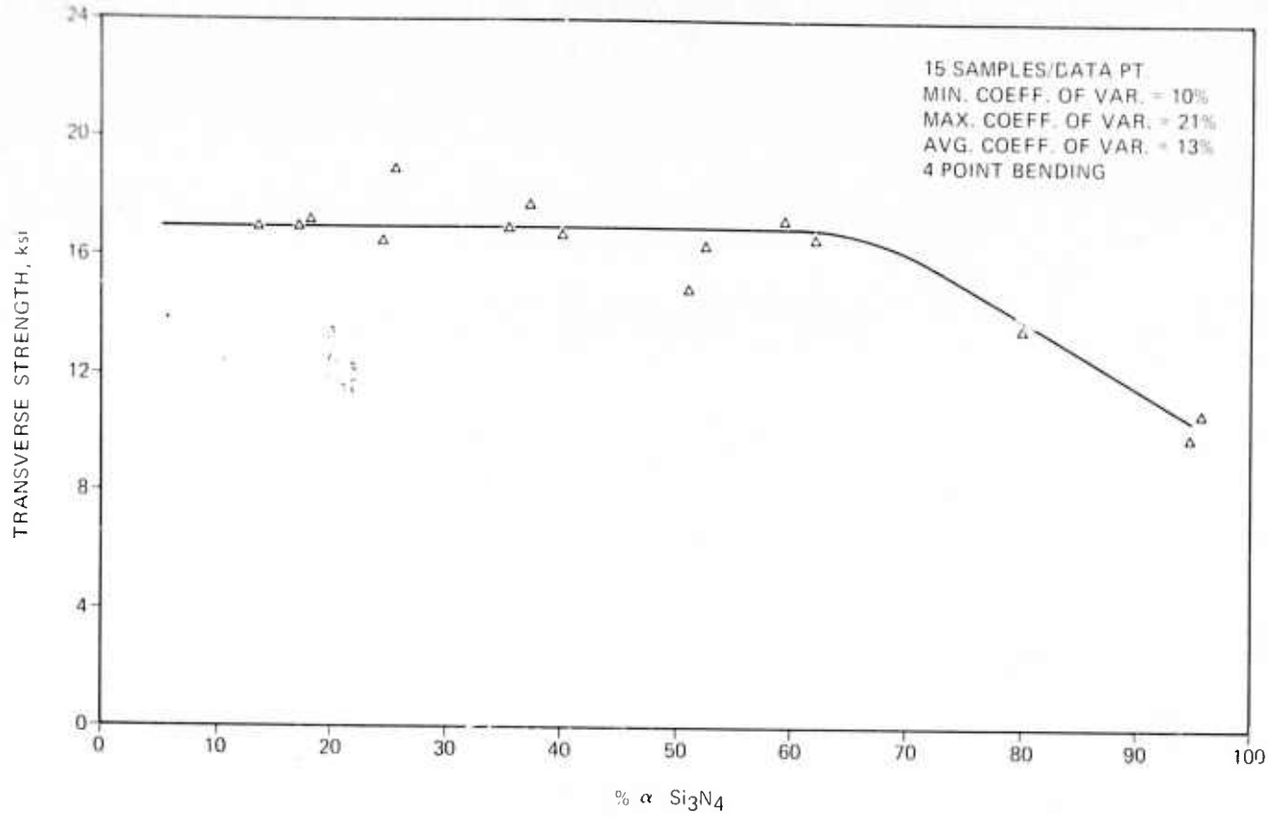


Figure 5.39 The Effect of Alpha-Beta Ratio on The Transverse Strength of Silicon Nitride

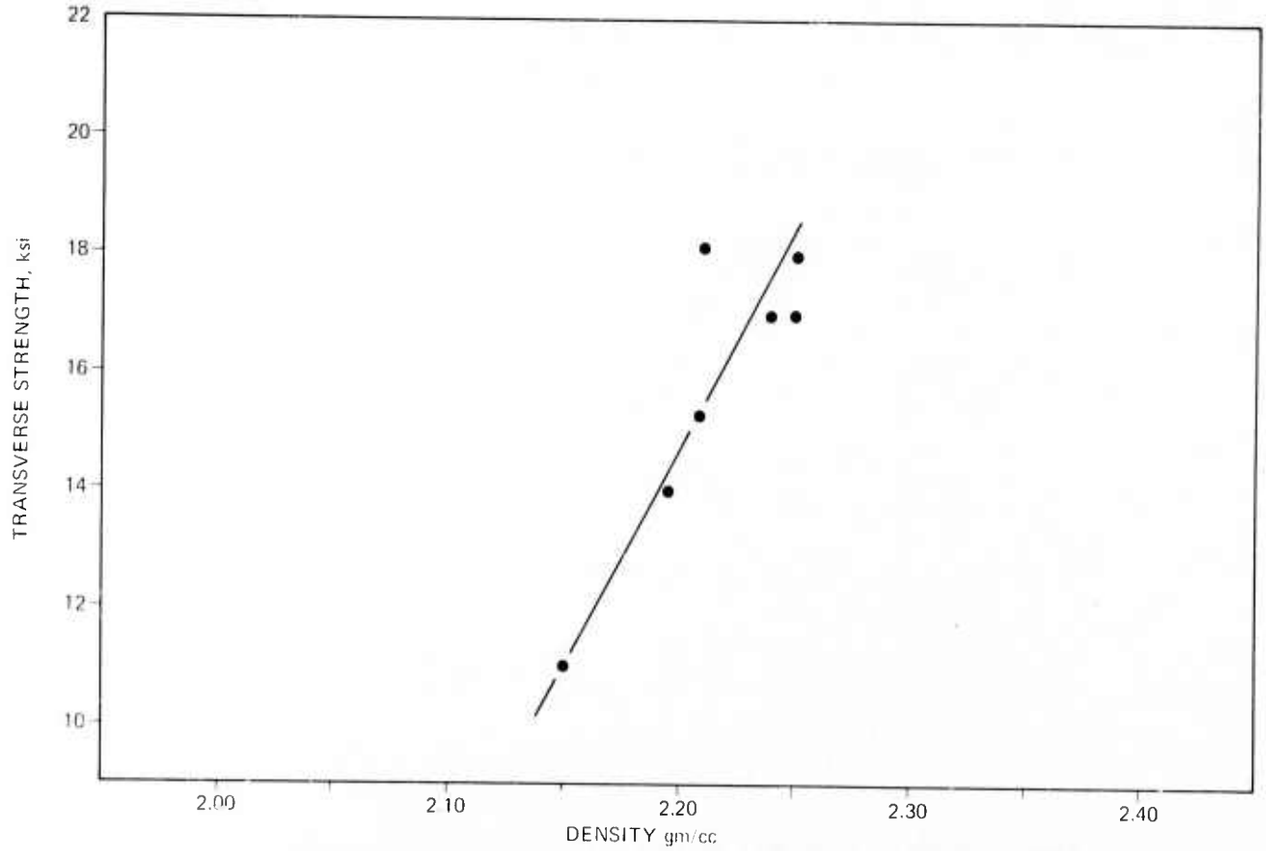


Figure 5.40 The Effect of Density on the Transverse Strength of Silicon Nitride

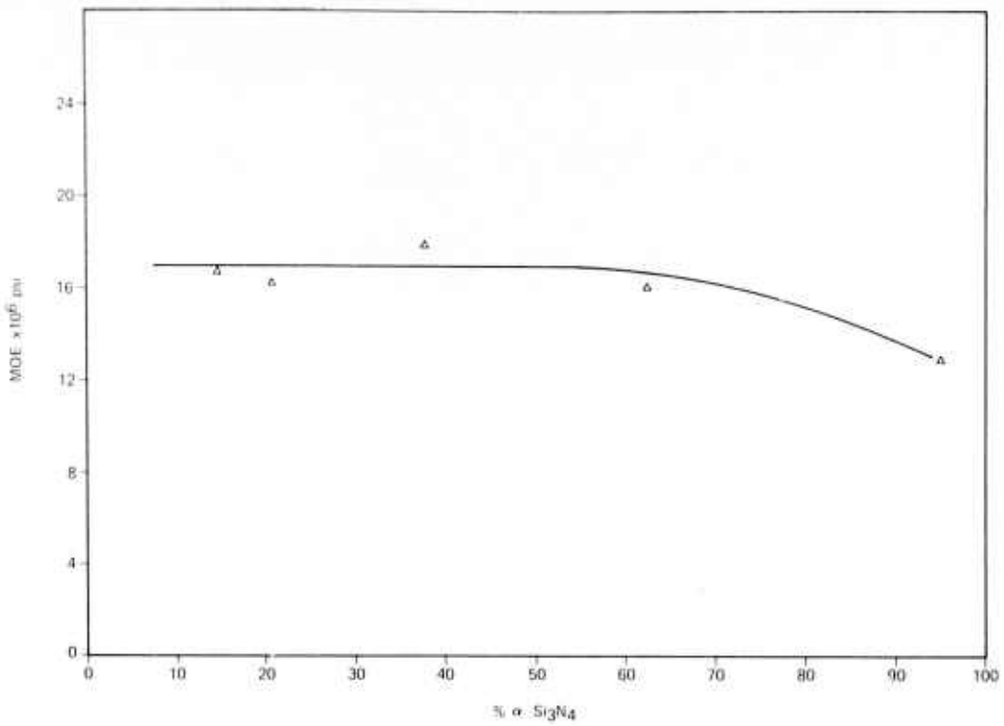


Figure 5.41 The Effect of Alpha-Beta Ratio on the Modulus of Elasticity of Silicon Nitride

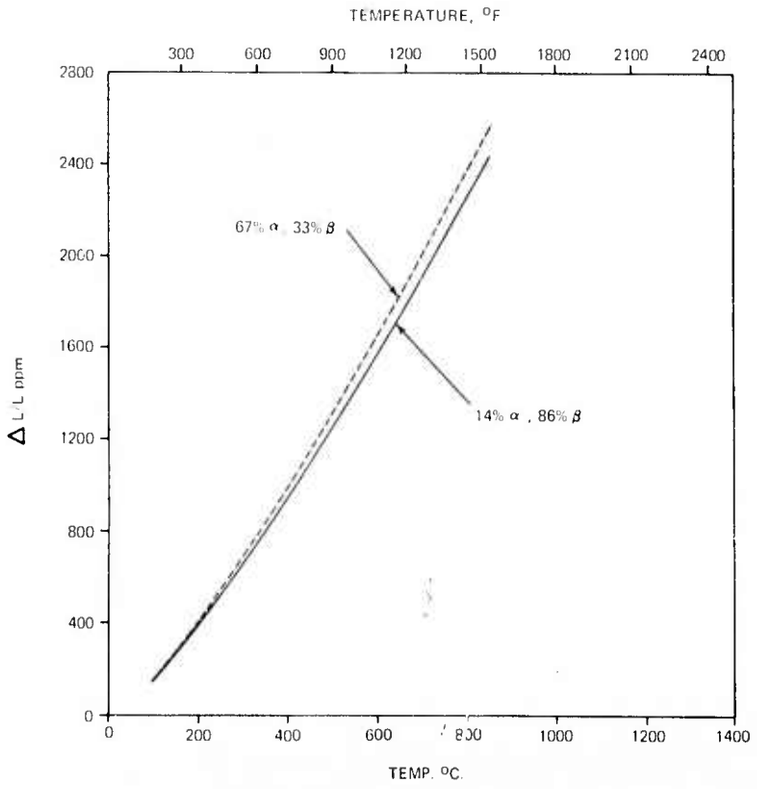


Figure 5.42 Thermal Expansion of Two Samples of Silicon Nitride of Differing Phase Compositions

TABLE 5.5

SUMMARY OF MECHANICAL PROPERTIES OF
REACTION-SINTERED SILICON NITRIDE

(14-67% ALPHA Si_3N_4)

Density	2.23 ± .02 g/cc
MOR	17,000 ± 2,500 psi
Weibull Modulus (m)	10*
MOE	17 x 10^6 psi

*Estimated from coefficient of variation and assuming $u = 0$[8]

The Effect Of Alpha/Beta Ratios On The Microstructure Of Reaction-Sintered Silicon Nitride

In the previous report[1], the microstructure of reaction-sintered Si_3N_4 was discussed relative to alpha/beta ratio, and differences noted were mainly in the grain boundaries. No differences were detected with respect to grain morphology. However, within each specimen various grain morphologies were observed, consisting of equiaxed and slightly elongated sub-micron grains along with 1-2 micron "large" grain clusters. Electron diffraction studies were initiated in an attempt to identify the various microstructural features. This knowledge will aid in microstructural analysis and also contribute information that will assist in attempts to change the microstructure to obtain optimum physical properties.

Extraction replicas of fractured surfaces were made of several Si_3N_4 samples. The predominate morphology of the extracted crystals was a characteristic needle shaped grain. Samples of both high alpha phase (75α/25β), Fig. 5.43, and high beta phase (10α/90β), Fig. 5.44, contained approximately the same number of these needle shaped crystals.

Electron difraction analyses of 3 needles from Fig. 5.44 showed all the needles to be β-Si_3N_4. Analyses of 5 needles from Fig. 5.43 found them to be α-Si_3N_4.

An examination of these needle shapes shows them to have slightly different characteristics. The alpha Si_3N_4 needles seem to have irregularly shaped sides and a length/width ratio of from 6/1 to 11/1. However, the beta crystals have regular shaped, straight sides with an length/width ratio of from 5/1 to 8/1.

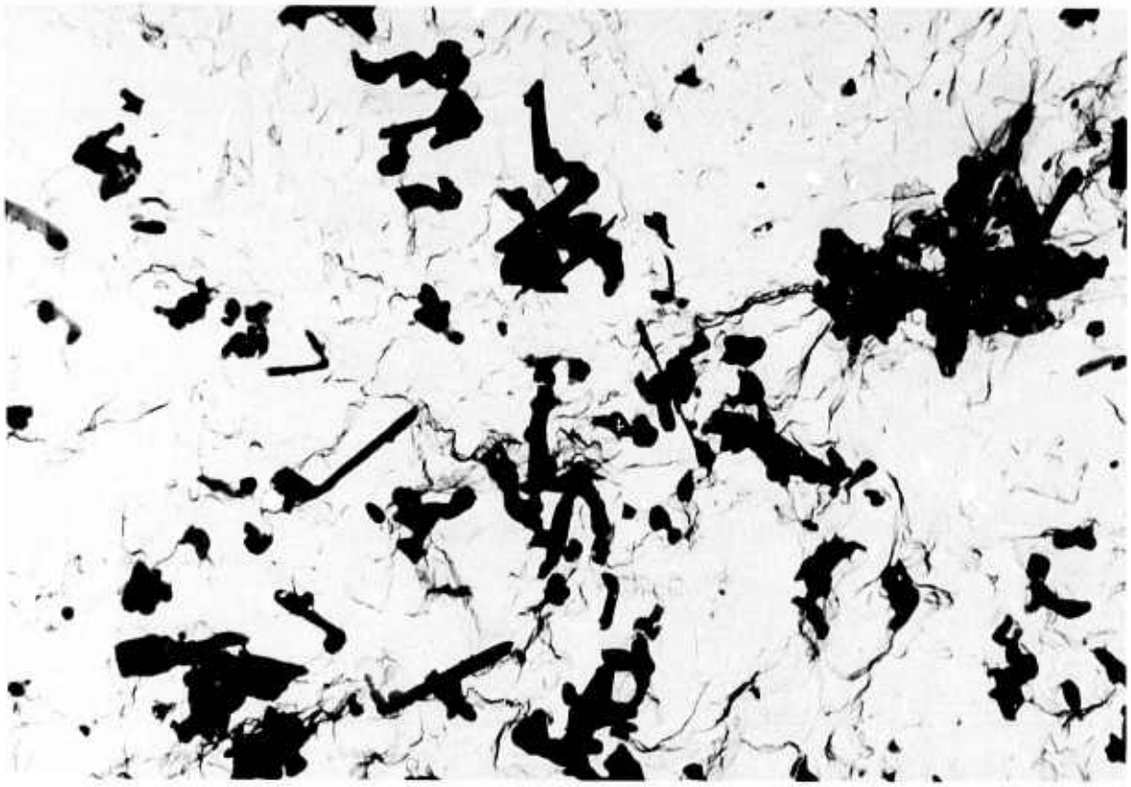


Figure 5.43 Microstructure of Silicon Nitride of Phase Composition 75% Alpha, 25% Beta 24,800X



Figure 5.44 Microstructure of Silicon Nitride of Phase Composition 10% Alpha, 90% Beta 24,800X

Oxidation of Reaction-Sintered Silicon Nitride

The purpose of this study was to define the oxidation characteristics of injection molded silicon nitride. The study involved measuring changes in weight with the purpose of (1) defining the oxidation kinetics, (2) studying the effect of phase composition on the oxidation kinetics, and (3) correlating the changes in weight with the amount of oxidation products formed. The phase compositions were chosen to give a wide range of α/β ratios.

The oxidation experiments were conducted in a static air-atmosphere furnace. The samples were mounted in a holder and inserted into the furnace while at temperature. After the designated time period had elapsed, the samples were removed from the hot furnace and weighed on a Mettler Balance.

Fig. 5.45 shows the weight gain (ΔW expressed per unit of geometric surface area) as a function of time at various temperatures. These results are shown for two samples of silicon nitride, one of high alpha and the other of high beta composition. As can be observed, the largest weight gains were observed for the lowest temperatures tested, and the lowest weight gains were observed for the highest temperatures. The high temperature samples developed a glassy coating during testing. This coating seemed uniform and coherent. After one or two hours, visible changes in the surface could be noted, showing that this surface coating started to develop after a short time. The low temperature samples did not develop any visible coating during the life of the test. The weight gain curves could be explained on the basis of this surface coating. At high temperatures, the coating develops rapidly and slows the oxidation reaction. As the coating becomes coherent, the oxidation reaction becomes a diffusion controlled process. At the low temperatures, since no protective coating is formed, the oxidation can proceed at a much faster rate.

Attempts were made to define the kinetics of the oxidation. The data was found to best fit the parabolic oxidation law:

$$\left(\frac{\Delta W}{\text{Area}}\right)^2 = kt + C_1$$

where k is the rate constant and C_1 is a constant of integration. However, when this data was applied to the Arrenius equation, the results showed an incorrect temperature dependence. It is felt that the problem lies in the choice of the value for area in the ΔW/Area term. The data was calculated using the geometric surface area of the test sample. However, since oxidation occurs at least partially on the interior of the sample, due to porosity, it is reasoned that a more correct choice of area would be the BET surface area, which is a measure of the total surface area of a material. This analysis would require data of surface area as a function of time at temperature. Experiments of this type were attempted, however, the results were not reproducible due to the small values obtained for the surface area.

Fig. 5.45 also shows the oxidation as a function of phase composition of the silicon nitride. For each temperature studied, the high alpha material exhibited larger weight gain. Again, it is felt that this is a function of the surface area of the material. The BET surface area analysis conducted on injection molded silicon nitride showed that the high alpha material has a higher surface area. Therefore, if the proper normalizing factor were employed, it is felt the oxidation rates would be similar.

The effect of the glassy coating on further oxidation is shown in Fig. 5.46. Test bars treated at 2500°F for 125 hours were returned to room temperature and further tested at 2030°F. The weight gain for the low temperature is the second portion of the curve. As can be seen, the weight gain for the 2030°F

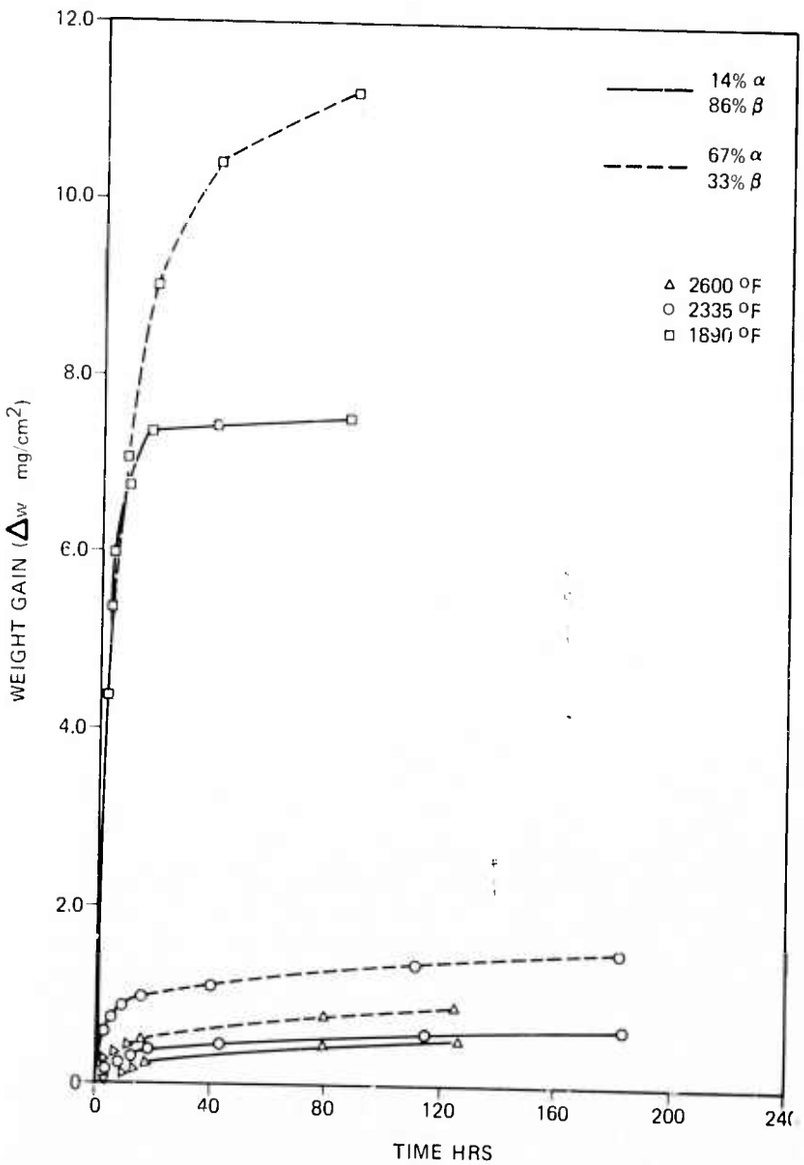


Figure 5.45 Oxidation of Silicon Nitride

treatment is less than the weight gain for the 2500°F treatment for a constant time. This can be compared to the weight gain at 2030°F without prior heat treatment (Fig. 5.45), which is approximately ten times the weight gain at 2500°F. This shows that the glassy coating formed is a protective one, and acts to retard the oxidation process.

The x-ray diffraction analysis of the samples indicated that the oxidation product was cristobalite. Hence the net oxidation equation is:

$$Si_3N_4\ (s) + 3O_2(g) \rightarrow 3SiO_2(s) + 2N_2(g)$$

According to this equation, a one percent weight gain is equal to the formation of 2.8 weight % of SiO_2. Table 5.6 shows the amount of cristobalite as calculated from measured weight gain, compared to the amount of cristobalite determined by x-ray analysis, for two samples. As can be seen, the percent cristobalite calculated from the weight gain shows a reasonable agreement to the determined amount by x-ray for the sample tested at 1890°F. However the comparisons for the sample tested at 2500°F shows a rather poor

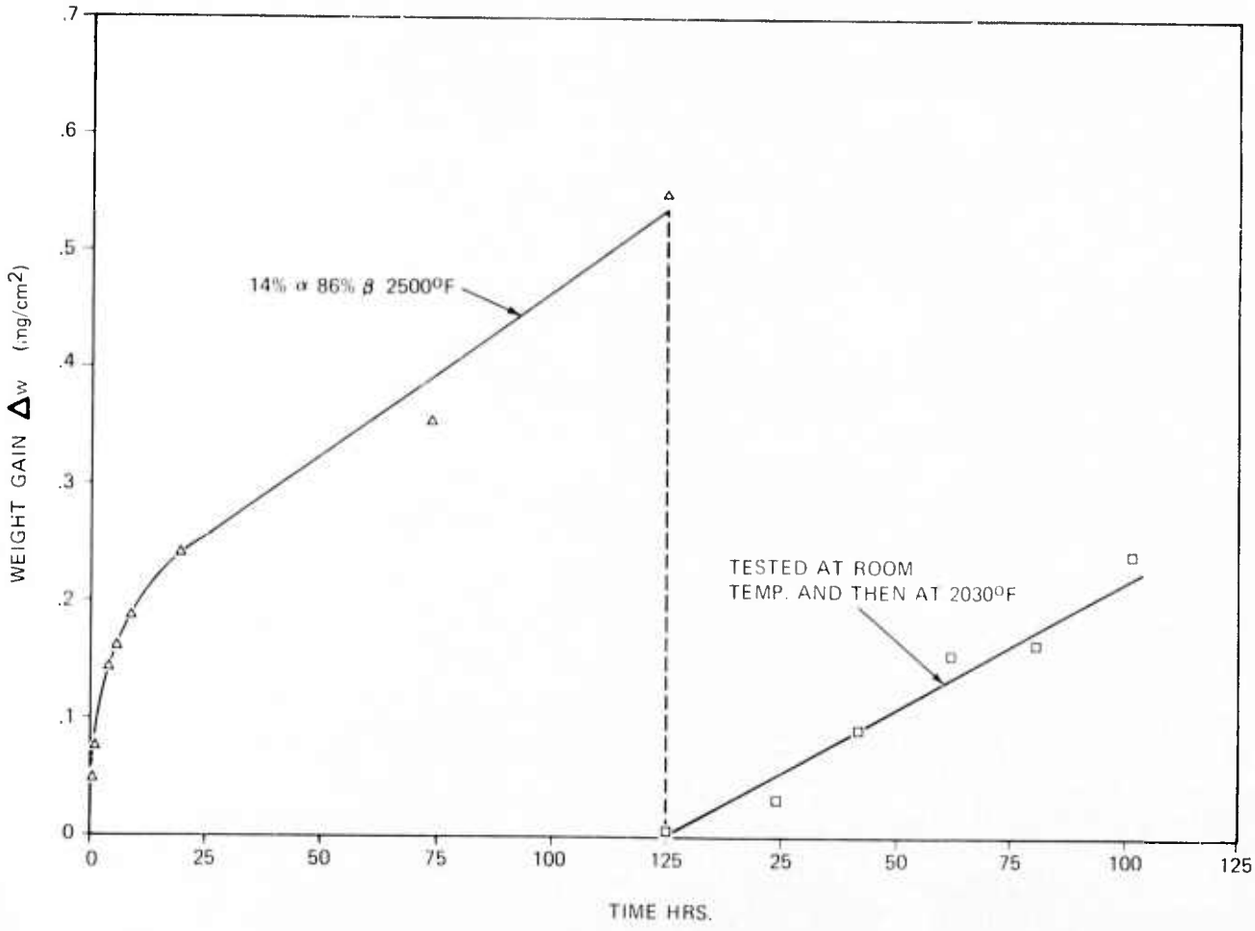


Figure 5.46 Effect of Glassy Coating on Further Oxidation

agreement between the calculated and analyzed amounts of cristobalite calculated from the weight gain shows a reasonable agreement between the calculated and analyzed amounts of cristobalite. This could possibly be due to the technique employed to measure weight gain. Cooling the sample to room temperature could cause some of the coating to pop off due to the high volume expansion of the cristobalite, and consequently effect the weight gain results.

TABLE 5.6

WEIGHT GAIN OF SILICON NITRIDE

Firing Cycle Phase Composition	ΔW (mg)	ΔW%	% Cristobalite (X-Ray)	% Cristobalite (Calculated)
1890°F - 179 hrs. 14α, 86%β	81	2.4	7.8	6.8
2500°F - 127 hrs. 14α, 86%β	6	0.2	2.4	0.6

Fig. 5.47 shows the concentration gradient of cristobalite as determined by x-ray analyses within the oxidation test specimens. It should be noted that when treated at a high temperature, the cristobalite forms primarily on the surface. The low temperature treatment causes cristobalite to form throughout the entire sample.

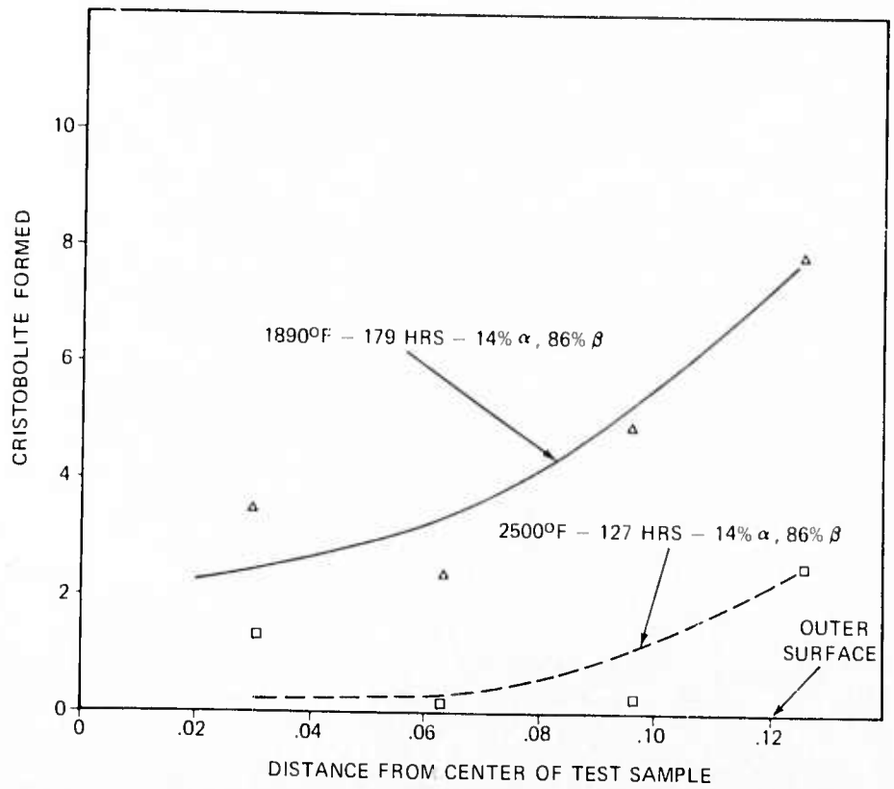
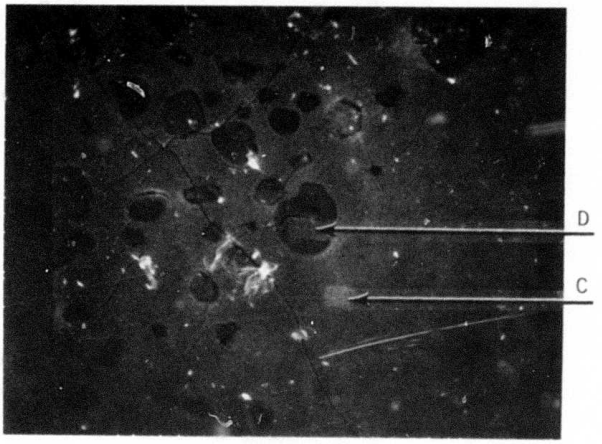
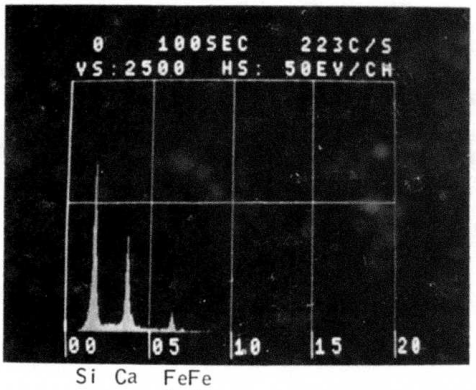


Figure 5.47 Profile of Cristobalite Formation

The glassy coating was analyzed using a non-dispersive x-ray technique in conjunction with the scanning electron microscope. Fig. 5.48A shows a typical glassy region. As can be seen, the glass is highly crazed, and does not appear to completely wet the surface. Elemental analyses were performed on the regions marked C and D, and the results are shown in Fig. 5.48B and Fig. 5.48C. The glassy region C shows high concentrations of silicon, calcium and iron. Table 5.7 shows analytical data on impurities present in several samples of reaction-sintered Si_3N_4. Calcium and iron constitute the major impurities. The region not wetted by the glass in region D shows the presence of silicon only. This confirms that the glassy coating is an iron-calcium-silicate glass.





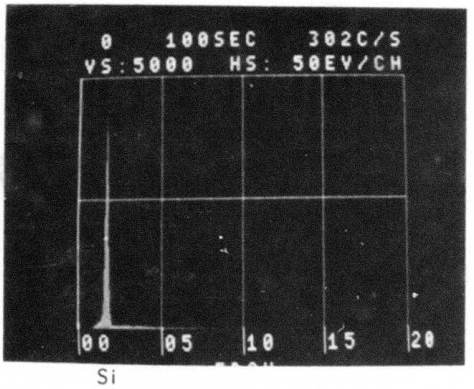


Figure 5.48 Analyses of Glassy Coating
5.48a Glassy Region. 600X
5.48b Analysis of Region C
5.48c Analysis of Region D

TABLE 5.7

IMPURITY LEVEL OF REACTION-SINTERED SILICON NITRIDE (wt %)

	A	B	C	D
Fe	1.05	.35	.76	.35
Al	.55	.30	.32	.30
Ca	.40	.20	.03	.05
Zn	<.01	<.01	.02	<.01
W	<.01	.15	--	.15
Co	<.01	.10	<.01	.10
V	--	.10	--	.10
Totals	2.0	1.20	1.13	1.05

Effect of Impurities on Hot MOR

The strength of injection molded Si_3N_4 was studied as a function of temperature. Four batches of material were tested, with the purity of the starting silicon metal as the principle variable. The major differences are the level of iron and calcium impurities. The high levels of tungsten cobalt and vanadium impurities in nitrided samples B and D (Table 5.7) are due to milling. The total impurity level was found to be between 1.0 and 2.0 wt percent.

Test bars were formed by injection molding and nitrided under identical conditions, with the phase composition held at 60% α/40% β Si_3N_4. Samples A and C (Table 5.7) also contained a minor amount of FeSi impurity (approximately 2 wt. % as determined by x-ray diffraction).

The transverse strength of the samples was determined at various temperatures in 3 point bending. The curve of strength vs temperature is shown in Fig. 5.49. The results are expressed as a percent of the room temperature strength. Ten samples were tested at each temperature. The distribution bars have been omitted in order to better show the trend in the data. Samples A and B (Table 5.7), both high in Ca but of different Fe impurity levels are statistically similar. A slight decrease in strength is observed up to 1600°F, followed by a large increase in strength at 2000°F. Above 2000°F, the strength again decreases. Noakes and Pratt[8] observed the same behavior in their study of reaction-sintered Si_3N_4. It should be noted that the strength at 2400°F has decreased below the room temperature value.

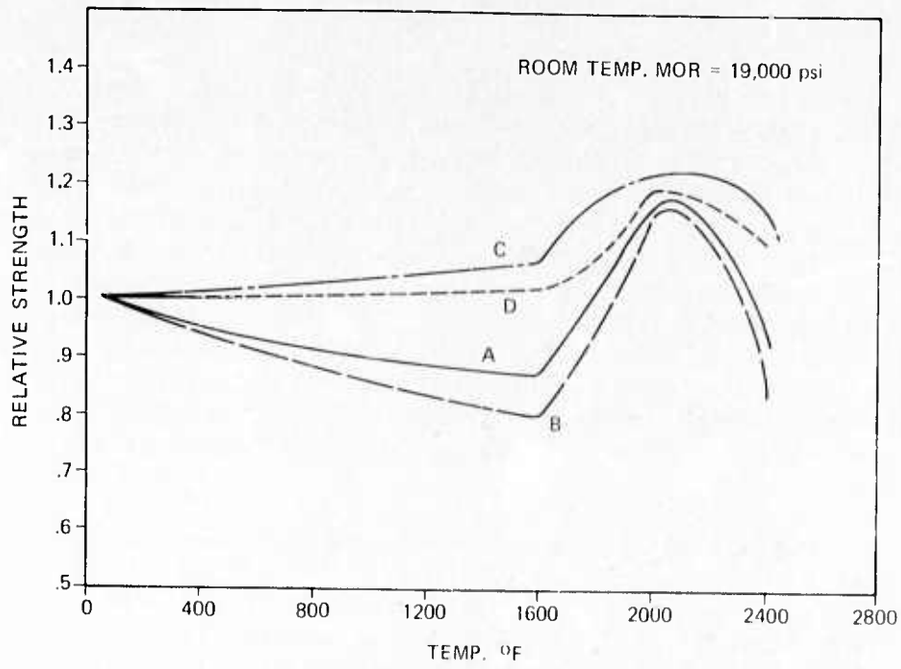


Figure 5.49 Transverse Strength of Silicon Nitride Compositions vs Temperature

The strength of samples C and D (Table 5.7), both low in Ca but of different Fe impurity levels, again are statistically identical; however, they are different from the strength levels of samples A and B at two temperatures -1600°F and 2400°F. It should be noted that no decrease in strength was observed up to 1600°F; however, more significantly, the strength at 2400°F is still above the room temperature strength.

Since both high Ca and low Ca samples are statistically identical, but have large differences in iron content, it can be concluded that iron does not play a primary role in the high temperature strength of silicon nitride. However, the variation in the calcium impurity level did have a significant effect on the high temperature strength, especially at 2400°F. Electron microprobe studies of the test bars showed that the iron, calcium and aluminum impurities were evenly distributed throughout.

Effect of Nitriding Cycle on Physical Properties of Silicon Nitride

The present nitriding cycle consists of 24 hours at peak temperatures between 2100°F and 2300°F, followed by 24 hours at 2660°F. This cycle was determined earlier as one that gave suitable physical properties. Work was undertaken to determine the effect of varying the nitriding cycle on the physical properties of reaction-sintered silicon nitride.

Initial tests were run in a tube furnace using a constant nitrogen flow and varying the sintering times at 2300°F and 2660°F. Test bars were nitrided and the physical properties determined. To date, only the flexural strength of the samples has been investigated.

Fig. 5.50 shows the average tranverse strength (MOR) as a function of time at 2300°F and 2660°F. The samples were 4 inches long and 1/4 inch in diameter, and were broken on a fixture using 1 inch top span and 3 inch bottom span at a cross head speed of 0.10 inches/min; at least six samples were measured for each data point. It can be noted that the baseline strength of 15.5 ksi when nitrided for 24 hours at 2300°F followed by 24 hours at 2660°F can be improved. The data revealed that reducing the 2660°F nitriding time results in a notable improvement in strength. For example, the 36/4 nitriding cycle exhibited a flexural strength of 20.3 ksi compared to 15.5 ksi at the 24/24 baseline condition. This represents an increase of 25%.

An examination of the microstructure revealed the 36/4 material to be more uniform than the 24/24 silicon nitride material. This can be seen in Fig. 5.51 which shows that the 36/4 material has fewer large crystal clusters and in general smaller crystals within these clusters. The 24/24 material, shown in Fig. 5.52 has much larger crystals within the clusters.

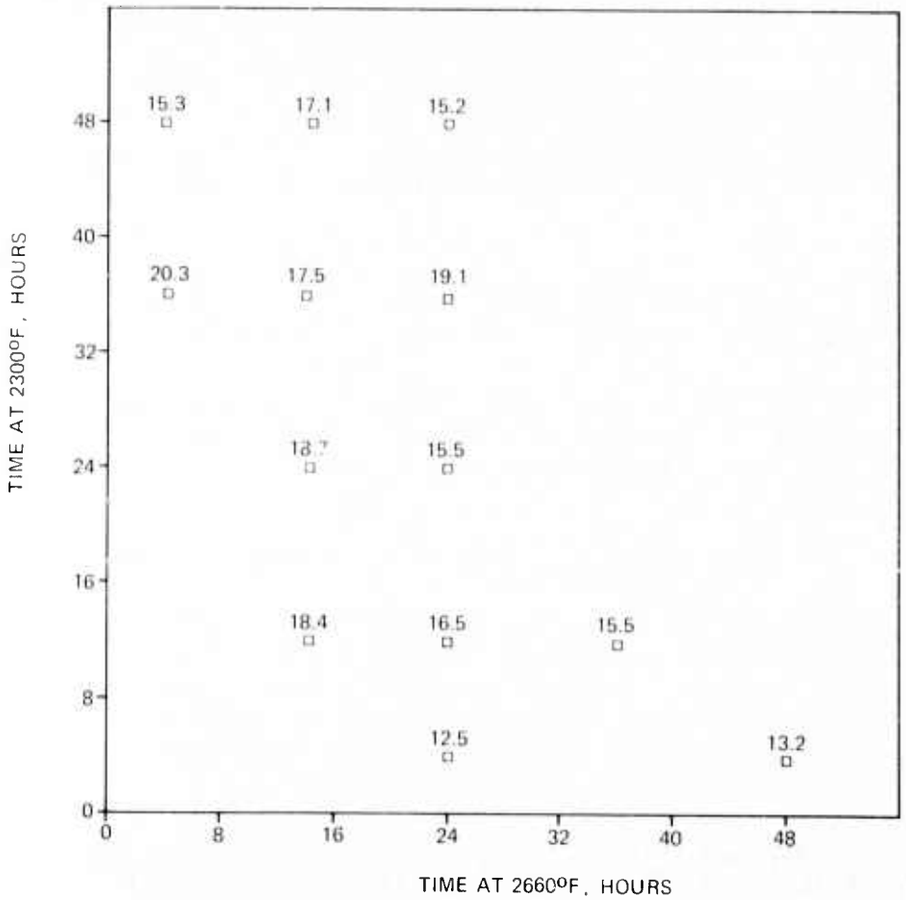


Figure 5.50 Plot of Transverse Strength of Silicon Nitride vs Various Time-Temperature Relationships

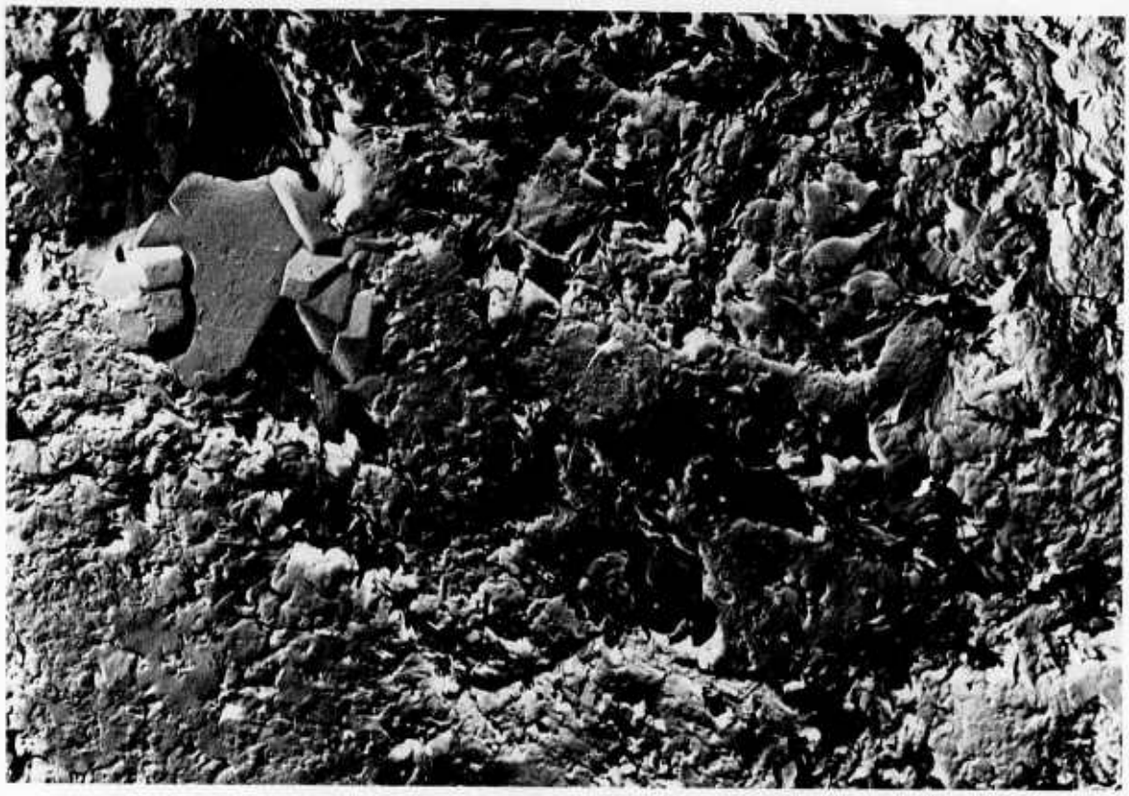


Figure 5.51 Microstructure of Silicon Nitride Reaction Sintered for 36 Hours at 2300°F Followed by 4 Hours at 2660°F. 9800X



Figure 5.52 Microstructure of Silicon Nitride Reaction Sintered for 24 Hours at 2300°F Followed by 24 Hours at 2660°F. 9800X

This work shows that the properties of the reaction-sintered material can be affected by the microstructure. Figure 5.50 reveals a trend toward higher strengths resulting from shorter nitriding times at higher temperatures. Further work must be done to fully optimize this cycle.

The alpha/beta Si_3N_4 ratio was determined on material nitrided on each time-temperature firing schedule. It was observed that for all of the samples nitrided, the phase composition was at least 75% α Si_3N_4 with the balance being β Si_3N_4. This indicates that the time at temperature in the nitriding cycle, at least in this study, did not significantly affect the phase composition. The flexural strength of the material did change significantly, even though the α/β ratio was held constant. This points out the importance of the microstructure, and supports the conclusion that the α/β ratio does not significantly affect the mechanical properties of reaction-sintered silicon nitride.

5.2.2 MICROSTRUCTURAL CHARACTERIZATION OF FULLY DENSE SILICON NITRIDE AND SILICON CARBIDE

Introduction

The importance of microstructure and its effect upon the mechanical properties of a material cannot be overstated. In the case of hot pressed silicon nitride and silicon carbide, grain morphology and composition significantly influence the mechanical and thermal properties. Since impurities and flaws control failure probability, the microstructure is fundamental to the performance and reliability of ceramic components. It is also a useful tool for material improvement and quality control.

A definite correlation between the high temperature flexural strength and impurity concentration has been established for Norton HS-130 silicon nitride. Low density inclusions, which degrade silicon nitride at all temperatures, have also been identified. Some fractures, characteristic to the microstructure of Norton's hot pressed silicon carbide are reported, and fracture studies of chemically vapor deposited silicon carbide are shown.

Silicon Nitride

Two grades of Si_3N_4, designated HS-110 and HS-130, were obtained from the Norton Company in the form of hot-pressed billets 6.3 x 6.3 x 1.3 inches thick. Detailed characterization of both materials has continued with particular emphasis on flaws that are related to the powder processing and hot pressing procedures and impurity content and distribution.

Spectrographic analyses of Norton HS-130 silicon nitride have been obtained for 10 billets. Typical results appear in Table 5.8. An

Table 5.8

SPECTROGRAPHIC ANALYSIS, HOT PRESSED Si_3N_4 (wt %)

Billet #	Al	B	Ca	Cr	Fe	K	Mg	Mn	Na	Ni	Ti	W	C
011072 B1 (HS-110)	0.8	0.01	0.5	0.2	0.6	0.01	0.6	0.02	0.01	0.01	0.01	~ 3	0.41
309902-1 (HS-130)	0.1	0.001	0.03	0.04	0.7	0.004	0.7	0.04	0.02	0.01	0.02	~ 4	0.43
309902-2 (HS-130)	0.1	0.02	0.07	0.04	0.6	0.003	0.8	0.03	0.004	0.01	0.02	~ 3	0.41
309902-3 (HS-130)	0.2	0.01	0.03	0.04	0.6	0.003	0.7	0.03	0.006	0.01	0.02	~ 3	0.36
309902-9 (HS-130)	0.08	0.001	0.03	0.04	0.4	0.006	0.6	0.03	0.008	0.01	0.02	0.5	0.07
309902-10 (HS-130)	0.09	0.004	0.04	0.04	0.5	0.004	0.5	0.03	0.008	0.01	0.02	0.3	0.04

ACCURACY: W and Fe by visual reading; accuracy 0.3 to 3 times amount present.
All other elements by direct reading; accuracy ± 50% of amount present.

analysis of the lower purity HS-110 material is included for comparative purposes. While impurities have been reduced in HS-130, significant variations in impurity level still persist, as shown in Table 5.9.

The combined concentration of calcium, sodium, and potassium is critical to the high temperature flexural strength of silicon nitride as indicated in Fig. 5.53. At 2370°F, for example, a reduction in strength from 55,000 psi to 30,000 psi was measured when the Ca concentration changed from 0.03 to 0.09%. The effect of composition on the creep properties is expected to be equally significant.

Table 5.9

RANGE OF IMPURITY CONCENTRATIONS (wt %) IN 10 BILLETS OF HS-130 GRADE Si_3N_4

Al	B	Ca	Na	K	W	C
0.07-0.12	0.001-0.03	0.02-0.08	0.003-0.020	.003-.010	0.3-4.0	0.03-0.42

Variance within each billet (two samples per billet) was in the range of accuracy. Variances in the concentrations of the other impurities (Table I) were also within the range of accuracy.

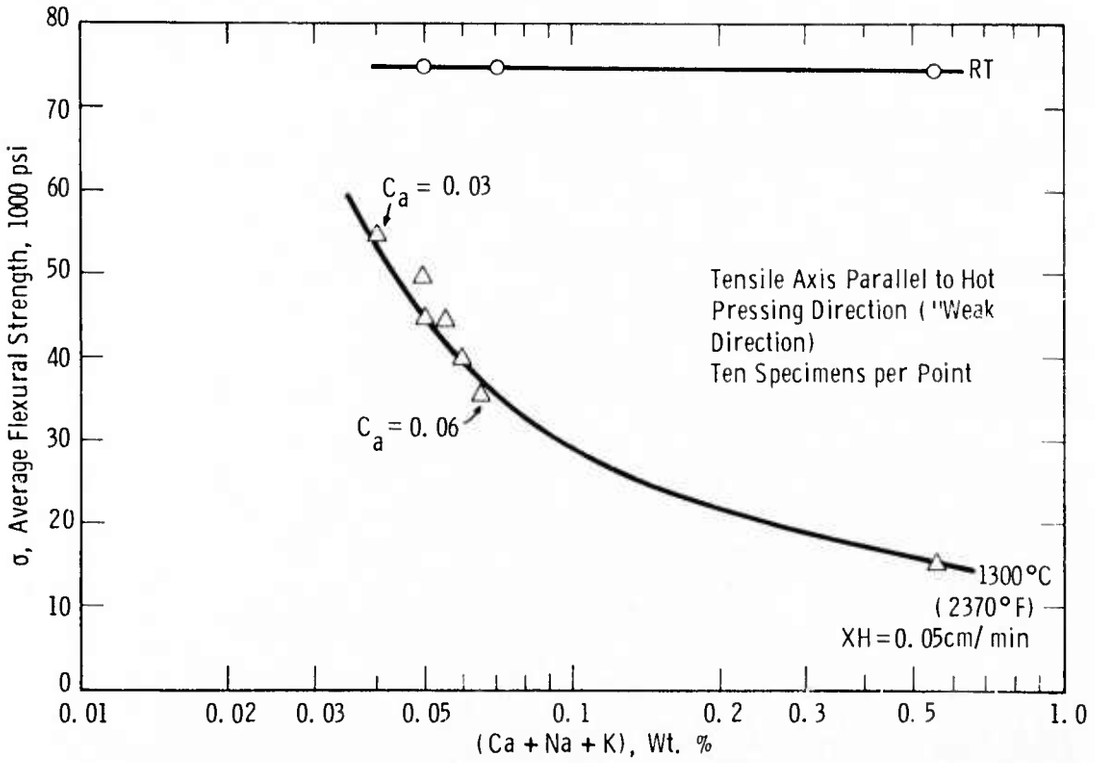


Figure 5.53 Effect of Impurities on Flexural Strength (4 pt. bend) of Silicon Nitride

The distribution of major impurity elements was examined by Auger analysis. Specimens of square cross section (0.1 in x 0.1 in) were placed in a vacuum chamber and evacuated over night at a pressure of 10^{-9} torr. The specimens were then broken to expose a virgin fractured surface. Since extensive examination of a large number of fracture surfaces indicates that the fracture is predominantly intergranular at all temperatures between RT and 2500°F, attention was paid to the grain boundary phase.

Semi-quantitative results were obtained by measuring the peak-to-peak height (I_x) of the major peak of each element present. From the known relative sensitivity, S_x, of each element with respect to a silver standard and the scale factor, K_x, the concentration of element x in atomic percent is given by

$$C_x = \frac{I_x 100}{S_x K_x} \Bigg/ \Sigma \frac{I_a}{S_a K_a}$$

where the sum is over one peak from each element present on the surface.

A typical Auger trace of a freshly fractured surface of HS-130 silicon nitride is shown in Fig. 5.54. Similar traces were obtained for HS-110 material. The major cation impurities were Ca, Na, K, and Mg, which combine with silicon, oxygen, and nitrogen to represent the grain boundary composition.

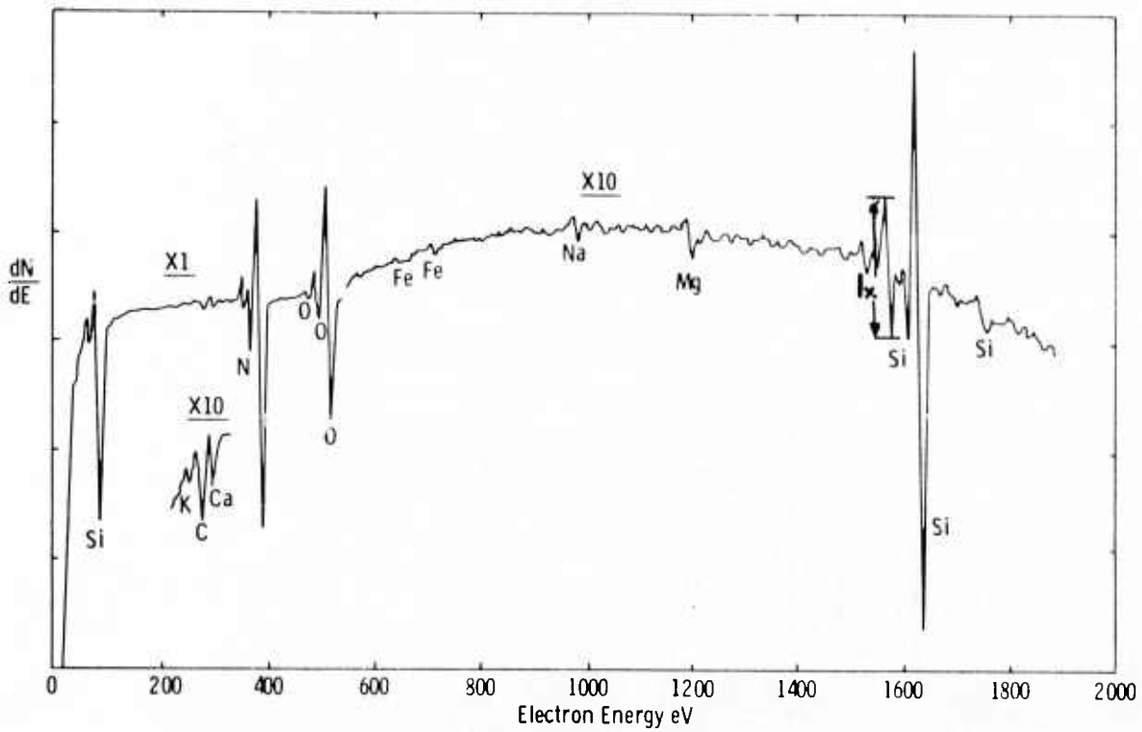


Figure 5.54 Typical Auger Analysis Trace, of a Fresh Fracture Surface

It was possible to reveal the transition and bulk composition by sputtering the fresh fractures in argon to remove material 2500 Å from these surfaces in 40 Å increments. The results of analyses after sputtering for both grades of Si_3N_4 appear in Fig. 5.55. Nitrogen

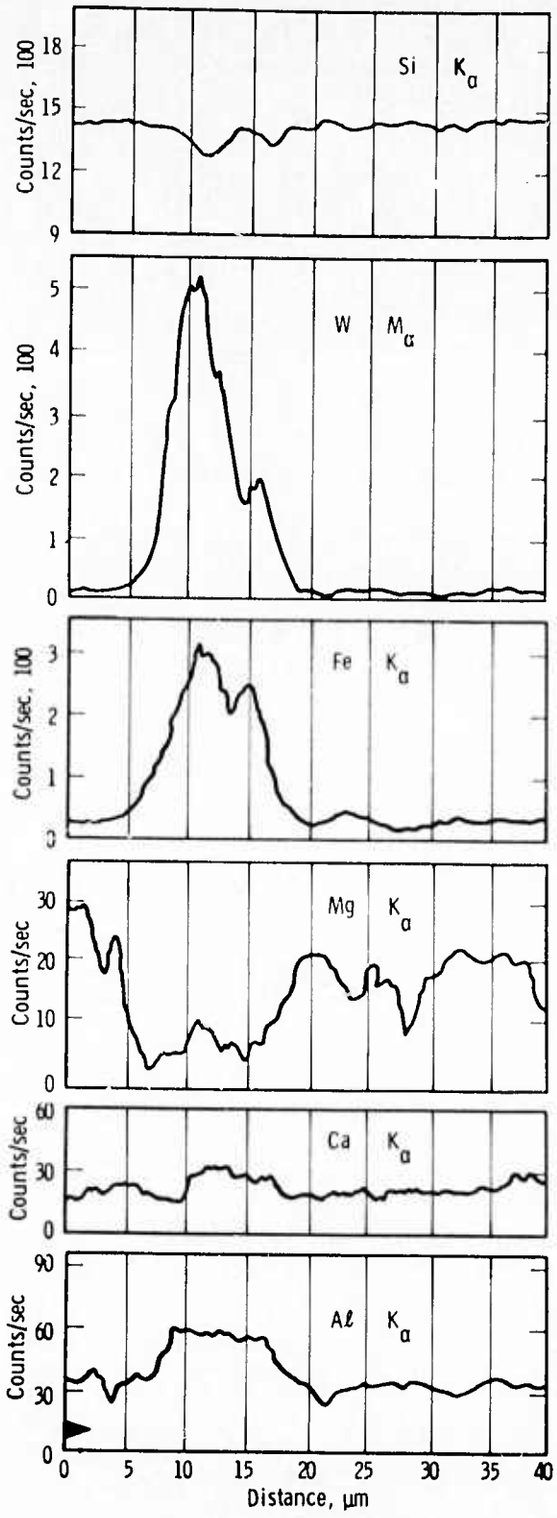


Figure 5.55 Elements Distribution Profiles, Hot Pressed Silicon Nitride Auger Analysis

and iron increase in the bulk composition while oxygen and the alkalies decrease.

The oxygen concentration converted from Auger profiles (Table 5.10) is consistent with AMMRC neutron activation analysis which show 2-5 and 6-9% oxygen in HS-130 and HS-110 silicon nitride, respectively.* (4) The high level of oxygen at the boundary indicates a glass phase composition approaching:

HS-110: $2MgO \cdot 2Al_2O_3 \cdot 9CaO \cdot 22SiO_2$

HS-130: $CaO \cdot MgO \cdot 8SiO_2$

The high concentration of CaO in the boundary glass phase is considered significant in that it can account for the substantial difference in high temperature creep strength between the HS-110 and HS-130 Si_3N_4. Preliminary creep data suggest that a major contribution to the observed deformation comes from the grain boundary sliding. The effect of Ca, and to a lesser degree Al, K and Na, can thus be related to an appreciable decrease in the viscosity of silicate glasses with small additions of CaO.(4)

Extensive x-ray radiography was conducted on flexural test specimens in an attempt to correlate detectable flaws with strength degradation. Groups of 10 specimens from each of five HS-130 Si_3N_4 billets listed in Table 5.8 were radiographed. Almost all specimens from billets 1, 2 and 3 showed high density spots. No high density spots were seen in specimens machined from billets 9 and 10. After testing all 50 specimens, it was quite obvious that the majority of the fractures in specimens tested both at 1800°F and 2370°F were not associated with the high density spots. On the other hand, in most of the samples that failed at stresses below the standard deviation range of the respective group, a white, powdery, particle was found to be associated with the fracture origin marked by an area of slow crack growth (Fig. 5.56). Scanning electron micrographs of an inclusion, densified Si_3N_4, and BN powder, are shown in Fig. 5.57.

Table 5.10

CONCENTRATION OF ELEMENTS
WITHIN THE Si_3N_4 GRAIN (w/o)

(Data Converted from Auger Profiles)

	Si	N	O	Fe	Al	Mg	Ca
HS-110	balance	34	8	1.2	1.4	0.9	0.8
HS-130	balance	36	6.5	1.2	---	0.7	---

*Data supplied by H. Priest.

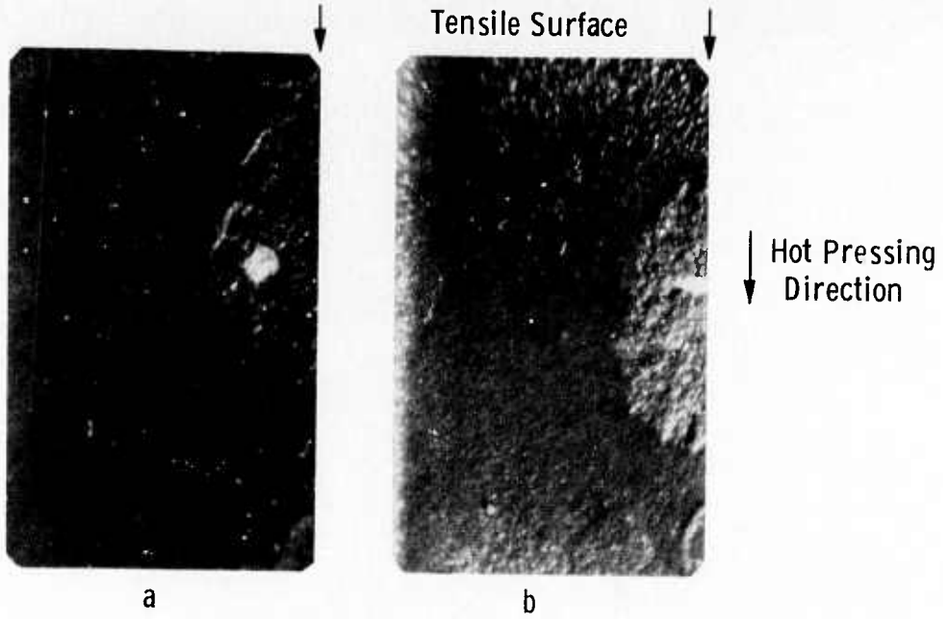


Figure 5.56 Light Micrographs Showing Orientation of Lenticular, Non-Densified Silicon Nitride Inclusion in Flexural Test Specimens with Respect to Hot Pressing Direction

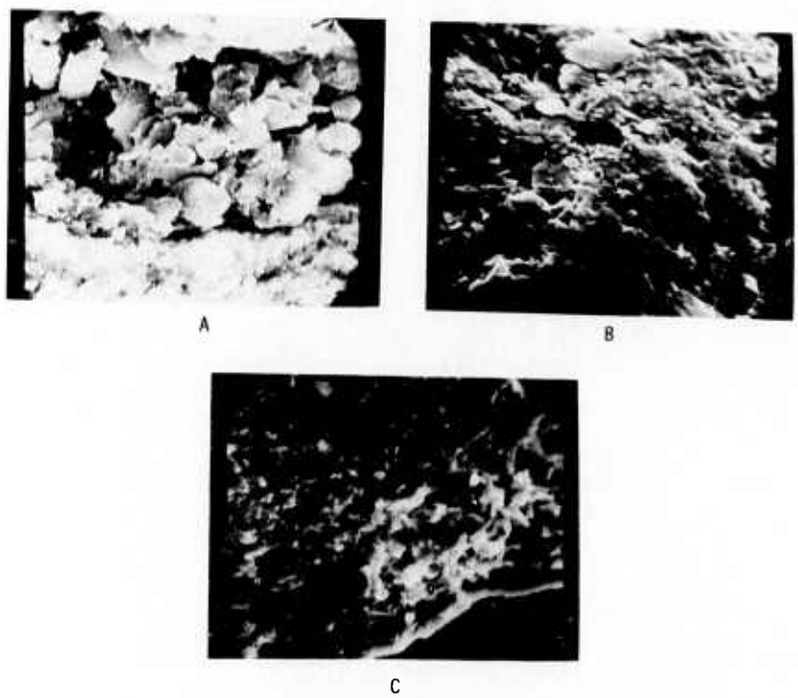


Figure 5.57 Scanning Electron Micrographs
A. White Inclusion in Si_3N_4 - 2800 X
B. BN Powder - 5500 X
C. White Inclusion in Si_3N_4 Matrix - 2000 X

Microprobe traces taken across these inclusions showed a lower concentration of Si and a higher non-uniform concentration of carbon, as compared to bulk Si_3N_4. A few of the inclusions were removed using a WC tool and subjected to a Debye-Scherrer x-ray diffraction. Faint lines, corresponding to hexagonal BN were seen along with strong lines from β-Si_3N_4. Laser-source emission spectroscopy also confirmed silicon but boron was only found in an inclusion from billet 1. These white powdery inclusions are considered to be small agglomerates of a non-densified Si_3N_4 which occasionally contain BN.

Pole-figure analysis indicates some preferred orientation in hot pressed Si_3N_4. Figure 5.58 is a reproduction of a (210) pole-figure obtained from a specimen from billet 309902-2. The hot pressing direction is vertical. The pole-figure (Fig. 5.58a) and the histograms (Fig. 5.58b) show that about 15% of the grains are oriented, with the basal planes within 20° of the hot pressing direction, or conversely, with the C axes within 70° of the hot pressing direction.

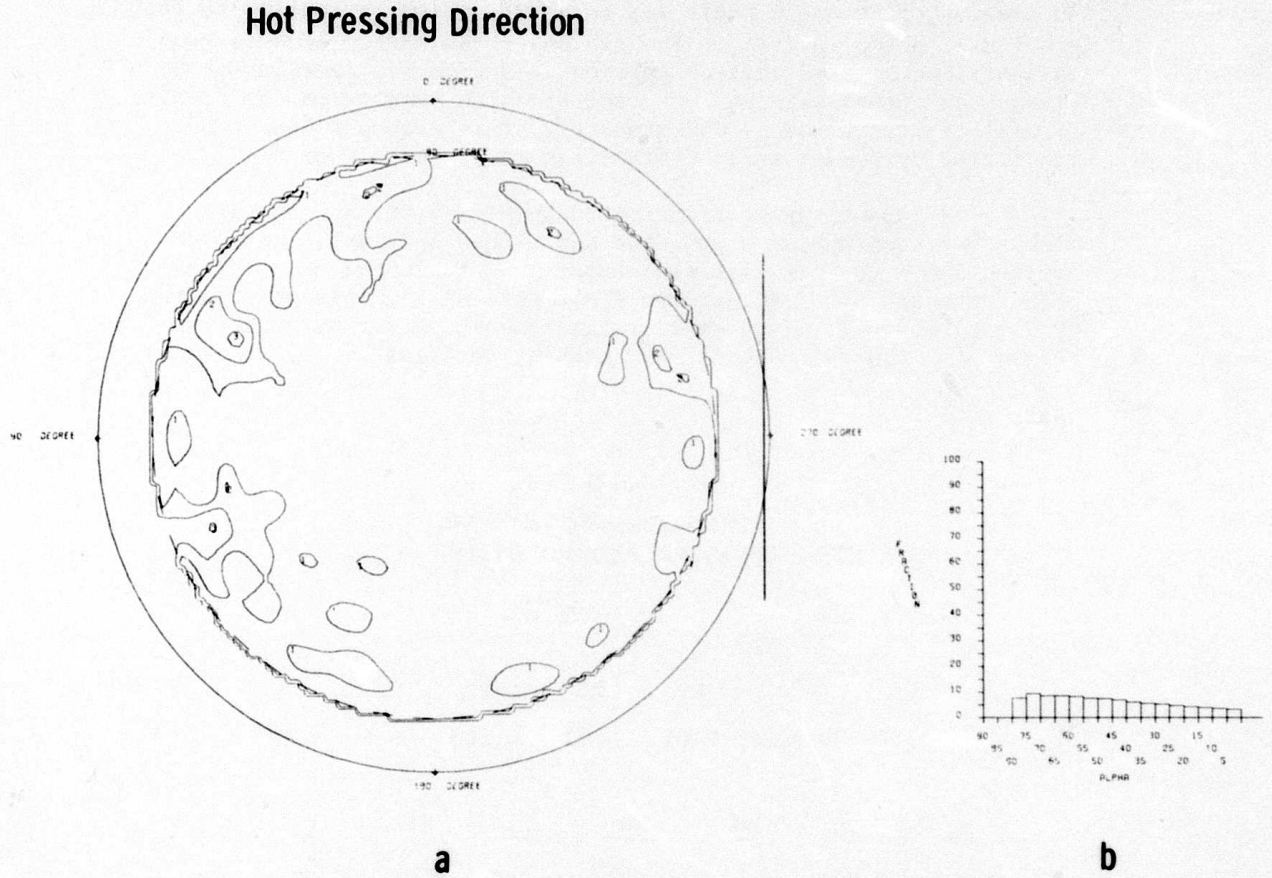


Figure 5.58 Pole Figure Analysis

Hot Pressed SiC

Typical spectrographic analysis of the major impurities in Norton hot pressed SiC is given in Table 5.11. The main impurity element is aluminum, which is added presumably to promote liquid phase sintering. Tungsten represents another major impurity which is present mainly in the form of WC, a residue of the ball milling operation. The source of iron contamination is not known. It may result from the crushing operation or it may occur as a natural impurity in the starting powder.

Powder x-ray diffraction data are shown in Table 5.12. WC is identified as the only impurity phase. Al_2O_3 was not detected indicating that it is either not present in sufficient quantity, or, more probably, that it is present as a constituent of an amorphous grain boundary phase.

The distribution of the impurities and the additives in hot pressed SiC are illustrated in Fig. 5.59. Alumina is the major constituent in the grain boundaries, which also contain a dispersion of W rich particles. Although the probe beam has to be defocused for an oxygen scan, it is apparent that the grain boundary phase contains oxygen also. An overlap of Fe and W peaks was observed, which is similar to that previously noted in Si_3N_4. In both cases the source of W is from ball milling with WC balls. Apparently during hot pressing at 3700°F, a reaction occurs between W, Fe and Si which results in the formation of a W-Fe-Si compound. Unfortunately, this compound cannot be identified by powder x-ray diffraction in either SiC or Si_3N_4.

Grain morphology is illustrated in Fig. 5.60, a scanning electron micrograph of a polished and etched specimen. Equiaxed grains, which vary in size from about 1 μm to 10 μm, are typical of hot pressed SiC. An average grain size of 3 μm was established by lineal analysis. The small bright particles are WC or W-rich inclusions. The black holes are etching cavities.

Table 5.11

SPECTROGRAPHIC ANALYSIS,
HOT PRESSED SiC, NORTON BILLET 472-2

(in wt %)

Al	B	Ca	Cr	Cu	Fe	K
1.0	0.002	0.01	0.01	0.005	0.1	0.001

Mg	Mn	Mo	Na	Ni	Ti	V	W
0.001	0.001	0.01	0.001	0.005	0.03	0.02	3-5

Table 5.12

POWDER X-RAY DIFFRACTION DATA HOT-PRESSED SiC, NORTON BILLET 472-3

(SiC Phase is a Mixture of the Hexagonal II and IV Polymorphs)

d, Å	Relative Intensity*	Phase	d, Å	Relative Intensity*	Phase
3.47	W	unknown	1.13	W	SiC
2.82	W	WC	1.09	W	SiC
2.62	M	SiC	1.045	W	SiC
2.58	W	SiC	1.015	VW	SiC, WC
2.51	S	SiC, WC	1.00	W	SiC
2.35	M	SiC	0.99	W	SiC
2.18	W	SiC	0.975	W	SiC
2.10	VW	SiC	0.955	W	SiC, WC
2.00	W	SiC	0.942	W	SiC, WC
1.87	W	WC	0.915	W	SiC
1.68	W	SiC	0.89	VW	SiC
1.60	VW	SiC	0.865	W	SiC
1.54	S	SiC	0.840	W	SiC
1.45	VW	SiC, WC	0.804	W	SiC
1.42	W	SiC, WC	0.790	W	SiC
1.33	VW	SiC			
1.31	VW	SiC			
1.29	W	SiC, WC			
1.26	W	SiC, WC			
1.23	VW	SiC, WC			
1.22	VW	SiC			
1.15	VW	WC			

* W = wear
VW = very weak
S = strong

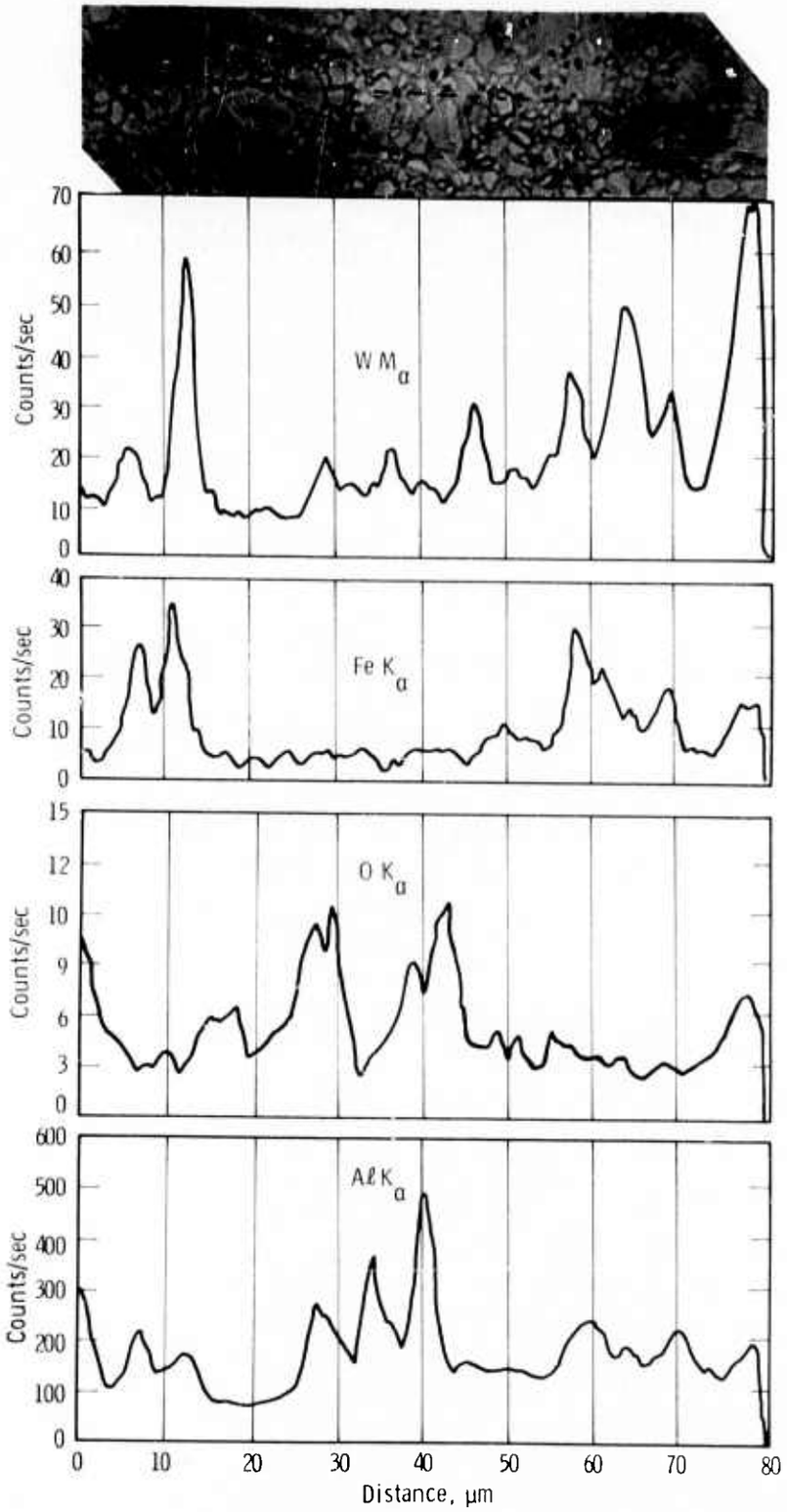


Figure 5.59 Microprobe Line Traces from Norton SiC

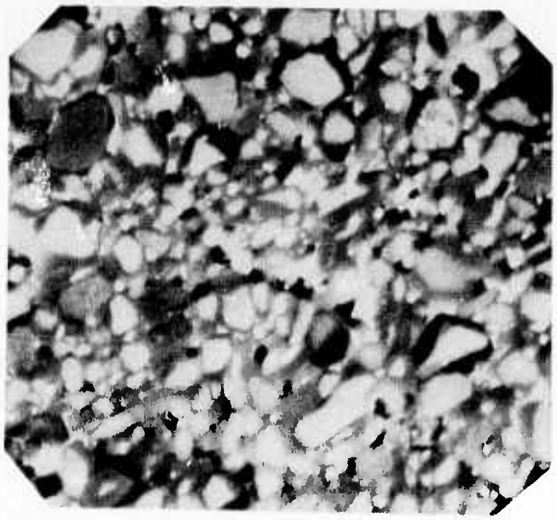


Figure 5.60 SEM Micrograph of Polished and Etched Surface of Hot Pressed SiC

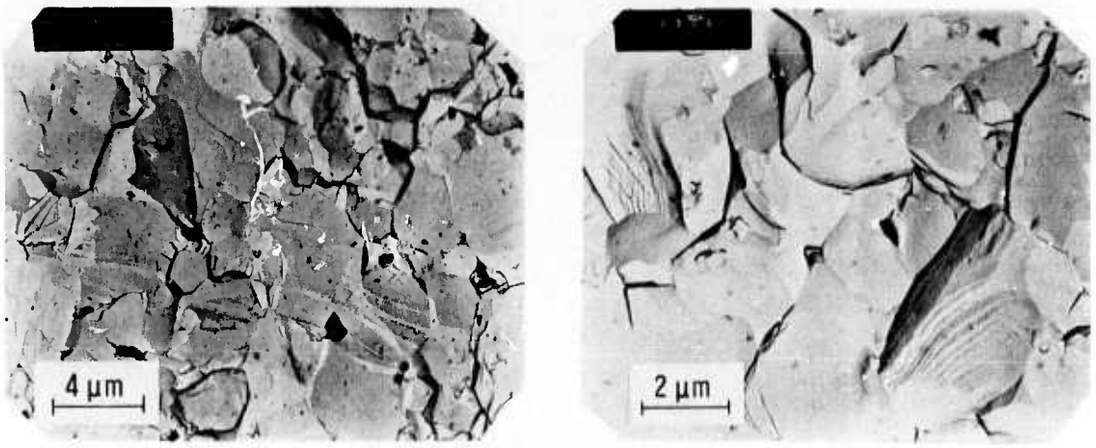
The gradual transition from a failure mode which is predominantly cleavage to predominantly intergranular is observed as a function of increasing temperature. Frequent cleavage steps and the smooth appearance of the fracture surface (Fig. 5.61) indicate that cleavage is the dominant mode of failure at room temperature. As temperature is increased to 1470°F, (Figs. 5.62 through 5.64), cleavage still prevails, but the fracture surface becomes rougher and secondary intergranular cracking is visible. Furthermore, large areas of a grain boundary phase are frequently exposed. This phase appears to have been molten at some previous time. The rounded nature of the grain edges is consistent with a liquid phase sintering phenomenon that involves partial dissolution at the grain-boundary interface. At 1832°F there is little evidence of cleavage. Intergranular cracking appears dominant in Fig. 5.65. The small square particles (Fig. 5.65b) are probably due to nucleation of a corrosion product.

Figure 5.66 shows SEM micrographs of fracture surfaces of specimens tested at 1115°F and 2000°F, respectively. The large grain in the center of Fig. 5.66a shows evidence of cleavage. The entire area shown in Fig. 5.66b contains the grain boundary phase which is somewhat lighter than the grain proper, indicating a higher molecular weight than SiC. Non-dispersive x-ray analysis (Fig. 5.67) shows that the grain boundary phase is rich in Fe.

The light phase in Fig. 5.66b is interpreted as being an Al_2O_3 rich boundary phase. Intergranular cracking is the dominant mode of failure at 2000°F.

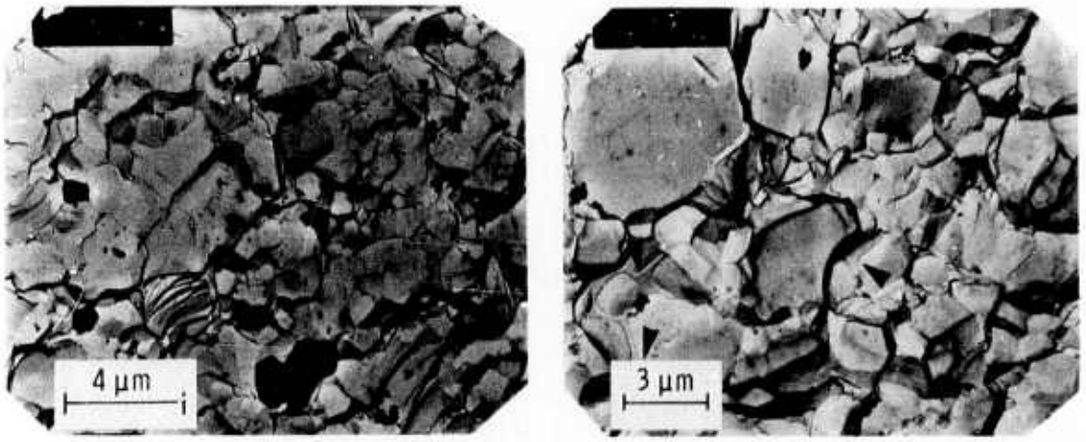
Chemically Vapor Deposited Silicon Carbide

Chemically vapor deposited silicon carbide is a high purity, non-conductive material which is extremely difficult to etch. Microstructural features were observed by examining fracture surfaces. Figure 5.68 shows a low magnification replica transmission micrograph of a specimen fractured at room temperature. Long columnar grains, about 3-5 μm wide, are typical of this material. Failure by cleavage is clearly evident.



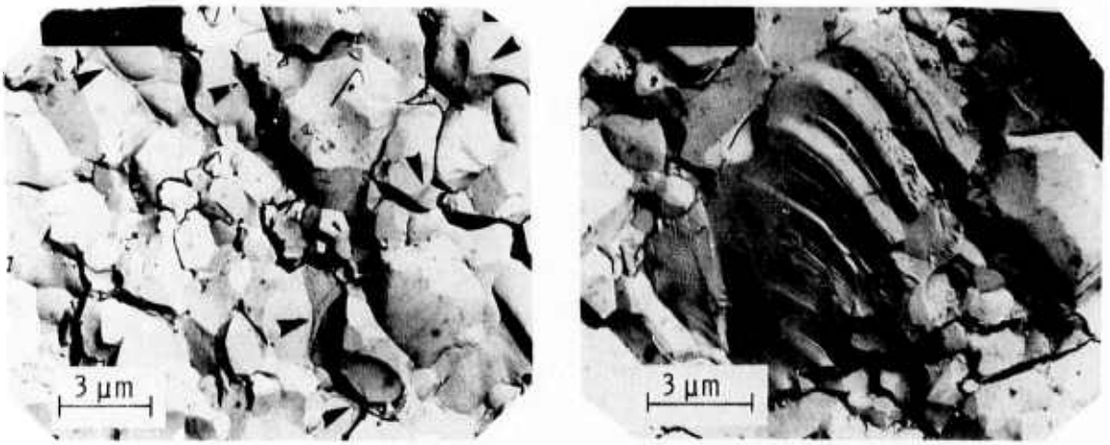
a b

Figure 5.61 Replica Transmission Micrographs of Room Temperature Fracture Surfaces - Norton Hot Pressed SiC



a b

Figure 5.62 Replica Transmission Micrograph of 752°F Fracture Surfaces - Norton Hot Pressed SiC



a b

Figure 5.63 Replica Transmission Micrographs of 1115°F Fracture Surfaces - Norton Hot Pressed SiC

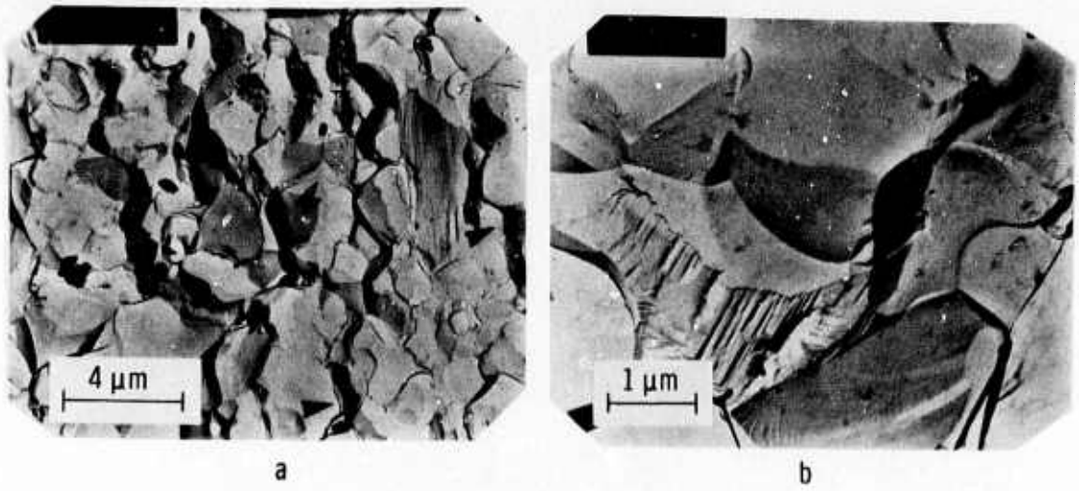


Figure 5.64 Replica Transmission Micrographs of 1472°F Fracture Surfaces - Norton Hot Pressed SiC

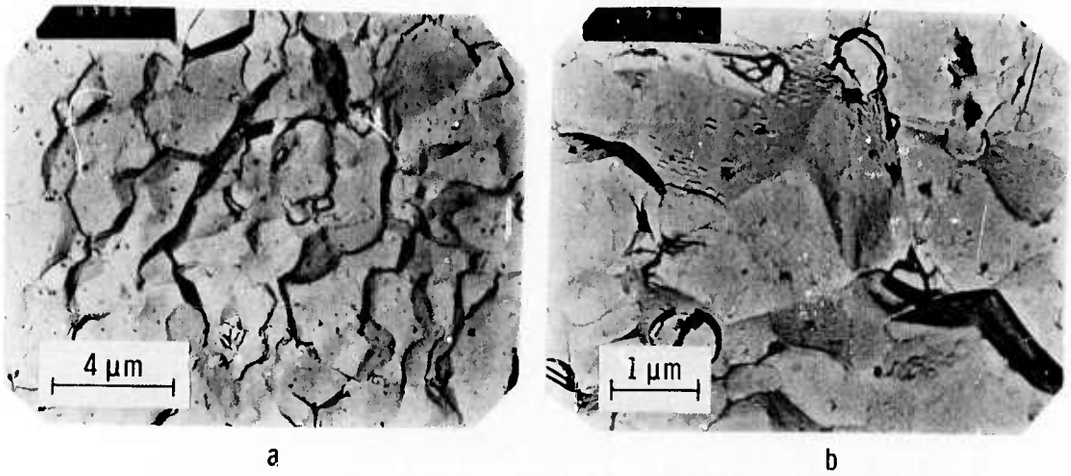


Figure 5.65 Replica Transmission Micrograph of 1832°F Fracture Surfaces - Norton Hot Pressed SiC

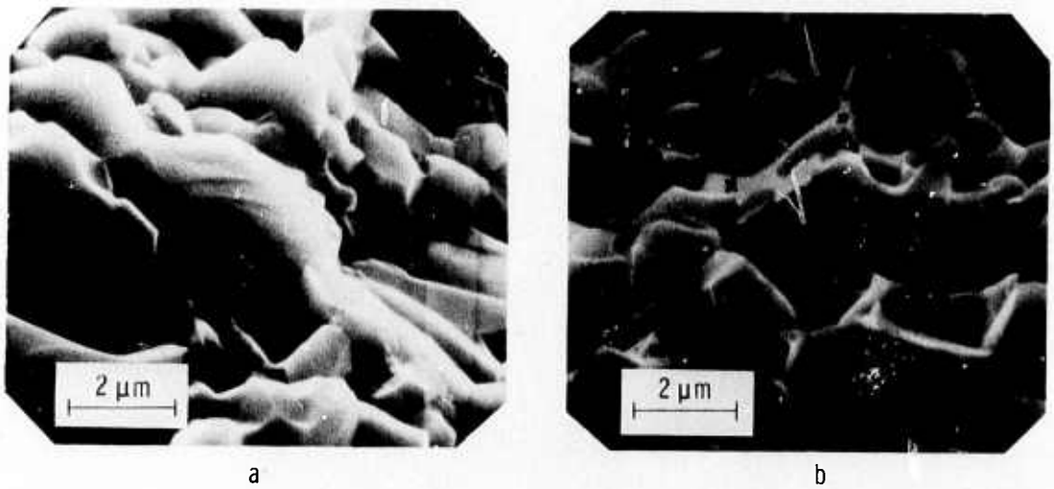


Figure 5.66 SEM Micrograph of Fracture Surfaces of Hot Pressed SiC

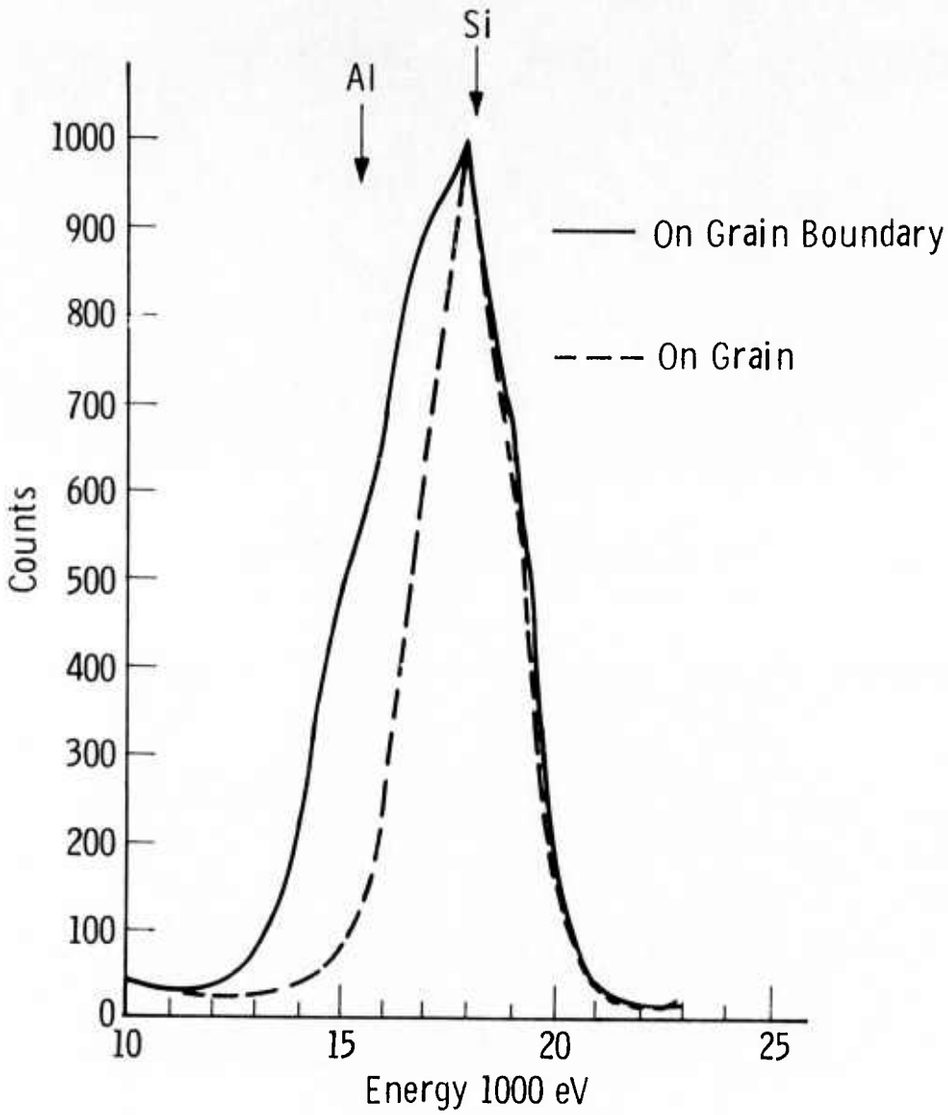


Figure 5.67 Non-Dispersive X-Ray Analysis, Fracture Surface - Norton Hot Pressed SiC

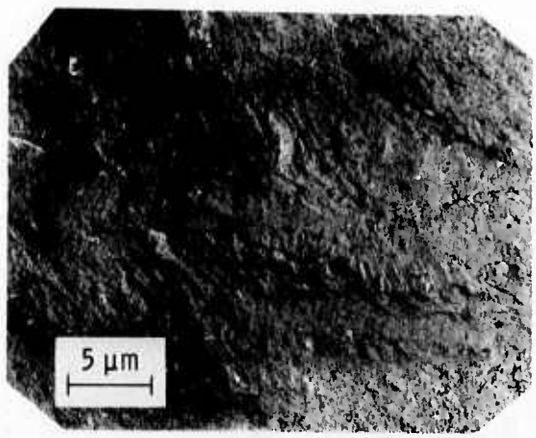


Figure 5.68 Columnar Structure in CVD-SiC Long Grains

Higher magnification micrographs are shown in Fig. 5.69. Figure 5.69a demonstrates secondary cracking along large-angle grain boundaries. A change in the direction of the cleavage steps delineates the columnar grain (Fig. 5.69b). This micrograph also shows a fine granular substructure within the columnar grains (arrows).

Fracture surfaces that were prepared at high temperature (> 2000°F) could not be examined due to the formation of a corrosion layer. Specimens tested in inert atmosphere are being studied.

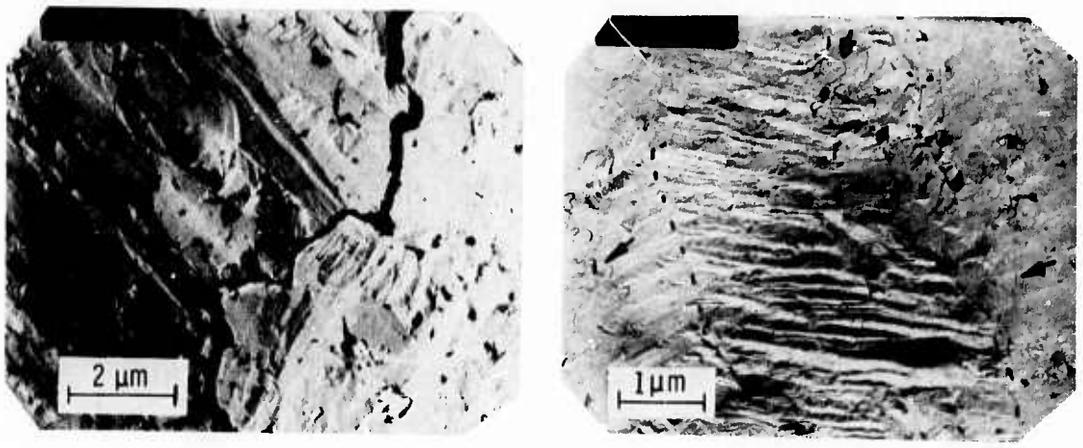


Figure 5.69 Replica Transmission Micrograph Room Temperature Fracture Surfaces - CVD-SiC

5.2.3 GAS-SOLID REACTIONS

Introduction

The work in progress to characterize the kinetic processes involved in the static oxidation and sulfidation of silicon nitride has been extended to include hot pressed silicon carbide. Thermochemical considerations, the static oxidation of silicon carbide, and the characterization of the surface oxide on SiC are discussed.

Thermochemical Considerations

When silicon carbide is exposed to oxidizing atmospheres at elevated temperatures, a passive layer of $SiO_2(s)$ is formed on the surface according to the following reactions:

$$SiC(s) + O_2 \rightarrow SiO_2(s) + CO(g) \quad (1)$$

$$SiC(s) + 2O_2 \rightarrow SiO_2(s) + CO_2(g) \quad (2)$$

At low oxygen pressures, several gaseous species, e.g., $Si(g)$, $Si_2(g)$, $Si_3(g)$, $SiO(g)$, $SiO_2(g)$ can form by the direct volatilization of this surface oxide. However, gas turbines operate with highly oxidizing gas mixtures with oxygen partial pressure close to 0.2 atm, the oxygen partial pressure in air. At this oxygen partial pressure, the predominant volatile species over $SiO_2(s)$ is $SiO_2(g)$ with a partial pressure of about 10^{-10} atm at 1600°K,[9] which is negligible. Therefore, any loss of surface $SiO_2(s)$ by direct volatilization is not significant in the oxidation of SiC in gas turbines.

However, $SiO_2(s)$ formed at the surface of silicon carbide can react at the $SiC(s)$ - $SiO_2(s)$ interface to produce $SiO(g)$ according to the reactions:

$$SiC(s) + 2\ SiO_2(s) \rightarrow 3\ SiO(g) + CO(g) \quad (3)$$

$$SiC(s) + 3\ SiO_2(s) \rightarrow 4\ SiO(g) + CO_2(g) \quad (4)$$

Mass spectrometric analyses have confirmed[9] that $CO(g)$ is formed by the reaction of $SiC(s)$ and $SiO_2(s)$. Therefore, reaction (3) is considered most significant.

At low enough oxygen pressures, if all the surface $SiO_2(s)$ reacts according to reaction (3), bare SiC surfaces are exposed to promote active oxidation of SiC by the formation of $SiO(g)$. Wagner[10] has developed a theory to interpret the transition between active oxidation of silicon (weight loss by the formation of $SiO(g)$) found at low oxygen partial pressures and passive oxidation (weight gain by the formation of $SiO_2(s)$) at higher oxidation partial pressures. This theory was used to calculate the oxygen partial pressure, $P_{O_2}(max)$, below which the surface oxide reacts with SiC to expose bare SiC surfaces and above which a stable $SiO_2(s)$ layer is maintained. The calculations are based upon the thermodynamic data appearing in Table 5.13, [11] assuming stoichiometric formation of $CO(g)$ and $SiO(g)$. The theoretical values

for oxygen pressures, $P_{O_2}(max)$, at different temperatures in the range 1200 to 1600°K, are listed in Table 5.14. Since the oxygen pressures in gas turbines are much higher than the $P_{O_2}(max)$ values in Table 5.14, a stable $SiO_2(s)$ layer will be maintained on the surface of silicon carbide.

Gulbransen and Jansson [12] have modified Wagner's treatment [10] for explaining the active to passive transition in the oxidation of SiC by taking into account the CO(g) pressures formed at the SiC(s) - $SiO_2(s)$ interface. However, the basic result remains the same as that expressed in the last paragraph.

Any SiO(g) formed at the SiC(s) - $SiO_2(s)$ interface diffuses outward through pores and fissures in the surface oxide layer and is oxidized to $SiO_2(s)$ by reaction with oxygen. However, CO(g) formed at this interface bursts through the oxide layer, creating pores and voids in the surface oxide.

TABLE 5.13

Thermochemical Data for the Si-C-O System [ ]

	ΔG_f°, cal mole^{-1}		
Compounds	1200°K	1400°K	1600°K
SiC(s)	- 15,263	- 14,905	- 14,548
$SiO_2(s)$	-166,296	-158,134	-150,027
SiO(g)	- 48,672	- 52,491	- 56,244
CO(g)	- 52,049	- 56,189	- 60,284

TABLE 5.14

Theoretical Values of Maximum Oxygen Pressures to Remove all the Oxide on SiC Surface

Temperature °K	P_{SiO}(eq), Reaction (3) atm	P_{O_2}(max) atm
1200	1.2×10^{-7}	4.8×10^{-8}
1400	2.0×10^{-5}	8.0×10^{-6}
1600	9.0×10^{-4}	3.6×10^{-5}

Static Oxidation of SiC

Since a gas turbine environment represents passive oxidation in a classic sense, the static oxidation behavior of silicon carbide reported here reflects this phenomenon only.

The silicon carbide specimens in the form of 0.5" x 0.5" x 0.070" flat plates, were cut from a billet of Norton hot pressed SiC. The specimen was suspended from the Cahn electrobalance with a sapphire fiber and maintained at desired temperatures in pure dried oxygen flowing at the rate of 50 ml/min. The changes in the weight of the specimen were continuously recorded as a function of time on a strip chart recorder.

As silicon carbide oxidizes to silicon oxide according to reactions (1) and (2), the difference in the molecular weights of SiC(40) and SiO_2(60) is reflected as weight gain during oxidation. Figure 5.70 shows the weight gain data for oxidation of SiC in 1 atm oxygen at temperatures in the range 2200° to 2500°F. The weight gained for oxidation at and below 2200°F was insignificant. The weight gain vs time curves at temperatures between 2300° and 2500°F follow a parabolic behavior after about an hour from the start of the oxidation. This parabolic behavior can be represented by the equation:

$$W^2 = K_p t$$

where W is the weight gain at time t and K_p is the parabolic rate constant. Figure 5.71 shows a plot of the square of the weight gain (W^2)

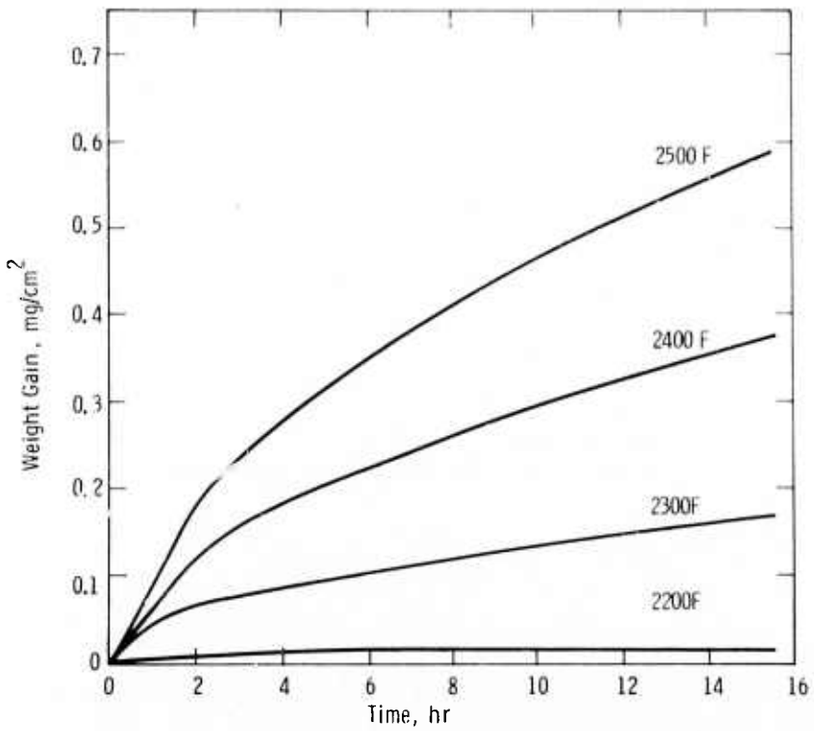


Figure 5.70 Oxidation Behavior of Norton's Hot-Pressed SiC in Oxygen at 1 atm Pressure

as a function of time (t) for temperatures from 2300 to 2500°F. The straight lines represent a region of parabolic oxidation at each temperature. The parabolic rate constants, K_p, for oxidation of SiC in 1 atm oxygen at different temperatures, are listed in Table 5.15. Each value of K_p was obtained from the slope of the straight lines in Fig. 5.71. A plot of log K_p vs reciprocal temperature (1/T) is shown in Fig. 5.72, where a straight line was drawn through the experimental points by a least mean square analysis. Using Arrhenius equation:

$$K_p = A \exp(-E/RT)$$

where E is the activation energy, R is the gas constant and T is the absolute temperature, an activation energy of 115 kcal/mole is obtained from the slope of the straight line in Fig. 5.72 for the oxidation of SiC in 1 atm oxygen in the temperature range 2300 to 2500°F.

Figures 5.70 and 5.71 show that the weight gained during the first hour of oxidation is somewhat less than the parabolic rate observed after this initial oxidation. The hot pressed SiC used in this study contained about 5% tungsten carbide. During initial oxidation, the tungsten carbide on the surface of SiC probably oxidizes to either solid tungsten oxide with a very high vapor pressure, or to various volatile tungsten oxides, causing a loss in weight. This loss in weight causes the initial weight gain obtained on oxidizing SiC to be somewhat less than the weight gain expected from the observed parabolic rate. The effect of WC on the oxidation of SiC is currently being examined in detail.

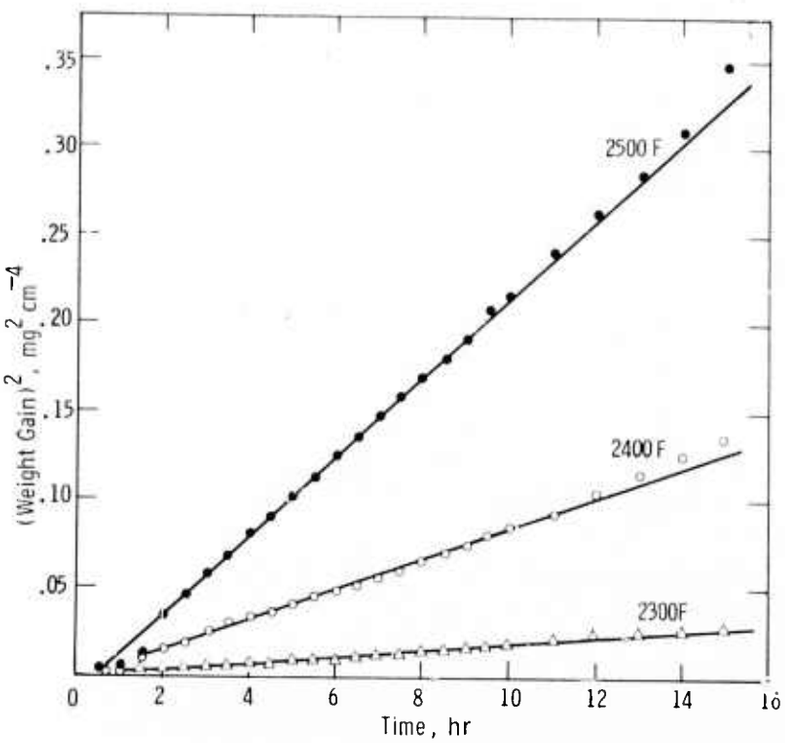


Figure 5.71 Parabolic Plot of Oxidation of SiC in Oxygen at 1 atm Pressure

After about 10 hours of oxidation, the weight gain observed exceeds that predicted by the parabolic rate as seen in Fig. 5.71. The CO(g) released at the SiC - SiO_2 interface bursts out through the oxide layer exposing a bare SiC surface which can oxidize further. This can cause the weight gain vs time curves to deviate from the parabolic behavior.

TABLE 5.15

Parabolic Rate Constants for Oxidation of SiC in 1 atm Oxygen

Temperature °F	Parabolic Rate Constant, Kp $g^2\ cm^{-4}\ sec^{-1}$
2300	4.84×10^{-13}
2400	2.32×10^{-12}
2500	6.23×10^{-12}

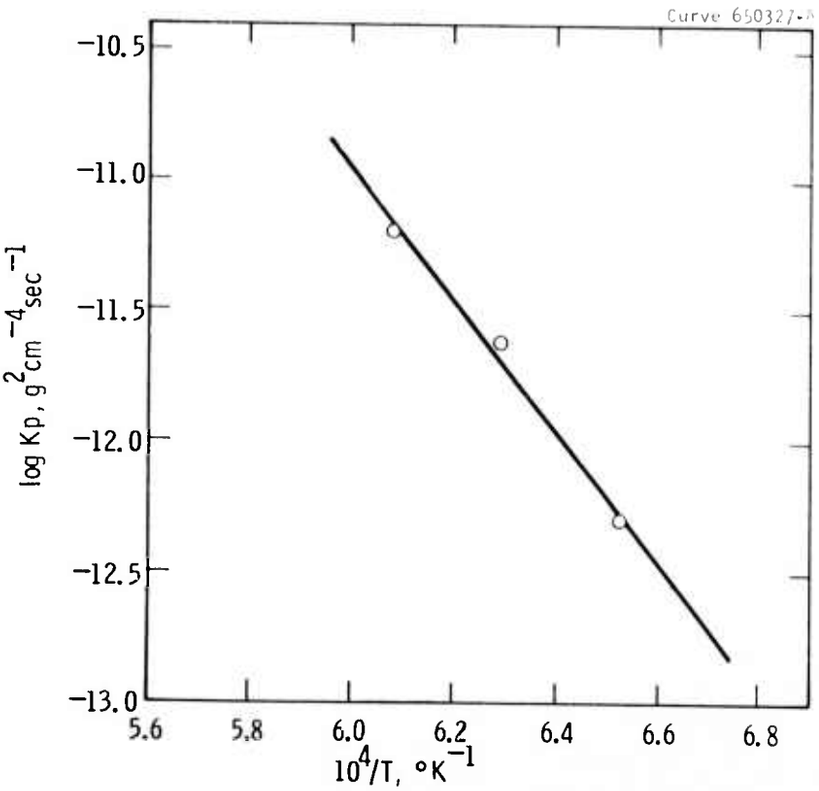


Figure 5.72 Arrhenius Type Plot Showing Parabolic Rate Constant for Oxidation of SiC in 1 atm Oxygen as a Function of Temperature

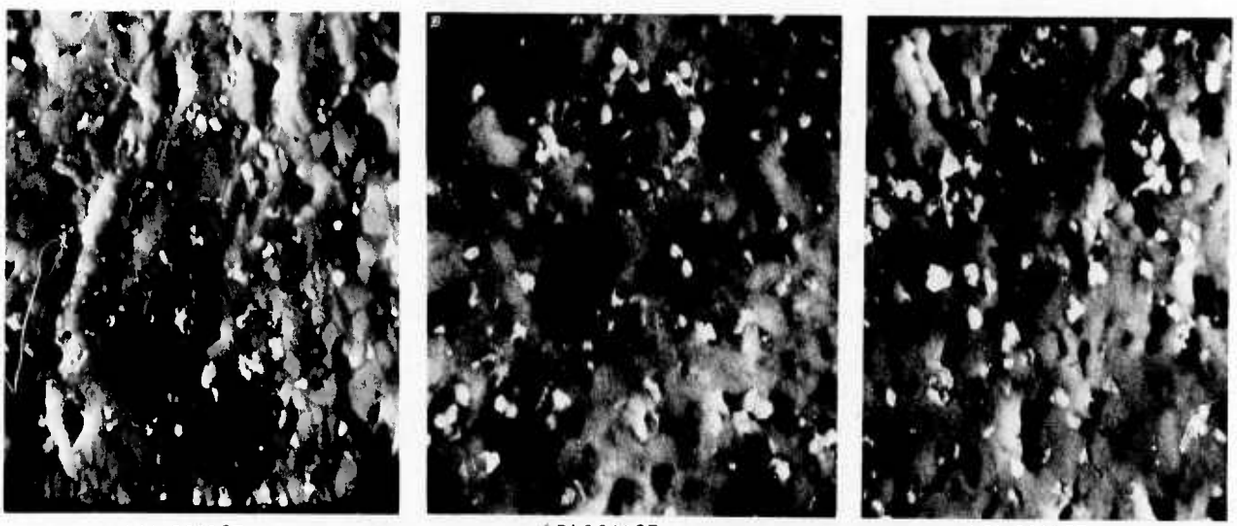
Characterization of the Surface Oxide

The surface films on SiC specimens oxidized for 20 hours in 1 atm oxygen at temperatures between 2000 and 2500°F were characterized using x-ray diffraction and scanning electron microscopy.

The oxide film from the surface of oxidized SiC specimens was scraped and analyzed by x-ray Debye-Scherrer patterns using Cu-K_α radiation. The surface layer formed at oxidation temperatures between 2000 and 2300°F was low-cristobalite; at 2400 and 2500°F small traces of Al_2O_3 were also observed in addition to the low cristobalite. There was no evidence of WO_2 in the x-ray patterns, indicating that either it's concentration was too small to be detected by x-ray diffraction or any tungsten oxides formed were removed by volatilization.

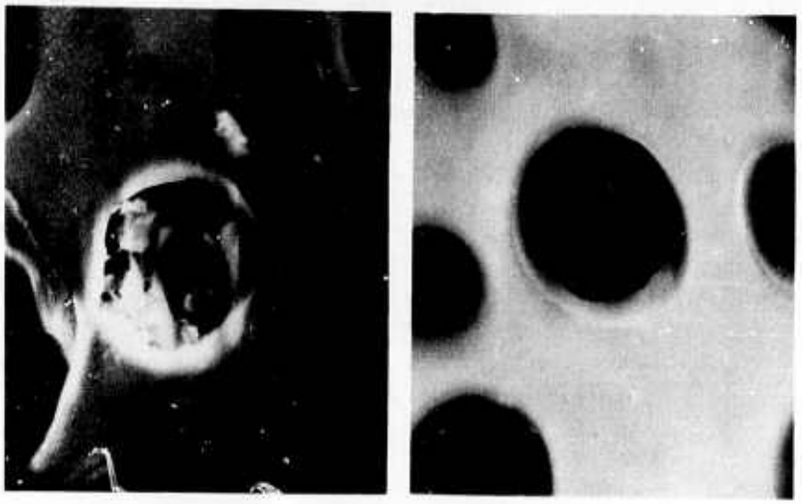
The surfaces of SiC specimens oxidized at different temperatures were examined by scanning electron microscopy to determine the surface morphology and other characteristic features of the oxide layer (Figs. 5.73 and 5.74). The specimen oxidized at 2000°F (Fig. 5.73a) showed that little oxide was formed leaving the SiC grain structure still visible at the surface. At oxidation temperatures of 2200 and 2300°F, (Figs. 5.73b and 5.73c) the surface was covered with a layer of silica with small white particles distributed throughout the surface. These white particles were identified as aluminum silicate. At oxidation temperatures of 2400 and 2500°F, (Fig. 5.74) the surface was uniformly covered with an oxide layer. At these high temperatures the alumina apparently reacts with silica, since no discrete alumina particles were observed.

Pores in the oxide layer, particularly at higher oxidizing temperatures, represent another prominent feature in scanning electron micrographs. During the oxidation of SiC, CO(g) is formed at the SiC(s) - SiO_2(s) interface which literally bursts out through the oxide layer, causing rupture. Pores in the oxidized film thus formed may be healed subsequently by gas phase transport.



(A) 2000°F (B) 2200°F (C) 2300°F

Figure 5.73 Scanning Electron Micrographs of Surfaces of Silicon Carbide Specimens Oxidized for 30 Hours in 1 atm Oxygen at Different Temperatures (2500X)



(D) 2400°F (E) 2500°F

Figure 5.74 Scanning Electron Micrographs of Surfaces of Silicon Carbide Specimens Oxidized for 20 Hours in 1 atm Oxygen at Different Temperatures (2500X)

5.3 NON-DESTRUCTIVE EVALUATION OF MATERIALS

SUMMARY

A very important aspect of the development of ceramic gas turbine engines is the need to meaningfully inspect and test ceramic components before installation in the engine. The objectives of the NDE work are to identify and classify defects and to gain as much information as possible on the properties of the material from which the component is manufactured. Both property and defect information are being related to performance of the component, leading eventually to routine inspection and acceptance/rejection based upon established actual performance. All available non-destructive means must be used to accomplish this goal and new methods must constantly be evaluated to determine their usefulness. Procedures utilizing ultrasonics, x-ray radiography, and acoustic emission (AE) are currently being applied to ceramic systems for evaluation purposes.

Work has been initiated on the utilization of a pulse-echo technique for the measurement of subsurface flaws in hot-pressed silicon nitride. This technique is particularily applicable to very small flaws that are not detectable using conventional NDE methods. The system combines flaw signal information with phase information associated with the flaw signal, and results in increased resolution and sensitivity.

A secondary method for measuring sonic velocities in gas turbine ceramic materials has been developed. This method introduces an elastic wave by electronic pulsation of the test specimen, and is capable of measurements within 1% of data obtained by the resonance techniques used in the past.

Several silicon nitride simulated turbine rotor segments were studied using ultrasonic c-scanning techniques. Although ideal instrument sensitivity levels were not available, test results did indicate the quality of the silicon nitride bond and produced a relative rating of the rotor segments.

A step block standard was fabricated for the purpose of studying subsurface flaws in hot-pressed silicon nitride using radiographic techniques. The standard will be used to optimize radiographic procedures for checking turbine rotor materials.

5.3.1 ULTRASONIC NDE

Introduction

The procedures used to ultrasonically evaluate ceramic materails continue to be updated and refined as progress is made in optimizing the instrumentation and evaluation methods. Methods proviously developed to ultrasonically evaluate specific components are inadequate for the detection of small subsurface flaws in critical components such as ceramic rotors. Successful operation of ceramic rotors may rely heavily on the ability to detect very small defects. The effect of flaw size on structural integrity has yet to be determined, although some progress in this area has been realized.

Ultrasonic NDE of Ceramic Rotors

It has been proposed that subsurface flaws of a size approaching the grain size of a material will determine a component's response to mechanical and thermal stress. High frequency instrumentation is needed to approach the sensitivity necessary to detect these very small flaws. A limited program is being conducted at the University of Michigan utilizing a technique which is capable of detection of subsurface flaws much smaller than those detected by available conventional means. This pulse-echo system was developed at the University of Michigan, and employs electronic methods to increase the signal-to-noise ratio while utilizing phase information associated with the flaw signal. This results in increased resolution and sensitivity while negating the electrical effects of the transducers. Hot-pressed Si_3N_4 is being evaluated using this technique, since the subsurface flaws normally found in billets of this material consist of impurities and very small voids; both are difficult to detect with conventional ultrasonic instrumentation.

Measuring the sonic velocity of a material permits the calculation of the dynamic modulus of elasticity and Poisson's ratio easily and non-destructively. Taking numerous measurements also yields information relating to density gradients within the part. Efforts are continuously being made to obtain this data as accurately as possible. Previously, the modulus of elasticity of ceramic rods and bars were measured by determining the longitudinal resonant frequency of the specimen. This was accomplished by coating one end of the specimen with silver conducting paint and iron powder so that the material could be electromagnetically excited to resonance. The other end was coated with silver conducting paint only and resonance detected by measuring the change in capacitance as the specimen was displaced.

Longitudinal velocities, within 1% of data calculated from these measurements, have been reproduced by another method. The basic system is shown in Fig. 5.75. The pulse generator consists of a pulser and magnetostrictive transducer with a needle-tipped lead-in which is pressure-coupled to the test

specimen. This pulser system emits a short, broadband pulse with a center frequency of approximately 100 KHZ at a constant repetition rate. The pulse travels the length of the test specimen, is detected and amplified by acoustic emission instrumentation, and displayed on an oscilloscope. The time the pulse takes to travel the length of the specimen can then be measured very accurately and the velocity calculated.

Several simulated duo-density rotor segments were ultrasonically C-scanned to determine if variations in fabricating procedures could be detected. A 5 MHZ focused transducer was used for this evaluation which was conducted with the objective to discern only relative differences in the segments.

The C-scans of the rotor segments are shown in Fig. 5.76 through Fig. 5.78. These recordings reflect arbitrarily selected instrumentation sensitivity levels, and therefore the dark indications may or may not correspond to actual flaws of the same size. Without establishing sensitivity levels from some standard small flaws could be completely missed or expanded larger than actual size during ultrasonic scanning. This effect is shown in these C-scans since the extent of specific flaws can be seen to vary as the instrumentation sensitivity changes.

The regions chosen for evaluation were hot-pressed/hot-pressed and hot-pressed/reaction-sintered interfaces. Only the interface beneath the hub is shown in the C-scans. Fig. 5.79 shows the method used for examining the various interfaces. Only segments were used for evaluation. Segment HP-129 does not have a hot-pressed/hot-pressed interface. Figures 5.76 and 5.78 reveal the apparent outer diameter of the center slug as shown by the C-scan of HP-139.

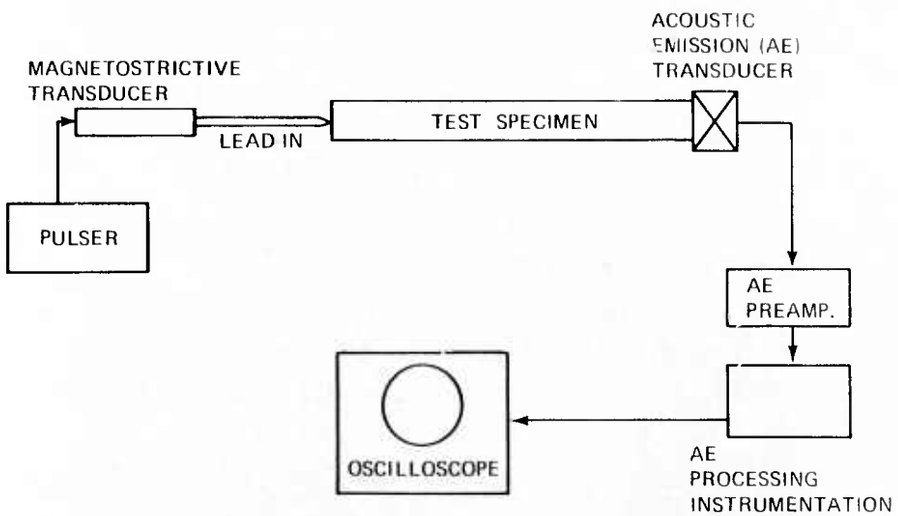


Figure 5.75 Block Diagram of Sonic Velocity Measurement System

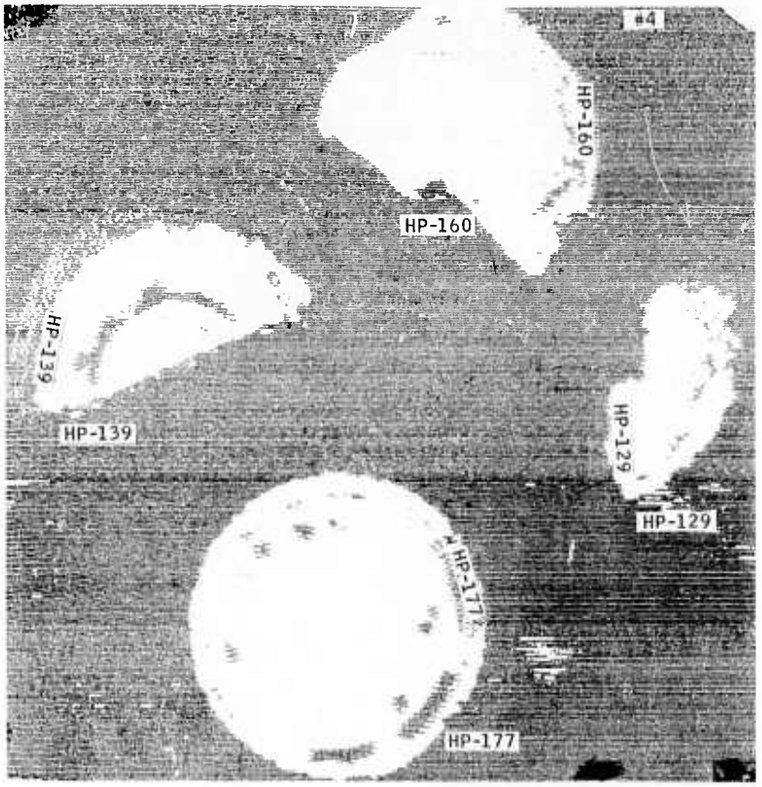


Figure 5.76 Ultrasonic C-Scan of Duo-Density Rotor Segment Lowest Sensitivity Setting

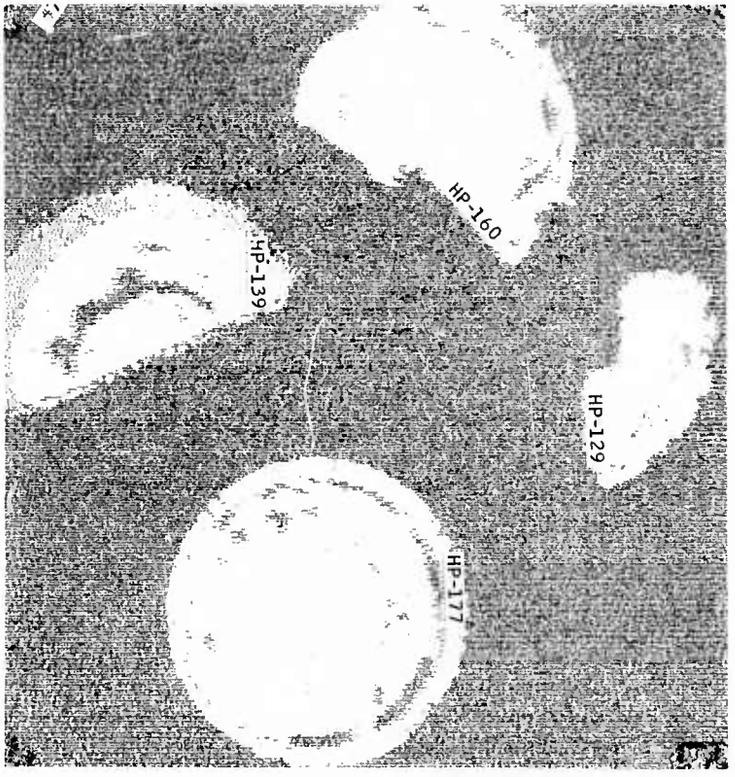


Figure 5.77 Ultrasonic C-Scan of Duo-Density Rotor Segment Intermediate Sensitivity Setting

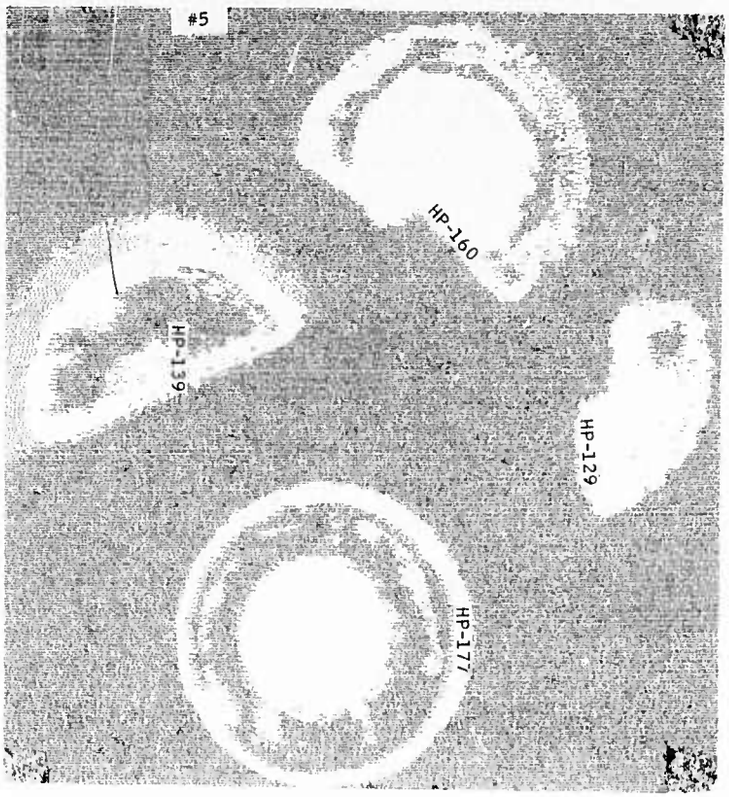


Figure 5.78 Ultrasonic C-Scan of Duo-Density Rotor Segment Highest Sensitivity Setting

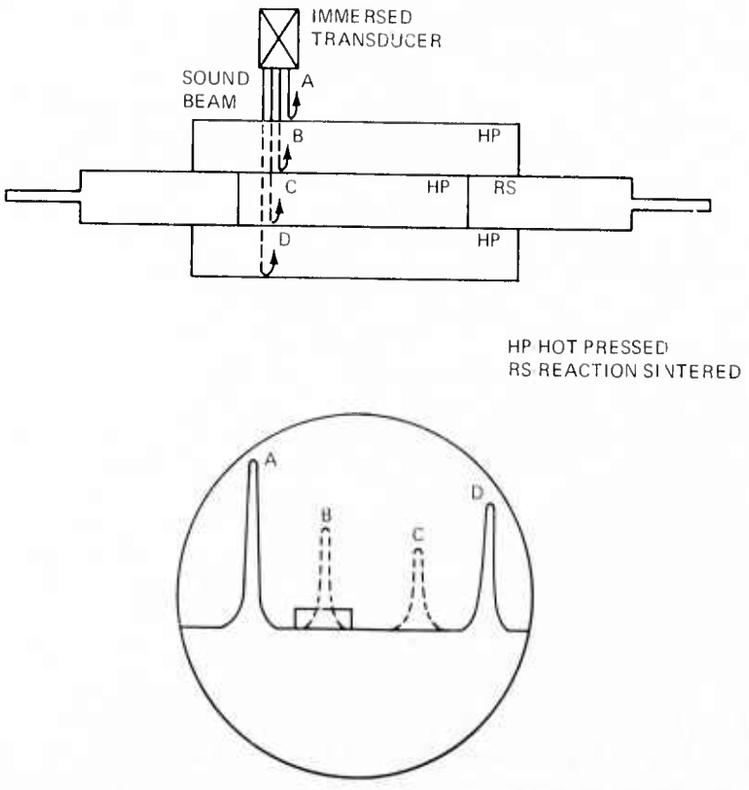


Figure 5.79 Method for Ultrasonically Scanning Interfaces of Duo-Density Rotors

The scans indicate the presence of defects located in the hot-pressed/reaction-sintered interface. No defects are observed in the hot-pressed/hot-pressed interface in the rotor segments. However, it must be emphasized that the procedures used were not optimized, and therefore it cannot be conclusively stated that perfect hot-pressed/hot-pressed bonding was achieved.

Ultrasonic NDE techniques are being utilized for the stationary turbine project for the detection of critical defects in billets, test samples, and turbine components made from hot-pressed Si_3N_4 and SiC.

Longitudinal velocities, within 1% of data calculated from these measurements, have been reproduced by another method. The basic system is shown in Fig. 5.75. The pulse generator consists of a pulser and magnetostrictive transducer with a needle-tipped lead-in which is pressure-coupled to the test specimen. This pulser system emits a short, broadband pulse with a center frequency of approximately 100 KHZ at a constant repetition rate. The pulse travels the length of the test specimen, is detected and amplified by acoustic emission instrumentation, and displayed on an oscilloscope. The time the pulse takes to travel the length of the specimen can then be measured very accurately and the velocity calculated.

Several simulated duo-density rotor segments were ultrasonically C-scanned to determine if variations in fabricating procedures could be detected. A 5 MHZ focused transducer was used for this evaluation which was conducted with the objective to discern only relative differences in the segments.

The C-scans of the rotor segments are shown in Fig. 5.76 through Fig. 5.78. These recordings reflect arbitrarily selected instrumentation sensitivity levels, and therefore the dark indications may or may not correspond to actual flaws of the same size. Without establishing sensitivity levels from some standard, small flaws could be completely missed or expanded larger than actual size during ultrasonic scanning. This effect is shown in these C-scans since the extent of specific flaws can be seen to vary as the instrumentation sensitivity changes.

The regions chosen for evaluation were hot-pressed/hot-pressed and hot-pressed/reaction-sintered interfaces. Only the interface beneath the hub is shown in the C-scans Fig. 5.79. Only segments were used for evaluation. Segment HP-129 does not have a hot-pressed/hot-pressed interface. Figures 5.76 and 5.78 reveal the apparent outer diameter of the center slug as shown by the C-scan of HP-139.

The scans indicate the presence of defects located in the hot-pressed/reaction-sintered interface. No defects are observed in the hot-pressed/hot-pressed interface in the rotor segments. However, it must be emphasized that the procedures used were not optimized, and therefore it cannot be conclusively stated that perfect hot-pressed/hot-pressed bonding was achieved.

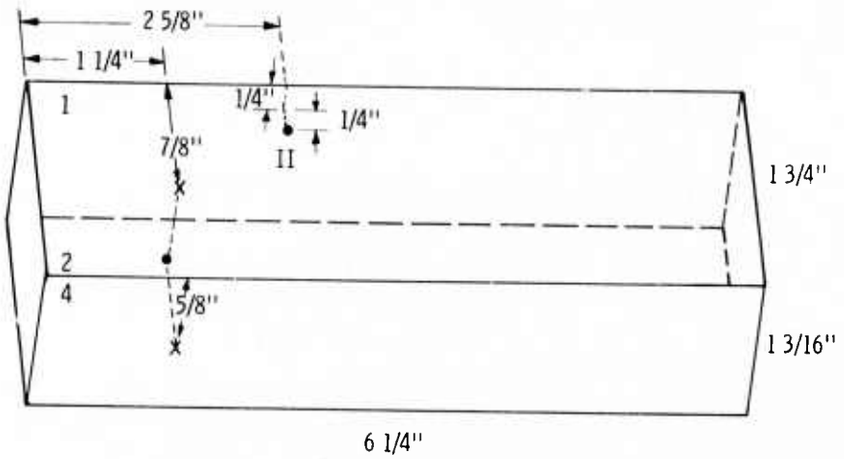
Ultrasonic NDE techniques are being utilized for the stationary turbine project for the detection of critical defects in billets, test samples, and turbine components made from hot-pressed Si_3N_4 and SiC.

Low density inclusions have been identified on hot-pressed Si_3N_4 by ultrasonics, and many of these have been confirmed by billet sectioning. Two types of inclusions have been identified; high density inclusions, which are rich in W and Fe, and low density inclusions, which occasionally contain BN.

A section of a hot-pressed billet of HS-130 material (Fig. 5.80) was subjected to X-ray radiography and ultrasonic testing. The defect marked II was detected by X-ray radiography but was not detected by the ultrasonic testing. This defect was later found to be an Fe rich inclusion.

The defect marked I was not detected by X-ray radiography, but was detected by ultrasonic testing.

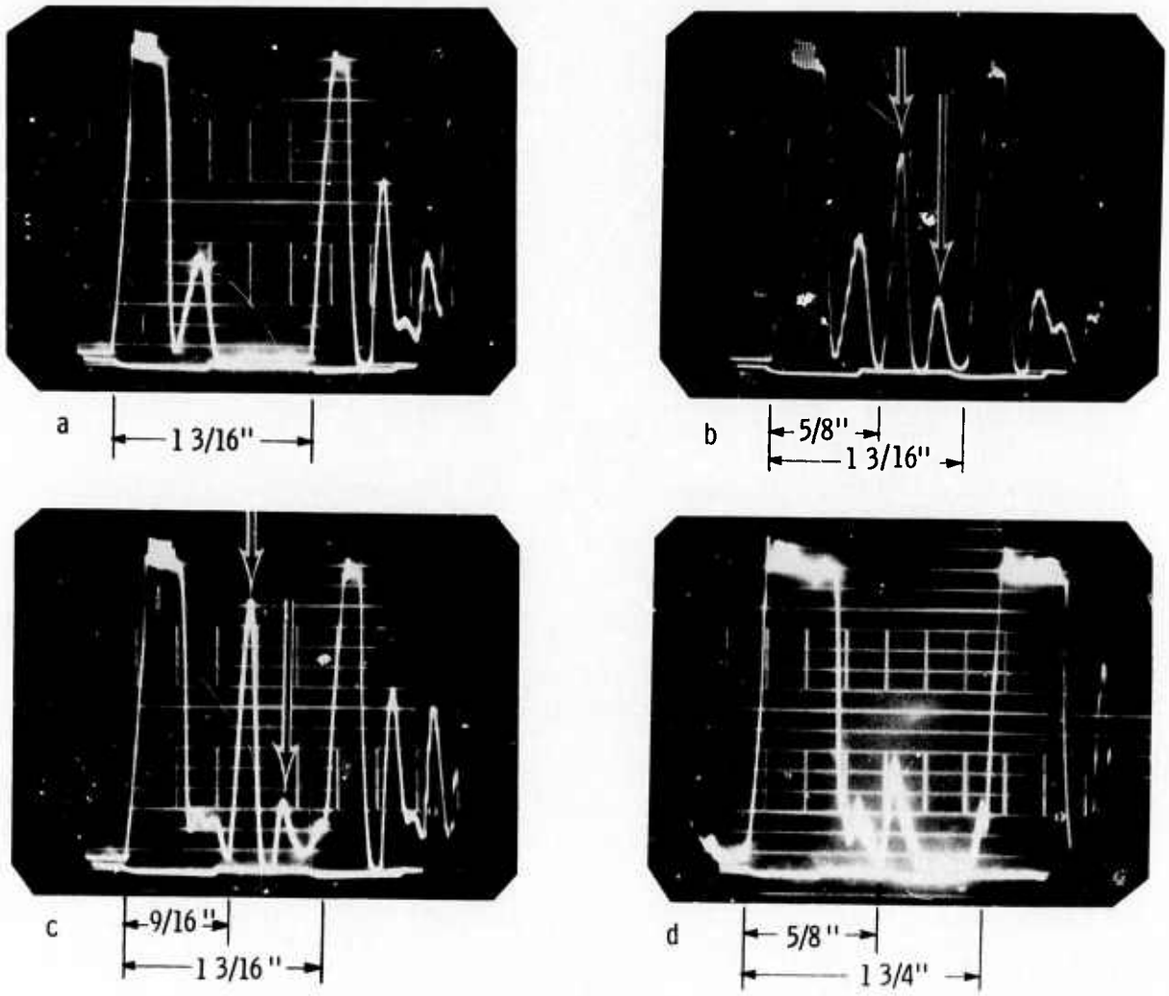
The ultrasonic testing is an "A Scan" water immersion test, utilizing a focused LiS transducer operating at a frequency of 10 MHZ. In this particular test a 2.5 in. focal-point-distance was used. The transducer slowly scanned the billet surface, (in this particular test, surface 1, Fig. 5.80.) A normal echo, at a given point, is shown in Fig. 5.81. The high peak on the left is the reflection of the sound wave from the top surface and the high peak to the right is the reflection from the bottom surface. The small peak is a secondary reflection. The distance between these two peaks represent the thickness of the test piece. At a point above flaw I, an extra peak (with the secondary reflection) appears between the main surface reflections, Fig. 5.81. The flaw is located about 5/8 in. below the top surface.



I. Low density inclusion detected by "A Scan"
II. High density inclusion detected by x-ray radiography

Figure 5.80 Schematic of Billet Used for Ultrasonic Flaw Evaluation

The billet was then turned around and the flaw was detected again, now at a distance of 9-1/16 in. below surface 2, Fig. 5.81. These two reflections confirm the location of the flaw along the 1-3/16 in. direction. The test was repeated with the transducer in surface 4, Fig. 5.81, to identify the exact location of the flaw.



a) Typical echoes from undisturbed material
b) Echoes from flaw I, transducer on Surface 1
c) Echoes from flaw I, transducer on Surface 2
d) Echoes from flaw I, transducer on Surface 4

Figure 5.81 10 Meghertz Shear Waves in Hot Pressed Silicon Nitride

5.3.2 ACOUSTIC EMISSION

On the stationary turbine project, preliminary tests using broader frequency ranged equipment indicate that silicon nitride emits little sound as it is loaded until just before failure, when the sound rate increases considerably. A few samples that failed at significantly lower load emitted more sound at low stresses. At present, thermal shocked specimens of hot-pressed silicon carbide having cracked surfaces are under test to determine emission levels from known flaws.

Ultrasonic flaw detection was applied to tensile specimens and showed some failures had occurred at points associated with areas causing sound reflections in the material's interior. A significant number of samples failed at surface flaws, such as grinding scratches. A block of silicon nitride has been thoroughly searched by ultrasonics for flaws. Each flaw will be cut out in a slab and subjected to x-ray search. Eventually the actual point that causes sound reflection will be studied directly. Fig. 5.82 show the oscillograph of the block. The large square peak on the left is the sound pulse and the smaller peaks indicate areas that are different enough to reflect sound. The right end peak represents the opposite end of the material.

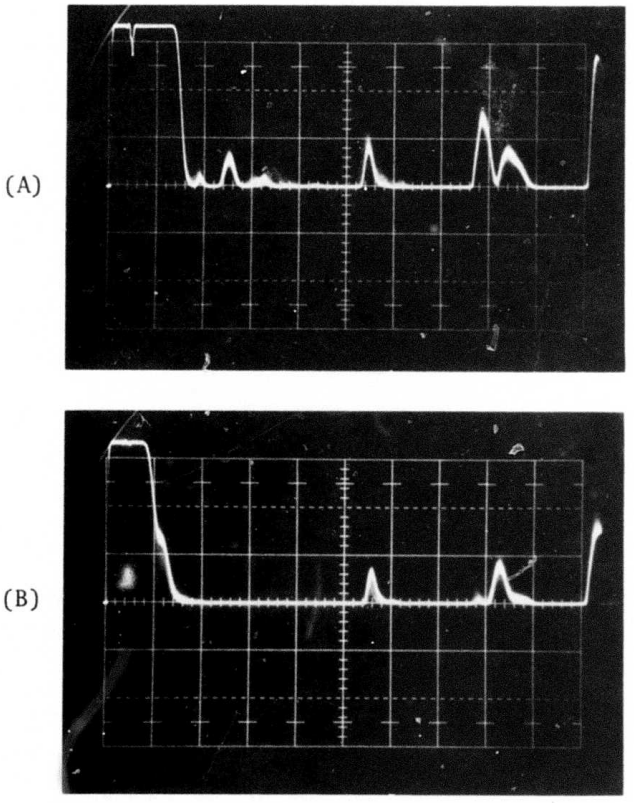


Figure 5.82 Ultrasonic "A Scan" Pulse Echoes from Silicon Nitride Billet

5.3.3 X-RAY RADIOGRAPHY

Radiographic analysis has not proven to be particularly effective in the detection of small subsurface flaws in ceramic material with thick sections. This technique, however, has afforded a means of finding gross flaws in complicated shapes. It is therefore a valuable tool which can be used for initial screening and elimination of grossly defective components.

Since several different shapes of silicon nitride may be used to fabricate a duo-density turbine rotor, it is necessary to determine the quality of the individual parts. Therefore, efforts have been specifically made to optimize radiographic techniques for hot-pressed silicon nitride. It became necessary to fabricate a standard from which all radiographic processes could be optimized and compared.

A billet of Norton hot-pressed silicon nitride (code HS-130) was selected and a step block was then fabricated following established practice to determine radiographic quality levels in metal systems.[13] The radiographic standard is shown in Fig. 5.83.

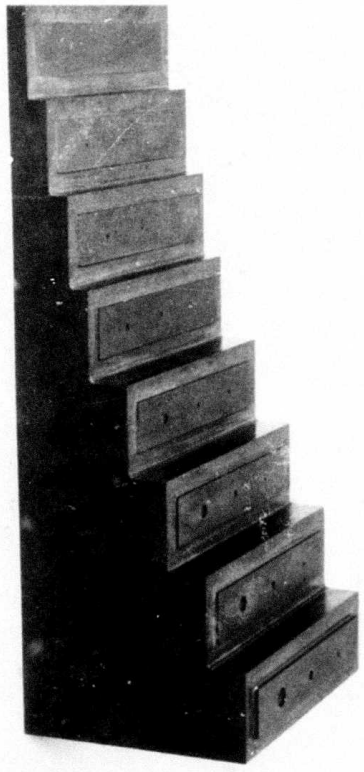


Figure 5.83 Hot Pressed Silicon Nitride Radiographic Step Block Standard

While penetrometers are normally placed on each step of the standard in metal systems, it was decided to make them an integral part of the ceramic standard. To accomplish this, sufficient stock was left on the surface of each step to machine the penetrameter by ultrasonic methods. The final thickness of the penetrameter, or height relative to the step surface, represents 2% of the step thickness and the depth of the corresponding 1T, 2T and 4T holes (T equals the penetrometer thickness). Processes such as xeroradiography and neutron radiography will also be evaluated using this ceramic standard as a basis for comparison.

PRECEDING PAGE BLANK-NOT FILMED

6. REFERENCES

1. McLean, A. F., Fisher, E. A., Bratton, R. J., "Brittle Materials Design, High Temperature Gas Turbine," AMMRC CTR 72-19, Interim Report, January 1, 1972 to June 30, 1972.

2. McLean, A. F., Fisher, E. A., and Harrison, D. E., "Brittle Materials Design, High Temperature Gas Turbine," AMMRC CTR 72-3, Interim Report, July 1, 1971 to December 31, 1971.

3. Rosin, R., Bersan, J., and Urbain, G. Rev. Hantes Temper et. Retract. 1, 159 (1964).

4. McLaren, J. R., Tappin, G., and Davidge, R. W., "The Relationship Between Temperature and Environment, Texture, and Strength of Self-Bonded Silicon Carbide," Proceeding of the British Ceramic Society, No. 20 (1972).

5. Shaffer, P.T.B. and Jun, L. K., "The Elastic Modulus of Dense Polycrystalline Silicon Carbide," Materials Research Bulletin 7, (1972) p. 63.

6. Lynch, J. F. and Duckworth, W. H., "Engineering Properties of Selected Ceramic Materials", American Ceramic Society, Columbus, Ohio (1966).

7. De Salvo, G. S., "Theory and Structural Design Applications of Weibull Statistics", Westinghouse Astronuclear Laboratory, WANC-TME-2668.

8. Noakes, P. B. and Pratt, P. L., "High Temperature Mechanical Properties of Reaction-Sintered Silicon Nitride", Special Ceramics 5, The British Ceramic Research Association (1972).

9. Gulbransen, E. A., Andrew, K. F., and Brassart, F. A., "The Oxidation of Silicon Carbide at 1150° to 1400°C and at 9×10^{-3} to 5×10^{-1} Torr Oxygen Pressure", J. Electrochem. Society, 113 (1966), p. 1311.

10. Wagner, C., "Passivity During the Oxidation of Silicon at Elevated Temperatures", J. Appl. Phys., 29 (1958) p. 1295.

11. Stull, D. R., Prophet, H., et al., JANAF Thermochemical Tables, NSRDS-NBS 37, (1971).

12. Gulbransen, E. A., and Jansson, S. A., "Thermochemical Analyses of the High Temperature Oxidation, Reduction, and Volatilization of Silicon and Silicon Carbide", Oxid. of Metals, 4, (1972) p. 181.

13. "Controlling Quality of Radiographic Testing", ASTM E142-68.

ARMY MATERIALS AND MECHANICS RESEARCH CENTER
WATERTOWN, MASSACHUSETTS 02172

TECHNICAL REPORT DISTRIBUTION

No. of Copies	To
1	Office of the Director, Defense Research and Engineering, The Pentagon, Washington, D.C 20301
12	Commander, Defense Documentation Center, Cameron Station, Building 5, 5010 Duke Street, Alexandria, Virginia 22314
1	Metals & Ceramics Information Center, Battelle Memorial Institute, 505 King Avenue, Columbus, Ohio 43201
2	Chief of Research and Development, Department of the Army, Washington, D.C. 20310 ATTN: Physical and Engineering Sciences Division (CRD PES - Dr. Sullivan)
1	Commanding Officer, Army Research Office (Durham), Bx CM, Duke Station Durham, North Carolina 27706 ATTN: Dr. H. M. Davis
1	Commanding General, U.S. Army Material Command, Washington D.C. 20315 ATTN: AMCRD-TC (Dr. El-Bisi)
1	ATTN: ANCDL (Dr. Dillaway)
1	Commanding General, U.S. Army Missile Command, Redstone Arsenal, Alabama 35809 ATTN: Technical Library
1	Commanding General, U.S. Army Munitions Command, Dover, New Jersey 07801 ATTN: Technical Library
1	Commanding General, U.S. Army Tank-Automotive Command, Warren, Michigan 48090 ATTN: AMSTA-BSL, Research Library Br
1	Commanding General, U.S. Army Weapons Command, Research and Development Directorate, Rock Island, Illinois 61201 ATTN: AMSWE-RDR
1	Commanding Officer, Aberdeen Proving Ground, Maryland 21005 ATTN: Technical Library, Building 313
1	Commanding Officer, U.S. Army Aviation Material Laboratories, Fort Eustis, Virginia 23604
1	Librarian, U.S. Army Aviation School Library, Fort Rucker, Alabama 36360 ATTN: Bldg. 5907
1	Commanding Officer, USACDC Ordance Agency, Aberdeen Proving Ground, Maryland 21005 ATTN: Library, Building 350

ARMY MATERIALS AND MECHANICS RESEARCH CENTER
WATERTOWN, MASSACHUSETTS 02172

TECHNICAL REPORT DISTRIBUTION

No. of Copies	To
1	U.S. Army Air Mobility Research and Development Laboratory ATTN: J. White, Assistant Technical Director, Eustis Directorate, Ft. Eustis, Virginia 23604
1	U.S. Army Air Mobility Research and Development Laboratory ATTN: R. Berrisford, Chief, Structures Division, Eustis Directorate, Ft. Eustis, Virginia 23604
1	U.S. Army Air Mobility Research and Development Laboratory ATTN: T. Coleman, Director, Langley Directorate, Langley Research Center, Langley Field, VA 23365
2	U.S. Army Air Mobility Research and Development Laboratory ATTN: J. Accurio, Director, Lewis Directorate, NASA, Lewis Research Center, 21000 Brookpark Road, Cleveland, Ohio 44135
1	Commanding General, U.S. Army Aviation Systems Command, ATTN: R. Long, Deputy Director RD&E, P.O. Box 209, St. Louis, MO 63166
1	Office Chief Research & Development, Department of Army, ATTN: Col. J. Barnett, Physical & Engineering Sciences Division, Washington, D.C. 20315
1	Office, Chief Research & Development, Department of Army, ATTN: Lt. Col. H. B. Snyder, The Pentagon, Washington, D.C. 20310
1	Commanding General, Army Missile Command, ATTN: AMCDL, Webb Taylor, 5001 Eisenhower Avenue, Alexandria, VA 22304
1	Commanding General, Army Missile Command, ATTN: AMCRD-F, J. Beebe, Washington, D.C. 20315
1	Office, Chief Research & Development, Department of the Army, ATTN: R. Ballard, Physical & Engineering Sciences Division, Washington, D.C. 20315
1	Commander, USA Foreign Science & Technology Center, ATTN: AMXST-SD3, Mr. C. Petschke, 220 7th Street NE, Charlottesville, VA 22901
1	Mr. Irving Machlin, High Temperature Materials Div., Materials and Processes Branch, (NAIR-52031D), Naval Air Systems Command, Department of the Navy, Washington, D.C. 20360

ARMY MATERIALS AND MECHANICS RESEARCH CENTER
WATERTOWN, MASSACHUSETTS 02172

TECHNICAL REPORT DISTRIBUTION

No. of Copies	To
1	Commanding Officer, U.S. Army Engineer Waterways Experiment Station, Vicksburg, Mississippi 39180 ATTN: Research Center Library
	Commanding Officer, U.S. Army MERDEC, Fort Belvoir, Virginia 22060
2	ATTN: SMEFB-EP (Mr. James Horton)
1	ATTN: SMEFB-EP (Mr. W. McGovern)
	Director, Army Materials and Mechanics Research Center, Watertown, Massachusetts 02172
2	ATTN: AMXMR-PL
1	AMXMR-PR
1	AMXMR-CT
1	AMXMR-AP
1	AMXMR-X (Dr. Gorum)
1	AMXMR-EO (Dr. Katz)
1	AMXMR-TM (Dr. Lenoe)
1	AMXMR-D (Dr. Priest)
1	AMXMR-EO (Dr. Messier)
2	AMXMR-P (Dr. Burke)
	Advanced Research Projects Agency, 1400 Wilson Blvd., Arlington, Virginia 22209
2	ATTN: Director
1	ATTN: Dep Director
1	ATTN: Director of Materials Sciences - Dr. Stickley
1	ATTN: Dep. Director Materials Sciences - Dr. van Reuth
1	ATTN: Tech. Information Office - Mr. F. A. Koether
1	Mr. R. M. Standahar, Office of the Director of Defense, Research and Engineering, Room 3D1085, Pentagon, Washington, D.C. 20301
1	Mr. Charles F. Bersch, Department of the Navy, Naval Air Systems Command, Washington, D.C. 20360
1	Dr. A. M. Diness, Metallurgy Branch, Code 471, Office of Naval Research, 800 N. Quincy Street, Arlington, Virginia 22217
2	U.S. Army Air Mobility Research and Development Laboratory, Advanced Systems Research Office, Ames Research Center, Moffett Field, California 94035 ATTN: F. Immen, J. Wheatly

ARMY MATERIALS AND MECHANICS RESEARCH CENTER
WATERTOWN, MASSACHUSETTS 02172

TECHNICAL REPORT DISTRIBUTION

No. of Copies	To
1	Mr. Keith Ellingsworth, Office of Naval Research, Power Program, Arlington, VA 22217
1	Mr. John Fairbanks, Naval Ships Engineering, Prince George Center, Hyattsville, Maryland 20782
1	Capt. D. Zabierek, Air Force Aeropropulsion Lab, Wright-Patterson Air Force Base, Ohio 45433
1	Capt. Smyth, Air Force Materials Laboratory, Wright-Patterson Air Force Base, Ohio 45433
1	Mr. S. Lyons, Wright-Patterson Air Force Base, Ohio 45433
3	Aerospace Research Laboratory, ATTN: ARL-LL, Wright-Patterson Air Force Base, Ohio 45433 ATTN: Dr. Henry Graham ATTN: Dr. James Wimmer ATTN: Maj. L. Jacobson
1	Mr. W. Sanders, NASA Lewis Research Center, 21000 Brookpark Road, Cleveland, Ohio 44135
1	Dr. Hubert Probst, NASA Lewis Research Center, 21000 Brookpark Road, Cleveland, Ohio 44135
1	Dr. G. C. Deutsch, Ass't Director of Research (Materials), Code RR-1 NASA, Washington, D.C. 20546
1	Mr. George Staber, Office of Coal Research, U.S. Department of the Interior, Washington, D.C. 20240
1	Dr. S. Wiederhorn, Physical Properties Section, Institute for Materials Research, National Bureau of Standards, Washington, D.C. 20234
1	Mr. R. Reynik, Director, Div. of Materials Research, National Science Foundation, 1800 G. Street, N.W., Washington, D.C. 20550
1	Dr. Robb Thomson, Senior Research Scientist, Rm B109, Bld. 225, National Bureau of Standards, Washington, D.C. 20234
1	Mr. H. Morrow, Eustis Directorate, AMRDL, Fort Eustis, VA 23604
1	Dr. R. Warren, Contact Officer, Defense Research & Development Staff, British Embassy, 3100 Massachusetts Avenue N.W., Washington, D.C. 20008

ARMY MATERIALS AND MECHANICS RESEARCH CENTER
WATERTOWN, MASSACHUSETTS 02172

TECHNICAL REPORT DISTRIBUTION

No. of Copies	To
1	Mr. Robert Schulz, Thermal & Mechanical Systems Branch, Div. of Advanced Automotive Power Systems Development, 2565 Plymouth Road, Ann Arbor, MI 48105
1	Mr. Thomas Sebestyen, Environmental Protection Agency, Div. of Advanced Automotive Systems, 2565 Plymouth Road, Ann Arbor, MI 48105
1	Dean Daniel C. Drucker, Engineering College, University of Illinois, Urbana, Illinois 61801
1	Professor Merton Flemings, Massachusetts Institute of Technology, Cambridge, Massachusetts 02139
1	Professor Edward E. Hucke, Materials and Metallurgical Engineering, The University of Michigan, Ann Arbor, MI 48104
1	Professor Frank A. McClintock, Department of Mechanical Engineering, Massachusetts Institute of Technology, Cambridge, Massachusetts 02139
1	Dr. R. M. Spriggs, Assistant to the President, Lehigh University, Bethlehem, Pennsylvania 18015
1	Mr. J. D. Walton, Jr., EES, Georgia Tech., Atlanta, Georgia 30332
1	Mr. Y. Baskin, Manager Inorganic Chemical Research, Technical Center, Ferro Corporation, 7500 East Pleasant Valley Road, Independence, Ohio 44131
3	Mr. Robert Beck, Dept. Head, Development Materials, Teledyne CAE, 1330 Laskey Road, Toledo, Ohio 43601 Dr. Eli Benstien, Director of Engineering Mrs. Marlene S. Dowdell, Librarian
1	Dr. J. E. Burke, General Electric Company, Corporate Research & Development, P.O. Box 8, Schenectady, New York 12301
1	Dr. C. A. Bruch, Manager, Advanced Studies, General Electric Company, Aircraft Engine Group, Cincinnati, Ohio 45215
1	Mr. A. R. Canady, Caterpillar Tractor Company, Technical Center Building F, Peoria, Illinois 61602
1	Mr. William B. Crandall, IIT Research Institute, 10 West 35th Street, Chicago, Illinois 43601

ARMY MATERIALS AND MECHANICS RESEARCH CENTER
WATERTOWN, MASSACHUSETTS 02172

TECHNICAL REPORT DISTRIBUTION

No. of Copies	To
1	Mr. L. M. Donley, Owens Illinois Glass, 1900 North Westwood Avenue, Toledo, Ohio 43601
1	Mr. E. J. Dulis, President, Colt Industries, Materials Research Center, Box 88, Pittsburgh, PA 15230
1	Mr. O. Prachar, Passenger Car Turbine Department, Engineering Staff, General Motors Technical Center, Warren, MI 48090
1	Mr. Winston Duckworth and Mr. Lewis E. Hulbert, Battelle Columbus Laboratories, 505 King Avenue, Columbus, Ohio 43201
1	Mr. R. Engdahl, Energy Research Corporation, Bethel, Connecticut 06801
1	Mr. Peter L. Fleischner, National Beryllia Corp., Haskell, New Jersey 07420
1	Mr. O. I. Ford, Technical Manager, Combustor Systems, Aerojet Liquid Rocket Company, P.O. Box 18222, Sacramento, Calif. 95813
1	Mr. Chester T. Sims, Manager, Advanced Materials General, Electric Company, Gas Turbine Products Div., Schenectady, N.Y. 12301
1	Mr. E. W. Hauck, Market Manager Engine, Components, Norton Company, 1 New Bond Street, Worcester, Massachusetts 01606
1	Mr. M. Herman, Detroit Diesel Allison Division, General Motors Corporation, Indianapolis Operations, P.O. Box 894, Indianapolis, Indiana 46206
1	Mr. J. B. Mann, Director of Research, Chrysler Corporation, P.O. Box 1118, Detroit, MI 48231
1	Mr. James F. Holloway, Materials Project Engineer, Pratt & Whitney Corporation, 400 Main Street, E. Hartford, Connecticut 06108
1	Dr. Paul Jorgensen, Associate Director, Materials Laboratory, Stanford Research Institute, Menlo Park, California 94025
1	Dr. A. V. Illyn, Technical Director, Refractories Division, Babcock & Wilcox, Old Savannah Road, Augusta, Georgia 30903
1	Mr. Paul F. Jahn, Vice President, Fiber Materials, Inc., Broadway and Main Streets, Graniteville, Massachusetts 01829

ARMY MATERIALS AND MECHANICS RESEARCH CENTER
WATERTOWN, MASSACHUSETTS 02172

TECHNICAL REPORT DISTRIBUTION

No. of Copies	To
1	Dr. Robert F. Kirby, Materials Engineering Dept. 93-393M, AiResearch Manufacturing Company, Div. of the Garrett Corporation, Sky Harbor Airport, 402 South 36th Street, Phoenix, Arizona 85034
1	Mr. John G. Lanning, Corning Glass Works, Corning, NY 14830
1	Mr. William D. Long, Manager, Product Development, K-Ramics, Kaman Sciences Corporation, Garden of the Gods Road, Colorado Springs, Colorado 80907
1	Mr. James Lynch, Metals & Ceramics Information Center, Battelle Columbus Laboratories, 505 King Avenue, Columbus Ohio 43201
1	Mr. L. Lucarelli, Manager of Materials, Corporate R&D Center, Kelsey-Hayes Company, 2500 Green Road, Ann Arbor, MI 48105
1	Mr. C. H. McMurtry, Project Manager, Research and Development Div., The Carborundum Company, Niagara Falls, New York 14302
1	Dr. Deo Mattoon, Sing Sing Road, Horseheads, New York 14845
1	Mr. G. Kookootsedes, Market Development, Resins and Chemicals, Dow Corning, Midland, Michigan 48640
1	Professor Burton Paul, Dept. of Mechanical Engineering, University of Pennsylvania, Philadelphia, Pennsylvania 19104
1	Mr. Y. K. Pei, Owens Illinois Glass, 1020 North Westwood Avenue, Toledo, Ohio 43607
1	Dr. Jerry D. Plunkett, President, Materials Consultants, Inc., 2150 South Josephine Street, Denver, Colorado 80210
1	Mr. J. A. Rubin, President, Ceradyne Incorporated, 8948 Fullbright Avenue, Chatsworth, California 91311
1	Mr. P. Hansen, Director of Corporate Dev., Kawecki-Berylco Industries, Inc., P.O. Box 1462, Reading, Pennsylvania 19603
1	Mr. Jack W. Sawyer, Gas Turbine International, 4519 Eighteen Street North, Arlington, VA 22207
1	Mr. D. W. McLaughlin, Research & Development Div., Mechanical Technology, Inc., 968 Albany-Shaker Road, Latham, New York 12110

ARMY MATERIALS AND MECHANICS RESEARCH CENTER
WATERTOWN, MASSACHUSETTS 02172

TECHNICAL REPORT DISTRIBUTION

No. of Copies	To
1	Mr. A. R. Stetson, Chief, Process Research Laboratories, Mail Zone R-1, Solar Div. of Int. Harvester Company, 2200 Pacific Highway, San Diego, California 92112
1	Dr. M. L. Torti, Norton Company, 1 New Bond Street, Worcester Massachusetts 01606
1	Dr. William Rhodes, Applied Technology Division, Avco Corp., Lowell Industrial Park, Lowell, Massachusetts 01851
1	Mr. Francis L. VerSnyder, Manager, Materials Engineering and Research Lab, Pratt & Whitney Corporation, 400 Main Street, E. Hartford, Connecticut 06108
1	Mr. McCoy, Materials Engineering, Garrett-AiResearch Dept. 93-393M, 412 South 36th Street, Phoenix, Arizona 85034
1	Mr. Donald E. Weyer, Dow Corning Corporation, Midland, MI 48640
1	Dr. Michael Guinan, B. Div./L-24, P.O. Box 808, Lawrence Livermore Laboratory, Livermore, California 94550
1	Dr. Mark Wilkins, B Div./L-24, P.O. Box 808, Lawrence Livermore Laboratory, Livermore, California 94550
1	Dr. Charles J. McMahon, Jr., Assoc. Prof. Materials Science, School of Metallurgy & Materials Science, University of Pennsylvania, 3231 Walnut Street, Philadelphia, Pennsylvania
1	Mr. Gaylord D. Smith, The International Nickel Co., Inc., 1 New York Plaza, New York, New York 10004
1	Mr. H. R. Schelp, Garrett Corporation, 9851 Sepulveda Blvd., Los Angeles, California 90009
1	Dr. Robert Widmer, President, Industrial Materials Technology 19 Wheeling Avenue, Woburn, Massachusetts
1	Dr. William Wells, Lawrence Livermore Lab, Livermore, California 94550
1	Prof. R. P. Kroon, University of Pennsylvania, Philadelphia, Pennsylvania
1	Dr. Paul G. Shewmon, D212, Argonne National Laboratory, 9700 South Cass Avenue, Argonne, Illinois 60439

ARMY MATERIALS AND MECHANICS RESEARCH CENTER
WATERTOWN, MASSACHUSETTS 02172

TECHNICAL REPORT DISTRIBUTION

No. of Copies	To
1	Dr. Thomas D. McGee, Professor of Ceramic Engineering, Iowa State University, Ames, Iowa 50010
1	Mr. Joe Glotz, Department of the Navy, Naval Air Propulsion Test Center, Trenton, New Jersey 08628
1	Mr. John Miguel, Naval Underwater System Center, Newport, Rhode Island
1	Mr. Robert Benham, AEP-22, U.S. Naval Air Propulsion Test Center (AE), Philadelphia, PA 19112
1	Mr. R. Barry Strachan, Williams Research Corp., Walled Lake, Michigan 48088
1	Mr. S. Walosin, Curtis-Wright Corp. One Passaic Street, Woodridge, N.J. 07075
1	Prof. Marc Richman, Engineering Division, Brown University, Providence, Rhode Island 02912
1	Mr. R. Rice, Naval Research Laboratory, Washington, D.C. 20390
1	Mr. George A. Wacker, Head Metal Physics Br., Naval Ships Research & Development Center, Annapolis, Md. 21402, ATTN: Code 2812
1	Dr. R. Charles, Manager Ceramics Branch, General Electric Co., Corporate R & D Center, P.O. Box 8, Schenectady, New York 12301
1	Mr. C. F. Cline, Manager, Strength Physics Department, Allied Chemical Corporation, P.O. Box 1021R, Morristown, New Jersey 07960
1	Dr. J. T. Bailey, American Lava Corp., Chattanoga, Tennessee 37405
1	Mr. S. T. Wlodek, Cabot Corp. Stellite Div., 1020 West Park Avenue, Kokomo, Indiana 46901
2	Cummins Engine Company, Inc., Columbus, Indiana 47201 Mr. R. Kano, Mr. K. J. Mather
1	Mr. J. D. Mote, EF Industries, Inc., 1301 Courtesy Rd. Louisville, Colorado 80027
1	Mr. William E. Gurwell, Eaton Corporation, Research Center 26201 Northwestern Highway, Southfield, MI 48076

ARMY MATERIALS AND MECHANICS RESEARCH CENTER
WATERTOWN, MASSACHUSETTS 02172

TECHNICAL REPORT DISTRIBUTION

No. of Copies	To
1	Mr. Robert W. Gibson, Jr., Head, Library Dept. General Motors Corporation GM Technical Center, Warren, MI 48090
1	Mr. R. L. Lormand, Lawrence Radiation Lab, P.O. Box 808, Livermore, California 94550
2	Ms. Bolick, National Aeronautics and Space Adminstration Goddard Space Flight Center, Greenbelt, Maryland 20771
1	Mr. Neil T. Saunders, Ch. Mat'ls Appl'n Branch, National Aeronautics and Space Administration, Lewis Research Center, Cleveland, Ohio 44135
1	Ms. Rayna Lee Caplan, Librarian, Northern Research and Engineering Corp., 219 Vassar Street, Cambridge, Mass. 02139
1	Mrs. Jame Bookmyer, Info. Services Div., PPG Industries, Inc., P.O. Box 11472, Pittsburgh, Pennsylvania 15238
1	Mr. P. W. Parsons, Manager, Commercial Research Dept., Stackpole Carbon Company, St. Marys, Pennsylvania 15857
1	Ms. Lucille Steelman, Order Librarian, Stanford Research Institute ATTN: G-037 Library, Menlo Park, Calif. 94025
1	Technical Library, TRW Equipment, TRW Inc., 23555 Euclid Avenue, Cleveland, Ohio 44117
1	Dr. E. P. Flint, U.S. Department of Interior, Bureau of Mines, Room 4513, Interior Bldg., Washington, D.C. 20240
1	Mr. W. Wheatfall, Naval Ship R & D Lab, Code 2812, Annapolis, Maryland 21402
1	Dr. Joseph E. Motherway, University of Bridgeport, Bridgeport, Connecticut 06602
1	Dr. Soloman Musikant, Manager, Metallurgy & Ceramics Lab General Electric Valley Forge, Valley Forge, PA
1	Dr. Bruce A. Ewing, Chief Mat'ls Development, Mat'ls & Process Technology Lab., Avco Corporation, 550 S. Main Street Stratford, Connecticut 06497
1	Mr. Donald Lapades, The Aerospace Corporation, P.O. Box 92957, Los Angeles, California 90009

ARMY MATERIALS AND MECHANCIS RESEARCH CENTER
WATERTOWN, MASSACHUSETTS 02172

TECHNICAL REPORT DISTRIBUTION

No. of Copies	To
1	Mr. Thomas J. Ahrens, Assoc. Prof. of Geophysics, California Institute of Technology, Seismological Laboratory, 295 San Rafael Avenue, P.O. Bin 2, Arroyo Annex, Pasadena, California 91109
1	Mr. Victor de Biasi, Editor, Gas Turbine World, P.O. Box 494, Southport, Connecticut 06490
1	SKF Industries, Inc., Engineering & Research Center, 1100 1st Avenue, King of Prussia, PA 19406, ATTN: Warren E. Jameson & Harish Dalal
1	Dr. Edward Reynolds, General Motors Technical Center, Passenger Car Turbine Division, Warren, MI 48090
1	Dr. Wm. R. Freeman, Jr., V.P. and Technical Director, Howmet Corporation, Superalloy Group, One Misco Drive, Whitehall, Michigan 47461
1	Mr. D. William Lee, Arthur D. Little, Inc. Acorn Park, Cambridge, Massachusetts 02140
1	Dr. Edward V. Clougherty, Project Director, Manlabs, Inc., 21 Erie Street, Cambridge, Massachusetts 02139
1	Prof. Morris E. Fine, Northwestern University, The Technological Institute, Dept. of Materials Science, Evanston, Illinois
1	Coors Porcelain Company, 600 Ninth Street, Golden, Colorado 80401, ATTN: Mr. M. R. Nadler
1	Prototype Developments Associates, Esplanade I, Suite 204 3001 Red Hill Avenue, Costa Mesa, California 92626, ATTN: Mr. John I. Slaughter, President
1	Raytheon Company, Research Division Library, Foundry Avenue, Waltham, Massachusetts 02154, ATTN: Ms. Madaleine Bennett, Librarian
1	Prof. T. L. Chu, Southern Methodist University, Institute of Technology, Electronic Sciences Center, Dallas, Texas 75222
1	Mr. H. Stuart Starrett, Head, Mechanics Section, Southern Research Institute, 2000 Ninth Avenue South, Birmingham, Alabama 35205

ARMY MATERIALS AND MECHANICS RESEARCH CENTER
WATERTOWN, MASSACHUSETTS 02172

TECHNICAL REPORT DISTRIBUTION

No. of Copies	To
1	Dr. O. Conrad Trulson, Union Carbide Corporation, Carbide Products Division, 270 Park Avenue, New York, New York 10017
1	Prof. Earl R. Parker, University of California, Department of Materials Science and Engineering, 286 Hearst Mining Building, Berkeley, California 94720
1	Mr. Willard H. Sutton Manager, Ceramics Projects, Special Metals Corporation, New Hartford, New York 13413
1	Dr. Maurice J. Sinnott, Department of Chemical & Metallurgical Engineering, The University of Michigan, Ann Arbor, MI 48104
1	Mrs. Benacguista, R.I.A.S., 1450 South Rolling Road, Baltimore, MD 21227
1	Prof. M. C. Shaw, Head, Department of Mechanical Engineering, Cornegie-Mellon University, Pittsburgh, Pennsylvania 15213
1	Mr. Gail Eichelman, Manufacturing Processes Div., Air Force Mateials Laboratory, Wright-Patterson AFB, Ohio 45433
1	Dr. J. C. Lewis, Metals & Minerals Economics Div. Battelle Memorial Institute, 505 King Avenue, [illegible]mbus, Ohio 43201
1	Massachusetts Institute of Technolog[illegible], Cambridge, Massachusetts, 02139, ATTN: Prof. D. W. Kingery, Rm. 13-4090
1	Prof. Michael F. Ashby, Gordon McKay Professor of Metallurgy, Pierce Hall, Harvard University, Cambridge, Massachusetts 02138
1	Dr. Richard G. McKaig, Owens-Illinois Development Center, P.O. Box 1035, Toledo, Ohio 43666
1	Prof. I. B. Cutler, University of Utah, College of Engineering Division of Materials Science and Engineering, Salt Lake City, Utah 84112
3	Authors
205	Total copies distributed

Army Materials and Mechanics Research Center, Watertown, Massachusetts 02172

AD _____
Distribution Limited

BRITTLE MATERIALS DESIGN
HIGH TEMPERATURE GAS TURBINE

Key Words

Arthur F. McLean, Eugene A. Fisher, Ford Motor Company, Dearborn, Michigan 48121
Raymond J. Bratton, Westinghouse Electric Corporation, Pittsburgh, Pennsylvania 15235

Technical Report AMMRC CTR 73-9 March 1973
223 pps - 186 illus. - 23 tables, Contract DAAG 46-71-C-0162, ARPA Order Number 1849, Interim Report, July 1, 1972 to December 31, 1972

Gas turbine engine
Brittle design
Ceramics
High temperature materials
Silicon nitride
Silicon carbide
Non-destructive tests
Mechanical properties

The "Brittle Materials Design, High Temperature Gas Turbine" program is to demonstrate successful use of brittle materials in demanding high temperature structural applications. A small vehicular gas turbine and a large stationary gas turbine, each utilizing uncooled ceramic components, will be used in this iterative design and materials development program. Both the contractor, Ford Motor Company, and the subcontractor, Westinghouse Electric Corporation, have had in-house research programs in this area prior to this contract.

In the vehicular turbine project, steady state and transient stresses were determined for a monolithic turbine rotor of hot-pressed silicon nitride. A new rotor concept, using both hot-pressed and reaction-sintered silicon nitride, has been analyzed for steady-state stresses; work on bonding the two materials appears promising. Improvements in chemically vapor deposited silicon carbide rotors include the forming of hoops of sufficient thickness and the production of material of considerably improved purity. Blade cracking of the first stage ceramic stator was duplicated on a thermal shock test rig, leading to improved durability through a change in the blade design. Some fabrication variables of reaction-sintered silicon nitride were studied, which indicate methods for material improvements.

In the stationary turbine project, a model of the 3-piece stator vane assembly demonstrated that design integrity was maintained when differential motion exceeded design limits fivefold. The 3-dimensional finite element stress and heat transfer analytical program has been applied to rotor blades, and preliminary results are presented. Statistical data treatment has been applied to hot-pressed silicon nitride, and additional property data plus corrosion testing results are presented for hot-pressed silicon carbide. It was found necessary to design and construct a new static rig, delaying testing under turbine conditions until August.

Army Materials and Mechanics Research Center, Watertown, Massachusetts 02172

AD _____
Distribution Limited

BRITTLE MATERIALS DESIGN
HIGH TEMPERATURE GAS TURBINE

Key Words

Arthur F. McLean, Eugene A. Fisher, Ford Motor Company, Dearborn, Michigan 48121
Raymond J. Bratton, Westinghouse Electric Corporation, Pittsburgh, Pennsylvania 15235

Technical Report AMMRC CTR 73-9 March 1973
223 pps - 186 illus. - 23 tables, Contract DAAG 46-71-C-0162, ARPA Order Number 1849, Interim Report, July 1, 1972 to December 31, 1972

Gas turbine engine
Brittle design
Ceramics
High temperature materials
Silicon nitride
Silicon carbide
Non-destructive tests
Mechanical properties

The "Brittle Materials Design, High Temperature Gas Turbine" program is to demonstrate successful use of brittle materials in demanding high temperature structural applications. A small vehicular gas turbine and a large stationary gas turbine, each utilizing uncooled ceramic components, will be used in this iterative design and materials development program. Both the contractor, Ford Motor Company, and the subcontractor, Westinghouse Electric Corporation, have had in-house research programs in this area prior to this contract.

In the vehicular turbine project, steady state and transient stresses were determined for a monolithic turbine rotor of hot-pressed silicon nitride. A new rotor concept, using both hot-pressed and reaction-sintered silicon nitride, has been analyzed for steady-state stresses; work on bonding the two materials appears promising. Improvements in chemically vapor deposited silicon carbide rotors include the forming of hoops of sufficient thickness and the production of material of considerably improved purity. Blade cracking of the first stage ceramic stator was duplicated on a thermal shock test rig, leading to improved durability through a change in the blade design. Some fabrication variables of reaction-sintered silicon nitride were studied, which indicate methods for material improvements.

In the stationary turbine project, a model of the 3-piece stator vane assembly demonstrated that design integrity was maintained when differential motion exceeded design limits fivefold. The 3-dimensional finite element stress and heat transfer analytical program has been applied to rotor blades, and preliminary results are presented. Statistical data treatment has been applied to hot-pressed silicon nitride, and additional property data plus corrosion testing results are presented for hot-pressed silicon carbide. It was found necessary to design and construct a new static rig, delaying testing under turbine conditions until August.

Army Materials and Mechanics Research Center, Watertown, Massachusetts 02172

AD _____
Distribution Limited

BRITTLE MATERIALS DESIGN
HIGH TEMPERATURE GAS TURBINE

Key Words

Arthur F. McLean, Eugene A. Fisher, Ford Motor Company, Dearborn, Michigan 48121
Raymond J. Bratton, Westinghouse Electric Corporation, Pittsburgh, Pennsylvania 15235

Technical Report AMMRC CTR 73-9 March 1973
223 pps - 186 illus. - 23 tables, Contract DAAG 46-71-C-0162, ARPA Order Number 1849, Interim Report, July 1, 1972 to December 31, 1972

Gas turbine engine
Brittle design
Ceramics
High temperature materials
Silicon nitride
Silicon carbide
Non-destructive tests
Mechanical properties

The "Brittle Materials Design, High Temperature Gas Turbine" program is to demonstrate successful use of brittle materials in demanding high temperature structural applications. A small vehicular gas turbine and a large stationary gas turbine, each utilizing uncooled ceramic components, will be used in this iterative design and materials development program. Both the contractor, Ford Motor Company, and the subcontractor, Westinghouse Electric Corporation, have had in-house research programs in this area prior to this contract.

In the vehicular turbine project, steady state and transient stresses were determined for a monolithic turbine rotor of hot-pressed silicon nitride. A new rotor concept, using both hot-pressed and reaction-sintered silicon nitride, has been analyzed for steady-state stresses; work on bonding the two materials appears promising. Improvements in chemically vapor deposited silicon carbide rotors include the forming of hoops of sufficient thickness and the production of material of considerably improved purity. Blade cracking of the first stage ceramic stator was duplicated on a thermal shock test rig, leading to improved durability through a change in the blade design. Some fabrication variables of reaction-sintered silicon nitride were studied, which indicate methods for material improvements.

In the stationary turbine project, a model of the 3-piece stator vane assembly demonstrated that design integrity was maintained when differential motion exceeded design limits fivefold. The 3-dimensional finite element stress and heat transfer analytical program has been applied to rotor blades, and preliminary results are presented. Statistical data treatment has been applied to hot-pressed silicon nitride, and additional property data plus corrosion testing results are presented for hot-pressed silicon carbide. It was found necessary to design and construct a new static rig, delaying testing under turbine conditions until August.

Army Materials and Mechanics Research Center, Watertown, Massachusetts 02172

AD _____
Distribution Limited

BRITTLE MATERIALS DESIGN
HIGH TEMPERATURE GAS TURBINE

Key Words

Arthur F. McLean, Eugene A. Fisher, Ford Motor Company, Dearborn, Michigan 48121
Raymond J. Bratton, Westinghouse Electric Corporation, Pittsburgh, Pennsylvania 15235

Technical Report AMMRC CTR 73-9 March 1973
223 pps - 186 illus. - 23 tables, Contract DAAG 46-71-C-0162, ARPA Order Number 1849, Interim Report, July 1, 1972 to December 31, 1972

Gas turbine engine
Brittle design
Ceramics
High temperature materials
Silicon nitride
Silicon carbide
Non-destructive tests
Mechanical properties

The "Brittle Materials Design, High Temperature Gas Turbine" program is to demonstrate successful use of brittle materials in demanding high temperature structural applications. A small vehicular gas turbine and a large stationary gas turbine, each utilizing uncooled ceramic components, will be used in this iterative design and materials development program. Both the contractor, Ford Motor Company, and the subcontractor, Westinghouse Electric Corporation, have had in-house research programs in this area prior to this contract.

In the vehicular turbine project, steady state and transient stresses were determined for a monolithic turbine rotor of hot-pressed silicon nitride. A new rotor concept, using both hot-pressed and reaction-sintered silicon nitride, has been analyzed for steady-state stresses; work on bonding the two materials appears promising. Improvements in chemically vapor deposited silicon carbide rotors include the forming of hoops of sufficient thickness and the production of material of considerably improved purity. Blade cracking of the first stage ceramic stator was duplicated on a thermal shock test rig, leading to improved durability through a change in the blade design. Some fabrication variables of reaction-sintered silicon nitride were studied, which indicate methods for material improvements.

In the stationary turbine project, a model of the 3-piece stator vane assembly demonstrated that design integrity was maintained when differential motion exceeded design limits fivefold. The 3-dimensional finite element stress and heat transfer analytical program has been applied to rotor blades, and preliminary results are presented. Statistical data treatment has been applied to hot-pressed silicon nitride, and additional property data plus corrosion testing results are presented for hot-pressed silicon carbide. It was found necessary to design and construct a new static rig, delaying testing under turbine conditions until August.

UNCLASSIFIED

Security Classification

DOCUMENT CONTROL DATA - R & D

(Security classification of title, body of abstract and indexing annotation must be entered when the overall report is classified)

1. ORIGINATING ACTIVITY *(Corporate author)*

Ford Motor Company
Dearborn, Michigan 48121

2a. REPORT SECURITY CLASSIFICATION

Unclassified

2b. GROUP

3. REPORT TITLE

Brittle Materials Design, High Temperature Gas Turbine

4. DESCRIPTIVE NOTES *(Type of report and inclusive dates)*

Interim Report, July 1, 1972 to December 31, 1972

5. AUTHOR(S) *(First name, middle initial, last name)*

Arthur F. McLean
Eugene A. Fisher
Raymond J. Bratton

6. REPORT DATE	7a. TOTAL NO. OF PAGES	7b. NO. OF REFS
March, 1973		13

8a. CONTRACT OR GRANT NO.	9a. ORIGINATOR'S REPORT NUMBER(S)
DAAG 46-71-C-0162 b. PROJECT NO. ARPA Order No. 1849 c. Project Code No. 1D10 d. Agency Accession No. DA OD 4733	AMMRC-CTR 73-9 9b. OTHER REPORT NO(S) *(Any other numbers that may be assigned this report)*

10. DISTRIBUTION STATEMENT

Distribution limited to U.S. Government agencies only; Test and Evaluation data; March 1973. Other requests for this document must be referred to the Director, Army Materials & Mechanics Research Center, ATTN: AMXMR-PL, Watertown, Massachusetts 02172

11. SUPPLEMENTARY NOTES	12. SPONSORING MILITARY ACTIVITY
	Army Materials and Mechanics Research Center, Watertown, Massachusetts 02172

13. ABSTRACT

The "Brittle Materials Design, High Temperature Gas Turbine" program is to demonstrate successful use of brittle materials in demanding high temperature structural applications. A small vehicular gas turbine and a large stationary gas turbine, each utilizing uncooled ceramic components, will be used in this iterative design and materials development program. Both the contractor, Ford Motor Company, and the subcontractor, Westinghouse Electric Corporation, have had in-house research programs in this area prior to this contract.

In the vehicular turbine project, steady state and transient stresses were determined for a monolithic turbine rotor of hot-pressed silicon nitride. A new rotor concept, using both hot-pressed and reaction-sintered silicon nitride, has been analyzed for steady-state stresses; work on bonding the two materials appears promising. Improvements in chemically vapor deposited silicon carbide rotors include the forming of hoops of sufficient thickness and the production of material of considerably improved purity. Blade cracking of the first stage ceramic stator was duplicated on a thermal shock test rig, leading to improved durability through a change in the blade design. Some fabrication variables of reaction-sintered silicon nitride were studied, which indicate methods for material improvements.

In the stationary turbine project, a model of the 3-piece stator vane assembly demonstrated that design integrity was maintained when differential motion exceeded design limits fivefold. The 3-dimensional finite element stress and heat transfer analytical program has been applied to rotor blades, and preliminary results are presented. Statistical data treatment has been applied to hot-pressed silicon nitride, and additional property data plus corrosion testing results are presented for hot-pressed silicon carbide. It was found necessary to design and construct a new static rig, delaying testing under turbine conditions until August.

DD FORM 1 NOV 68 1473 REPLACES DD FORM 1473, 1 JAN 64, WHICH IS OBSOLETE FOR ARMY USE.

Security Classification

14 KEY WORDS	LINK A		LINK B		LINK C	
	ROLE	WT	ROLE	WT	ROLE	WT
Gas turbine engine						
Brittle design						
Ceramics						
High-temperature materials						
Silicon nitride						
Silicon carbide						
Non-destructive tests						
Mechanical properties						